Delft University of Technology

On Multiaxial Fatigue of Welded Joints in Steel Maritime Structures
Strength and mechanism contributions

Bufalari, G.

Important note
To cite this publication, please use the final published version (if applicable).
Please check the document version above.

On
Multiaxial Fatigue of Welded Joints
in
Steel Maritime Structures

strength and mechanism contributions

Gabriele Bufalari

ON

MULTIAXIAL FATIGUE OF WELDED JOINTS IN STEEL MARITIME STRUCTURES

STRENGTH AND MECHANISM CONTRIBUTIONS

ON

MULTIAXIAL FATIGUE OF WELDED JOINTS IN STEEL MARITIME STRUCTURES

STRENGTH AND MECHANISM CONTRIBUTIONS

Dissertation

for the purpose of obtaining the degree of doctor
at Delft University of Technology
by the authority of the Rector Magnificus, prof. dr. ir. T.H.J.J. van der Hagen,
chair of the Board for Doctorates
to be defended publicly on
Wednesday 4, December 2024 at 10:00 o'clock

by

Gabriele BUFALARI

Master of Science in Yacht Design,
University of Genova, Italy
born in Orvieto (TR), Italy

This dissertation has been approved by the promotors.

Composition of the doctoral committee:

Rector Magnificus,	chairperson
Em. prof. dr. ir. M.L. Kaminski,	Delft University of Technology, *promotor*
Dr. ir. J.H. den Besten,	Delft University of Technology, *copromotor*

Independent members:

Dr. ir. J.J. Van der Cammen,	Bluewater Energy Services, NL
Em. prof. dr. C.M. Sonsino,	Fraunhofer Institute, DE
Prof. dr. L. Susmel,	University of Sheffield, UK
Prof. dr. M. Veljkovic,	Delft University of Technology
Prof. dr. ir. B.J. Boersma,	Delft University of Technology, reserve

An electronic copy of this dissertation is available at
`https://repository.tudelft.nl/`.

The Buddha taught that the three basic realities of the universe are that everything is constantly changing, nothing has any enduring essence, and nothing is completely satisfying

Yuval Noah Harari

CONTENTS

SUMMARY

Maritime structures, including offshore support vessels and floating wind turbines, are exposed to loads varying in time because of environmental factors (wind, waves) and operational conditions (machinery). Fatigue, a progressive crack growth mechanism appearing when loading is cyclic, a damage process, is a critical issue.

Fatigue cracks typically initiate at stress concentration areas. At materials level, stress concentrations appear at microscopic and mesoscopic scale as a result of defects, for example. At macro scale, stress concentrations typically develop at structures level. Connections like arc-welded joints as commonly used in steel structures to connect the members – plates and beams – are particularly fatigue sensitive.

The structural response in a maritime environment can be multiaxial, dependent on loading, geometry, and material properties. Simultaneously occurring external loads from wind, waves, heavy lifting operations and rotating turbine blades, amongst others, provide an important contribution. Geometry or material anisotropy induced variations in stiffness can introduce multiple load transfer mechanisms along dissimilar paths. The internal mode-I, mode-II and mode-III loading components can be in-phase; proportional (P), or out-of-phase; non-proportional (NP), respectively synchronous and asynchronous.

In plates and beams, the thickness is typically small relative to other dimensions, meaning internal mode-I loading components: normal forces and bending moments, are dominant. Mode-II in-plane shear forces are generally negligible. However, out-of-plane shear forces and torsion moments, mode-III components, can affect the primary mode-I response, meaning multiaxiality has to be considered for accurate fatigue life time estimates of arc-welded joints.

Fatigue damage modeling uses both intact and cracked geometry parameters to assess respectively the initiation and growth contributions. Fatigue life time N is predominantly spent in the notch-affected region, suggesting a notch characteristic intact geometry parameter can be used as the fatigue strength parameter S. However, for welded joints N is typically crack-growth defined, meaning a cracked geometry parameter makes sense as well. In steel maritime structures, the response is predominantly linear elastic, meaning S is typically stress-based, especially for mid- and high-cycle fatigue. The relationship between S and N often shows a log-log linear dependency according to Basquin's equation: $\log(N) = \log(C) - m \cdot \log(S)$.

The intercept $\log(C)$ and slope m represent strength and mechanism contributions, different for mode-I and mode-III. Fatigue tests show that mode interaction, especially in NP cases, can be detrimental and a straightforward superposition is insufficient.

Focus of the research as presented in this thesis is on multiaxial fatigue of arc-welded joints in steel maritime structures. Subdivided into an introduction (Chapter 1), a fundamental scope (Chapters 2 to 4) and an experimental part (Chapter 5), aim is to provide an accurate, reliable, yet simple methodology.

Multiaxial fatigue modeling aspects in the fundamental scope are about the type of criterion, taking similarities between static and fatigue strength into account, as well the differences between finite and infinite life criteria. To handle random multiaxial loading conditions, the assessment includes selection of the damage plane and cycle counting to address the challenges related to non-proportionality. Last but not least, fatigue damage accumulation model considerations are essential to be able to provide accurate life time estimates.

Since the topology of maritime structures is responsible for a predominant mode-I response contribution and at the same time the fatigue life time is crack growth defined (rather than initiation, a shear controlled process) because of welding induced defects, the choice of a normal stress based von Mises failure criterion is – no matter if S is a an intact or cracked geometry parameter – straightforward. However, a response level dependent shear strength coefficient $\beta(N(S))$ has been introduced, rather than a constant one. Based on fatigue test data from literature, the strength and mechanism contributions have been established using mode-specific coefficients. Cracks typically develop first in the plate thickness direction, identifying the fracture plane as the critical one for damage evaluation. Cycle counting is performed in the von Mises plane to account for non-proportionality cycle-by-cycle. A linear damage accumulation model has been adopted, since good performance with advanced fatigue strength criteria was already obtained before. For mid-cycle fatigue, a resistance related non-linearity is not required.

Strength and mechanism contributions are already available for mode-I fatigue of arc-welded joints, either based on intact or cracked geometry parameters, but still had to be obtained for mode-III. Starting with the effective notch stress S_e as intact geometry parameter, mode-III characteristics are investigated using test data from literature. Novel, semi-analytical, through-thickness weld toe notch stress distribution formulations along the critical fracture plane for mode-III loading in plates and beams with circular cross-section are established first as input for S_e. Most likely material characteristic length ρ^* and mean stress coefficient γ estimates, mode-specific strength and mechanism contributions, have been determined. Evaluation of the mode-III arc-welded joint fatigue resistance data shows an improved accuracy of the fatigue life time estimates for S_e in comparison to results obtained using parameters from literature.

Analysis of mode-{I, III} multiaxial fatigue resistance data from literature using S_e with the uniaxial mode-I and mode-III coefficients shows superior performance in comparison to results obtained using other existing methodologies as available in codes, guidelines and literature. The impressive performance confirms the necessity of involving mode-specific strength and mechanism contributions. However, mode interaction appears to be the next step to further improve life time estimates in case of multiaxial response conditions and can be addressed in future research.

Since notches contain welding induced defects, the initiation contribution to the fatigue life is negligible, meaning crack growth is the governing factor.

The semi-analytical weld notch stress distribution formulations for intact geometries are converted to a cracked geometry equivalent, introducing the weld notch stress intensity factor (SIF) K. New mode-III formulations are established for plates and beams with a circular cross-section. For cyclic loading conditions, K turns into a crack growth driving force ΔK, potentially developing defects into cracks. The Paris relation is modified to incorporate both the elastoplasticity affected notch stress intensity as well as the elastic far field contribution, introducing a two-stage crack growth model as used to establish the total stress parameter S_T. Uniaxial mode-I estimates for the elastoplasticity coefficient n and mean stress coefficient γ, a strength and mechanism contribution, are already available, but mode-III estimates are established using fatigue test data from literature.

The life time estimate performance for S_T and S_e is comparable, both for uniaxial mode-III and multiaxial mode-{I, III} fatigue. Like for S_e, mode interaction is observed for S_T as well. With respect to S_e, the scatter in multiaxial proportional fatigue data is relatively small for S_T and can be attributed to the elastoplasticity coefficient. While n appears to be a more explicit measure affecting one-to-one crack growth behavior, ρ^* is rather an averaging implicit measure reflecting the material characteristic length for (mixed) mode-{I, III} response conditions. In this respect, S_T can be considered as one step closer to the actual physics of the fatigue damage process. At the same time, the averaging mechanism of S_e seems superior in accommodating a large variety of data sets. In general, S_T provides slightly more accurate lifetime estimates, but in view of increased parameter complexity and computational efforts, S_e might be preferred to use for multiaxial fatigue assessment.

The fatigue data available in literature has been used to establish a single $S - N$ design curve for general applications based on average weld quality, where both $S = S_e$ or $S = S_T$ can be used. Depending on weld quality, a specific data set may be closer to either the lower or upper bound of the data scatter band.

However, the amount of available data in literature is limited because of the challenges to generate a multiaxial stress state, especially in case of non-proportionality. In order to be able to do multiaxial fatigue tests for a wide range of application and flexibility with respect to specimen size and material strength, a multiaxial test rig with high loading capacity in six degrees of freedom, a hexapod (Stewart platform), has been developed. The hexapod offers unparalleled performance in terms of loading combinations, accuracy, and system stability.

In the experimental scope, uniaxial and multiaxial mode-{I, III} fatigue tests of offshore-quality welds have been conducted using the hexapod, revealing a very high fatigue resistance. Life time estimates based on the $S - N$ design curves for average weld quality are, however, too conservative. A dedicated curve for high-quality welds has been established based on both S_e or S_T with representative coefficients. Despite the lower coefficient confidence because of limited data size, the lifetime estimates are more accurate, justifying a dedicated design curve.

SAMENVATTING

Maritieme constructies, zoals schepen voor offshore dienstverlening en drijvende windturbines, worden blootgesteld aan wisselende belastingen die een gevolg zijn van omgevingsfactoren (wind, golven) en operationele omstandigheden (machines). Vermoeiing, een progressief scheurgroei mechanisme dat optreedt bij wisselende belastingen, is derhalve een groot probleem.

Vermoeiingsscheuren ontstaan meestal op hoogbelaste locaties, zoals gebieden met spanningsconcentraties. Op materiaal niveau betreft het concentraties op micro- en mesoschaal die o.a. het resultaat zijn van defecten. Op macroschaal zijn de concentraties die ontstaan op constructie niveau bij het veelal toegepaste booglassen om de elementen – platen en dunwandige balken – te verbinden, het meest kritisch.

De constructie respons in een maritieme omgeving kan multiaxiaal zijn. De mate waarin is afhankelijk van de belasting, de geometrie en de materiaaleigenschappen. Het gelijktijdig optreden van verschillende externe belastingen ten gevolge van bijvoorbeeld wind, golven, zware hijswerkzaamheden en draaiende windturbine bladen, draagt hieraan bij. Variaties in stijfheid door geometrie of materiaalanisotropie zorgen voor meerdere mechanismen waarbij de interne belasting vanuit verschillende richtingen wordt overgedragen. De mode-I, mode-II en mode-III componenten kunnen zowel in-fase (proportioneel) als uit-fase (niet-proportioneel) optreden, respectievelijk synchroon en asynchroon.

Van platen en dunwandige balken is de dikte afmeting klein ten opzichte van de andere dimensies, waardoor de interne mode-I belastingscomponenten: normaalkrachten en buigend momenten, dominant zijn. De mode-II schuifkrachten in het vlak zijn doorgaans verwaarloosbaar. Echter, schuifkrachten uit het vlak en torsiemomenten, mode-III componenten, kunnen de mode-I gedomineerde respons beïnvloeden, waardoor multiaxialiteit niet buiten beschouwing kan worden gelaten voor het nauwkeurig schatten van de vermoeiingslevensduur van met name lasverbindingen.

Vermoeiingsschademodellen maken gebruik van zowel intacte- als scheur gerelateerde geometrieparameters om initiatie en groei bijdragen te kunnen beoordelen. Omdat de vermoeiingslevensduur N zich voornamelijk afspeelt in het spanningsconcentratie gebied, is het gebruik van een intacte geometrieparameter S als vermoeiingssterkteparameter gerechtvaardigd. Vanwege defecten is N voor lasverbindingen echter voornamelijk scheurgroei bepaald, wat een scheur gerelateerde parameter een gelijkwaardig alternatief maakt. In maritieme constructies van staal, waarbij het materiaal zich voornamelijk lineair elastisch gedraagt, is S meestal gebaseerd op spanningen, vooral bij vermoeiing van midden- en hoogcyclische aard. De relatie tussen S en N laat zich veelal log-log lineair beschrijven m.b.v. de formulering van Basquin: $\log(N) = \log(C) - m \cdot \log(S)$.

Het snijpunt met de horizontale as $\log(C)$ en de helling m vertegenwoordigen respectievelijk een bijdrage in termen van sterkte en mechanisme, die bovendien verschillend zijn voor mode-I en mode-III. Vermoeiingstesten tonen aan dat mode-interactie, vooral in het geval van een niet-proportionele respons, nadelig kan zijn en dat een superpositie niet toereikend is.

Het onderzoek zoals gepresenteerd in dit proefschrift richt zich op het beoordelen van multiaxiale vermoeiingsschade van gelaste verbindingen in maritieme constructies van staal. Onderverdeeld in een inleiding (Hoofdstuk 1), een fundamentele scope (Hoofdstukken 2-4) en een experimenteel gedeelte (Hoofdstuk 5) is het onderzoek uitgevoerd met als doel om een nauwkeurige, betrouwbare en toch eenvoudige methode te realiseren.

De modelvormingsaspecten van multiaxiale vermoeiing van de fundamentele scope hebben in eerste instantie betrekking op het type criterium, met inachtname van de overeenkomsten tussen statische- en vermoeiingssterkte, evenals de verschillen tussen criteria voor eindige en oneindige levensduur. Om generiek elke multiaxiale respons conditie te kunnen handelen, zijn selectie van het schadevlak en het tellen van cycli uiterst relevant, inclusief manieren om niet-proportionaliteit in rekening te brengen. Tenslotte zijn de overwegingen m.b.t. het vermoeiingsschade accumulatie model essentieel.

Omdat de tolopogie van maritieme constructies zodanig is dat in principe de mode-I respons bijdrage domineert en omdat de vermoeiingslevensduur voornamelijk wordt bepaald door scheurgroei t.g.v. defecten in de las (en niet door initiatie; een schuifspanning gedomineerd proces), ligt – afgezien van een intacte- of scheur gerelateerde geometrie parameter – de keuze voor een op normaalspanning gebaseerd von Mises faalcriterium voor de hand. Als schuifsterktecoëfficiënt is echter geen constante, maar een responsniveau afhankelijkheid geïntroduceerd: $\beta(N(S))$. Met behulp van vermoeiingstestgegevens uit de literatuur zijn hiervoor de bijdragen van sterkte en mechanisme geanalyseerd d.m.v. mode specifieke coëfficiënten. Aangezien scheuren zich meestal eerst ontwikkelen in de richting van de plaatdikte, is het breukvlak als kritisch beschouwd voor het vaststellen van de vermoeiingsschade. Cycli worden geteld in de von Mises ruimte en niet-proportionaliteit wordt per wisseling meegenomen. Er is een lineair schade accumulatiemodel geïmplementeerd, dat reeds eerder goede prestaties heeft laten zien in combinatie met geavanceerde vermoeiingsparameters. Voor vermoeiing van midden-cyclische aard is een vermoeiingsweerstand gerelateerde niet-lineariteit overbodig.

De bijdragen van sterkte en mechanisme zijn al eerder bepaald voor mode-I vermoeiing van gelaste verbindingen, zowel voor intacte- als voor scheur gerelateerde geometrieparameters, maar moest nog worden onderzocht voor mode-III.

Met behulp van de effectieve spanningsparameter S_e, een intacte geometrie beschrijving, zijn de mode-III kenmerken bepaald op basis van test data uit de literatuur. Hiervoor zijn eerst semi-analytische formuleringen van de spanningsverdeling bij de lasteen langs het kritische breukvlak opgesteld, die zowel kunnen worden gebruikt voor platen als voor dunwandige balken met een cirkelvormige doorsnede. Vervolgens zijn de meest waarschijnlijke waarden van de materiaalkarakteristieke lengte ρ^* en de gemiddelde

spanningscoëfficiënt γ vastgesteld; mode specifieke mechanisme en sterkte aspecten. Evaluatie van de vermoeiingsweerstand op basis van S_e toont aan dat ten opzichte van andere parameters een nauwkeuriger schatting van de levensduur kan worden verkregen.

Analyse van mode-{I, III} multiaxiale vermoeiingsdata uit de literatuur m.b.v. de uniaxiale mode-I en mode-III coefficienten voor S_e bewijst dat in vergelijking met methoden zoals beschikbaar in voorschriften, richtlijnen en literatuur een significante verbetering kan worden behaald. De indrukwekkende resultaten bevestigen de noodzaak van het in rekening brengen van mode specifieke bijdragen in termen van sterkte en mechanisme. Wat wel opvalt is dat mode interactie een volgende stap lijkt om de schatting van levensduur in geval van multiaxialiteit nog verder te verbeteren. Hier kan vervolgonderzoek in voorzien.

Omdat lassen defecten bevatten is de bijdrage van initiatie aan de vermoeiingslevensduur verwaarloosbaar, wat scheurgroei tot de bepalende factor maakt.

De semi-analytische spanningsverdelingen voor de intacte geometrie zijn derhalve omgezet naar een spanningsintensiteit K. Nieuwe formuleringen voor mode-III zijn opgesteld voor platen en dunwandige balken met cirkelvormige doorsnede. Voor een cyclische belasting wordt K de drijvende kracht achter scheurgroei: ΔK, waardoor defecten kunnen uitgroeien tot scheuren. De Paris-relatie is aangepast om zowel de door elastoplasticiteit beïnvloede bijdrage van de intensiteit in het spanningsconcentratiegebied alsook de elastische bijdrage van de verre veldspanning te beschrijven: een twee fasen scheurgroei model dat is gebruikt om de totale spanning S_T te bepalen. De uniaxiale mode-I elastoplasticiteitscoefficient n en de gemiddelde spanningscoëfficiënt γ, een bijdrage m.b.t. sterkte en mechanisme, waren al beschikbaar voor mode-I, maar voor mode-III zijn ze m.b.v. test data uit de literatuur vastgesteld.

De prestaties voor het schatten van de levensduur m.b.v. S_T zijn vergelijkbaar met die van S_e, voor zowel uniaxiale mode-III als multiaxiale mode-{I, III} vermoeiing. Ook voor S_T blijkt mode interactie een waarneembaar fenomeen. Ten opzichte van S_e is de spreiding in multiaxiale proportionele vermoeiingsdata kleiner, wat op conto van de elastoplasticiteitscoefficient kan worden geschreven. Terwijl n een maat lijkt te zijn die direct invloed heeft op scheurgroei gedrag, is ρ^* een meer indirecte maat die de materiaalkarakteristieke lengte voor mode-{I, III} vermoeiing beschrijft. In dat opzicht kan S_T als een stap dichter bij de fysica van het vermoeiingsschadeproces worden beschouwd. Tegelijkertijd lijkt het middelingsmechanisme van S_e effectief in het accommoderen van een grote verscheidenheid aan data sets. In het algemeen geeft S_T een iets nauwkeuriger schatting van de levensduur, maar afgezet tegen een grotere parameter complexiteit en meer rekeninspanning kan S_e beter worden gebruikt voor een multiaxiale vermoeiingsanalyse.

De vermoeiingsdata die beschikbaar is in de literatuur, is gebruikt om op basis van gemiddelde laskwaliteit een enkele S-N ontwerpcurve voor algemene toepassingen vast te stellen, waarbij zowel $S = S_e$ als $S = S_T$ kunnen worden gebruikt. Afhankelijk van de laskwaliteit kan een specifieke dataset meer tegen de onder- of bovengrens van de data spreidingsbandbreedte aan zitten.

De hoeveelheid beschikbare data in de literatuur is bovendien schaars vanwege de uitdagingen bij het genereren van een multiaxiale spanningstoestand, vooral in het geval van niet-proportionaliteit. Om proefstukken voor een brede toepassingsrange en flexibel m.b.t. grootte en materiaalsterkte te kunnen testen op multiaxiale vermoeiing is derhalve een nieuwe opstelling in hexapod configuratie ontwikkeld met een enorme capaciteit in zes graden van vrijheid. Deze opstelling biedt ongeëvenaarde prestaties voor wat betreft mogelijke belastingcombinaties, nauwkeurigheid en systeemstabiliteit.

Er zijn in de experimentele scope uniaxiale en multiaxiale mode-{I, III} vermoeiingstesten van lasverbindingen met offshore kwaliteit uitgevoerd m.b.v. de hexapod die een zeer goede vermoeiingsweerstand blijken te hebben. Een schatting van de levensduur op basis van de S-N ontwerpcurves voor gemiddelde laskwaliteit is daarom te conservatief. Derhalve is een specifieke curve voor lassen van hoge kwaliteit bepaald op basis van zowel S_e en S_T met representatieve coëfficiënten. Ondanks de lagere betrouwbaarheid van de coëfficiënten vanwege de beperkte data omvang is de schatting van de levensduur meer accuraat, wat een specifieke curve rechtvaardigt.

PREFACE

I knew nothing about fatigue. It was no more than just another limit state. The first time I might have heard of fatigue was probably in my second or third year of bachelor studies. There was an aura of complexity mixed with "who cares" around it. And by then, this seemed enough of an argument to simply park the world of fatigue somewhere in my brain, quite deeply honestly.

Years later, I find myself writing a PhD thesis about multiaxial fatigue. I should say that curiosity had driven me, but I must admit that this is not true. What drove me, was the enthusiasm that I could feel when something new was unveiled; the panic that arise when you know you are opening another Pandora box, not knowing where it will end up; the adrenaline that comes from achieving a very good result – at the end. Fatigue needs up and down, and so you need them in your life to study it.

There have been plenty of different paths to follow, this is the one I chose – or found – I don't know anymore. My MSc thesis has been the start and the journey continued during my years as young researcher first and as PhD candidate later. Whatever is written hereafter, comes from years of study, research and hard work in the laboratory. I hope the reader will find it interesting to read my thoughts now that I know a bit more about fatigue.

Gabriele Bufalari

NOMENCLATURE

Latin symbols

a	crack size
a_f	final crack size
a_i	initial crack size
C	fatigue resistance curve intercept
C_{bw}	weld load carrying normal stress coefficient
c_m	material characteristic non-proportionality coefficient
C_{np}	path characteristic non-proportionality coefficient
C_{tw}	weld load carrying shear stress coefficient
f_n	line normal force
F_n	nodal normal force
f_s	line shear force
F_s	nodal shear force
h_w	weld leg height
I_N	notch crack growth integral
I_r	irregularity factor of spectrum
K	stress intensity factor
l_w	weld leg length
m	fatigue resistance curve slope
m_b	line bending moment
M_b	nodal bending moment
M_{kn}	S_t related notch factor
m_t	line torsion moment
M_t	nodal torsion moment
n	number of counted cycles / elastoplasticity coefficient
N	fatigue lifetime in number of cycles
O	coordinate system origin
r	radial coordinate

r_0	radial distance of coordinate system origin to notch tip
r_{σ_s}	structural normal stress ratio
r_{τ_s}	structural shear stress ratio
R	loading & response ratio
R_r	response ratio including S_r
R_t	tube outer radius
S	fatigue strength parameter
S_e	effective notch stress parameter
S_n	nominal stress parameter
S_r	(mean) residual stress
S_t	traction equivalent stress parameter
S_T	total stress parameter
S_∞	fatigue strength limit
t_b	base plate thickness
t_c	cross plate thickness
t_p	plate thickness
$T_{\sigma S}$	10%–90% strength scatter band index
Y_f	far field factor
Y_{fb}	far field factor bending component
Y_{fm}	far field factor membrane component
Y_{fs}	far field factor shear component
Y_{ft}	far field factor torsion component
Y_n	notch factor
$\mathscr{L}$	log-likelihood
$\hat{}$	circumflex indicating parameter MLE
$_I$	mode-I index
$_{III}$	mode-III index

Greek symbols

α	(half) notch angle
β	particular stress angle
$\beta(N)$	lifetime dependent shear strength coefficient
Δ	prefix indicating stress range
ϵ	residual

γ	loading & response ratio coefficient
λ	eigenvalue
λ_ω	width of spectrum
λ_τ	first mode-III eigenvalue
μ	mean
μ_ω	mean value of spectrum
$\mu_{\tau F}$	force equilibrium coefficient
$\mu_{\tau M}$	moment equilibrium coefficient
ω	frequency component of spectrum
Φ	parameter vector
ρ	(real) weld notch radius
ρ^*	material characteristic length
ρ_τ	normal to shear stress ratio
ρ_{S_∞}	mid- to high- cycle fatigue transition curvature parameter
σ	standard deviation / normal stress
σ_e	mode-I effective notch stress
σ_N	fatigue lifetime standard deviation
$\sigma_n\,(r/t_p)$	weld toe notch stress distribution
σ_s	(structural) normal stress
σ_y	material yield strength
σ_{fe}	mode-I linear structural field stress
$\sigma_{n,max}$	mode-I max. nominal stress after cut off
σ_{sb}	M_b induced structural stress component
σ_{se}	mode-I self equilibrium stress
σ_{sm}	F_n induced structural stress component
τ	shear stress
τ_e	mode-III effective notch shear stress
τ_s	(structural) shear stress
τ_{fe}	mode-III (equilibrium equivalent) linear structural field stress
$\tau_{n,max}$	mode-III max. nominal shear stress after cut off
τ_{nom}	nominal shear stress
τ_{ns}	pure shear force induced τ_n
τ_{nt}	pure torsion moment induced τ_n

$\tau_n \, (r/t_p)$ mode-III weld toe notch shear stress distribution

τ_{se} mode-III self equilibrium stress

τ_{ss} F_s induced structural shear stress component

τ_{st} M_t induced structural shear stress component

τ_{tw} weld load carrying shear stress

θ generic stress angle

$\{\zeta_{\sigma a}, \zeta_{\sigma s}\}$ first mode-I blunt body eigenvalue of (anti-)symmetry part

$\{\chi_{\sigma a}, \chi_{\sigma s}\}$ first mode-I eigenvalue coefficient of (anti-)symmetry part

$\{\lambda_{\sigma a}, \lambda_{\sigma s}\}$ first mode-I eigenvalue of (anti-)symmetry part

$\{\mu_{\sigma a}, \mu_{\sigma s}\}$ mode-I equilibrium coefficient of (anti-)symmetry part

$\{\omega_{\sigma a}, \omega_{\sigma s}\}$ first blunt body eigenvalue coefficient of (anti-)symmetry part

Abbreviations

AW   as-welded

BM   base material

CA   constant amplitude

DoF   degrees of freedom

DS   double side

FE   finite element

FZ   fusion zone

HAZ   heat affected zone

MLE   maximum likelihood estimate

NP   non-proportional

P   proportional

SIF   stress intensity factor

SR   stress-relieved

SS   single side

VA   variable amplitude

VAR   variance

1

INTRODUCTION

The beginning is the most important part of the work.

Plato, philosopher

1.1. BACKGROUND

Maritime structures like offshore support vessels and floating offshore wind turbines (Fig. 1.1a) are exposed to environment (wind, waves) and service (machinery) induced loading conditions, varying over time. Fatigue: a local, progressive, crack evolution induced structural damage process [1] in cyclic response conditions, is often a governing limit state [2–5].

| (a) | (b) |

Figure 1.1.: Maritime structures (a) and fatigue crack at an arc-welded joint connecting structural members (b).

Turning an intact geometry into a cracked one typically initiates at locations showing an increased response level, like at stress concentrations. Fatigue sensitive locations for plane geometries are the microscopic and mesoscopic stress concentrations at material scale. For notched geometries, the macroscopic stress concentrations at structural scale; hot spots, facilitating microscopic and mesoscopic ones [6], are identified as fatigue sensitive, either as part of structural members

(e.g. cut-outs) or at structural member connections (e.g. joints). The arc-welded joints typically connecting the planar or tubular structural members (Fig. 1.1b) for commonly applied metals like steel are the weakest links in that respect [7–9].

In general, maritime structural response conditions can be multiaxial with potential contributions from loading, geometry and/or even material sources. External environment and service loading components, like wind and waves from different directions, as well as heavy lifting operations and rotating turbine blades (Fig. 1.1a), can occur simultaneously. Stiffness variations because of changing geometry or material anisotropy enable multiple – internal – load transfer mechanisms along dissimilar paths. Normal mode-I, in-plane shear mode-II and/or out-of-plane mode-III shear components (Fig. 1.2) can be involved, either proportional (P); i.e. in-phase (predominantly geometry and material source related), or non-proportional (NP); i.e. out-of-phase (often related to the loading source) because of asynchronous behaviour and/or different frequencies [10].
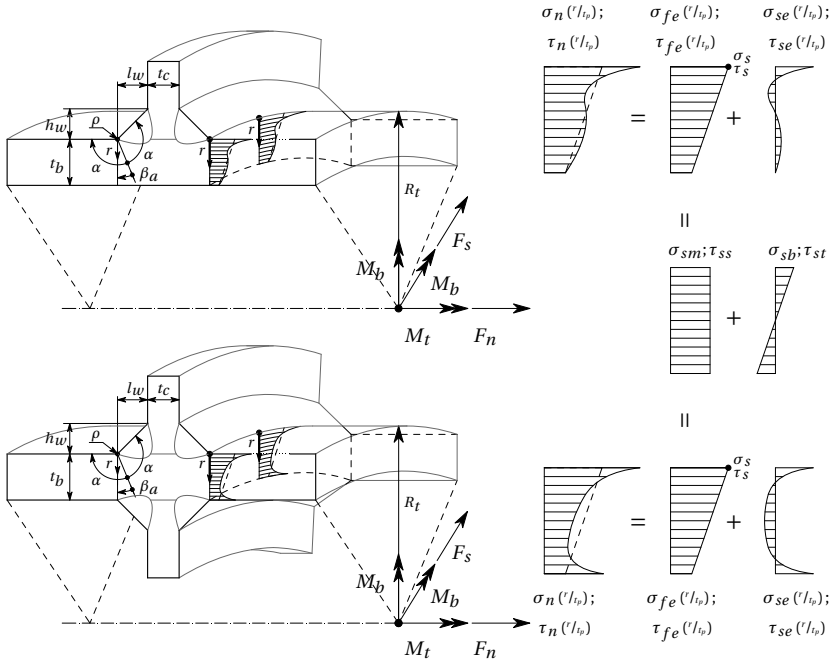
Figure 1.2.: Arc-welded T-joint connecting tubular structural members with internal load components..

Since the (curved) plate thickness is often relatively small in comparison to the other structural member dimensions and the external loading is typically a distributed one, the internal mode-I loading components: normal force F_n as well as the in-plane and out-of-plane bending moments $M_{b,ip}$ and $M_{b,op}$, are typically governing. Any in-plane shear force $f_{s,ip}$ mode-II component is in general negligibly small. At the same time, the out-of-plane shear force $F_{s,op}$ and torsion moment

M_t mode-III components affect in specific cases [11, 12] the predominant mode-I response and multiaxiality has to be taken into account for accurate fatigue strength and life time estimates [e.g. 10].

Adopting respectively intact and cracked geometry parameters [6], the initiation and growth contributions to the fatigue damage process can be modelled [1]. The fatigue life time N is predominantly spent in the notch affected region [13], meaning a notch characteristic intact geometry parameter can be adopted as fatigue strength parameter S rather than a cracked geometry one, even if N for welded joints is typically crack growth defined. Since far field response spectra of welded joints in steel maritime structures reflect predominantly linear elastic behaviour, S is typically of the stress – rather than strain or energy – type, in particular for mid- and high-cycle fatigue [14]. Correlation of S and N typically reveals a log–log linear dependency and a Basquin type of resistance relation is naturally adopted: $\log(N) = \log(C) - m \cdot \log(S)$. Intercept $\log(C)$ and slope m reflect respectively a strength and mechanism contribution, suggesting the mode-I and mode-III values are different. Available fatigue test data showed that mode interaction effects, in particular for NP cases, can be detrimental [e.g. 15] and a straight forward superposition turned out to be insufficient.

1.2. MOTIVATION

Different fatigue strength parameters and corresponding resistance curves have been developed and reviewed over time, aiming to obtain more accurate fatigue lifetime estimates, balanced with parameter complexity and computational efforts [16]. A classification has been proposed [17] based on:

1. information level; i.e. global or local,

2. geometry type; i.e. intact or cracked,

3. response measure; i.e. stress (intensity), strain (intensity) or energy (density) based,

4. process zone; i.e. point, line, area or volume.

Modelling developments and trends towards complete strength, multi-scale and total life parameters have been identified. Incorporating all four (interacting) fatigue resistance dimensions: material, geometry, loading & response and environment, a complete strength fatigue parameter appears. Considering macro-, meso- and micro-scale information provides a multi-scale fatigue parameter. Correlation of crack initiation and growth matches intact and cracked geometry contributions, revealing a total life fatigue parameter [6].

Regression analysis on a large sample of as-welded joint mode-I fatigue resistance data for steel structures shows the best performance in terms of life time standard deviation σ_N and fatigue strength scatter band index $T_{\sigma S}$ [14, 16, 18] using the effective notch stress and total stress, both local stress based line parameters, respectively of the intact and cracked geometry type. In comparison to σ_N and

1

$T_{\sigma S}$ values for – different – existing mixed mode-{I, III} multiaxial fatigue strength parameters (Table 3.4), significant room for improvement can be observed and consensus about the one providing the best overall performance is still lacking. Mode and material characteristic strength and mechanism contributions are expected to play a key-role in that respect, explaining the aim to extend the mode-I S_e and S_T parameter formulation to a multiaxial one; a complete strength parameter type of development. At the same time, availability of multiaxial fatigue test data for validation purposes is limited.

EFFECTIVE NOTCH STRESS

More generalised S formulations can be obtained if both the notch and far field contributions are incorporated in order to meet fatigue scaling requirements. The number of involved fatigue resistance curves reduces accordingly (i.e. ultimately to one), like for the effective notch stress concept [16, 17, 19–23]. Embedded in the critical distance theory [24], applications are not limited to welded joints but extents for example to 3D printed materials and structures [25–28]. Taking advantage of semi-analytical weld notch stress distribution expressions [16, 29], the effective notch stress S_e can be calculated averaging the notch stress distribution along the expected crack path over a material characteristic length ρ^*, introducing another mechanism contribution. Solid finite element (FE) models to estimate S_e are not required anymore.

Uniaxial mode-I investigations for arc-welded joints in steel structures revealed a dedicated material characteristic length ρ_I^* as well as resistance curve intercept $\log(C_I)$ and slope m_I value [14, 16, 29]. Since a response cycle needs two parameters for a complete spatial description, e.g. range and ratio, a mode-I specific response ratio coefficients γ_I containing another strength contribution have been proposed as well [14, 16, 29]. However, the mode-III equivalent parameters have not been investigated before, although the resistance curve related strength and mechanism parameters are expected to be different, as well as the mixed mode-{I, III} S_e performance.

TOTAL STRESS

Since the notches inevitably contain welding induced defects, the actual initiation (i.e. nucleation) contribution to the total fatigue life time is virtually eliminated and growth is governing. The intact geometry related semi-analytical weld notch stress distribution formulations can be turned into cracked geometry ones, introducing the weld notch stress intensity factor (SIF) K. Cyclic loading & response conditions turn K into a crack growth driving force ΔK and defects may develop into cracks. Since the growth rate initially shows elastoplastic wake field affected anomalies [18], a modified Paris' equation has been established, including the weld notch- and far field characteristic contributions: a generalised two-stage crack growth relation. Applying an integral operator provides a log-log linear resistance relation of the Basquin type, correlating the fatigue life time N and an equivalent fatigue strength parameter: the total stress S_T [6, 18]. Uniaxial mode-I intercept $\log(C_I)$ and slope m_I, as well as response ratio coefficient γ_I and elastoplasticity coefficient n_I

estimates have already been obtained for welded joints in steel structures [14, 16]. The S_T and S_e performance in terms of life time scatter σ_N and strength scatter band index $T_{\sigma S}$ proved to be similar. Whereas ρ^* is a mode specific and material characteristic length defining S_e to incorporate the notch stress gradient, S_T includes the stress (intensity) gradient along the full plate thickness t_p defined final crack length a_f, suggesting ρ^* and a_f serve the same purpose. However, S_T contains an additional mechanism related parameter n and may increase insight in the mode specific and material characteristic behaviour. The uniaxial mode-III and multiaxial mode-{I, III} S_T performance have not been established before and a key question is if the mode coupling is equally important for S_T as for S_e. At the same time, a cracked geometry parameter seems one step closer to the actual damage process than an intact one, hypothesising a fatigue strength parameter S_T may outperform S_e for multiaxial fatigue.

FATIGUE TEST DATA

The performance of a fatigue strength parameter S depends on the test data; i.e. the fatigue life time N depends on the quality of the specimen manufacturing process as well as of the test rig. Influence factors not explicitly incorporated define the resistance data scatter band. Using available data sets from different literature sources, average quality based parameter coefficient estimates can be obtained using regression analysis in order to obtain one $S - N$ design curve for general engineering applications. However, depending on the specimen quality, a particular set may be on the lower or upper bound of the data scatter band. In particular for high-performance welded joints, the average quality based $S - N$ design curve may provided over conservative fatigue strength and life time estimates. A dedicated one with representative parameter coefficient estimates might be a better option, reflecting the actual quality. Existing multiaxial fatigue test rigs are relatively new, either equipment in a standard series or custom built for a particular purpose. Common denominator seems a limited loading capacity – imposing a restriction on specimen size and material strength – as well as number of degrees of freedom (DoF) and wide range of application. At the same time, the availability of multiaxial fatigue test data sets in literature is limited. To be able to test high-performance welded joints in maritime applications for multiaxial fatigue research, a custom-built high loading capacity 6 DoF multiaxial fatigue test rig, a hexapod (i.e. a Steward platform), has been developed (Fig. 1.3).

Both uniaxial and multiaxial, constant and variable amplitude test data is generated in the 4DFatigue Joint Industry Project and the best performing fatigue strength parameter available has identified [10, 30–32]. However, the obtained strength and mechanism properties are in comparison to data from literature significantly better. If S_e and S_T would provide a better fit with an average quality based resistance data scatter band is unknown. A dedicated resistance curve might even be a better option for the sake of accurate fatigue strength and life time estimates as well as parameter confidence, but has to be investigated.
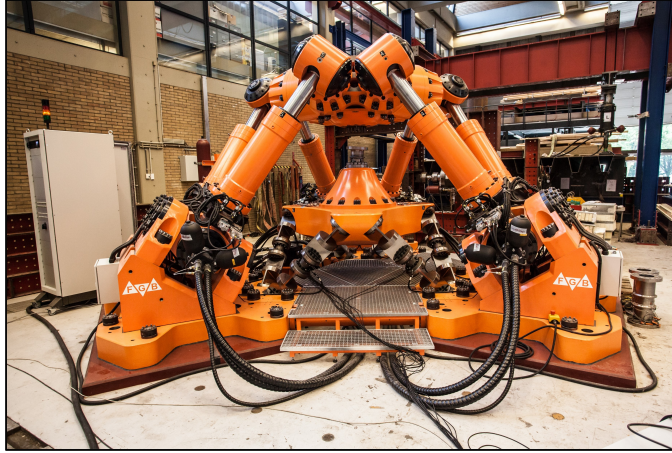
1

Figure 1.3.: TU Delft hexapod; a high loading capacity 6 DoF fatigue test rig, unique in the world.

1.3. Research questions

Evaluating the different multiaxial, mixed mode-{I, III} fatigue damage criteria developed over time, the performance as typically reflected in the life time scatter σ_N and strength scatter band index $T_{\sigma S}$ is not even close to the uniaxial reference mode-I values. However, the ways the mode specific strength and mechanism contributions as reflected in the resistance curves intercept and slope are incorporated – even if any – leaves significant room for improvement, raising the research question:

"Will incorporating adequate (mixed) mode-{I, III} strength and damage mechanism contributions improve the multiaxial fatigue life time estimates for arc-welded joints in steel (maritime) structures?"

The fatigue life time for arc-welded joints is typically spent in the notch affected region, characterised using an intact geometry based notch stress parameter. However, the welding process comes along with defects, virtually eliminating the crack nucleation contribution to fatigue life time, justifying at the same time a cracked geometry based notch stress intensity parameter. For mode-I fatigue, the intact and cracked geometry parameters S_e and S_T, respectively the effective notch stress and total stress, already proved excellent performance in comparison to other fatigue parameters, introducing the sub questions:

1. Do S_e and S_T show the same level of performance for mode-III fatigue of arc-welded joints and what are the differences with respect to mode-I?

2. Will mode specific strength and mechanism contributions for S_e and S_T be sufficient, or is even a mixed mode contribution; an interaction effect, required to obtain the best performance for multiaxial fatigue?

3. Balancing accuracy, complexity and efforts for fatigue assessment of arc-welded joints, is an intact geometry parameter like S_e be preferred, or a cracked geometry one like S_T?

In case of mixed mode-{I, III} response non-proportionality or amplitude variability, a cycle counting algorithm and damage accumulation model are required for a time domain formulation in order to provide fatigue life time estimates, arising the sub-questions:

4. How to incorporate strength and mechanism contributions for multiaxial cycle counting?

5. Is a combination of an advanced fatigue strength criterion like S_e or S_T, a multiaxial cycle counting algorithm and a linear damage accumulation model sufficient to obtain fatigue life time estimates with the same accuracy as the uniaxial, constant amplitude equivalent?

The performance of S_e and S_T can be assessed using all relevant multiaxial fatigue data sets available in literature, reflecting at least up to some extent an average weld quality, representative for a broad range of applications including arc-welded joints in maritime structures. However, would high-performance welds, or individual data sets in general, be better off with a dedicated resistance curve and strength and mechanism parameters in order to improve the fatigue life time estimate accuracy, introducing the sub-question:

6. Does distinct, e.g. high-performance, weld quality justify dedicated strength and mechanism parameters with respect to the average for improved fatigue life estimate accuracy?

Basically it is about up to what extent individual data sets fit within the total data scatter band, as well as the sample size affected parameter coefficient confidence.

1.4. Scope definition

Because of the expected material characteristic contributions involved, the research will be limited to steel alloys as commonly used in (maritime) structures. Although the aim is to develop a fatigue strength parameter applicable for other welded metals like aluminium and magnesium as well – the damage mechanism are expected to be similar, dedicated parameter coefficients have to be re-established and findings can be different. Focus will be on arc-welded joints – still most often used – connecting the steel structural members. However, joints produced using different type of techniques, e.g. laser welding, are expected to allow for a similar investigation. Strength and mechanism contributions will most likely change because of different weld geometry and heat input affected material properties at micro-scale. Although the fatigue life time of arc-welded joints is growth dominated, at this stage of the research multiaxial fatigue resistance (involving the total life time) rather than crack growth resistance will be considered; mid-cycle fatigue, $N = (10^4...10^6)$ cycles,

1

in particular. High-cycle fatigue is important because the strength and mechanism contributions are different from mid-cycle fatigue, as well as from maritime structure operation conditions perspective, but test data in literature is not available (yet). Multiaxial fatigue will be investigated in the time domain first, since analysis results typically serve as a reference for results obtained in the frequency domain. Cycle counting for non-proportional mode-I and mode-III signals, accounting at the same time for the distinguished strength and mechanism contributions, is considered to be non-trivial, as well as the damage accumulation.

1.5. THESIS OUTLINE

Mode-III weld notch stress distribution formulations will be established first in order to define the intact geometry parameter $S_{e,III}$. Using uniaxial mode-III fatigue test data from literature, the $S_{e,III}$ fatigue strength and mechanism parameters, $\{C_{III}, \gamma_{III}\}$ and $\{m_{III}, \rho_{III}^*\}$ respectively, will be established, paying particular attention to the $S_{e,III}$ performance in terms of σ_N and $T_{\sigma S}$ in comparison to the $S_{e,I}$ results (Chapter 2).

Literature will be reviewed with respect to types of failure criterion, damage plane selections, cycle counting algorithms, non-proportionality measures and damage accumulation models, before a generalised mixed mode-{I, III} S_e ($S_{e,I}$, $S_{e,III}$) formulation will be defined, incorporating both strength and mechanism contributions (Chapter 3).

Using constant and variable amplitude (mixed) mode-{I, III} fatigue test data from literature the S_e ($S_{e,I}$, $S_{e,III}$) performance will be compared to existing multiaxial fatigue strength parameters, highlighting interaction effects. Turning the mode-III notch stress formulations into notch stress intensity formulations will be the input for a cracked geometry parameter $S_{T,III}$ (Chapter 4).

For the same multiaxial fatigue assessment procedure as for S_e, the S_T ($S_{T,I}$, $S_{T,III}$) performance will be compared to S_e ($S_{e,I}$, $S_{e,III}$) addressing especially the strength and mechanism indued mode-coupling effects. Multiaxial fatigue test results for high-performance welded joints, obtained using the hexapod, will be unveiled and assessed using S_e ($S_{e,I}$, $S_{e,III}$) as well as S_T ($S_{T,I}$, $S_{T,III}$). Fitting of individual data sets in the total data scatter band will be evaluated with respect to (average) weld quality and parameter coefficient confidence (Chapter 5).

Last but not least, the gained key insights will be shared and conclusions will be drawn based on the obtained results (Chapter 6). An outline for future research will be proposed as well, serving as a roadmap to further explore the frontiers in the field of multiaxial fatigue.

2

MODE-III WELD NOTCH STRESS DISTRIBUTIONS AND S_e BASED RESISTANCE

(Fatigue) strength lies in differences, not in similarities.

Stephen Covey, educator and author

2.1. INTRODUCTION

The through-thickness weld toe and weld root notch stress distributions along the expected (2D) crack path are assumed to be a key element in defining an appropriate fatigue design and detectable repair criterion [16]. Analytical expressions have already been established for mode-I [14, 16, 18], related to the welded joint far field stress as typically can be obtained using relatively coarse meshed shell/plate finite element (FE) models. However, expressions for mode-III are not available yet and will be established for weld toe notches in double side (DS) welded T-joints and DS welded cruciform-joints, reflecting respectively non-symmetry and symmetry with respect to half the plate thickness (Section 2.2).

Different fatigue assessment concepts, relating the fatigue life time *N* and a fatigue strength criterion *S* using a resistance curve, have been developed over time aiming to obtain more accurate life time estimates, balanced with criterion complexity and computational efforts [16]. Incorporating local (notch) information provides more generalised *S* formulations and the number of involved fatigue resistance curves reduces accordingly (i.e. ultimately to one), like for the effective notch stress concept

2

[16, 17, 19–23]. Taking advantage of the weld notch stress distribution expressions, the effective notch stress S_e can be calculated averaging the notch stress distribution along the expected crack path over a material characteristic length ρ^*, meaning solid FE models to estimate S_e are not required anymore. Following mode-I investigations [14, 16], a mode-III mid-cycle fatigue $S_e - N$ curve will be established for welded joints in steel structures (Section 2.3), paying particular attention to the material characteristic length since ρ^* seems never been investigated before. The conclusions and outlook (Section 2.4) provide half of the information (i.e. S_e related only), required to answer research sub-question 1 (Section 1.3).

2.2. MODE-III WELD TOE NOTCH SHEAR STRESS DISTRIBUTIONS

In order to capture the mode-III through-thickness weld toe notch shear stress distributions $\tau_n(r/t_p)$ along the expected (2D) crack path with plate thickness t_p either the base plate or cross plate value, t_b or t_c, the welded joint far field response is assumed to be linear elastic. Adopting a linear superposition principle [18] a far field related equilibrium equivalent and self-equilibrium part will be distinguished, τ_{fe} and τ_{se} (Fig. 2.1) involving three components: the notch stress (Section 2.2.1), the weld-load carrying stress (Section 2.2.2) and the far field stress (Section 2.2.3). Formulations will be derived for both non-symmetry (Section 2.2.4) and symmetry (Section 2.2.5) with respect to half the plate thickness ($t_p/2$), using respectively a DS welded T-joint and DS welded cruciform joint for illustration purposes, in case of both zero and finite notch radius ρ. Please note that the cruciform joint in IIW standard [33] and Eurocode [34] is referred to as two-sided transverse attachment, considering both the geometry and loading applied at the continuous member. The adopted joint annotation is based on geometry only, since the variety in loading conditions can be large, in particular in case of multiaxiality.

2.2.1. NOTCH STRESS COMPONENT

The singular stress distribution at a V-shaped notch for a fillet weld geometry with $\rho = 0$ (Fig. 2.2) can be obtained [35–39] assuming symmetry with respect to the notch bisector ($\theta = 0$). A tangential component formulation for a particular stress angle ($\theta = \beta$) has been established (A), including a relation to the far field stress parameter τ_s (Section 2.2.3):

$$\tau_{x\theta}\left(\frac{r}{t_p}\right) = \tau_s \left(\frac{r}{t_p}\right)^{\lambda_\tau - 1} \mu_{\tau F} \cos(\lambda_\tau \beta) \tag{2.1}$$

with

$$\mu_{\tau F} = \frac{C_1' t_p^{\lambda_\tau - 1}}{\tau_s} \tag{2.2}$$

and

$$\lambda_\tau = \frac{\pi}{2\alpha}. \tag{2.3}$$
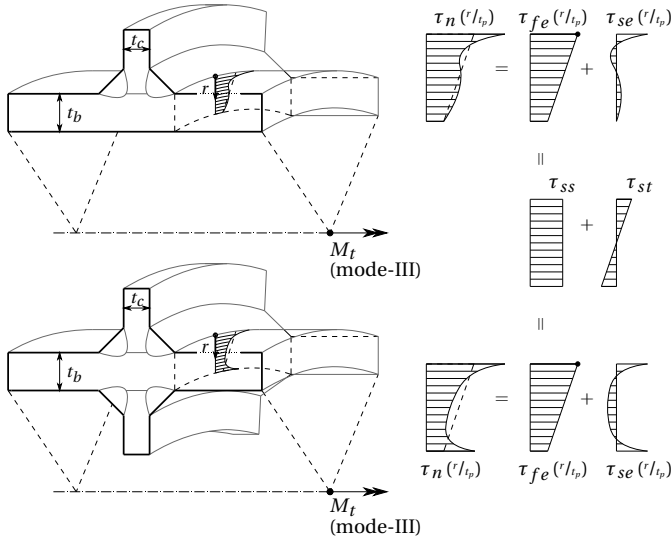
Figure 2.1.: Linear superposition of an equilibrium equivalent and self-equilibrium part for the mode-III weld toe notch shear stress distribution of a DS welded T-joint and DS welded cruciform joint.
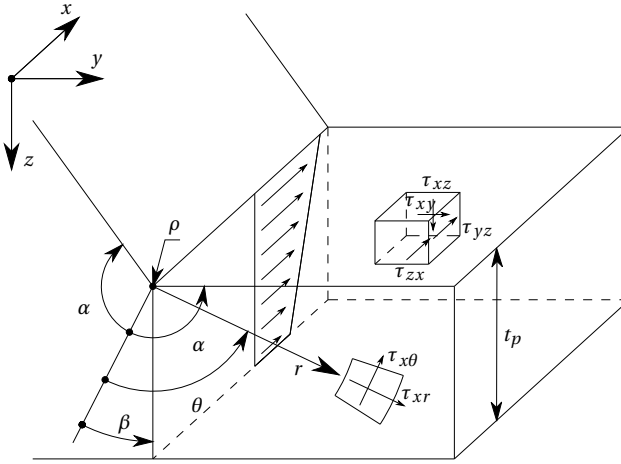
Figure 2.2.: Notch stress components in Cartesian and Polar coordinates for $\rho = 0$.

Although the real weld notch radius ρ is often virtually zero – justifying the $\rho = 0$ assumption, in some cases the influence of $\rho > 0$ (Fig. 2.3) cannot be neglected. The coordinate system origin will be transformed ($O' \to O$), keeping the Polar axis parallel to the original one:

$$r'^2 = r^2 + 2\cos(\beta - \theta) r_0 r + r_0^2 \tag{2.4}$$

with

$$r_0 = \rho \left(1 - \frac{\pi}{2\alpha}\right).$$ (2.5)

Figure 2.3.: Notch stress components in Cartesian and Polar coordinates for $\rho > 0$.

For a particular stress angle $\theta = \beta$, the tangential component becomes (A):

$$\tau_{x\theta}\left(\frac{r}{t_p}\right) = \tau_s \left(\frac{r'}{t_p}\right)^{\lambda_\tau - 1} \mu_{\tau F} \cos(\lambda_\tau \beta) \left\{1 + \left(\frac{r_0}{t_p}\right)^{2\lambda_\tau} \left(\frac{r'}{t_p}\right)^{-2\lambda_\tau}\right\}$$ (2.6)

Comparing $\tau_{x\theta}(r/t_p)$ for zero and finite notch radius (Eqs. (2.1) and (2.6)), the ($\rho = 0$) formulation is basically th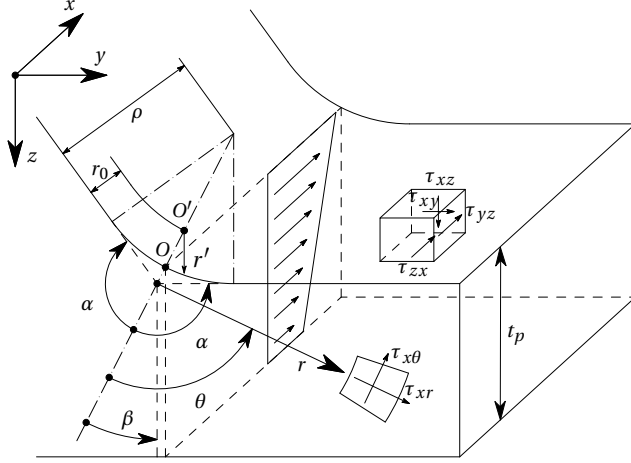e ($\rho > 0$) limit case. In contrast to the mode-I formulation [14, 16, 18], only one singular term is involved rather than two.

2.2.2. Weld load carrying stress component

The weld geometry causes a local change in stiffness, meaning the centre of twist varies from section to section along the y-axis (Fig. 2.4). Each welded joint section is basically a rectangle containing two axes of symmetry, meaning the centre of twist is located at the intersection and coincides at the same time with the centroid. Connecting the centres of twist of each section introduces the elastic axis (Fig. 2.4) and coincides with the neutral axis. A torsion moment induced linear shear stress distribution $\tau_{tw}(r/t_p)$ appears and the weld becomes load carrying up to some extent. Considering a weld toe notch as typically encountered in a partial penetrated DS welded T-joint at the base plate without symmetry with respect to $(t_p/2)$, the torsion moment is counter-clockwise for f_s pointing in x-direction and counter-clockwise m_t in the x-z plane and the weld load carrying (shear) stress

distribution yields:

$$\tau_{tw}\left(\frac{r}{t_p}\right) = \tau_s C_{tw}\left\{2\left(\frac{r}{t_p}\right) - 1\right\} \text{ for } \{0 \le \left(\frac{r}{t_p}\right) \le 1\}. \tag{2.7}$$

The far field stress (Section 2.2.3) related magnitude $\tau_s C_{tw}$ is geometry and loading dependent. If symmetry with respect to $(t_p/2)$ is detected, like for a DS welded cruciform joint (Fig. 2.4), the $\tau_{tw}(r/t_p)$ distribution is based on half the plate thickness only:

$$\tau_{tw}\left(\frac{r}{t_p}\right) = \tau_s C_{tw}\left\{4\left(\frac{r}{t_p}\right) - 1\right\} \text{ for } \{0 \le \left(\frac{r}{t_p}\right) \le 1\}. \tag{2.8}$$
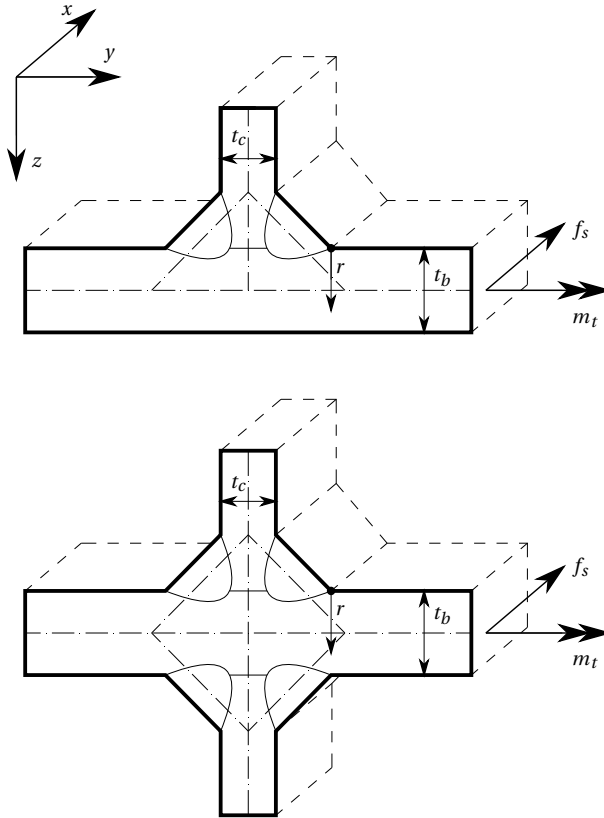

Figure 2.4.: Weld geometry induced shift of centre of twist for the non-symmetry and symmetry case.

2.2.3. FAR FIELD STRESS COMPONENT

The linear structural field stress distribution $\tau_{fe}(r/t_p)$ in the cross-section at a weld toe (Fig. 2.1), in compliance with the fracture mechanics defined far field stress [40, 41], is characterised using the structural shear stress τ_s and structural shear stress ratio r_{τ_s}:

$$\tau_{fe}\left(\frac{r}{t_p}\right) = \tau_s \left\{1 - 2r_{\tau_s}\left(\frac{r}{t_p}\right)\right\} \text{ for } \left\{0 \leq \left(\frac{r}{t_p}\right) \leq 1\right\}. \tag{2.9}$$

A relatively coarse meshed shell/plate FE model is typically sufficient to estimate the far-field stress of welded joints in maritime structures [42, 43], naturally embedding the constant membrane (mode-I) / shear (mode-III) and linear bending (mode-I) / torsion (mode-III) components [44]. If the welded joint structural stiffness – either in planar or tubular structures – does not significantly affect the stress distribution, like in general for groove welds (e.g. in butt joints), the weld does not need to be modelled and the far field stress information can be obtained at the intersection line of the connected structural members [45]. However, if weld modelling is required – like often for fillet welds (e.g. in T-joints and cruciform joints), several options are available including inclined shell elements, inclined rigid elements or shell elements with increased local thickness at the joint location [46]. For the considered mode-III loading & response conditions, inclined shell element modelling has been adopted (Fig. 2.5) as it seems to be most convenient in engineering practice [44]. Transforming the nodal shear forces $F_{s,i}$ and torsion moments $M_{t,i}$ along the weld
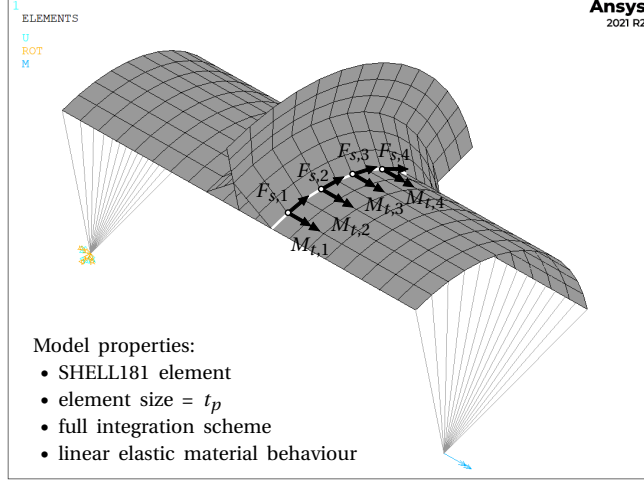

Figure 2.5.: Part of a shell FE model of a (non-symmetric) T-joint in a tubular structure.

seam to line forces and moments $f_{s,i}$ and $m_{t,i}$, $\{F_s\} = [T]\{f_s\}$ and $\{M_t\} = [T]\{m_t\}$ [41, 47, 48], the shear force and torsion moment induced structural stress components

τ_{ss} and τ_{st} can be calculated to obtain the structural shear stress:

$$\tau_s = \tau_{ss} + \tau_{st} \tag{2.10}$$

with

$$\tau_{ss} = f_s / t_p \tag{2.11a}$$

$$\tau_{st} = 6m_t / t_p^2. \tag{2.11b}$$

The structural shear stress ratio ($-\infty < r_{\tau_s} \leq 1$) represents the relative contribution of τ_{st} to τ_s, i.e. the far field stress gradient:

$$r_{\tau_s} = \tau_{st} / \tau_s. \tag{2.12}$$

Rewriting τ_{ss} and τ_{st} in terms of τ_s (Eq. 2.10) and r_{τ_s} (Eq. 2.12) yield:

$$\tau_{ss} = \tau_s(1 - r_{\tau_s}) \tag{2.13a}$$

$$\tau_{st} = r_{\tau_s}\tau_s. \tag{2.13b}$$

2.2.4. STRESS DISTRIBUTION FOR NON-SYMMETRY WITH RESPECT TO $(t_p/2)$

Using the notch stress component $\tau_{x\theta}$ (Eq. 2.1), the weld load carrying stress τ_{tw} (Eq. 2.7) and structural field stress formulation τ_{fe} (Eq. 2.9), the mode-III stress distribution for the non-symmetry case (Fig. 2.6) – along the (2D) crack path – can be obtained for $\rho = 0$:

$$\tau_n\left(\frac{r}{t_p}\right) = \tau_s\left[\left(\frac{r}{t_p}\right)^{\lambda_\tau - 1}\mu_{\tau F}\cos(\lambda_\tau\beta) - (C_{tw} + \mu_{\tau M})\left\{2\left(\frac{r}{t_p}\right) - 1\right\} - 2r_{\tau_s}\left(\frac{r}{t_p}\right)\right]. \tag{2.14}$$

The self-equilibrium stress part $\tau_{se} + 1$, $(r/t_p)^{\lambda_\tau - 1}\mu_{\tau F}\cos(\lambda_\tau\beta) - (C_{tw} + \mu_{\tau M})\{2(r/t_p) - 1\}$ is scaled and projected – using τ_s and r_{τ_s} – onto the structural field stress. For $r_{\tau_s} > 0$ the stress distribution will be monotonic; in case $r_{\tau_s} \leq 0$ non-monotonic. Involving $\tau_{x\theta}$ (Eq. 2.6), the distribution for $\rho > 0$ can be obtained as well:

$$\tau_n\left(\frac{r}{t_p}\right) = \tau_s\left[\left(\frac{r'}{t_p}\right)^{\lambda_\tau - 1}\mu_{\tau F}\cos(\lambda_\tau\beta)\left\{1 + \left(\frac{r_0}{t_p}\right)^{2\lambda_\tau}\left(\frac{r'}{t_p}\right)^{-2\lambda_\tau}\right\} - \right.$$
$$\left. (C_{tw} + \mu_{\tau M})\left\{2\left(\frac{r'}{t_p}\right) - 1\right\} - 2r_{\tau_s}\left(\frac{r'}{t_p}\right)\right]. \tag{2.15}$$

Although principally the notch stress component in Cartesian coordinates is required, a transformation (Eq. A.2) does not affect the formulation: $\tau_{xz} = \tau_{xr}\cos(\theta) - \tau_{x\theta}\sin(\theta) = \tau_s(r/t_p)^{\lambda_\tau - 1}\mu'_{\tau F}\cos(\lambda_\tau\beta)$ for $\rho = 0$, explaining why $\tau_{x\theta}$

(Eq. 2.1) has been used. The involved eigenvalue λ_τ (Fig. A.1) and the stress angle $\beta = (\alpha - \pi/2)$ are notch angle α dependent. For fillet welds (Fig. 2.6):

$$\alpha = \frac{1}{2}\left\{\pi + \arctan\left(\frac{h_w}{l_w}\right)\right\}. \tag{2.16}$$
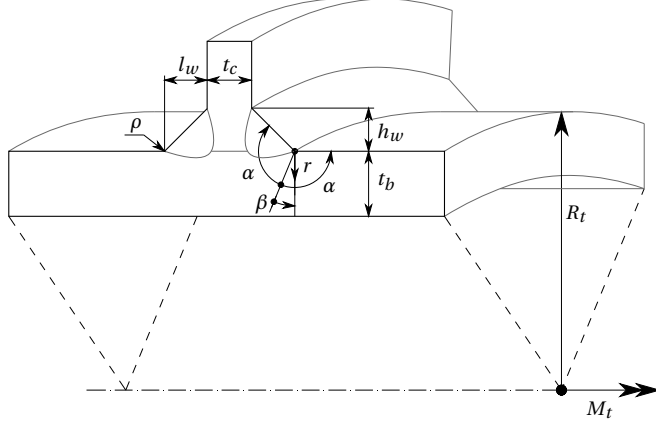
Figure 2.6.: DS welded T-joint showing non-symmetry with respect to $(t_b/2)$, either in a tubular or planar $(R_t \to \infty)$ structure.

Like for the mode-I formulation [14, 16, 18], two constants are required in order to satisfy both force and moment equilibrium. Since just one constant $\mu_{\tau F}$ is naturally available – comparable to the symmetric mode-I term – a linear anti-symmetric term $-\mu_{\tau M}\{2(r/t_p) - 1\}$ has been introduced to be able to achieve self-equilibrium. Rather than solving the system of force and moment equilibrium equations for $\mu_{\tau F}$ and $\mu_{\tau M}$, like for mode-I, the two equations can be solved sequentially since force equilibrium is identically satisfied for the anti-symmetric term. Force equilibrium in a weak form:

$$\int_0^1 \tau_n\left(\frac{r}{t_p}\right)d\left(\frac{r}{t_p}\right) = \int_0^1 \tau_s\left\{1 - 2r_{\tau_s}\left(\frac{r}{t_p}\right)\right\}d\left(\frac{r}{t_p}\right) \tag{2.17}$$

provides for $\rho = 0$

$$\mu_{\tau F} = \frac{\lambda_\tau}{\cos(\lambda_\tau \beta)}. \tag{2.18}$$

For $\rho > 0$ the coordinate system transformation (Eqs. (2.4) and (2.5)) becomes involved and force equilibrium in weak form:

$$\int_{\left(\frac{r_0}{t_p}\right)}^1 \tau_n\left(\frac{r}{t_p}\right)d\left(\frac{r}{t_p}\right) = \int_0^1 \tau_s\left\{1 - 2r_{\tau_s}\left(\frac{r}{t_p}\right)\right\}d\left(\frac{r}{t_p}\right) \tag{2.19}$$

with

$$\frac{r_0}{t_p} = \frac{\rho}{t_p}\left(1 - \frac{\pi}{2\alpha}\right) \tag{2.20}$$

provides

$$\mu_{\tau F} = -\frac{\lambda_\tau\left\{\mu_{\tau M}\left[\left(\frac{r_0}{t_p}\right)^2 - \left(\frac{r_0}{t_p}\right)\right] - \left(\frac{r_0}{t_p}\right)^2 r_{\tau_s} - 1\right\}}{\cos(\lambda_\tau\beta)\left[1 - \left(\frac{r_0}{t_p}\right)^{2\lambda_\tau}\right]}. \tag{2.21}$$

Note that with the obtained μ_{τ_F} formulation $\tau_n(r/t_p)$ turns out to be stress angle β independent. Moment equilibrium in a weak form for $\rho = 0$:

$$\int_0^1 \tau_n\left(\frac{r}{t_p}\right)\cdot\left(\frac{r}{t_p}\right)d\left(\frac{r}{t_p}\right) = \int_0^1 \tau_s\left\{1 - 2r_{\tau_s}\left(\frac{r}{t_p}\right)\right\}\left(\frac{r}{t_p}\right)d\left(\frac{r}{t_p}\right) \tag{2.22}$$

yields $\mu_{\tau M} = \{3(\lambda_\tau - 1) + C_{tw}(\lambda_\tau + 1)\}/(\lambda_\tau + 1)$. However, substitution in $\tau_n(r/t_p)$ provides a C_{tw} independent equation, since the introduced anti-symmetric term and the weld load carrying stress have the same form. Ignoring the weld load carrying stress contribution denotes:

$$\mu_{\tau M} = \frac{3(\lambda_\tau - 1)}{(\lambda_\tau + 1)}. \tag{2.23}$$

For $\rho > 0$ the same considerations apply:

$$\int_{\left(\frac{r_0}{t_p}\right)}^1 \tau_n\left(\frac{r}{t_p}\right)\cdot\left(\frac{r}{t_p}\right)d\left(\frac{r}{t_p}\right) = \int_0^1 \tau_s\left\{1 - 2r_{\tau_s}\left(\frac{r}{t_p}\right)\right\}\left(\frac{r}{t_p}\right)d\left(\frac{r}{t_p}\right) \tag{2.24}$$

providing

$$\mu_{\tau M} = \frac{\begin{array}{l}6\lambda_\tau(\lambda_\tau + 1)\left(\frac{r_0}{t_p}\right)^{2\lambda_\tau+1} - 3(\lambda_\tau^2 - 1)\left(\frac{r_0}{t_p}\right)^{2\lambda_\tau+2} - 12\lambda_\tau\left(\frac{r_0}{t_p}\right)^{\lambda_\tau+2} - 3(\lambda_\tau + 1)^2\left(\frac{r_0}{t_p}\right)^{2\lambda_\tau} + \\ 12\lambda_\tau\left(\frac{r_0}{t_p}\right)^{\lambda_\tau+1} + 3\left[\left(\frac{r_0}{t_p}\right) - 1\right](\lambda_\tau - 1)\left\{\left[\left(\frac{r_0}{t_p}\right) - 1\right]\lambda_\tau + \left(\frac{r_0}{t_p}\right) + 1\right\}\end{array}}{\begin{array}{l}6\lambda_\tau(\lambda_\tau + 1)\left(\frac{r_0}{t_p}\right)^{2\lambda_\tau+1} - (9\lambda_\tau^2 + 6\lambda_\tau - 3)\left(\frac{r_0}{t_p}\right)^{2\lambda_\tau+2} - 12\lambda_\tau\left(\frac{r_0}{t_p}\right)^{\lambda_\tau+2} - (\lambda_\tau^2 - 1)\left(\frac{r_0}{t_p}\right)^{2\lambda_\tau} + \\ 12\lambda_\tau\left(\frac{r_0}{t_p}\right)^{\lambda_\tau+3} + (\lambda_\tau - 1)\left\{\left[-4\left(\frac{r_0}{t_p}\right)^3 + 9\left(\frac{r_0}{t_p}\right)^2 + 4\left(\frac{r_0}{t_p}\right)^{2\lambda_\tau+3} - 6\left(\frac{r_0}{t_p}\right) + 1\right]\lambda_\tau - \\ 4\left(\frac{r_0}{t_p}\right)^3 + 3\left(\frac{r_0}{t_p}\right)^2 + 4\left(\frac{r_0}{t_p}\right)^{2\lambda_\tau+3} + 1\right\}\end{array}}. \tag{2.25}$$

The $\mu_{\tau F}$ and $\mu_{\tau M}$ expressions obtained for $\rho = 0$ are basically $\rho > 0$ limit values. Although moment equilibrium is not exactly satisfied since the weld load carrying stress has been ignored, at least $\tau_s C_{tw}\{2(r/t_p) - 1\}$ is still part of $\tau_n(r/t_p)$ to take care of the welded joint geometry and loading dependent weld notch stress contributions.

2
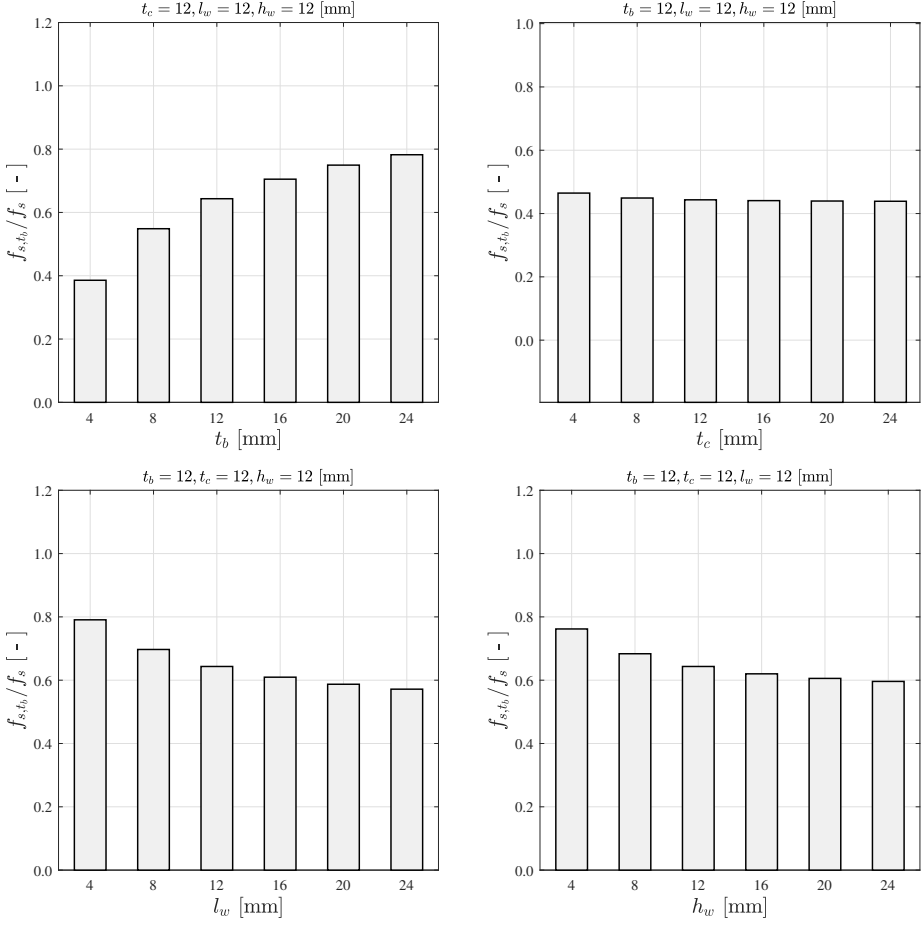
Figure 2.7.: Relative base plate shear load for a DS welded T-joint, varying t_b, t_c, l_w and h_w for $R_t \rightarrow \infty$.

The weld load carrying stress magnitude $\tau_s C_{tw}$ is assumed to be a linear superposition of a shear force f_s and torsion moment m_t induced component, meaning C_{tw} is r_{τ_s} dependent. For a tubular structure with attachment involving a DS welded T-joint and exposed to a torsion moment M_t (Fig. 2.6), the structural stress ratio r_{τ_s} changes for varying ratio of tube radius R_t and thickness t_p. For the limit cases, respectively $R_t \rightarrow t_b$ (corresponding to a solid shaft) and $R_t \rightarrow \infty$ (corresponding to a quasi-planar structure), the pure torsion and pure shear case appear. However, the pure torsion case introduces geometrical symmetry at the same time. Investigating the relative load path contributions using a 2D axisymmetric FE model (Fig. 2.12), the pure shear case will be considered to identify the weld load carrying mechanism for non-symmetry with respect to $(t_p/2)$. If a torsion moment
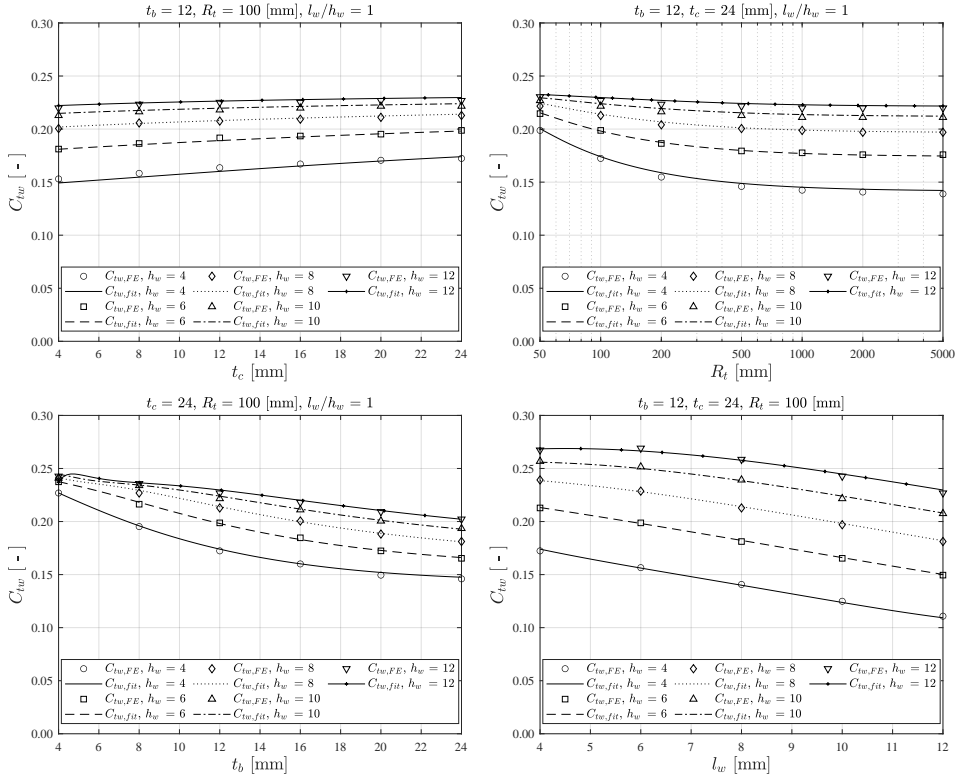
Figure 2.8.: Required C_{tw} value and fit estimate for a DS welded T-joint varying t_b, t_c, l_w, h_w and R_t.

is applied to the tube with $R_t \to \infty$ (Fig. 2.6), the DS welded T-joint contains two parallel load paths: one through the base plate and one through the weld and cross plate. The shear stiffness and torsion stiffness of the load paths define how the loading is divided. The base plate load path related shear stiffness dominates generally speaking the weld and cross plate load path related torsion stiffness, explaining the $(f_{s,t_b}/f_s)$ values closer to 1 (Fig. 2.7). For increasing t_b, the shear force through the base plate increases because of increasing base plate load path stiffness. The weld and cross plate load path torsion stiffness increases for increasing t_c, l_w, and h_w, meaning the base plate load path contribution decreases. The considered range of dimensions is representative for maritime structures consisting of structural members with relatively small plate thickness in comparison to the width and length.

In order to obtain the required C_{tw} values, FE solutions and analytical results (Eq. 2.14) for a range of geometry dimensions have been used to establish a 4$^{\text{th}}$ order polynomial fitting function (Eq. B.1). Geometry contributions – including the notch angle (l_w/h_w) – and two load path parameters: (l_w/t_b) and the log-ratio of $(t_c/2+l_w)/t_b$ are involved, as well as (t_b/R_t) implicitly representing the internal

2
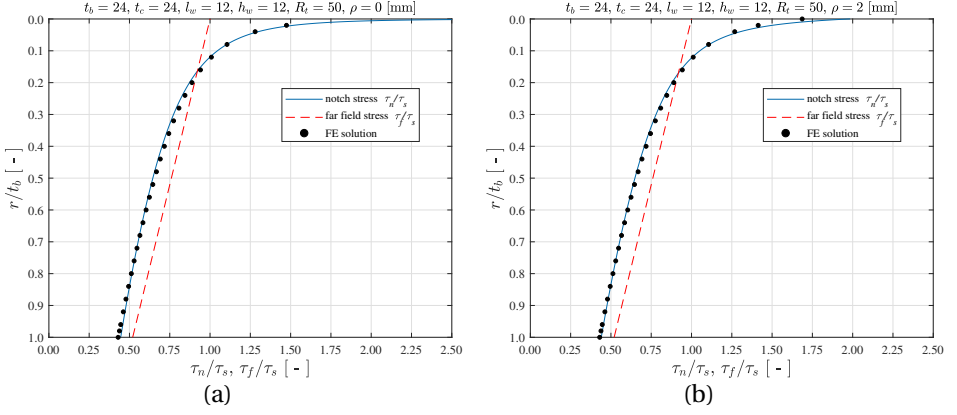
Figure 2.9.: Weld toe notch stress distribution for $\rho = 0$ (a) and $\rho > 0$ (b) for a DS welded T-joint; $r_{\tau_s} = 0.24$.
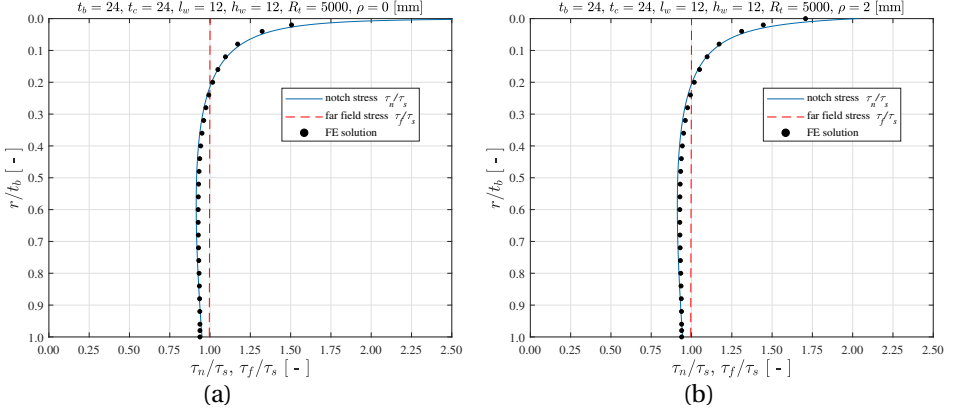
Figure 2.10.: Weld toe notch stress distribution for $\rho = 0$ (a) and $\rho > 0$ (b) for a DS welded T-joint; $r_{\tau_s} = 0$.

loading contribution in terms of r_{τ_s} (Appendix B). The weld load carrying stress turns out to be virtually ρ independent for realistic values: $(\rho/t_b) \leq 0.2$, and has been neglected in establishing the C_{tw} fitting function.

Comparing the required C_{tw} values to the estimates (Fig. 2.8) reflect a good match. Depending on the joint dimensions, the weld load carrying stress level for the weld toe notch at the base plate can be up to about 30 [%] of the structural stress τ_s. For varying t_b, t_c, and h_w, the trends are the same and opposite to the relative base plate loads (Fig. 2.7) as expected because of the same physics. Increasing t_b decreases C_{tw} since the relative stiffness contribution of the weld and cross plate load path decreases. For increasing t_c and h_w, the C_{tw} values increase because the
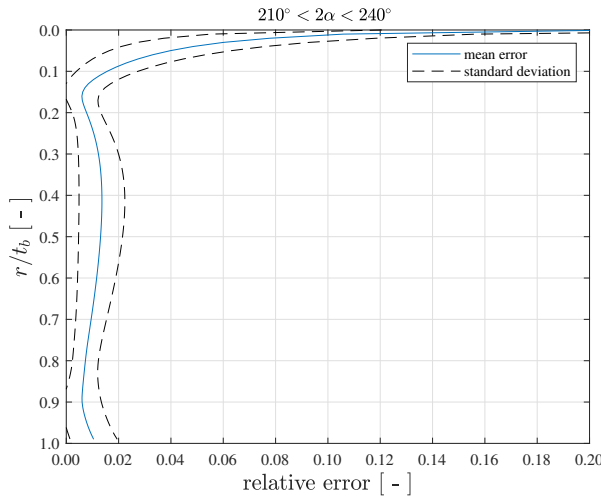
Figure 2.11.: Relative stress distribution error for DS welded T-joint, comparing the FE solutions and the analytical results. The fillet weld angle is in between 30 and 60 [deg], i.e $210° < 2\alpha < 240°$.
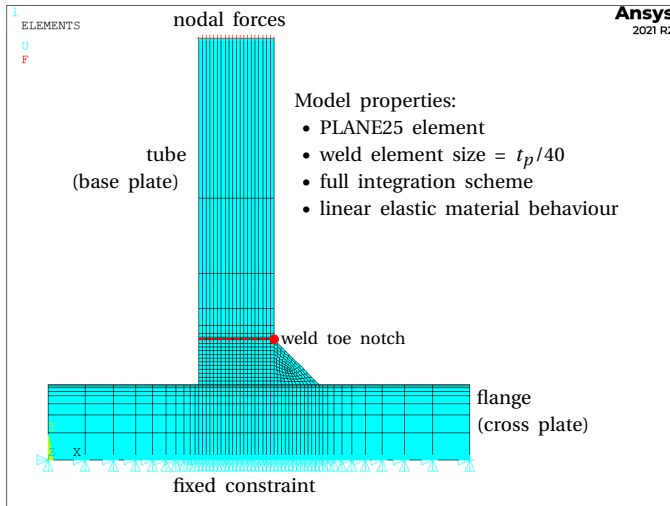
Figure 2.12.: Two-dimensional harmonic axisymmetric FE model for a non-symmetric T-joint.

relative weld and cross plate load path stiffness increases. For increasing l_w, the load through the base plate decreases; the load through the weld and cross plate increases accordingly. However, C_{tw} decreases for increasing l_w, meaning the weld notch becomes less effective. Asymptotically decreasing C_{tw} behaviour – related to the pure shear limit case ($r_{\tau_s} = 0$) – can be observed for increasing R_t, meaning C_{tw} is relatively small in comparison to the pure torsion case ($r_{\tau_s} = 1$).

A monotonic through-thickness stress distribution at the weld toe notch of the base plate is shown (Fig. 2.9) for a combined load case ($r_{\tau_s} = 0.24$); the torsion moment is applied counter-clockwise. A non-monotonic one is shown (Fig. 2.10) for a pure shear force ($r_{\tau_s} = 0$). The joint dimensions are arbitrary, but realistic for maritime structures. A comparison of the weld toe notch stress- and far field stress distributions indicate that force and moment equilibrium is (approximately) satisfied indeed. Converged solid FE model solutions (Fig. 2.12) are added for comparison (Figs. 2.9 and 2.10), showing that the semi-analytical $\tau_n(r/t_p)$ formulations (Eqs. (2.14) and (2.15)) provide accurate stress distributions. In general, the relative error (Fig. 2.11) – obtained considering all stress distributions for the full parameter range – is within 5 [%]. Like for the mode-I formulations, three zones can be identified: the zone 1 peak stress value, the zone 2 notch-affected stress gradient and the zone 3 far-field dominated stress gradient, demonstrating stress field similarity.

2.2.5. STRESS DISTRIBUTION FOR SYMMETRY WITH RESPECT TO ($t_p/2$)

Weld toe notches appear at both sides of a plate/shell if stress distribution symmetry with respect to ($t_p/2$) is detected, as shown for a DS welded cruciform joint (Fig. 2.13). The self-equilibrium stress part components, $\tau_{x\theta}$ (Eq. 2.1) and τ_{tw} (Eq. 2.8) are assumed to be important for fatigue crack development at the considered notch location only and another τ_{se} contribution for the symmetry part will be ignored. The far field stress component is assumed to be dominant for $\{1/2 < (r/t_p) < 1\}$, meaning that no τ_{tw} correction is required for this region. For a pure out-of-plane shear force $F_{s,op}$ induced load case ($\tau_s = \tau_{ss}$), the notch stress formulation for $\rho = 0$ becomes:

$$\tau_{ns}\left(\frac{r}{t_p}\right) = \tau_s f_{\rho=0}\left(\frac{r}{t_p}\right)$$
$$= \tau_s\left[\left(\frac{r}{t_p}\right)^{\lambda_\tau - 1}\mu_{\tau F}\cos(\lambda_\tau\beta) - \mu_{\tau M}\left\{2\left(\frac{r}{t_p}\right) - 1\right\} - C_{tw}\left\{4\left(\frac{r}{t_p}\right) - 1\right\}\right]$$

$$(2.26)$$

and for $\rho > 0$:

$$
\begin{aligned}
\tau_{ns}\left(\frac{r}{t_p}\right) &= \tau_s f_{\rho>0}\left(\frac{r}{t_p}\right) \\
&= \tau_s\left[\left(\frac{r'}{t_p}\right)^{\lambda_\tau-1}\mu_{\tau F}\cos(\lambda_\tau\beta)\left\{1+\left(\frac{r_0}{t_p}\right)^{2\lambda_\tau}\left(\frac{r'}{t_p}\right)^{-2\lambda_\tau}\right\}- \right. \\
&\qquad \left. \mu_{\tau M}\left\{2\left(\frac{r'}{t_p}\right)-1\right\}-C_{tw}\left\{4\left(\frac{r'}{t_p}\right)-1\right\}\right].
\end{aligned}
\tag{2.27}
$$
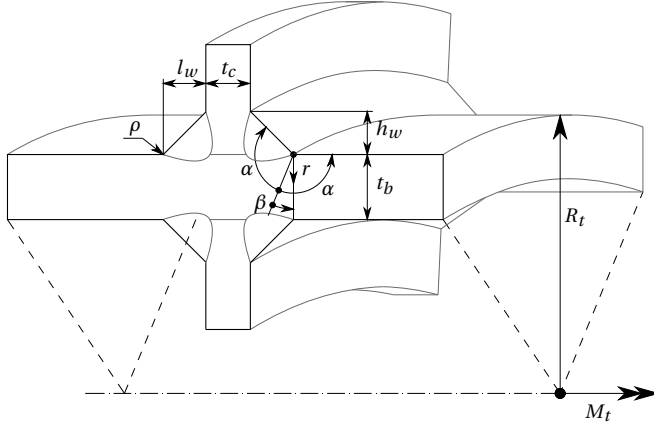
Figure 2.13.: DS welded cruciform joint showing symmetry with respect to $(t_b/2)$, either in a tubular or planar $(R_t \rightarrow \infty)$ structure.

To calculate the coefficients $\mu_{\tau F}$ and $\mu_{\tau M}$, half the plate thickness is considered. Using force and moment equilibrium only is not sufficient and a symmetry condition has been added as 3rd equation. However, the system of equations has become over determined, meaning a least squares solution will be obtained. Allowing for some relaxation, i.e. ignoring moment equilibrium, provides quite accurate results – like for mode-I [18]. Force equilibrium in a weak form for $\rho = 0$:

$$
\int_0^{1/2}\tau_n\left(\frac{r}{t_p}\right)\mathrm{d}\left(\frac{r}{t_p}\right) = \int_0^{1/2}\tau_s\,\mathrm{d}\left(\frac{r}{t_p}\right)
\tag{2.28}
$$

provides

$$
\mu_{\tau F} = \frac{\lambda_\tau\left(C_{tw}+1\right)}{\cos\left(\lambda_\tau\beta\right)2^{1-\lambda_\tau}\left(1+\frac{\lambda_\tau}{2}\left(\lambda_\tau-1\right)\right)}.
\tag{2.29}
$$

In case $\rho > 0$, the coordinate system transformation (Eqs. (2.4) and (2.5)) becomes

2

involved and force equilibrium in weak form:

$$\int\limits_{\left(\frac{r_0}{t_p}\right)}^{\left(\frac{2r_0+1}{2t_p}\right)} \tau_n\left(\frac{r}{t_p}\right) d\left(\frac{r}{t_p}\right) = \int\limits_{0}^{1/2} \tau_s\, d\left(\frac{r}{t_p}\right)$$

(2.30)

denotes

$$\mu_{\tau F} = \frac{\begin{array}{c} \lambda_\tau\left\{\lambda_\tau\left(\frac{r_0}{t_p}\right)^{2\lambda_\tau}\left(\frac{2r_0+1}{2t_p}\right)\left(\frac{4r_0+1}{4t_p^2}\right)\left\{2^{\lambda_\tau-1}+C_{tw}2^{\lambda_\tau}\left(\frac{1}{2t_p}\right)\right\}- \\ 2^{\lambda_\tau+1}C_{tw}\left[\left(\frac{2r_0+1}{2t_p}\right)^2\left(\frac{r_0}{t_p}\right)^{\lambda_\tau}-\left(\frac{2r_0+1}{2t_p}\right)\left(\frac{r_0}{t_p}\right)^{\lambda_\tau+1}-\left(\frac{2r_0+1}{2t_p}\right)^{2+\lambda_\tau}+ \\ \left(\frac{r_0}{t_p}\right)\left(\frac{2r_0+1}{2t_p}\right)^{\lambda_\tau+1}\right]-2^{\lambda_\tau}\left[\left(\frac{r_0}{t_p}\right)^{\lambda_\tau}\left(\frac{2r_0+1}{2t_p}\right)-\left(\frac{2r_0+1}{2t_p}\right)^{\lambda+1}\right]\right\}\end{array}}{\begin{array}{c}\cos\left(\lambda_\tau\theta\right)\left(\frac{2r_0+1}{2t_p}\right)\left\{\lambda_\tau\left[\left(\frac{4r_0+1}{4t_p^2}\right)\right]\left(\frac{r_0}{t_p}\right)^{2\lambda_\tau}-2\left(\frac{r_0}{t_p}\right)^{\lambda_\tau}+2\left(\frac{2r_0+1}{2t_p}\right)^{\lambda_\tau}\right\}. \\ \left\{\left(\frac{2r_0+1}{2t_p}\right)\lambda_\tau2^{\lambda_\tau}\left[\left(\frac{1}{2t_p}\right)\right]\left(\frac{r_0}{t_p}\right)^{2\lambda_\tau}+2^{\lambda_\tau}\left[\left(\frac{2r_0+1}{2t_p}\right)^{\lambda_\tau}-\left(\frac{r_0}{t_p}\right)^{\lambda_\tau}\right]+\frac{\lambda_\tau(\lambda_\tau-1)}{2t_p^2}\right\}\end{array}}.$$

(2.31)

Imposing symmetry:

$$\left.\frac{d\tau_n\left(\frac{r}{t_p}\right)}{d\left(\frac{r}{t_p}\right)}\right|_{\left(\frac{r}{t_p}=\frac{1}{2}\right)} = 0$$

(2.32)

yields $\mu_{\tau M} = (2\lambda_\tau(\lambda_\tau-1)-4C_{tw})(\lambda_\tau^2-\lambda_\tau+2)^{-1}$ for $\rho=0$. However, like observed for moment equilibrium in case of non-symmetry (Section 2.2.4), substitution in $\tau_n(r/t_p)$ provides a C_{tw} independent equation, since the introduced anti-symmetric term and the weld load carrying stress have the same form. Ignoring the weld load carrying stress contribution yields for $\rho=0$:

$$\mu_{\tau M} = \frac{2\lambda_\tau(\lambda_\tau-1)}{\lambda_\tau^2-\lambda_\tau+2}$$

(2.33)

and for $\rho>0$, considering the notch radius induced shift of the coordinate system origin (Eqs. (2.4) and (2.5)):

$$\mu_{\tau M} = \frac{\left(\frac{2r_0+1}{2t_p}\right)^2\lambda_\tau\left\{2^{\lambda_\tau}\left(\frac{r_0}{t_p}\right)^{2\lambda_\tau}+4(\lambda_\tau-1)\right\}}{\left\{\lambda_\tau2^{\lambda_\tau}\left(\frac{r_0}{t_p}\right)^{2\lambda_\tau}\left(\frac{2r_0+1}{4t_p^2}\right)+2^{\lambda_\tau}\left[\left(\frac{2r_0+1}{2t_p}\right)^{\lambda_\tau}-\left(\frac{r_0}{t_p}\right)^{\lambda_\tau}\right]+\frac{\lambda_\tau(\lambda_\tau-1)}{2t_p^2}\right\}}.$$

(2.34)

In order to acquire the pure torsion moment M_t induced notch stress distribution in a similar formulation as for non-symmetry (Eq. 2.15), i.e. including a far field torsion stress projection, $\tau_{ns}(r/t_p)$ needs to be shifted first by $\{1-f(r/t_p=1/2)\}$ – with $f(r/t_p) = f_{\rho=0}(r/t_p)$ or $f(r/t_p) = f_{\rho>0}(r/t_p)$ for respectively $\rho=0$ and $\rho>0$ – in order to meet the condition $\tau_{nt}(r/t_p=1/2)=0$. To satisfy anti-symmetry, the τ_{nt}
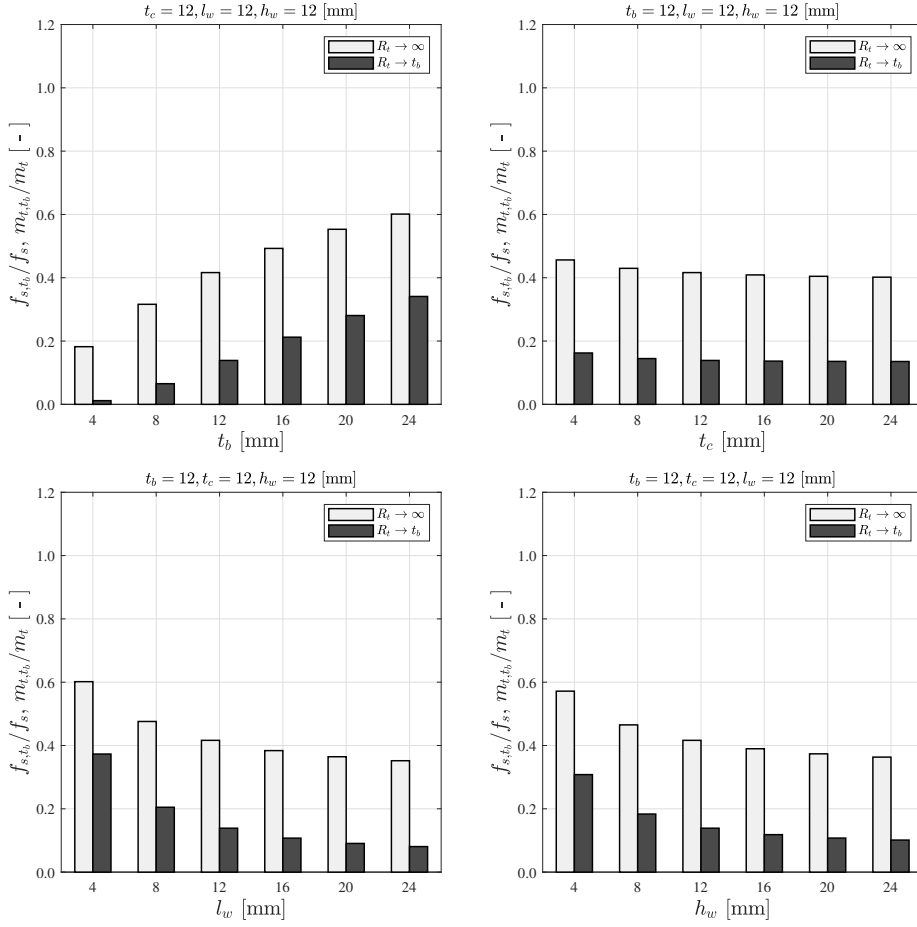
Figure 2.14.: Relative base plate shear load for a DS welded cruciform joint, varying t_b, t_c, l_w and h_w for both $R_t \to \infty$ and $R_t \to t_b$.

gradient at $(r/t_p = 1/2)$ should be equal to the far field torsion value -2. Subtracting the shift in terms of a torsion stress gradient $-2\{1 - f(r/t_p = 1/2)\}$ from the unit stress 1, the obtained formulation needs to be scaled using $\{2f(r/t_p = 1/2) - 1\}$ and becomes for $\rho = 0$:

$$\tau_{nt}\left(\frac{r}{t_p}\right) = \tau_s\left[2f_{\rho=0}\left(\frac{r}{t_p} = \frac{1}{2}\right) - 1\right]\left\{f_{\rho=0}\left(\frac{r}{t_p}\right)\left[1 - f_{\rho=0}\left(\frac{r}{t_p} = \frac{1}{2}\right)\right] - 2\left(\frac{r}{t_p}\right)\right\} \quad (2.35)$$

with

$$f_{\rho=0}\left(\frac{r}{t_p} = \frac{1}{2}\right) = \left[\left(\frac{1}{2}\right)^{\lambda_\tau - 1}\mu_{\tau F}\cos(\lambda_\tau \beta) - C_{tw}\right] \quad (2.36)$$

and for $\rho > 0$:

$$\tau_{nt}\left(\frac{r'}{t_p}\right) = \tau_s \left[2f_{\rho>0}\left(\frac{r'}{t_p} = \frac{1}{2}\right) - 1\right]\left\{f_{\rho>0}\left(\frac{r'}{t_p}\right) + \left[1 - f_{\rho>0}\left(\frac{r'}{t_p} = \frac{1}{2}\right)\right] - 2\left(\frac{r'}{t_p}\right)\right\} \quad (2.37)$$

2
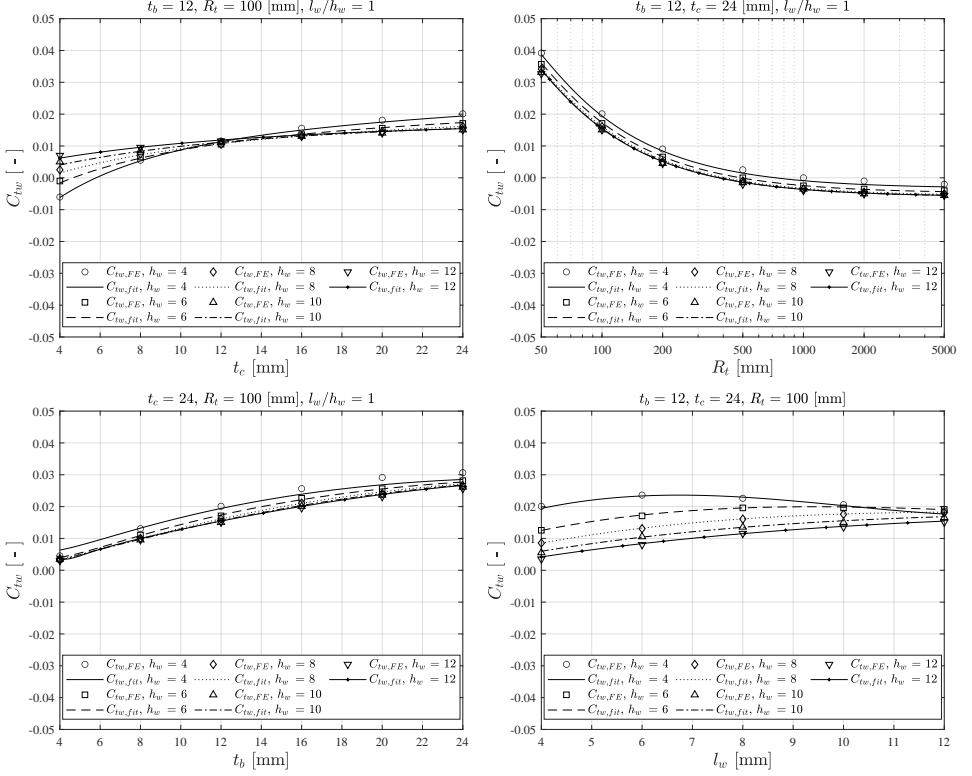
Figure 2.15.: Required C_{tw} value and fit estimate for a DS welded cruciform joint, varying t_b, t_c, l_w , h_w and R_t.

with

$$f_{\rho>0}\left(\frac{r'}{t_p} = \frac{1}{2}\right) = \left[\left(\frac{2r_0+1}{2t_p}\right)^{\lambda_\tau - 1}\mu_{\tau F}\cos(\lambda_\tau \beta) \cdot \left\{1 + \left(\frac{r_0}{t_p}\right)^{2\lambda_\tau}\left(\frac{2r_0+1}{2t_p}\right)^{-2\lambda_\tau}\right\} - \right.$$
$$\left. \mu_{\tau M}\left\{2\left(\frac{2r_0+1}{2t_p}\right) - 1\right\} - C_{tw}\left\{4\left(\frac{2r_0+1}{2t_p}\right) - 1\right\}\right]. \quad (2.38)$$

Finally, adopting a linear superposition principle, the mode-III stress distribution for symmetry can be obtained for $\rho = 0$ using the τ_{ns} and τ_{nt} formulations

(Eqs. (2.26) and (2.35)) as well as structural stress relations (Eq. 2.13):

$$
\tau_n\left(\frac{r}{t_p}\right) = \tau_s\left(\left[1 - 2r_{\tau_s}\left\{1 - f_{\rho=0}\left(\frac{r}{t_p} = \frac{1}{2}\right)\right\}\right]f_{\rho=0}\left(\frac{r}{t_p}\right) + \right.
$$
$$
\left.\left[2f_{\rho=0}\left(\frac{r}{t_p} = \frac{1}{2}\right) - 1\right]\left\{\left[1 - f_{\rho=0}\left(\frac{r}{t_p} = \frac{1}{2}\right)\right] - 2\left(\frac{r}{t_p}\right)\right\}\right).
$$
(2.39)

The same formulation applies for $\rho > 0$, using $f_{\rho>0}(r/t_p = 1/2)$ rather than $f_{\rho=0}(r/t_p = 1/2)$; i.e. (Eq. 2.27) and (Eq. 2.37). Like for non-symmetry (Section 2.2.4), the $\rho = 0$ expressions are a $\rho > 0$ limit case. For a tubular structure with attachment involving a DS welded cruciform joint and exposed to a torsion moment M_t (Fig. 2.13), the structural stress ratio r_{τ_s} changes for varying tube radius R_t. For the limit cases, respectively $R_t \to t_b$ (corresponding to a solid shaft) and $R_t \to \infty$ (corresponding to a quasi-planar structure), the pure torsion and pure shear case appear, meaning that for symmetry – in contrast to non-symmetry (Section 2.2.4) – both extremes can be considered to establish the r_{τ_s} dependent weld load carrying stress $\tau_s C_{tw}$ behaviour.

Investigating the relative load path contributions for the DS welded cruciform joint, three parallel load paths are involved: one through the base plate and two through the weld and cross plate. The shear forces through the base plate (Fig. 2.14; $R_t \to \infty$) are relatively small in comparison to the DS welded T-joint values (Fig. 2.7) because of the smaller stiffness contribution of each load path. The trends for f_s (Fig. 2.7 for the T-joint – as well as Fig. 2.14; $R_t \to \infty$ for the cruciform joint) and m_t (Fig. 2.14; $R_t \to t_b$) are the same. For m_t, the radius dependent torsion stiffness is involved for all load paths and becomes larger towards the outer load path through the weld and cross plate, clarifying the relatively small $(m_{t,t_b}/m_t)$ values. For increasing t_b, the shear force and torsion moment through the base plate increase because of increasing base plate load path stiffness. The weld and cross plate load path torsion stiffness increases for increasing t_c, l_w, and h_w, meaning the base plate load path contribution decreases. Like for non-symmetry (Section 2.2.4), a 4$^{\text{th}}$ order polynomial fitting function (Eq. B.2) has been established to capture C_{tw} estimates. The weld load carrying stress turns out to be virtually ρ independent for realistic values: $(\rho/t_b) \leq 0.2$ and has been neglected in establishing the C_{tw} fitting function.

For DS welded cruciform joints, the weld load carrying stress level does not even reach 5 [%] of τ_s (Fig. 2.15). Since $R_t = 100$ [mm], the far field stress involves both a (constant) shear force and (linear) torsion moment induced contribution. For varying t_c and l_w, the trends (Fig. 2.15) are the same and opposite to the relative base plate loads (Fig. 2.14) as expected because of the same physics. Although, a decreasing C_{tw} might be expected for increasing t_b and h_w (Fig. 2.14), the increased radius dependent torsion stiffness for the outer load path through the weld and cross plate is responsible for counteracting behaviour and provides even a small C_{tw} increase. Like for the non-symmetry case (Section 2.2.4), asymptotically decreasing C_{tw} behaviour – related to the pure shear limit case ($r_{\tau_s} = 0$) – can be observed for increasing R_t, meaning C_{tw} is relatively small in comparison to the pure torsion case ($r_{\tau_s} = 1$).

2
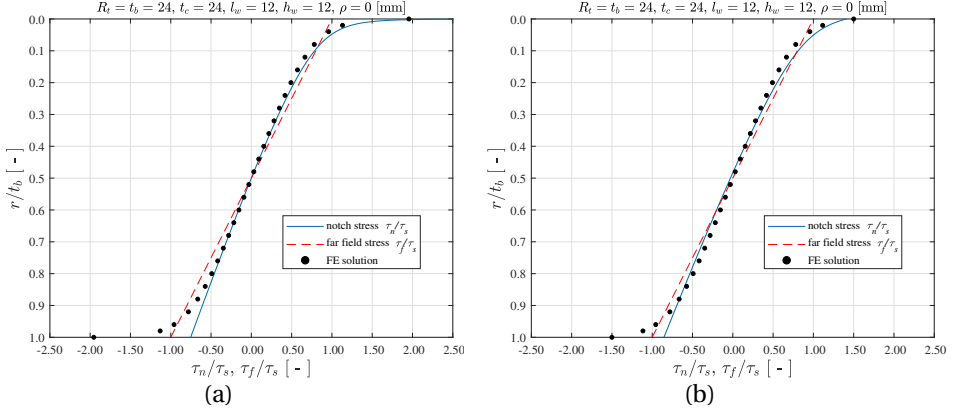
Figure 2.16.: Weld toe notch stress distribution for $\rho = 0$ (a) and $\rho > 0$ (b) for a DS welded cruciform joint; $r_{\tau_s} = 1$.
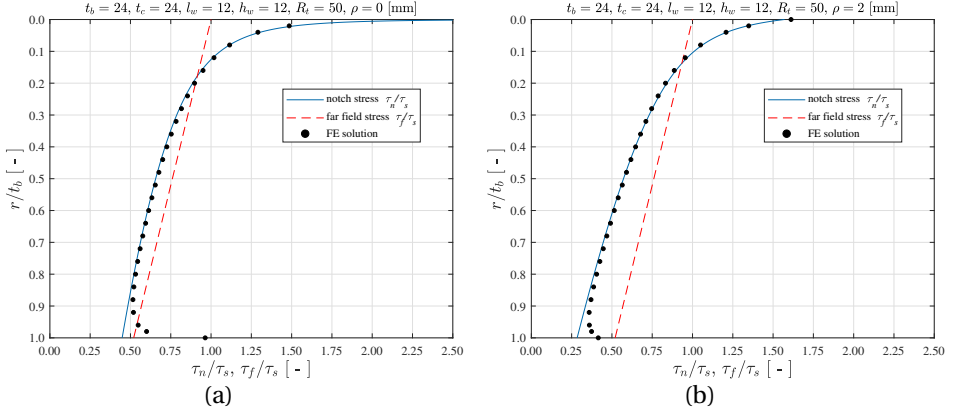
Figure 2.17.: Weld toe notch stress distribution for $\rho = 0$ (a) and $\rho > 0$ (b) for a DS welded cruciform joint; $r_{\tau_s} = 0.24$.

Monotonic through-thickness stress distributions at the weld toe notch of the base plate are shown (Figs. 2.16 and 2.17) for a pure torsion moment ($r_{\tau_s} = 1$) and combined load case ($r_{\tau_s} = 0.24$); the torsion moment is applied counter-clockwise. A non-monotonic one is shown (Fig. 2.18) for a pure shear force ($r_{\tau_s} = 0$). For $\{0 \leq (r/t_b) \leq (1/2)\}$ equilibrium conditions are (approximately) satisfied as imposed. The (anti-)symmetry condition (Eq. 2.32) ensures a stress gradient close to r_{τ_s} for $\{(1/2) \leq (r/t_b) \leq 1\}$. Converged solid FE model solutions are added for comparison, showing that the semi-analytical $\tau_n(r/t_p)$ formulations (Eq. 2.39) provide accurate weld notch stress distributions. Like for the non-symmetry case (Section 2.2.4), three zones can be identified meaning stress field similarity is maintained. In general,
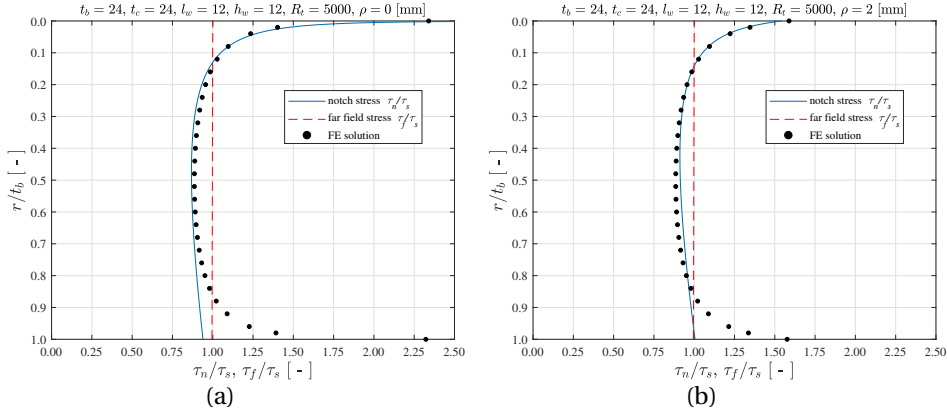
Figure 2.18.: Weld toe notch stress distribution for $\rho = 0$ (a) and $\rho > 0$ (b) for a DS welded cruciform joint; $r_{\tau_s} = 0$.
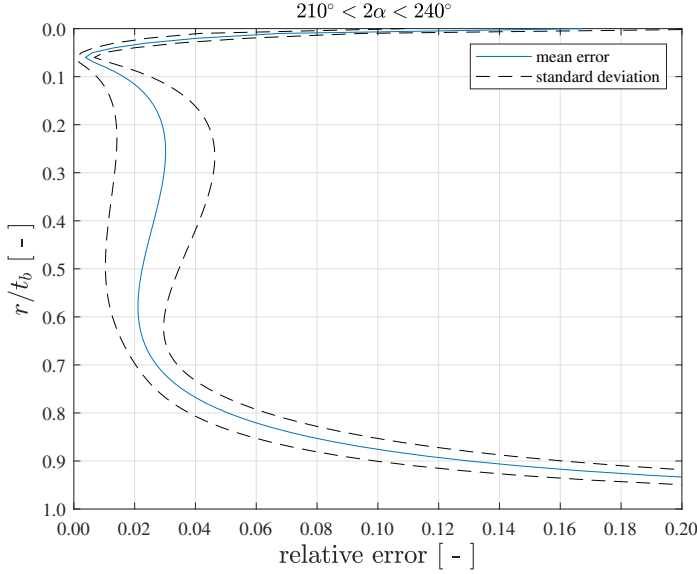
Figure 2.19.: Relative stress distribution error for DS welded cruciform joint, comparing the FE solutions and the analytical results. The fillet weld angle is in between 30 and 60 [deg], i.e $210° < 2\alpha < 240°$.

the relative error (Fig. 2.19) – obtained considering all stress distributions for the full parameter range – is within 5 [%] for $\{0 \leq (r/t_b) \leq (1/2)\}$. Relatively large errors appear in the far field dominated stress gradient zone since the notch contribution for the symmetry part in $\{(1/2) \leq (r/t_b) \leq 1\}$ has been neglected.

2.3. MODE-III WELDED JOINT FATIGUE RESISTANCE

Using fatigue resistance data from literature (Section 2.3.1), the mode-III welded joint mid-cycle fatigue resistance characteristics will be established using the nominal stress concept (Section 2.3.2), as well as the effective notch stress concept (Section 2.3.3) employing the semi-analytical weld notch stress formulations (Section 2.2).

2.3.1. FATIGUE RESISTANCE DATA

Principally, only data series involving steel specimens with circular cross-sections – typical tubular structural joints – are considered (Fig. 2.20 and table 2.1), in order to ensure pure mode-III response conditions at the governing fatigue sensitive location; a DS welded T-joint geometry showing non-symmetry with respect to $(t_p/2)$ of the hot spot type C [16, 18]. Only specimens showing weld toe induced fatigue damage are included, involving predominantly failures and some run-outs. The sample size is ∼ 50.

Table 2.1.: Fatigue resistance data from literature

source	t_b [mm]	t_c [mm]	l_w [mm]	h_w [mm]	R_t [mm]	ρ [mm]	R [-]	no. specimens	thermal condition
[15] Sonsino	10.0	25.0	9.0	9.0	44.45	0.45	-1	4	SR
[49] Yousefi	8.0	25.0	10.0	10.0	42.42	n.a.	[0;-1]	[9;8]	SR
[50] Siljander	9.5	9.5	8.0	8.0	25.40	0.18	[0;-1]	[2;6]	SR
[51] Witt	8.0	16.0	9.0	9.0	44.45	n.a.	-1	11	SR
[52] Seeger	8.0	20.0	6.3	6.3	54.00	1.00	-1	6	SR
[53] Yung	8.0	8.0	7.7	7.7	23.80	n.a.	-1	2	AW

The external loading basically involves a torsion moment M_t. For gripping and/or load application purposes, the specimens typically contain flanges. In case of non-circular cross-sections, warping constrains will introduce a mode-I response contribution at the governing hot spot, explaining why the often used square cross-section data [54, 55] is not included this time.

Specimens involving attachments [56] are not included as well. Although the external loading involves a torsion moment M_t, the attachment locally affects the stiffness distribution and the governing hot spot – type A – response involves a mode-I contribution.

The loading & response ratio $R = -1$ for most data series, meaning the loading & response condition is fully reversed and the mean component is zero. For some data series $R = 0$, reflecting a repeated (impact) loading & response condition with non-zero mean. Since the thermal condition for the majority of the specimens is stress-relieved and for some as-welded – introducing a welding induced mean component as well, the influence of mean stress will be investigated. Looking at the life time range of the considered data, $N = (10^4 \sim 5.10^6)$ cycles, meaning virtually all data reflects mid-cycle fatigue characteristics. Correlating a fatigue strength criterion S to the fatigue life time N, typically a (n approximately)

log-log linear dependency is observed and a Basquin type of relation is naturally adopted [14]: $\log(N) = \log(C) - m\mathring{u}\log(S)$. One way to estimate the single slope curve parameters, intercept $\log(C)$ and slope m as respectively the endurance and damage mechanism coefficient, is using linear regression on fatigue life time: $\log(N) = \log(C) - m\log(S) + \sigma\epsilon$, introducing the scatter (i.e. performance) parameter σ. The maximum likelihood approach [18, 57] will be employed to obtain the most likely parameter vector estimate $\widehat{\Phi}: \max_{\Phi}\{\mathcal{L}(\Phi; N|S)\}$ with $\Phi = \{\log(C), m, \sigma\}$.
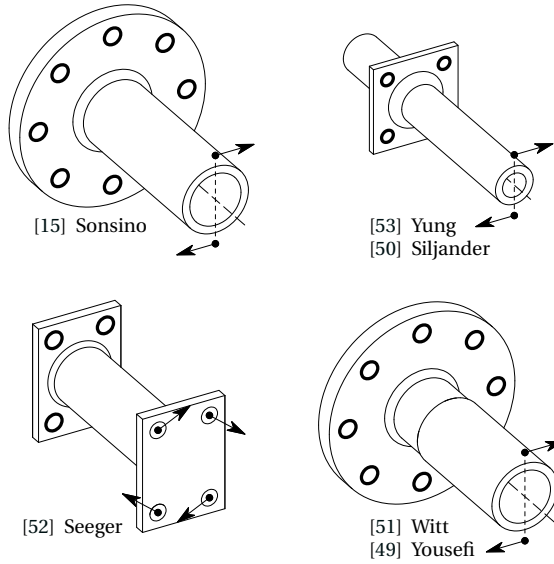
Figure 2.20.: Fatigue test specimen geometry, external loading (arrows) and constraints (thick lines).

2.3.2. NOMINAL STRESS ASSESSMENT

For reference purposes, the nominal stress criterion $S_n = \Delta\tau_{nom}$, a global structural detail- and linear elastic intact geometry parameter [6], will be used to establish the mid-cycle fatigue resistance characteristics. The intercept $\log(C)$ defines the fatigue strength and is typically expressed in terms of FATigue classes and detail CATegories. The damage mechanism is assumed to be similar for all structural details, meaning the slope m is invariant. As long as material, geometry, loading & response, environment as well as failure location and weld quality fit the FAT or CAT description, computational effort is limited and concept complexity is relatively low. However, local geometry and loading & response variations are not explicitly considered, paying off in terms of fatigue resistance accuracy since S_n is processed as point criterion, as 'local' nominal stress, meaning (notch stress gradient induced) size effects are not taken into account explicitly and have to be corrected for. Although a spatial description of a loading & response cycle requires two parameters,

e.g. range and ratio $R = (M_{t,\min}/M_{t,\max}) = (\tau_{\min}/\tau_{\max})$, the ratio – reflecting a mean stress effect – is typically not explicitly considered. However, Walker's mean stress model will be adopted, typically providing the best results for welded joints [14, 16, 58] and turning the nominal stress criterion into an effective one:

$$S_{n,\text{eff}} = \Delta\tau_{n,\text{eff}} = \frac{\Delta\tau_{nom}}{(1-R)^{1-\gamma}} \quad \forall\ 0 \le \gamma \le 1. \tag{2.40}$$

For $\gamma \to 1$, the nominal stress range $\Delta\tau_{nom}$ dominates the fatigue resistance; the mean stress becomes governing for $\gamma \to 0$. The loading & response ratio coefficient γ is a fitting parameter and will be added to the parameter vector: $\Phi\{\log(C), m, \gamma, \sigma\}$. Assuming that the fatigue life time N is most likely log(Normal) distributed, maximum likelihood based regression analysis of the mode-III welded joint fatigue resistance data confirms the log-log linear behaviour (Fig. 2.21). The parameter confidence is relatively large (Table 2.2), and in agreement with expectations considering the sample size (Section 2.3.1).
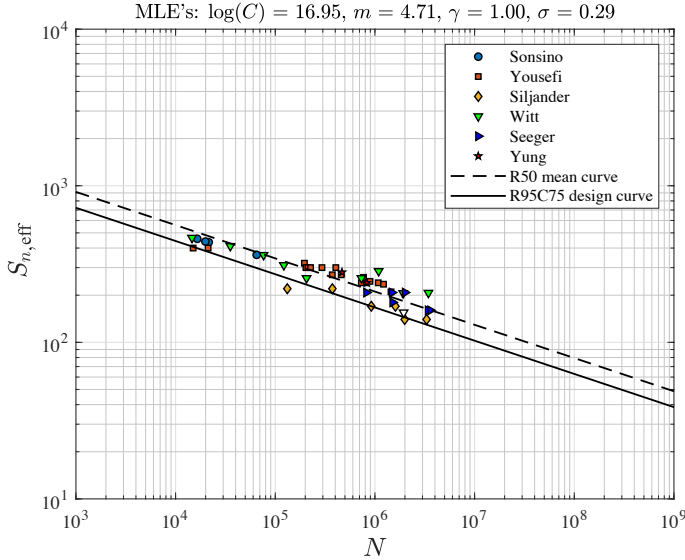
Figure 2.21.: Nominal stress based fatigue resistance including mean stress correction.

The fatigue strength as reflected in $\log(\widehat{C})$ is for the R95C75 design curve - reliability level is 95 [%] and confidence level is 75[%] - at $N = 2 \cdot 10^6$ cycles ~ 150 [MPa], meaning that the IIW FAT80 [33] and Eurocode CAT80 [34] seem conservative. Slope $\widehat{m} \sim 4.7$ is close to the typical design value $m = 5$ [33, 34]. The standard deviation $\widehat{\sigma} \sim 0.29$ can be used to calculate the strength scatter band index $T_{\sigma S_n} = 1 : (S_{n,10}/S_{n,90}) = 1 : 1.25$, the fatigue strength ratio for 10 [%] and 90 [%] probability of survival, and turns out to be already small in comparison to a typical value of 1 : 1.5 [21].

Table 2.2.: Nominal stress based parameter estimates and 75[%] lower and upper confidence bounds.

parameter		
$\log(C)$	16.95	[16.06, 17.85]
m	4.71	[4.34, 5.08]
ρ^*	/	
γ	1.00	[0.97, 1.00]
σ	0.29	[0.26, 0.33]

Walker's loading & response ratio coefficient $\hat{\gamma} \sim 1$, meaning that the mean stress does not affect the mode-III fatigue resistance, in contrast to mode-I [14, 16]. The external loading induced mean shear stress contribution for the considered data sets with $R = \{0, -1\}$ is insignificant and at the same time the contribution of the quasi-constant welding induced residual stress seems negligible as well, since the stress-relieved and as-welded data match the same scatter band. Whether the welding induced residual stress would be a mode-I or mode-III component – or even a mixed one – is unknown, although the mode-I component effect is typically small in the mid-cycle fatigue region as well [59], but can become more significant when shifting to the high-cycle fatigue region [1]. The statement that stress-relieve clearly influences mode-III fatigue resistance [55] seems to be a result of a comparison to a mode-I fatigue resistance curve. Different mean stress effects have been reported for various materials and geometries – both plane and notched [60–64]. However, common denominator seems that for mode-III mean stress effects are less significant than for mode-I, at least in case more ductile materials like steel are involved. Since $\gamma \sim 0.9$ for mode-I [14], the same observation applies to the fatigue resistance of welded joints in steel (maritime) structures.

2.3.3. EFFECTIVE NOTCH STRESS ASSESSMENT

Although for welded joints (short and long) crack growth dominates the damage process, the fatigue life time N is predominantly spent in the notch affected region [13], meaning a local notch characteristic intact geometry parameter rather than a cracked geometry one can be adopted as fatigue strength criterion as well. Since the (as) weld(ed) notch radius ρ is typically small, a zone 1 peak stress criterion would be too conservative. Adopting a micro- and meso-structural notch support hypothesis, an effective notch stress estimate τ_e can be obtained by averaging the notch stress distribution along the expected crack path over a material characteristic micro- and meso-structural length ρ^*, partially incorporating a zone 2 notch stress gradient – and zone 3 far field stress gradient contribution as well [14, 16, 17, 19–21, 65]:

$$\tau_e = \frac{t_p}{\rho^*} \int_0^{\frac{\rho^*}{t_p}} \tau_n \left(\frac{r}{t_p} \right) \mathrm{d} \left(\frac{r}{t_p} \right). \tag{2.41}$$

Typically, a solid FE model solution is required in order to estimate τ_e. However, taking advantage of the stress distribution formulations (Eqs. (2.14), (2.15) and (2.39)), the effective notch stress criterion $S_e = \Delta\sigma_e$ in case of non-symmetry becomes for $\rho = 0$:

2

$$S_e = \frac{\Delta\tau_s}{\lambda_\tau} \frac{t_p}{\rho^*} \left\{ \cos(\lambda_\tau\beta)\mu_{\tau F} \left(\frac{\rho^*}{t_p}\right)^{\lambda_\tau} - \lambda_\tau \left(\frac{\rho^*}{t_p}\right) \left[\left(\frac{\rho^*}{t_p}\right)(\mu_{\tau M} + r_{\tau_s} + C_{tw}) - \mu_{\tau M} - C_{tw} \right] \right\}$$
(2.42)

and for $\rho > 0$:

$$S_e = \frac{\Delta\tau_s}{\lambda_\tau} \left(\frac{t_p}{r_0 + \rho^*}\right) \left\{ \cos(\lambda_\tau\beta)\mu_{\tau F} \left[\left(\frac{r_0 + \rho^*}{t_p}\right)^{\lambda_\tau} - \left(\frac{r_0}{t_p}\right)^{\lambda_\tau} \right] - \right.$$
$$\cos(\lambda_\tau\beta) \left(\frac{r_0}{t_p}\right)^{2\lambda_\tau} \mu_{\tau F} \left[\left(\frac{r_0 + \rho^*}{t_p}\right)^{-\lambda_\tau} - \left(\frac{r_0}{t_p}\right)^{-\lambda_\tau} \right] - $$
$$\left. \lambda_\tau \frac{\rho^*}{t_p} \left[\left(\frac{2r_0 + \rho^*}{t_p}\right)(\mu_{\tau M} + r_{\tau_s} + C_{tw}) - \mu_{\tau M} - C_{tw} \right] \right\}.$$
(2.43)

In case of symmetry with respect to $(t_p/2)$ and $\rho = 0$:

$$S_e = \frac{2\Delta\tau_s}{\lambda_\tau} \frac{t_p}{\rho^*} \left\{ \cos(\lambda_\tau\beta)\mu_{\tau F} \left(\frac{\rho^*}{t_p}\right)^{\lambda_\tau} \left\{ \frac{1}{2} + r_{\tau_s} \left[f_{\rho=0} \left(\frac{r}{t_p} = \frac{1}{2}\right) - 1 \right] \right\} - \right.$$
$$\lambda_\tau \left(\frac{\rho^*}{t_p}\right) \left[\left(\frac{\rho^*}{t_p}\right) \left\{ \frac{\mu_{\tau M}}{2} + f_{\rho=0} \left(\frac{r}{t_p} = \frac{1}{2}\right) + C_{tw} - \frac{1}{2} + \right. \right.$$
$$\left[f_{\rho=0} \left(\frac{r}{t_p} = \frac{1}{2}\right) - 1 \right] (\mu_{\tau M} + 2C_{tw}) r_{\tau_s} \right\} - $$
$$\left[f_{\rho=0} \left(\frac{r}{t_p} = \frac{1}{2}\right) - 1 \right] (\mu_{\tau M} + C_{tw}) r_{\tau_s} + \left[f_{\rho=0} \left(\frac{r}{t_p} = \frac{1}{2}\right) \right]^2 - $$
$$\left. \frac{1}{2} \left[\mu_{\tau M} + 3 f_{\rho=0} \left(\frac{r}{t_p} = \frac{1}{2}\right) + C_{tw} - 1 \right] \right] \right\}$$
(2.44)

and for $\rho > 0$:

2

$$
\begin{aligned}
S_e = &\frac{2\Delta\tau_s}{\lambda_\tau}\left(\frac{t_p}{r_0 + \rho^*}\right)\cdot \\
&\left\langle\left[\cos(\lambda_\tau\beta)\mu_{\tau F}\left\{\frac{1}{2} + \left[f_{\rho>0}\left(\frac{r}{t_p} = \frac{1}{2}\right) - 1\right]r_{\tau_s}\right\}\right]\cdot\right. \\
&\left\{\left(\frac{r_0}{t_p}\right)^{2\lambda_\tau}\left[\left(\frac{r_0}{t_p}\right)^{-\lambda_\tau} - \left(\frac{r_0 + \rho^*}{t_p}\right)^{-\lambda_\tau}\right] - \left[\left(\frac{r_0}{t_p}\right)^{\lambda_\tau} - \left(\frac{r_0 + \rho^*}{t_p}\right)^{\lambda_\tau}\right]\right\} - \\
&\lambda_\tau\frac{\rho^*}{t_p}\left\{r_{\tau_s}\left[f_{\rho>0}\left(\frac{r}{t_p} = \frac{1}{2}\right) - 1\right]\left[(\mu_{\tau M} + 2C_{tw})\left(\frac{2r_0 + \rho^*}{t_p}\right) - \mu_{\tau M} - C_{tw}\right] + \right. \\
&\frac{\rho^*}{t_p}\left[\frac{\mu_{\tau M}}{2} + C_{tw} + f_{\rho>0}\left(\frac{r}{t_p} = \frac{1}{2}\right) - \frac{1}{2}\right] + \left[\left(\frac{r_0}{t_p}\right) - \frac{3}{2}\right]f_{\rho>0}\left(\frac{r}{t_p} = \frac{1}{2}\right) + \\
&\left.\left.\left[f_{\rho>0}\left(\frac{r}{t_p} = \frac{1}{2}\right)\right]^2\left(\frac{\mu_{\tau M}}{2} + C_{tw} - \frac{1}{2}\right)\left(\frac{r_0}{t_p}\right) + \frac{1}{2} - \frac{\mu_{\tau M}}{2} - \frac{C_{tw}}{2}\right\}\right\rangle.
\end{aligned}
\tag{2.45}
$$

Incorporating Walker's mean stress model turns the notch stress criterion into an effective one:

$$
S_{e,\text{eff}} = \frac{S_e}{(1-R)^{1-\gamma}}.
\tag{2.46}
$$

In order to obtain a most likely material characteristic length ρ^* and loading & response ratio coefficient γ estimate, both parameters will be added to the parameter vector $\Phi(\log C, m, \gamma, \rho^*, \sigma)$.

Adopting the Basquin type of relation (Section 2.3.1), maximum likelihood based regression analysis of the fatigue resistance data confirms the log-log linear behaviour (Fig. 2.22 and table 2.3). Results are obtained for a most likely log(Normal) distributed fatigue life time N. Since ρ is typically a stochastic variable along the weld seam and quite small, $\rho = 0$ has been assumed.

Table 2.3.: Effective notch stress based parameter estimates and 75[%] lower and upper parameter confidence bounds.

parameter	$\rho = 0$		$\rho > 0$	
$\log(C)$	21.67	[20.25, 23.10]	18.80	[18.06, 19.53]
m	4.74	[4.40, 5.09]	5.08	[4.79, 5.35]
ρ^*	0.00	[0.00, 0.13]	0.12	[0.06, 0.21]
γ	1.00	[0.97, 1.00]	1.00	[0.98, 1.00]
σ	0.27	[0.24, 0.31]	0.21	[0.19, 0.24]

Obviously, the fatigue strength parameter $\log(\widehat{C})$ is different from the nominal stress concept value (Section 2.3.2), since local information is included. As can be expected for log–log linear mid-cycle fatigue behaviour, the scaled co-variance matrix (Table 2.4) shows a highly correlated intercept $\log(C)$ and slope m. However, the introduced $\log(C) - \rho^*$ correlation seems responsible for the decreased parameter confidence. In comparison to the nominal stress value, slope m has hardly changed. The most likely material characteristic length $\widehat{\rho^*}$ is virtually zero, suggesting the

2

Figure 2.22.: Effective notch stress based fatigue resistance including mean stress correction for $\rho = 0$.

Table 2.4.: $S_e - N$ normalized co-variance matrix for $\rho = 0$.

parameter	$\log(C)$	m	ρ^*	γ	σ
$\log(C)$	1.00	-0.47	-0.33	0.35	-0.56
m		1.00	0.79	-0.61	0.79
ρ^*			1.00	0.00	0.33
γ				1.00	-0.83
σ					1.00

notch stress gradient hardly affects the fatigue resistance. However, since ρ^* basically covers size (i.e. thickness) effects, the limited variation in t_b values (Table 2.1) could be at least partially responsible for the $\rho^* \to 0$ result, since the notch gradient induced scaling of all S_e values is approximately the same. On the other hand, the confidence bounds (Table 2.3) indicate that $\rho^* \to t_b$ is not likely, since at the same time the obtained scatter and performance parameter σ has decreased a bit in comparison to the nominal stress based result, introducing the hypothesis that the mode-III fatigue damage process might even be a more near-surface phenomenon than the mode-I process. Experimental results involving t_p values in the range of 5, 15 and even 20 [mm] could help to investigate the validity of this hypothesis. The loading & response ratio coefficient estimate for a local strength criterion like S_e is not different from a global one like S_n: $\hat{\gamma} \to 1$, suggesting mean (shear) stress hardly affects the mode-III fatigue resistance. Performance parameter σ, the

standard deviation, has slightly improved in comparison to the nominal stress based result (Table 2.3), suggesting that the notch stress gradient contributes at least up to some extent to the effective notch stress performance. However, since the $\rho = 0$ assumption is in conflict with S_e ($\rho^* \to 0$) estimates, results for $\rho > 0$ needs to be explored.

Real notch radius values are not available for all data sets (Table 2.1). In order to establish a reasonable ρ estimate, regression analysis results for a range of real notch radii provides insight (Fig. 2.23). Note that $\gamma = 1$ for all cases. Any $0 \le \rho \le 2$ [mm] could be realistic based on the available information (Table 2.1). Adopting $\rho \sim 1.3$ [mm] seems to provide an optimum, i.e. most likely σ. Using the same ρ value for all data sets (Fig. 2.24), however, shows that the most likely results are obtained for $\rho \to 0$. Since $\rho^* \to 0$ at the same time, results would not improve and $\rho \sim 1.3$ [mm] has been selected as most likely – average – estimate for the data sets with unknown real notch radius.
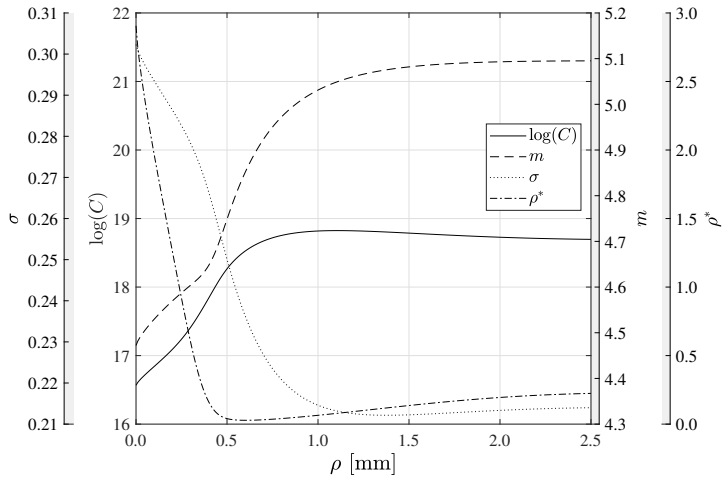
Figure 2.23.: Most likely parameter estimates as function of adopted real notch radius for specimens with unknown ρ.

The $S_e - N$ and parameter profile likelihood plots (Figs. 2.25 and 2.26) as well as the normalized co-variance matrix (Table 2.5) show the analysis results. In comparison to the $\rho \to 0$ result (Fig. 2.22 and table 2.4), the most likely fatigue strength parameter estimate $\log(\widehat{C})$ has decreased since S_e typically gets smaller for $\rho > 0$. The confidence has increased, mainly as a result of the ρ^* confidence and $\log(C) - \rho^*$ correlation (Table 2.5), confirming that ρ^* effectively contributes to the fatigue strength characterisation of welded joints, since ρ^* affects S_e and $\log(C)$ accordingly. Damage mechanism parameter, slope $\widehat{m}$, virtually equals the well-known value $m \sim 5$.

The most likely $\widehat{\rho^*} \sim 0.12$ for welded joint mode-III fatigue resistance in steel structures is still relatively small and quite different from the obtained mode-I

2
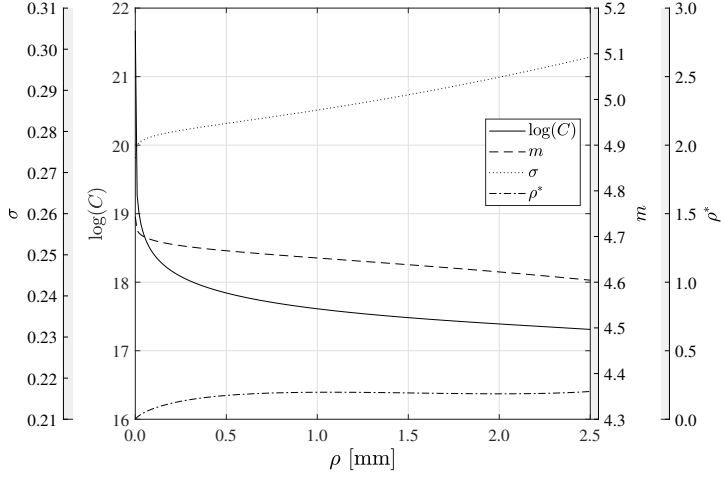
Figure 2.24.: Most likely parameter estimates as function of adopted real notch radius for all specimens.
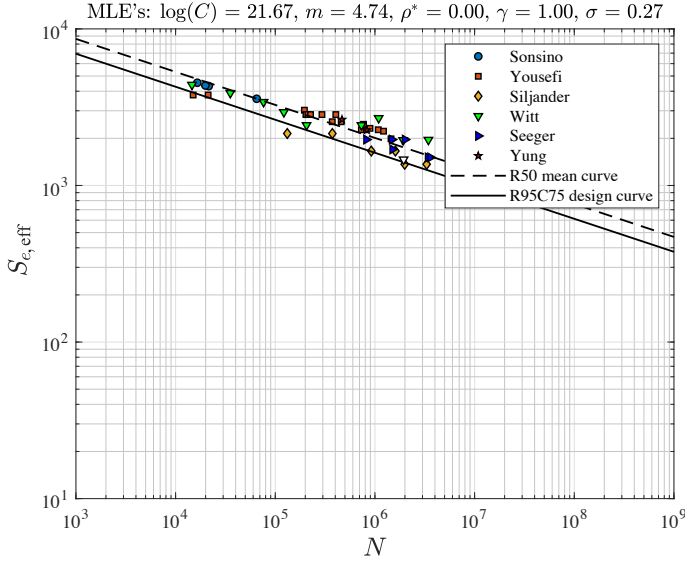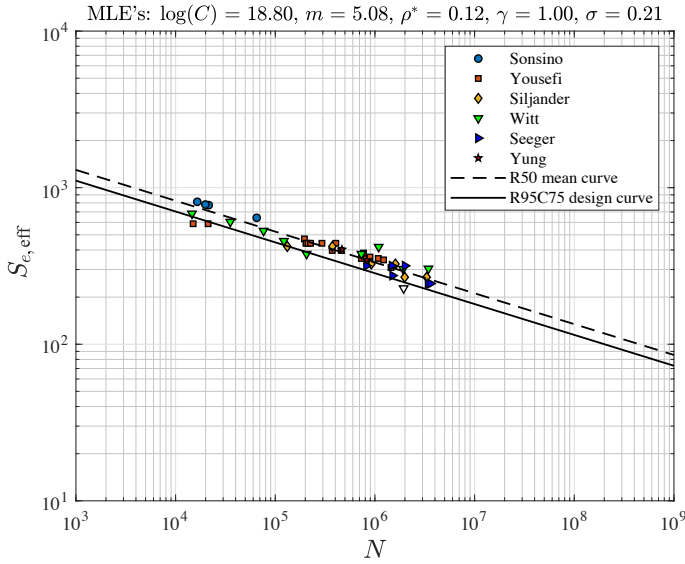

Figure 2.25.: Effective notch stress based fatigue resistance including mean stress correction for $\rho > 0$.

value: $\widehat{\rho^*} \sim 1.14$ [14], meaning ρ^* would be at least both a material and damage mechanism (i.e. mode) characteristic parameter. The ρ^* confidence is quite large (Table 2.3). Since physically speaking ρ^* reflects the length in which the majority of
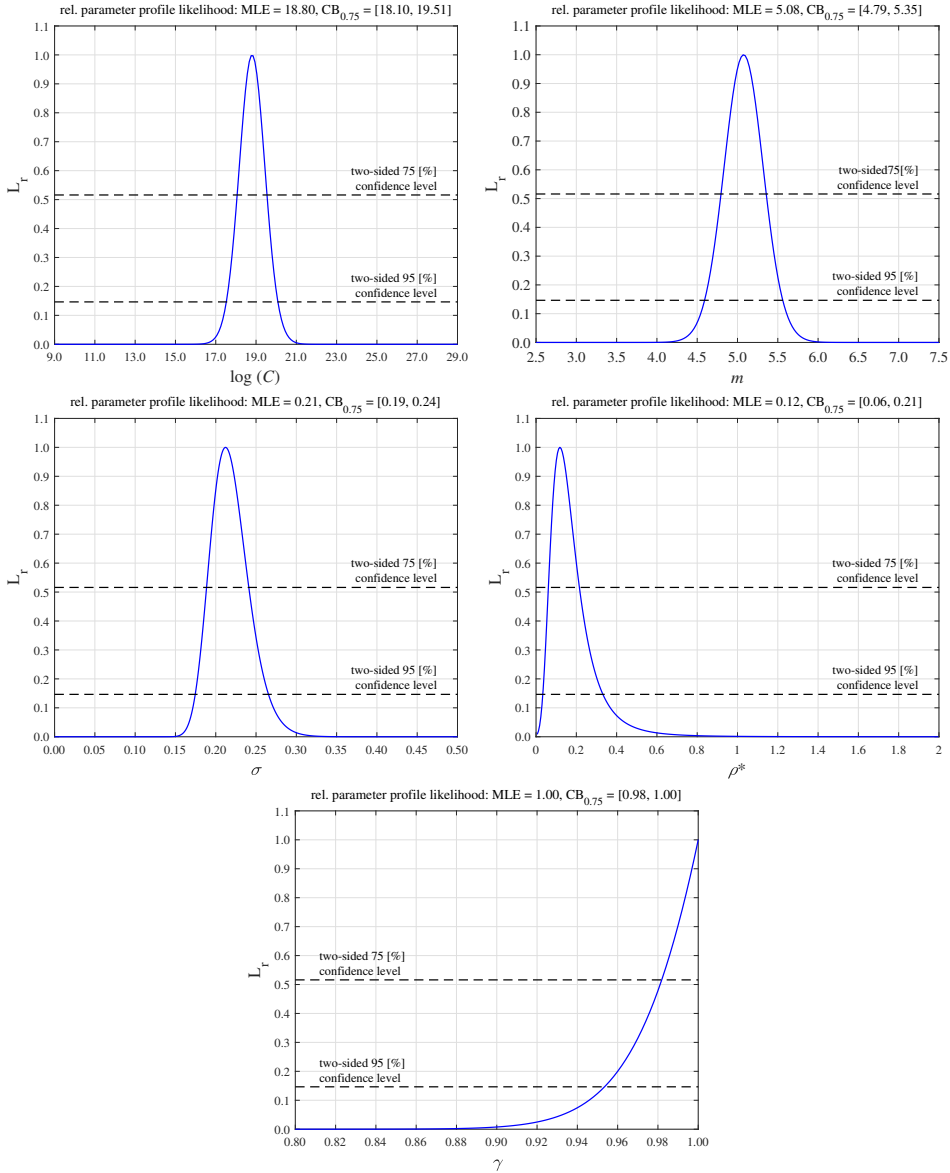
Figure 2.26.: Effective notch stress based parameter profile likelihood plots including two-sided 75% and 95% confidence bounds for $\rho > 0$.

the fatigue life has been spent, a relatively small mode-III value in comparison to the mode-I ρ^* supports the hypothesis that the fatigue damage process in mode-III might even be more a near-surface phenomenon than in mode-I. At the same time, the slope m for mode-III is larger than the mode-I value (i.e. $\sim 5 > 3$), meaning

Table 2.5.: $S_e - N$ normalized co-variance matrix for $\rho > 0$.

parameter	log(C)	m	ρ^*	γ	σ
log(C)	1.00	0.88	-0.25	-0.26	0.24
m		1.00	-0.35	-0.68	0.63
ρ^*			1.00	0.49	-0.47
γ				1.00	-0.94
σ					1.00

the relative contribution of initiation – a (near) surface phenomenon – to the total fatigue life time seems larger for mode-III. Anyway, if ρ^* for mode-III is that small indeed, the real (weld) notch radius stochastics $\rho(\mu, \sigma)$ will be important to capture accurately the zone 2 notch stress gradient. Although a mean stress contribution to the fatigue resistance would seriously affect all parameters, as reflected in the co-variance matrix (Table 2.5) the stress-relieved and as-welded data does not show any effect, $\hat{\gamma} \sim 1$ and the confidence is quite large (Table 2.3). Another local fatigue strength criterion, the Battelle structural stress [55], provides for the same data $\sigma \sim 0.32$ – rather than $\sigma \sim 0.26$ as confirmed by the authors – meaning the effective notch stress performance is much better, since $\hat{\sigma} \sim 0.21$ and the related scatter index has improved to $T_{\sigma S_e} = 1 : 1.22$.

2.4. Conclusions and Outlook

Assuming stress distributions along the expected (2D) crack path are a key element to obtain accurate mode-III fatigue strength and life time estimates, semi-analytical expressions related to the far field stress have been developed for weld toe notches in DS welded T-joints and DS welded cruciform joints, reflecting respectively non-symmetry and symmetry with respect to half the plate thickness. Results for wide range of geometry parameters show an excellent match with solid FE model solutions. For accurate far field stress information, the weld has to be modelled using inclined shell/plate elements. Like for the mode-I formulations, three zones can be identified for all weld notch stress distributions: the zone 1 peak stress value, the zone 2 notch-affected stress gradient and the zone 3 far-field dominated stress gradient, demonstrating stress field similarity. Taking advantage of the developed semi-analytical weld notch stress distributions, the effective notch stress has been adopted as fatigue strength criterion to establish the welded joint mode-III mid-cycle fatigue resistance characteristics. The involved material characteristic micro- and meso-structural length for mode-III has not been investigated before and the most likely estimate $\rho^* \sim 0.1$ turns out to be different from the mode-I value $\rho^* \sim 1.1$ [14] and is relatively small (*research sub-question 1a*), meaning ρ^* would be at least both a material and damage mechanism (i.e. mode) dependent parameter. Since ρ^* basically covers size (i.e. thickness) effects, the limited variation in t_b values (Table 2.1) could be at least partially responsible for $\rho^* \to 0$, since the notch gradient induced scaling of all S_e values is approximately the same. On the other hand, the

confidence bounds indicate that $\rho^* \to t_b$ is not likely, introducing the hypothesis that the mode-III fatigue damage process might even be a more near-surface phenomenon than the mode-I process. Physically speaking ρ^* reflects the length in which the majority of the fatigue life has been spent, meaning a relatively small mode-III value in comparison to the mode-I ρ^* supports the hypothesis. At the same time, the slope m for mode-III is larger than the mode-I value (i.e. $\sim 5 > 3$), meaning the relative contribution of initiation – a (near) surface phenomenon – to the total fatigue life time seems larger for mode-III indeed (*research sub-question 1a*). However, since the available amount and variety of data is limited, conclusive answers cannot be provided yet. Anyway, if ρ^* for mode-III is that small indeed, the real (weld) notch radius stochastics $\rho(\mu, \sigma)$ will be important to capture accurately the zone 2 notch stress gradient. Walker's loading & response ratio coefficient $\gamma \sim 1$, implying that mean stress does not affect the mode-III fatigue resistance. The external loading induced mean shear stress contribution for the considered data sets with $R = \{0, -1\}$ is insignificant and at the same time the contribution of the quasi-constant welding induced residual stress seems negligible as well, since the stress-relieved and as-welded data match the same scatter band. Different mean stress effects have been reported and common denominator seems that for mode-III the mean stress effects are less significant than for mode-I (*research sub-question 1a*), at least in case more ductile materials like steel are involved. Since $\gamma \sim 0.9$ for mode-I [14, 16], the same observation applies to the fatigue resistance of welded joints in steel (maritime) structures.

3

S_e BASED MIXED MODE-{I, III} MULTIAXIAL FATIGUE RESISTANCE

The whole is (not always) greater than the sum of its parts.

Aristotle, philosopher

3.1. INTRODUCTION

Correlation of a fatigue strength parameter S and the fatigue life time N typically reveals a log–log linear dependency and a Basquin type of resistance relation is naturally adopted: $\log(C) = \log(N) - m \cdot \log(S)$. Intercept $\log(C)$ and slope m reflect respectively a strength and mechanism contribution, suggesting the mode-I and mode-III values are different. Adopting the effective notch stress, S_e introduces the material characteristic length ρ^*; another mechanism contribution. Uniaxial mode-I and mode-III investigations revealed distinguished $\{\rho_I^*, \rho_{III}^*\}$ as well as $\{\log(C_I), \log(C_{III})\}$ and $\{m_I, m_{III}\}$ values [14, 16, 29]. Since a response cycle needs two parameters for a complete spatial description, e.g. range and ratio, mode specific response ratio coefficients $\{\gamma_I, \gamma_{III}\}$ containing another strength contribution have been proposed as well [14, 16, 29]. However, consequences for mixed mode-{I, III} multiaxial fatigue have not been investigated before. Aiming to reduce the still relatively large multiaxial fatigue resistance scatter [66, 67], dedicated mode-{I, III} strength and mechanism related contributions, respectively $\{\log(C), \gamma\}$ and $\{m, \rho^*\}$, will be incorporated in order to obtain improved lifetime estimates. An S_e based multiaxial fatigue strength parameter will be defined considering all relevant assessment aspects for a time domain approach (Section 3.2) and the performance

will be evaluated using multiaxial fatigue resistance data from literature (Section 3.3). The conclusions and outlook (Section 3.4) provide answers to research sub-question 4 and provide half of the information (i.e. S_e related only) required for sub-questions 2, 3 and 5 (Section 1.3).

3.2. MULTIAXIAL FATIGUE ASPECTS

Based on fatigue damage criteria classification [6], particular attention will be paid first to modelling aspects for different types of criteria, looking at static and fatigue strength similarities, as well as differences between infinite and finite life criteria (Section 3.2.1). In order to be able to deal with random multiaxial response conditions, damage plane selection (Section 3.2.2) and cycle counting aspects will be addressed (Section 3.2.3), including ways to deal with non-proportionality (Section 3.2.4). Last but not least, fatigue damage accumulation model considerations will be discussed (Section 3.2.5).

3.2.1. FAILURE CRITERION

Classical failure criteria for more ductile isotropic materials, including polycrystalline metals like steel, already aim to estimate yielding of materials for monotonic — ultimate strength related -– multiaxial response (i.e. stress) conditions [68].

Any stress tensor can be decomposed into the sum of a hydrostatic (mean) and deviatoric (shear induced) part. Whereas the hydrostatic part introduces a volume change only without deformation, the deviatoric one is associated with shape change, distortion. Polycrystalline metals comprise of grains with different shape, size and orientation, meaning for any loading condition each grain shows a different amount of slip; a shear induced response, changing the shape. After failure, slip bands turn out to be visible at the fracture surface, i.e. experimental evidence suggesting the Tresca maximum shear stress criterion is decisive [69]. For shell/plate type of structures only the mode-III component is relevant: $S = \max(\tau_{III}) \leq \sigma_y$, since the mode-II contribution is negligible. At the same time, experimental evidence shows that ductile materials do not fail in case of a hydrostatic stress component only (e.g. metals in deep ocean waters), introducing the distortion based von Mises maximum deviatoric stress criterion [69]. For shell/plate type of structures principally containing a governing mode-I normal and mode-III shear component only: $S = \max\left\{\sqrt{\sigma_I^2 + \beta \cdot \tau_{III}^2}\right\} \leq \sigma_y$. The von Mises criterion is essentially an equivalent normal stress formulation. Shear strength coefficient β is a material constant. For steel $\beta = 3$ is typically adopted [69].

For cyclic – fatigue strength related – multiaxial response conditions, linear and non-linear failure criteria have been proposed for the infinite life region [e.g 70–72]. A fatigue resistance limit is naturally introduced, defining the threshold for an unlimited number of cycles: $S_\infty(N \to \infty)$. Based on different modelling philosophies, the criteria are principally a combination of two parameters: a primary governing term and a secondary correcting one. The linear criteria: $S = \max\left\{C_1 \cdot f(S_1) + C_2 \cdot g(S_2)\right\} \leq S_\infty(N \to \infty)$, seem of the Tresca type; the non-linear

ones: $S = \max\{\sqrt{C_1 \cdot f(S_1)^2 + C_2 \cdot g(S_2)^2}\} \le S_\infty (N \to \infty)$, of the von Mises type. Parameters S_1 and S_2 are for example the deviatoric and (max) hydrostatic stress, respectively, taking the complete stress state into account. The shear stress – assuming crack initiation provides the major contribution to the fatigue lifetime – and (max) hydrostatic stress can be used as well. Alternatively, the shear stress τ_{III} and (max) normal stress σ_I are adopted [e.g. 73], reflecting the multiaxial mode-I and mode-III contributions. Constants C_1 and C_2 are (fitted) material dependent coefficients. Since a response cycle requires two parameters for a complete definition in space, e.g. the stress range S and the response ratio $R = S_{min}/S_{max}$, both may affect the fatigue strength and the criteria may even turn into: $S = \max\{C_1 \cdot f(S_1, R_1) + C_2 \cdot g(S_2, R_2)\} \le S_\infty (N \to \infty)$ for an equivalent shear stress and $S = \max\{\sqrt{C_1 \cdot f(S_1, R_1)^2 + C_2 \cdot g(S_2, R_2)^2}\} \le S_\infty (N \to \infty)$ for an equivalent normal one.

For the finite life region, principally the same type of criteria could be adopted, although the coefficients will become response level dependent and the fatigue limit will turn into a lifetime dependent fatigue resistance relation because of the finite number of response cycles N: $S = \max\{C_1(S_1) \cdot f(S_1, R_1) + C_2(S_2) \cdot g(S_2, R_2)\} \le S(N)$ and $S = \max\{\sqrt{C_1(S_1) \cdot f(S_1, R_1)^2 + C_2(S_2) \cdot g(S_2, R_2)^2}\} \le S(N)$. The governing mode-I and mode-III log-log linear mid-cycle fatigue resistance relations (Fig. 3.1): $\log(N) = \log(C) - m \cdot \log(S) \to \log(S) = \{\log(C) - \log(N)\}/m \to S(N) = (N/C)^{-1/m}$, have characteristic intercept and slope parameters $\{\log(C), m\}$, respectively reflecting different fatigue strengths and mechanisms. In case initiation dominates the fatigue lifetime, the shear stress is in control and a Tresca type of criterion seems straightforward. If growth provides the major contribution, an equivalent normal stress based von Mises type of criterion makes sense.
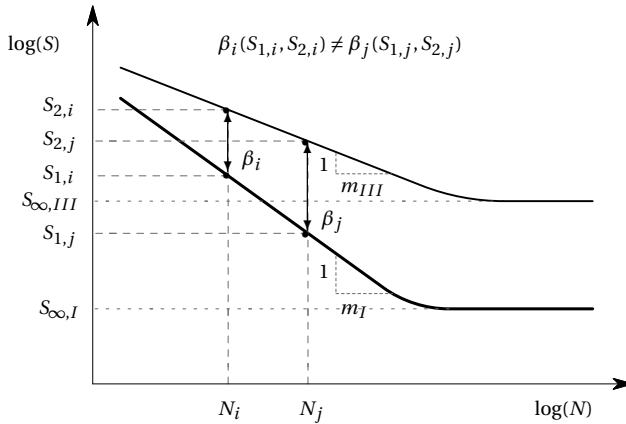

Figure 3.1.: Lifetime dependent mode-I and mode-III fatigue strength ratio.

Adopting an (equivalent) shear stress $S = \max[\text{VAR}\{\tau_{III}(t)\}]$ based on a primary governing term only, a response based normal to shear stress ratio has been

3

introduced to establish the failure criterion [66, 74–76]: $\rho_\tau = \Delta\sigma_I/\Delta\tau_{III} = \sqrt{[2\cdot\text{VAR}\{\sigma_I(t)\}]}/\sqrt{[2\cdot\text{VAR}\{\tau_{III}(t)\}]}$. Incorporating the relative mode-I and mode-III contributions, a response representative – rather than mode-III equivalent – resistance curve has been proposed with $\log\{C(\rho_\tau)\} = a\cdot\rho_\tau + b$ and $m(\rho_\tau) = c\cdot\rho_\tau + d$, turning the criterion into: $S = \max[\text{VAR}\{\tau_{III}(t)\}] \le \{N/C(\rho_\tau)\}^{-1/m(\rho_\tau)}$. Coefficients {$a$, b, c, d} are based on the mode-I and mode-III reference resistance curve parameters. Since both the resistance and response information define $[\log\{C(\rho_\tau)\}, m(\rho_\tau)]$, the intercept and slope can become out of (resistance) control. Bounds have been provided [76, 77], but remain a modelling limitation. Involving the mean stress as a 2nd parameter to define a cycle in space, the equivalent shear stress turns into an effective one [75]: $S = \max[\text{VAR}\{\tau_{III}(t)\}_{eff}] \le \{N/C(\rho_\tau)\}^{-1/m(\rho_\tau)}$. A similar ratio has been proposed to establish a shear stress fitting coefficient $C_2\{\Delta\tau_{III}/\Delta\sigma_I\}$, aiming to obtain a mode-III equivalent resistance curve [78]. Explicit model limitations do not seem to exist, although the multiaxial test data fitted $C_2(\Delta\tau_{III}/\Delta\sigma_I)$ formulation implicitly determines up to what extent the criterion: $S = \max[S_1 + C_2\{\Delta\tau_{III}/\Delta\sigma_I\}\cdot S_2] \le \{N/C_{III}\}^{-1/m_{III}}$ with $S_1 = \Delta\tau_{III}$ and $S_2 = \Delta\sigma_I$, is applicable.

For a finite lifetime, the ratio of the mode-I and mode-III fatigue strength depends on the number of cycles N until failure (Fig. 3.1), meaning that for an equivalent normal stress criterion the shear strength coefficient has to be response level dependent rather than constant [e.g. 73]: $S = \max\left[\sqrt{\sigma_I^2 + \beta\{\sigma_I(N), \tau_{III}(N)\}\cdot\tau_{III}^2}\right]$, with $\beta = \Delta\sigma_I(N)/\Delta\tau_{III}(N) = C\cdot N^M$, $C = 10^{\{m_{III}\cdot\log(C_I) - m_I\cdot\log(C_{III})\}/\{m_I\cdot m_{III}\}}$ and $M = (m_I - m_{III})/(m_I\cdot m_{III})$. Both uniaxial and multiaxial mode-{I, III} fatigue test data should fit in the mode-I resistance data scatter band, reflecting the same equivalent strength and mechanism, i.e. intercept and slope: $S = \max[\sqrt{\sigma_I^2 + \beta\{\sigma_I(N), \tau_{III}(N)\}\cdot\tau_{III}^2}] \le \{N/C_I\}^{-1/m_I}$. The $S(N)$ formulation is fully resistance defined and $\beta(\sigma_I, \tau_{III})$ bounds, either real or artificial, are not required.

Although the shear strength coefficient should be response level dependent, still a constant β has been used since the fatigue resistance data scatter would hardly reduce [79, 80]. However, at least the uniaxial mode-I and mode-III data is not aligned since the mode-III data is mode-I equivalent at one particular number of cycles only, rather than over the full finite lifetime range. Hardly observing a reduction in fatigue resistance scatter seems a consequence of unbalanced uniaxial mode-I, mode-III and multiaxial mode-{I, III} data in general, or at least ignoring the resistance characteristics for the particular groups of data. Adopting a constant β, regression analysis will principally provide biased, i.e. averaged, fatigue strength and damage mechanism contributions with respect to $\{\log(C), m\}$. In case the mode-I parameters are simply adopted, the mode-III contribution is not properly taken into account. A mean stress correction is typically limited to a mode-I contribution, introducing an effective normal stress $\sigma_{I,eff}$ [e.g. 73, 81].

Rather than a resistance based shear strength coefficient, a response dependent one: $\beta(\Delta\sigma_I, \Delta\tau_{III})$ – similar to the normal to shear stress ratio ρ_τ for the equivalent shear stress criterion, has been proposed [15, 66, 82, 83]. The uniaxial mode-I and mode-III reference conditions can be represented, although for a multiaxial response

$\beta(\Delta\sigma_I, \Delta\tau_{III})$ can take unrealistic values since fatigue resistance related limitations are lacking.

3.2.2. DAMAGE PLANE

Whereas for proportional (i.e. in-phase) multiaxial mode-{I, III} response conditions in a particular 2D $\{S_1, S_2\}$ plane with angle ϕ only the stress tensor magnitude is changing (Fig. 3.2), the tensor additionally rotates for non-proportional (i.e. out-of-phase) ones and the plane angle $\phi(t)$ is varying in time.

Incorporating the damage contribution of all planes explicitly introduces typically
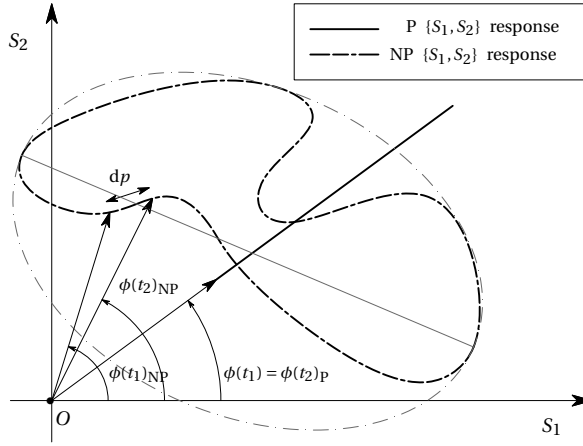
Figure 3.2.: Temporal evolution of stress in the $\{S_1, S_2\}$- stress plane .

an equivalent fatigue strength parameter: $S_{eq} = (1/2\pi) \cdot \int S(\phi) d\phi$, representing the integral plane [e.g. 15, 82, 84]. Alternatively, an enclosing surface like an ellipse can be established in the von Mises stress plane based on the perimeter p (Fig. 3.2) – an implicit angle measure, meaning: $S_{eq} = (1/p) \cdot \int S(p) dp$ [e.g. 85].

Rather than the integral plane, only the governing, i.e. critical plane can be considered, e.g. based on the maximum value of the adopted fatigue strength parameter S, either an equivalent shear stress [e.g. 74–76]: $S = \max[\text{VAR}\{\tau_{III}(\phi)\}]$, or an equivalent normal one [e.g. 73, 85, 86]: $S = \max[\sqrt{\sigma_{I,max}^2(\phi) + \beta\{\sigma_I(N), \tau_{III}(N)\} \cdot \Delta\tau_{III}^2(\phi)}]$. Since the stiffness distribution of (maritime) structures in stiffened panel configuration is predominantly orthotropic and cracks at the weld notches typically develop first in plate thickness direction, the fracture plane can be used as well to obtain S [e.g. 79].

The full stress tensor of a volume element consists of 3 normal- and 6 shear stress components. For (quasi) isotropic materials (like steel) in static equilibrium, element rotation is prevented for and tensor symmetry appears: $\tau_{ij} = \tau_{ji}$, reducing the tensor content to 3 normal- and 3 shear stress components only. Certain symmetric stress tensor properties are coordinate system rotation (i.e. plane) independent,

introducing invariants. Both tensor parts (Section 3.2.1) can be incorporated in terms of invariants to take the complete stress state into account [e.g. 84, 87]. The hydrostatic part, equal to one third of the first tensor invariant I_1, is basically the average normal stress; a mean value. The square root of the second invariant of the deviatoric stress $\sqrt{J_2}$ represents the other part, often incorporated as a von Mises type of criterion: $\sqrt{\beta \cdot J_2}$; a stress range, with the shear stress coefficient β either constant or response level dependent. Both invariants represent up to some extent 2 parameters defining a cycle in space.

3.2.3. CYCLE COUNTING

Although for a mode-I or mode-III uniaxial response cycle counting – i.e. identification of the number of closed hysteresis loops – is principally required for variable amplitude (VA) conditions, in case of a mode-{I- III} multiaxial one cycle counting can already be relevant for constant amplitude (CA) conditions, in particular when a phase shift is involved and/or the frequencies are different. However, if multiaxial cycle counting is required, depends on the adopted failure criterion (Section 3.2.1) and selected damage plane (Section 3.2.2).

For an equivalent fatigue strength parameter $S_{eq}(t)$ at the integral plane – either of the Tresca or von Mises type, at each time instant $S_{eq}(t)$ can be established. Reducing the time series to a peak-valley sequence, uniaxial (rain flow) counting can be adopted in order to obtain the equivalent stress spectrum $\{S_{eq}(n)\}$ [e.g. 15].
In case of a Tresca type of criterion at the critical plane, $S(t)$ can still be processed using uniaxial rain flow counting [e.g. 76]. Virtual cycles have been counted based on zero crossings [88], rather than closed hysteresis loop criteria, but suggest at least that mean stress effects cannot be incorporated. Adopting a von Mises type of criterion, several ways of cycle counting have been considered. The uniaxial rain flow counting algorithm can be straightforward applied to $S(t)$, but sign information – lost by definition – should be incorporated [e.g. 89, 90]. However, sign changes may cause artificial anomalies affecting the von Mises time series and providing unrealistic counting results. Introducing a primary and secondary channel, multiaxial rain flow counting has been proposed. In fact, one von Mises stress component is counted (e.g. the mode-I normal stress) at the primary channel and the corresponding other one (e.g. the mode-III shear stress) at the secondary channel is a projection at the primary channel peak-valley location [e.g. 91]. Although at least the mode-I and mode-III components have been incorporated up to some extent, the established cycles are not likely multiaxial closed hysteresis loops. However, an algorithm continuously searching for the maximum range in the time series (segments) at the von Mises plane (Fig. 3.3) provides cycles reflecting closed hysteresis loops [e.g. 79, 80, 92–94]. In case the structural response is uniaxial, the results are the same as obtained with rain flow counting.

If in terms of invariants only the damage related tensor component, i.e. the deviator, is involved, uniaxial rain flow counting is straightforward applied. When the hydrostatic component is involved as well, multiaxial rain flow counting can be used adopting a primary and secondary channel [e.g. 87].
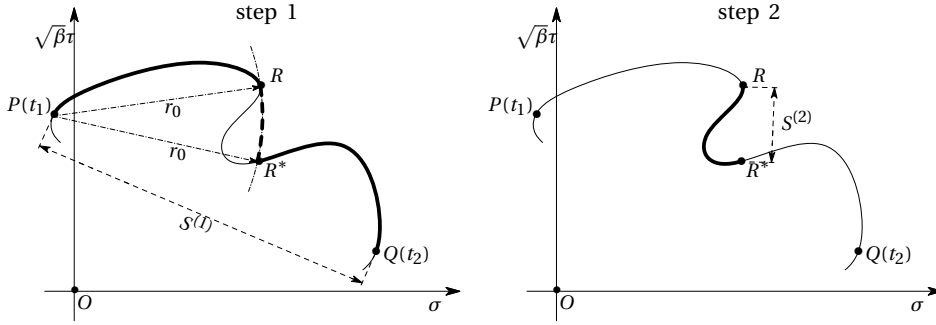
Figure 3.3.: Cycle counting illustration in the von Mises plane, searching for the max. range [e.g. 79, 80, 92–94].

3.2.4. Non-proportionality

The normal mode-I and shear mode-III stress components are not necessarily proportional, e.g. because of asynchronous behaviour, different frequencies or time varying amplitudes. How non-proportionality is incorporated typically depends on the adopted type of criterion (Section 3.2.1), selected damage plane (Section 3.2.2) and cycle counting procedure (Section 3.2.3).

Since an equivalent fatigue strength parameter (Section 3.2.2) takes the damage contribution of all planes into account, any type of non-proportionality is principally incorporated in the criterion. Adopting for example a von Mises type of criterion; an equivalent normal stress, non-proportionality is considered introducing a shear stress variations $\tau(\phi)$ based correction: $S_{eq} = S(\phi = 0) \cdot f\{\tau(\phi)\}$, assuming $\tau(\phi)$ to be the basic requirement to develop fatigue damage [15, 82].

Although for an equivalent shear stress like $S = \max[\text{VAR}\{\tau_{III}(t)\}]$ [76], the normal stress component is not explicitly considered, the response based normal to shear stress ratio $\rho_\tau = \Delta\sigma_I/\Delta\tau_{III} = \sqrt{[2 \cdot \text{VAR}\{\sigma_I(t)\}]}/\sqrt{[2 \cdot \text{VAR}\{\tau_{III}(t)\}]}$ defining the characteristic resistance curve incorporates at least an average non-proportionality measure. Using a similar ratio $C_2\{\tau(t)/\sigma(t)\}$, the equivalent shear stress takes the instantaneous $\{\sigma(t), \tau(t)\}$ contributions into account, meaning non-proportionality is explicitly considered: $S = [S_1 + C_2\{\tau(t)/\sigma(t)\} \cdot S_2]$ with $S_1 = \tau(t)$ and $S_2 = \sigma(t)$ [88].

For an equivalent normal stress of the von Mises type at the critical plane, non-proportionality can be considered in different ways. Using the instantaneous normal and shear stress contributions $\{\sigma(t), \tau(t)\}$, non-proportionality is explicitly incorporated. Even if only a single component has been counted (e.g. the mode-I normal stress) at the primary channel and the corresponding other one (e.g. the mode-III shear stress) at the secondary channel is a projection at the primary channel peak-valley location, meaning the non-proportional time series are basically turned into quasi-proportional ones, non-proportionality is implicitly included up to some extent [e.g. 91]. Cycle counting in the von Mises stress (critical) plane (Section 3.2.3) allows to capture at least the stress range. However, the actual response path or perimeter has been identified as being crucial (Fig. 3.4). Introducing an effective

stress range $S_{eff} = S(1 + c_m \cdot C_{np})$, with $C_{np} = \int_{\widetilde{S}} \{r \cdot |\sin(\theta)|\}^n \mathrm{d}p / \int_S \{R \cdot |\sin(\theta)|\}^n \mathrm{d}p$ and $n = \{0, 1, 2\}$ for respectively either a 0th order moment (representing length), 1st order (static) moment or 2nd order moment (of inertia) based path correction factor incorporating the level of non-proportionality for each cycle relative to the straight line defined stress range (Fig. 3.4). Any material characteristic non-proportionality effect is reflected in fitting coefficient c_m [79, 80, 93, 94].
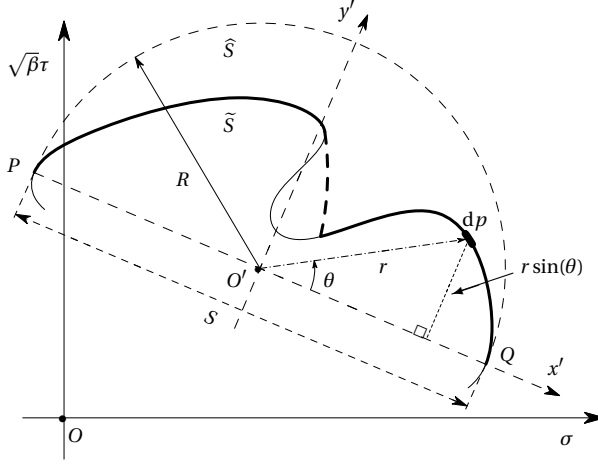
Figure 3.4.: Cycle-by-cycle response path based non-proportionality in the von Mises plane.

Adopting a failure criterion based on the full stress tensor, multiaxial rain flow counting of the invariants $\sqrt{J_2}$ or $\sqrt{\beta \cdot J_2}$ and the projection of the corresponding I_1 at respectively the primary and secondary channel [87] implicitly includes non-proportionality up to some extent.

3.2.5. DAMAGE ACCUMULATION

Fatigue damage is progressive and accumulates cycle-by-cycle, meaning history counts. Both linear and non-linear models have been developed over time [e.g. 95, 96], although typically for uniaxial response conditions. Application extends to multiaxial ones as well, since the failure criteria are typically of the equivalent stress type (Section 3.2.1) and even multiaxial rain flow counting (Section 3.2.3) is limited to the primary channel, meaning a single time series is considered for damage accumulation.

The linear damage model $D = \sum \{n_i(S_i)/N_i(S_i)\} \leq 1$; the sum of the ratios of the number of response cycles at a particular level $n_i(S_i)$ and the corresponding resistance defined number of cycles to failure $N_i(S_i)$ [97, 98], is the universal standard for fatigue design, as reflected in applications for criteria defined at the integral plane [15], the critical plane [76, 78, 79] and the invariant plane [87].

However, numerous test results have shown the deficiency, including possible

non-conservative D estimates [e.g. 96]. Sequence effects turned out to be an important one from response perspective and D for example proved to be different for a single overload in comparison to a single underload and for a low-to-high sequence different from a high-to-low one [e.g. 99]. Even for random response conditions as typically observed for a wave loading induced response of maritime structures, $D \neq 1$ is obtained for different types of spectra [e.g. 100–103]. From resistance perspective, cycles with a stress range below the (random) fatigue limit affect D as well [e.g. 104]. Still adopting the linear model, the maximum allowed damage is typically reduced to a value below one, depending on the variable amplitude response characteristics [e.g. 15].

Most non-linear models [e.g. 95, 96] addressing the response aspects are basically of the type: $D = \sum [C_i \cdot \{n_i(S_i)/N_i(S_i)\}^{f(S_i)}] \leq 1$, considering the linear one as a special case for $C_i = f(S_i) = 1$. Simplifications typically concern a bi-linearisation. Fitting coefficient C_i and fitting function $f(S_i)$ are meant to incorporate any material specific contribution as well. So far, applications for multiaxial fatigue seem limited, although a non-linear model of this type has been adopted for S defined at the critical plane [73, 91].

Anyway, a generalised, all-encompassing model overall outperforming the linear one is not available yet [e.g. 96]. At the same time, the damage accumulation model performance seems related to the adopted fatigue strength criterion. For and advanced S formulation the linear model still proved to be sufficient since variable amplitude fatigue resistance data fits the constant amplitude data scatter band [18, 79, 99].

When both mid- and high- cycle fatigue are involved, a resistance induced damage accumulation non-linearity appears as well, because of the changing slope (i.e. changing mechanism) as reflected in the 2-slope resistance curve formulations [e.g. 14]. For a bi-linear one with a finite high-cycle fatigue slope, still $D = \sum \{n_i(S_i)/N_i(S_i)\} \leq 1$, but the resistance part involves different slope contributions m based on the number of cycles at the mid- to high- cycle fatigue transition N_t: $\log\{N_i(S_i)\} = \log(C) - m \cdot \log(S_i)$ with $m = m_{mid}$ for $N_i \leq N_t$ and $m = m_{high}$ for $N > N_t$ [96, 105]. However, D estimates are quite often observed to be non-conservative [e.g. 106]. In case of an infinite high-cycle fatigue slope, like for the generalised random fatigue limit formulation [14, 99, 107]: $\log N_i(S_i) = \log(C) - m \cdot \log(S_i) - \rho_{S_\infty} \cdot \log\{1 - S_\infty(\mu, \sigma; D)/S_i\}$, the fatigue limit S_∞ decreases for increasing D, meaning the damage accumulation calculation becomes an iterative process: $D = \sum \{n_i(S_i)/N_i(S_i; D)\} \leq 1$.

3.3. Effective notch stress assessment

For mixed mode-{I, III} multiaxial response conditions of planar and tubular maritime structures, the mode-I contribution is governing (Section 3.1), meaning the normal stress σ_I is predominant. At the same time, the fatigue lifetime of arc-welded joints is growth – rather than shear induced initiation – controlled because of the welding induced defects, explaining why an equivalent normal stress based von Mises type of failure criterion will be adopted (Section 3.2.1). Since cracks at weld notches

typically develop first in plate thickness direction, the fracture plane is identified as the critical one and will be selected for criterion evaluation (Section 3.2.2). Cycles will be counted – because of the time domain approach – in the von Mises plane (Section 3.2.3), in order to be able to incorporate non-proportionality cycle-by-cycle (Section 3.2.4). The linear damage accumulation model will be used, since good performance has been shown for advanced fatigue strength criteria. Including a response related non-linearity may correct for fatigue strength parameter deficiencies because of the fitting involved, which should be identified first. Starting with mid-cycle fatigue, the resistance related non-linearity is not required as well (Section 3.2.5).

Opting for an effective notch stress based fatigue strength parameter, a failure criterion $S = S_e = \sqrt{\left\{ S_{e,I}^2 + \beta(N) \cdot S_{e,III}^2 \right\}}$ will be established first (Section 3.3.1) and includes a lifetime dependent shear stress coefficient $\beta(N)$. Using fatigue test data from literature (Section 3.3.2) the strength and mechanism contributions, reflected in respectively mode specific $\{\log(C), \gamma\}$ and $\{m, \rho^*\}$ coefficients, will be investigated (Section 3.3.3).

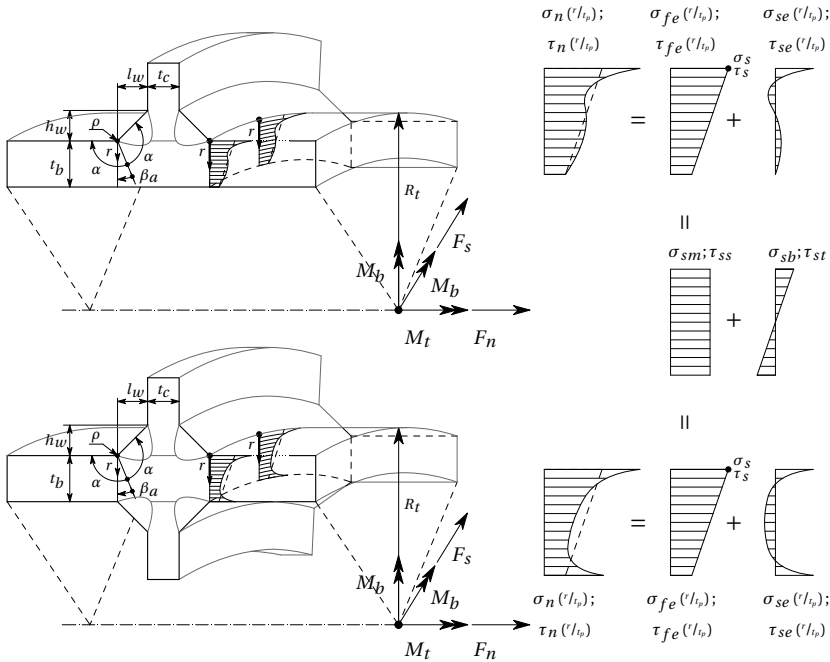### 3.3.1. FATIGUE STRENGTH PARAMETER FORMULATION

Figure 3.5.: Linear superposition of an equilibrium equivalent and self-equilibrium part for the mode-{I, III} weld toe notch shear stress distribution of a DS welded T-joint and DS welded cruciform joint in a tubular structure.

The through-thickness weld notch stress distributions along the expected (2D) crack path – defining the fracture plane – are assumed to be a key element for an appropriate fatigue design and detectable repair criterion [16]. Semi-analytical formulations $\{\sigma_I(r/t_p), \tau_{III}(r/t_p)\}$, with plate thickness t_p either the base plate or cross plate value, t_b or t_c, have been developed for both non-symmetry and symmetry with respect to half the plate thickness ($t_p/2$), using respectively a double side (DS) welded T-joint and DS welded cruciform joint for illustration purposes (Fig. 3.5), in case of both zero and finite notch radius ρ [16, 29]. Adopting a linear superposition principle [18], far field related equilibrium equivalent and self-equilibrium parts $\{\sigma_{fe}, \sigma_{se}; \tau_{fe}, \tau_{se}\}$ have been distinguished (Fig. 3.5), involving three components: the notch stress, the weld-load carrying stress and the far field stress. Typically three zones can be identified in all distributions: the zone 1 peak stress value, the zone 2 notch-affected stress gradient and the zone 3 far-field dominated stress gradient, demonstrating stress field similarity.

Since the (as) weld(ed) notch radius ρ is typically small, a zone 1 peak stress fatigue strength parameter would be too conservative. Adopting a micro- and meso-structural notch support hypothesis, an effective notch stress estimate $\{\sigma_{e,I}, \tau_{e,III}\}$ has been obtained by averaging the notch stress distribution along the expected crack path over a material characteristic micro- and meso-structural length ρ^* – rather than introducing a fictitious notch radius, partially incorporating a zone 2 notch stress gradient – and zone 3 far field stress gradient contribution as well [33, 79, 87, 108–111]. Physically speaking, ρ^* reflects the length in which the majority of the fatigue lifetime has been spent. For mode-I if $\rho = 0$ [16]:

$$\sigma_e = \frac{t_p}{\rho_I^*} \int_0^{\frac{\rho_I^*}{t_p}} \sigma_n\left(\frac{r}{t_p}\right) d\left(\frac{r}{t_p}\right). \tag{3.1}$$

The effective notch stress parameter $S_{e,I} = \Delta\sigma_e$ becomes in case of non-symmetry with respect to ($t_p/2$) [16, 18]:

$$S_{e,I} = \Delta\sigma_s \left(\frac{t_p}{\rho_I^*}\right) \left\{ \frac{1}{\lambda_{\sigma s}} \left(\frac{\rho_I^*}{t_p}\right)^{\lambda_{\sigma s}} \mu_{\sigma s} \lambda_{\sigma s}(\lambda_{\sigma s}+1) \cdot \left[\cos\{(\lambda_{\sigma s}+1)\beta_a\} - \chi_{\sigma s}\cos\{(\lambda_{\sigma s}-1)\beta_a\}\right] + \right.$$
$$\frac{1}{\lambda_{\sigma a}} \left(\frac{\rho_I^*}{t_p}\right)^{\lambda_{\sigma a}} \mu_{\sigma a} \lambda_{\sigma a}(\lambda_{\sigma a}+1) \cdot \left[\sin\{(\lambda_{\sigma a}+1)\beta_a\} - \chi_{\sigma a}\sin\{(\lambda_{\sigma a}-1)\beta_a\}\right] +$$
$$\left. C_{bw}\left\{\left(\frac{\rho_I^*}{t_p}\right)^2 - \left(\frac{\rho_I^*}{t_p}\right)\right\} - r_{\sigma s}\left(\frac{\rho_I^*}{t_p}\right)^2 \right\}. \tag{3.2}$$

In case $\rho > 0$ and non-symmetry with respect to $(t_p/2)$ applies [16, 18]:

$$
\begin{aligned}
S_{e,I} = \Delta\sigma_s \left(\frac{t_p}{r_0 + \rho_I^*}\right) &\left\{ \frac{1}{\lambda_{\sigma s}} \left[\left(\frac{r_0 + \rho_I^*}{t_p}\right)^{\lambda_{\sigma s}} - \left(\frac{r_0}{t_p}\right)^{\lambda_{\sigma s}} \right] \mu_{\sigma s} \lambda_{\sigma s} (\lambda_{\sigma s} + 1) \cdot \right. \\
&\left[\cos\{(\lambda_{\sigma s} + 1)\beta_a\} - \chi_{\sigma s} \cos\{(\lambda_{\sigma s} - 1)\beta_a\} \right] + \\
&\frac{1}{\zeta_{\sigma s}} \left[\left(\frac{r_0 + \rho_I^*}{t_p}\right)^{\zeta_{\sigma s}} - \left(\frac{r_0}{t_p}\right)^{\zeta_{\sigma s}} \right] \left(\frac{r_0}{t_p}\right)^{\lambda_{\sigma s} - \zeta_{\sigma s}} \lambda_{\sigma s} \frac{\left(\frac{2\alpha}{\pi}\right)}{4\left\{\left(\frac{2\alpha}{\pi}\right) - 1\right\}} \cdot \\
&\left[\omega_{\sigma s1} \cos\{(\zeta_{\sigma s} + 1)\beta_a\} + \omega_{\sigma s2}(\zeta_{\sigma s} + 1)\cos\{(\zeta_{\sigma s} - 1)\beta_a\} \right] + \\
&\frac{1}{\lambda_{\sigma a}} \left[\left(\frac{r_0 + \rho_I^*}{t_p}\right)^{\lambda_{\sigma a}} - \left(\frac{r_0}{t_p}\right)^{\lambda_{\sigma a}} \right] \mu_{\sigma a} \lambda_{\sigma a}(\lambda_{\sigma a} + 1)[\sin\{(\lambda_{\sigma a} + 1)\beta_a\} - \\
&\chi_{\sigma a} \sin\{(\lambda_{\sigma a} - 1)\beta_a\}] + \\
&\frac{1}{\zeta_{\sigma a}} \left[\left(\frac{r_0 + \rho_I^*}{t_p}\right)^{\zeta_{\sigma a}} - \left(\frac{r_0}{t_p}\right)^{\zeta_{\sigma a}} \right] \left(\frac{r_0}{t_p}\right)^{\lambda_{\sigma a} - \zeta_{\sigma a}} \frac{\lambda_{\sigma a}}{4(\zeta_{\sigma a} - 1)} \cdot \\
&\left[\omega_{\sigma a1} \sin\{(\zeta_{\sigma a} + 1)\beta_a\} + \omega_{\sigma a2}(\zeta_{\sigma a} + 1)\sin\{(\zeta_{\sigma a} - 1)\beta_a\} \right] + \\
&\left. C_{bw}\left\{ \left(\frac{r_0 + \rho_I^*}{t_p}\right)^2 - \left(\frac{r_0}{t_p}\right)^2 - \left(\frac{2r_0 + \rho_I^*}{t_p}\right) \right\} - r_{\sigma_s}\left[\left(\frac{r_0 + \rho_I^*}{t_p}\right)^2 - \left(\frac{r_0}{t_p}\right)^2 \right] \right\}.
\end{aligned}
$$
(3.3)

For mode-III if $\rho = 0$ [29]:

$$
\tau_e = \frac{t_p}{\rho_{III}^*} \int_0^{\frac{\rho_{III}^*}{t_p}} \tau_{s,III}\left(\frac{r}{t_p}\right) \mathrm{d}\left(\frac{r}{t_p}\right).
$$
(3.4)

The effective notch stress parameter $S_{e,III} = \Delta\tau_e$ becomes in case of non-symmetry with respect to $(t_p/2)$:

$$
\begin{aligned}
S_{e,III} = \frac{\Delta\tau_s}{\lambda_\tau} \frac{t_p}{\rho_{III}^*} &\left\{ \cos(\lambda_\tau \beta_a) \mu_{\tau F}\left(\frac{\rho_{III}^*}{t_p}\right)^{\lambda_\tau} - \lambda_\tau\left(\frac{\rho_{III}^*}{t_p}\right) \cdot \right. \\
&\left. \left[\left(\frac{\rho_{III}^*}{t_p}\right)(\mu_{\tau M} + r_{\tau_s} + C_{tw}) - \mu_{\tau M} - C_{tw} \right] \right\}.
\end{aligned}
$$
(3.5)

In case $\rho > 0$ and non-symmetry with respect to $(t_p/2)$ applies [29]:

$$S_{e,III} = \frac{\Delta\tau_s}{\lambda_\tau}\left(\frac{t_p}{r_0 + \rho_{III}^*}\right)\left\{\cos(\lambda_\tau\beta_a)\mu_{\tau F}\left[\left(\frac{r_0 + \rho_{III}^*}{t_p}\right)^{\lambda_\tau} - \left(\frac{r_0}{t_p}\right)^{\lambda_\tau}\right] - \right.$$
$$\left(\frac{r_0}{t_p}\right)^{2\lambda_\tau}\cos(\lambda_\tau\beta_a)\mu_{\tau F}\left[\left(\frac{r_0 + \rho_{III}^*}{t_p}\right)^{-\lambda_\tau} - \left(\frac{r_0}{t_p}\right)^{-\lambda_\tau}\right] - \quad\quad (3.6)$$
$$\left.\lambda_\tau\frac{\rho_{III}^*}{t_p}\left[\left(\frac{2r_0 + \rho_{III}^*}{t_p}\right)(\mu_{\tau M} + r_{\tau_s} + C_{tw}) - \mu_{\tau M} - C_{tw}\right]\right\}.$$

Mode-{I, III} formulations for symmetry with respect to $(t_p/2)$ have been developed as well, both for $\rho = 0$ and $\rho > 0$ (C). The far field stress parameters $\{\Delta\sigma_s, r_{\sigma_s}; \Delta\tau_s, r_{\tau_s}\}$ can be obtained using nodal force output of relatively coarse meshed shell/plate FE models [41, 112, 113], naturally providing the constant membrane and linear bending contribution: $\sigma_s = \sigma_{sm} + \sigma_{sb}$, as well as the constant shear and linear torsion contribution: $\tau_s = \tau_{ss} + \tau_{st}$. The structural normal and shear stress ratios: $\{r_{\sigma_s} = \sigma_{sb}/\sigma_s, r_{\tau_s} = \tau_{st}/\tau_s\}$ reflect the far field stress gradients [16, 29]. Eigenvalues $\{\lambda_{\sigma s}, \lambda_{\sigma a}, \lambda_\tau\}$, eigenvalue coefficients $\{\chi_{\sigma s}, \chi_{\sigma a}\}$ and stress angle β_a can be obtained using the notch angle α. Coefficients $\{\mu_{\sigma s}, \mu_{\sigma a}, \mu_{\tau F}, \mu_{\tau M}\}$ are obtained using force and moment equilibrium. The mode-I bending and mode-III torsion related weld load carrying stress coefficients, respectively C_{bw} and C_{tw}, are loading and geometry dependent. Fitting functions have been established [16, 29]. A complete spatial description of a response cycle requires 2 parameters to be involved, important for modelling of sequence effects. The ranges $\{S_{e,I}, S_{e,III}\}$ and ratios $\{R_I = S_{e,I,min}/S_{e,I,max}, R_{III} = S_{e,III,min}/S_{e,III,max}\}$ are selected for this purpose. Adopting Walker's mean stress model, typically providing the best results for welded joints [14, 29], the effective notch stress parameter becomes:

$$S_{e,eff} = \frac{S_e}{(1-R)^{1-\gamma}} \quad\quad (3.7)$$

with $\{S_{e,eff} = S_{e,eff,I}, S_e = S_{e,I}, R = R_I, \gamma = \gamma_I\}$ for the mode-I and $\{S_{e,eff} = S_{e,eff,III}, S_e = S_{e,III}, R = R_{III}, \gamma = \gamma_{III}\}$ for the mode-III effective notch stress component. The response ratio coefficient γ is a fitting parameter. For $\gamma \to 1$, the range dominates the fatigue resistance; the mean stress becomes governing for $\gamma \to 0$. However, an environment and service loading induced mean stress component is not the only one. Arc-welding adds a thermal loading induced – typically high-tensile – quasi-constant residual (mean) stress, affecting the fatigue strength. An explicit residual stress measure is typically not included, since for fatigue design in general only joints in as-welded condition are considered [e.g. 33, 34, 114], meaning any residual stress affecting the fatigue resistance is just implicitly incorporated in the most likely fatigue resistance parameter estimates. A stress relieving heat treatment can be applied, being one way to virtually eliminate residual stress and improve the fatigue strength. If both as-welded and stress-relieved test data are jointly considered, an explicit residual stress measure S_r has to be introduced to cover the

thermal condition, meaning a re-formulation of the response ratio is required:

$$R_r = \frac{S_{e,min} + S_r}{S_{e,max} + S_r} = \frac{R \cdot S_e + S_r(1 - R)}{S_e + S_r(1 - R)}. \tag{3.8}$$

From fatigue design perspective, the as-welded condition is still adopted to define the reference resistance, meaning the stress-relieved data – principally without any residual stress – is expected to provide a compressive S_r estimate. Note that the extended R formulation most likely affect the mean stress sensitivity coefficient γ as well.

Because of the arc-welding induced heat input, the material crystallography changes, introducing a heat affected zone in between the weld and base material at the fatigue sensitive weld toe notch location. The hardness in the heat affected zone is typically large in comparison to the base material value. Since the weld material hardness is in general in between the heat affected zone and base material value, an M-shaped hardness characteristic appears [115]. Applying a post-welding heat treatment is principally meant to reduce the hardness – in particular in the heat affected zone – and the aim is to obtain a more uniform hardness distribution across the material up to a certain extent, depending on parameters like heat rate, maximum temperature and treatment duration [115–117]. In general, an increased hardness reflects a smaller grain size and the other way around, introducing fatigue resistance consequences; i.e. changing crack initiation and growth behaviour. Since for a smaller grain size the initiation resistance seems to increase and at the same time the growth resistance decreases – for a larger grain size the opposite applies [118], dedicated material characteristic ρ^* parameters seem required for the as-welded and the stress-relieved condition.

Because of the mode-I and mode-III finite lifetime specific strength and mechanism fatigue resistance characteristics, a response level dependent shear strength coefficient $\beta(N)$ is adopted, rather than a constant one (Section 3.2.1). For a single-slope resistance relation $N = C \cdot S_e^m$:

$$\beta(N) = \frac{S_{e,I}(N)}{S_{e,III}(N)} = C_\beta \cdot N^{M_\beta} \tag{3.9}$$

with

$$C_\beta = 10^{\frac{\log(C_I)m_{III} - \log(C_{III})m_I}{m_I \cdot m_{III}}} \tag{3.10}$$

and

$$M_\beta = \frac{m_I - m_{III}}{m_I \cdot m_{III}}. \tag{3.11}$$

Since only the uniaxial mode-{I, III} number of cycles {N_I, N_{III}} are known in advance, the actual $\beta(N)$ value has to be obtained in an iterative cycle counting process in order to capture N for the equivalent normal stress based von Mises type of criterion:

$$S_{e,eff} = \sqrt{\left\{ S_{e,eff,I}^2 + \beta(N) \cdot S_{e,eff,III}^2 \right\}}. \tag{3.12}$$

Counting iteratively the effective von Mises notch stress (Fig. 3.6) at the critical fracture plane (Section 3.2.2), the range $S_{e,i}$ including the normal and equivalent shear stress projections $\{S_{e,I,i}, \beta(N) \cdot S_{e,III,i}\}$ and corresponding ratios $\{R_I = S_{e,I,min,i}/S_{e,I,max,i}, R_{III} = \beta(N) \cdot S_{e,III,min,i}/[\beta(N) \cdot S_{e,III,max,i}]\}$ can be obtained for each cycle i (Section 3.2.3). Adopting a 0th, 1st or 2nd order moment approach (Section 3.2.4), differences between the actual response path and the (straight) range have been used to incorporate a non-proportionality effect cycle-by-cycle in terms of C_{np}, including a material characteristic contribution in terms of c_m [79, 80, 93, 94]:

$$S_{e,eff,i} = S_{e,i} \left(1 + c_m \cdot C_{np,i}\right) \tag{3.13}$$

with

$$C_{np,i,n} = \frac{\int_{\tilde{S}} (r \cdot |\sin(\theta)|)^n \mathrm{d}p}{\int_S (R \cdot |\sin(\theta)|)^n \mathrm{d}p} \quad \text{for } n = 0, 1, 2. \tag{3.14}$$

Although $C_{np,i}$ and c_m are meant to reflect respectively the path and material characteristic part, c_m may correct for any cycle counting and/or non-proportionality related model deficiency as well, since data fitting is used to obtain an estimate. A compromised value may be acquired, meaning interpretation becomes more difficult. In order to obtain a mid-cycle fatigue related equivalent effective notch
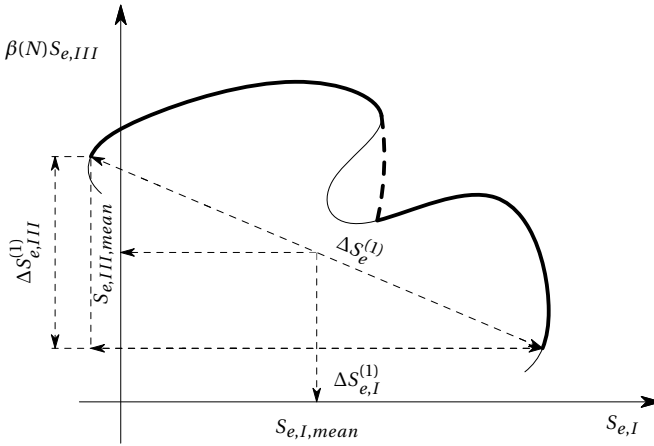
Figure 3.6.: Effective notch stress cycle characteristics in the von Mises plane.

stress parameter $S_{e,eq}$ for variable amplitude data fitting the constant amplitude data scatter band; i.e. $N(S_e) = C \cdot S_e^{-m}$ with $S_e = S_{e,eq}$, the linear damage model is adopted: $D = \sum \{n_i(S_{e,i})/N_i(S_{e,i})\} \leq 1$ with $N_i(S_{e,i}) = C \cdot S_{e,i}^{-m}$. For $D = 1$, reflecting failure, the formulation becomes:

$$S_{e,eq} = \left[\frac{\sum \{n_i(S_{e,i}) \cdot S_{e,i}^m\}}{N} \right]^{1/m}. \tag{3.15}$$

Recall $N = \sum \{n_i(S_{e,i})\}$, the iteratively obtained total number of effective von Mises

notch stress cycles.

3.3.2. TEST DATA

Data series containing steel specimens with both tubular and planar structural joints have been considered (Fig. 3.7 and Tables 3.1 and 3.2), involving respectively circular/square hollow and plate cross-sections with specified joint dimensions (Fig. 3.5). Most data is obtained for constant amplitude loading conditions, but some variable amplitude data is included as well. Uniaxial mode-I, uniaxial mode-III and multiaxial mode-{I, III} response conditions – both proportional and non-proportional – have been introduced at the governing fatigue sensitive locations: SS welded butt joints and DS welded T-joints, as well as DS welded cruciform joints showing respectively non-symmetry and symmetry with respect to ($t_p/2$) [16, 18, 29]. The governing hot spot is typically of the type C along the weld seam, although some of the type A at the weld end exist as well. Only specimens showing weld toe induced fatigue damage are included, involving predominantly failures and some run-outs. The data size is ~ 500.
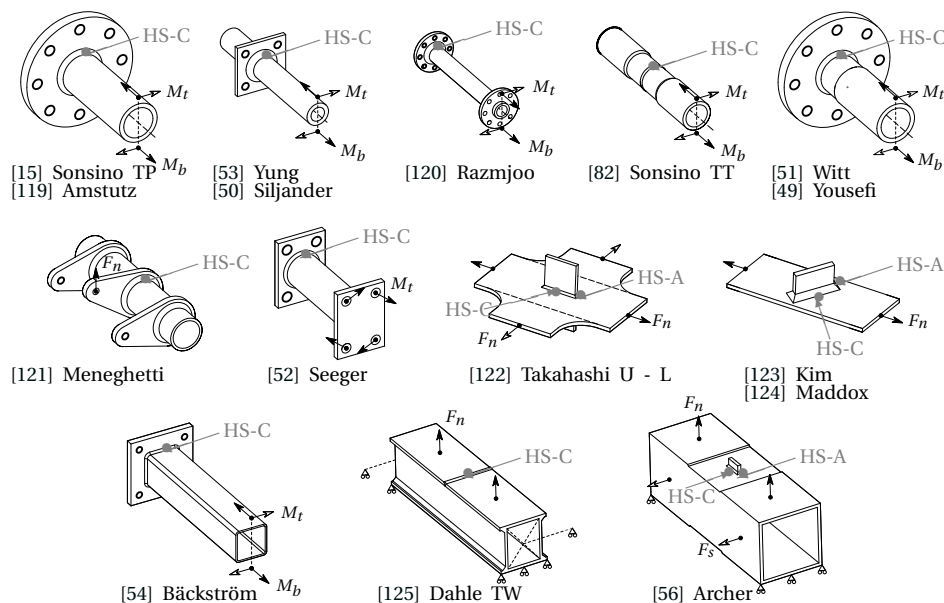
Figure 3.7.: Fatigue test specimen geometry, external loading (arrows) and constraints (thick lines or ⚓ symbols).

3

Table 3.1.: Specimen characteristics of the fatigue resistance data from literature.

source	t_b [mm]	t_c [mm]	l_w [mm]	h_w [mm]	joint dimension [mm]	ρ [mm]	weld geometry	hot spot type	thermal condition
[15] Sonsino TP	10.0	25.0	9.0	9.0	⌀44.4 * 10.0	0.45	SS T-joint	C	SR
[49] Yousefi	8.0	25.0	10.0	10.0	⌀42.4 * 8.0	n.a.	SS T-joint	C	SR
[50] Siljander	9.5	9.5	8.0	8.0	⌀25.4 * 9.5	0.18	SS T-joint	C	SR
[51] Witt	8.0	16.0	9.0	9.0	⌀44.4 * 8.0	n.a.	SS T-joint	C	SR
[52] Seeger	8.0	20.0	6.3	6.3	⌀54.0 * 8.0	1.00	SS T-joint	C	SR
[82] Sonsino TT	6.0	/	10.0	1.0	⌀44.4 * 6.0	0.45	SS butt joint	C	SR
[119] Amstutz	7.7	25.0	9.0	9.0	⌀42.1 * 7.7	1.00	SS T-joint	C	SR
[120] Razmjoo	3.2	12.0	11.0	11.0	⌀24.3 * 3.2	0.18	SS T-joint	C	AW
[53] Yung	8.0	8.0	7.7	7.7	⌀23.8 * 8.0	n.a.	SS T-joint	C	{SR, AW}
[121] Meneghetti	8.0	20.0	12.0	12.0	⌀50.8 * 8.0	2.00	SS T-joint	C	{SR, AW}
[54] Bäckström	5.0	20.0	6.0	6.0	□100 * 100 * 5.0	1.00	SS T-joint	C	AW
[56] Archer	6.0	10.0	9.0	9.0	□200 * 200 * 6.0	n.a.	SS T-joint	{A, C}	AW
[125] Dahle TW	10.0	/	12.0	2.0	□150 * 150 * 10.0	n.a.	SS butt joint	C	AW
[122] Takahashi	12.0	12.0	6.0	6.0	▪1000 * 1000 * 12.0	n.a.	DS Cruciform joint	{A, C}	AW
[124] Maddox	12.5	12.5	9.0	9.0	▮700 * 160 * 12.5	n.a.	SS T-joint	{A, C}	AW
[123] Kim	9.0	9.0	9.0	9.0	▬1000 * 200 * 9.0	n.a.	SS T-joint	{A, C}	AW

3

Table 3.2.: Loading characteristics of the fatigue resistance data from literature.

source	uniaxial mode-I		uniaxial mode-III		multiaxial mode-{I, III}				no. specimens		
	R_I	loading	R_{III}	loading	R_I	R_{III}	loading	type	I	III	{I, III}
[15] Sonsino TP	−1	M_b	−1	M_t	−1	−1	M_b+M_t	{CA, VA}	21;	9;	29
[49] Yousefi	[0;−1]	M_b	−1	M_t	[0;−1]	[0;−1]	M_b+M_t	{CA, VA}	38;	14;	82
[50] Siljander	[0;−1]	M_b	[0;−1]	M_t	[0;−1]	[0;−1]	M_b+M_t	CA	10;	8;	20
[51] Witt	−1	M_b	−1	M_t	[0;−1]	[0;−1]	M_b+M_t	CA	11;	11;	19
[52] Seeger	/	/	−1	M_t	/	/	/	CA	0;	6;	0
[82] Sonsino TT	−1	M_b	/	/	−1	−1	M_b+M_t	CA	14;	0;	24
[119] Amstutz	[0;−1]	M_b	−1	M_t	[0;−1]	[0;−1]	M_b+M_t	CA	12;	7;	19
[120] Razmjoo	0	F_n	−1	M_t	0	0	F_n+M_t	CA	7;	8;	13
[53] Yung	−1	M_b	−1	M_t	−1	−1	M_b+M_t	CA	5;	2;	7
[121] Meneghetti	/	/	/	/	0.1	0.1	F_n	CA	0;	0;	14
[54] Bäckström	[0.1 ... 0.7]	M_b	−1	M_t	[0.4 ... 1.1]	[−1.3 ... 0]	M_b+M_t	CA	5;	4;	13
[56] Archer	0	M_b	−1	F_s	0	−1	M_b+F_s	CA	1;	12;	18
[125] Dahle TW	−1	M_b	/	/	−1	−1	M_b	CA	3;	0;	5
[122] Takahashi	0	F_n	/	/	0	0	F_n+F_n	CA	6;	0;	11
[124] Maddox	0	F_n	/	/	0	0	F_n	CA	6;	0;	12
[123] Kim	0	F_n	/	/	0	0	F_n	CA	13;	0;	27

The external loading consists of a normal force F_n or bending moment M_b for the mode-I response and a shear force F_s or torsion moment M_t for the mode-III response. Multiaxiality is often either loading [15, 49–51, 53, 54, 56, 82, 119, 120, 122] or geometry [121, 123–125] induced. In case a mode-I and mode-III response related external loading component (e.g. M_b and M_t) are applied and at the same time the specimen contains a non-circular cross-section and warping constraints, multiaxiality includes even both a loading and geometry contribution [54, 56]. The response is proportional by definition if multiaxiality is a result of geometry only. The response ratio $R = 0$ for the majority of the data series, reflecting a pulsating loading induced response condition with non-zero mean. For a significant amount of data $R = -1$, meaning the response condition is fully reversed and the mean component is zero. For the remaining data series, $R \neq \{0; -1\}$. Since data with both as-welded and stress-relieved thermal conditions are considered, the influence of (mean) residual stress has to be addressed as well. A von Mises based structural
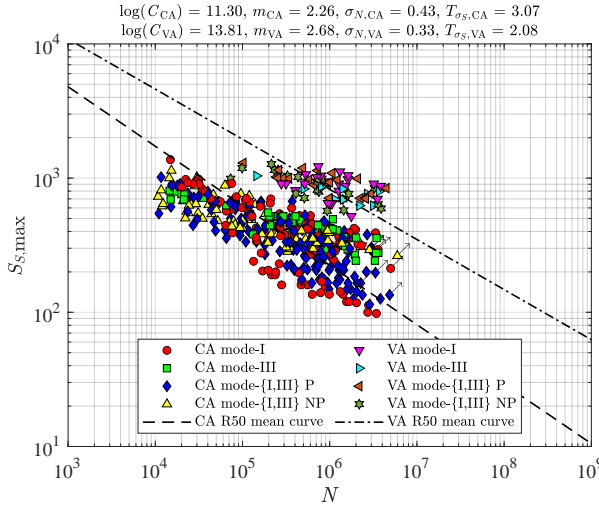
Figure 3.8.: Structural stress based fatigue resistance.

stress fatigue assessment (Fig. 3.8) of the involved fatigue test data (Fig. 3.7 and Tables 3.1 and 3.2) shows the initial data scatter and the clear distinction between constant amplitude and (maximum range) variable amplitude results. Since no cycle counting is involved for the multiaxial data, N corresponds to the mode-I lifetime.

3.3.3. Strength and mechanism contributions

The life time range of the considered data (Fig. 3.7 and Tables 3.1 and 3.2) virtually reflects mid-cycle fatigue characteristics only: $N = (10^4 \sim 5 \cdot 10^6)$ cycles. A log-log linear formulation of the Basquin type typically relates N to a fatigue strength parameter S [14]: $\log(N) = \log(C) - m \cdot \log(S)$. Linear regression on life time is adopted to estimate the single-slope curve parameters: intercept $\log(C)$ and slope m,

respectively the endurance and damage mechanism coefficient, introducing the life time scatter (i.e. performance) parameter σ_N. For strength performance evaluation purposes, the strength scatter band index $T_{\sigma S} = 1 : (S_{10}/S_{90})$ will be used, the fatigue strength ratio for 10 [%] and 90 [%] probability of survival [111]. Maximum likelihood based regression [18, 57] will be employed to obtain the most likely parameter vector estimate $\Phi : \max_{\Phi}\{\mathscr{L}(\Phi; N|S)\}$ with $\Phi = \{\log(C), m, \sigma_N\}$, assuming fatigue lifetime N is most likely log(Normal) distributed [16, 29]. For $S = S_{e,eff}$ (Section 3.3.1), the response ratio coefficient and material characteristic length as respectively a strength and mechanism coefficient are introduced, principally extending the parameter vector to: $\Phi = \{\log(C), \gamma, m, \rho^*, \sigma_N\}$. Note that ideally the uniaxial mode-I and mode-III, as well as the multiaxial proportional and non-proportional mode-{I, III} data (Fig. 3.7 and Tables 3.1 and 3.2) would have been balanced for appropriate S_e performance evaluation, meaning that except the σ_N and $T_{\sigma S}$ parameters as global indicators for all data, the individual data groups behaviour have to be carefully considered as well.

Starting with the uniaxial reference fatigue resistance in terms of S_e, the mode specific strength and mechanism coefficients will be established first (Section 3.3.3) in order to obtain $\beta(N)$. The S_e performance for multiaxial fatigue resistance data will be investigated accordingly (Section 3.3.3). Particular attention will be paid to the consequences of mode specific strength and mechanism for mixed mode-{I, III} fatigue and the influence of non-proportionality. Since S_e is an equivalent normal stress von Mises type of parameter, the fitting of the multiaxial data in the mode-I uniaxial data scatter band will be verified, as well as the fitting of VA data in the CA data scatter band in order to establish the performance of the adopted linear damage accumulation model for $S_{e,eff}$ based fatigue assessment.

UNIAXIAL REFERENCE FATIGUE RESISTANCE

The S_e based mode-I mid-cycle fatigue resistance formulation for planar structures in steel (maritime) structures, involving hot spot types {A, B, C} and various as-welded joint geometries, has already been established for CA data [126] and shows an excellent performance as reflected in the lifetime standard deviation: $\sigma_N = 0.21$. The intercept and slope values are: $\log(C_I) \sim 13.28$ and slope $m_I \sim 3.12$. Note that the slope is close to the typical design value $m = 3$ [33, 34]. Assuming $\rho = 0$, a most likely $\rho_I^* \sim 1.34$ has been obtained, suggesting the major part of the fatigue lifetime is spent in the notch affected region indeed. The response ratio coefficient $\gamma_{I,AW} \sim 0.90$ implies a predominant contribution of stress range over mean stress as a consequence of the typically high-tensile welding induced residual stress. Since the data size of the considered (predominant) tubular and (some) planar mode-I data (Tables 3.1 and 3.2) is ~ 140, relatively small in comparison to the ~ 2500 assessed before [126], enforcing $\log(C_I) \sim 13.28$, $m_I \sim 3.12$, $\rho_I^* \sim 1.34$ and $\gamma_{I,AW} \sim 0.90$ seems straightforward from parameter confidence perspective. For the stress-relieved joints, $\gamma_{I,AW} \sim 0.90$ is initially still adopted in case $R \geq 0$, although expected to be too large because of eliminated residual stress. Assuming only the tensile part of the cycle contributes to fatigue damage accumulation, $\gamma_{I,SR} = 0$ has been used for $R < 0$, based on a crack opening mode-I requirement [14].
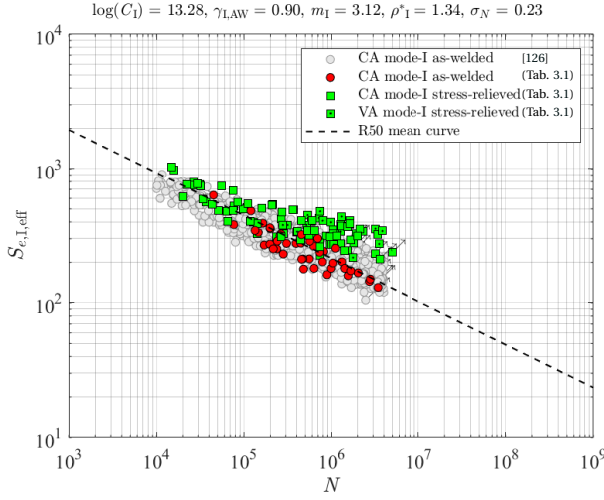
Figure 3.9.: Mode-I data effective notch stress based fatigue resistance, including mean stress correction.

Figure 3.10.: Mode-I data effective notch stress based fatigue resistance, including mean and residual stress correction.

The parameter vector becomes: $\Phi = \{\sigma_N\}$. Regression analysis of all data shows that the strength and mechanism parameters, intercept $\log(C)$ and slope m, hardly changed in comparison to the reference data values [126], since the amount of added data (Fig. 3.7 and Tables 3.1 and 3.2) is relatively small. The as-welded data

fits the reference data scatter band reasonably well (Fig. 3.9). However, the fatigue strength and mechanism of stress-relieved data seems different, as reflected in the scatter and non-fitting behaviour, explaining the increased σ_N. Introducing for the stress-relieved data a residual stress S_r and response ratio coefficient $\gamma_{I,SR}$, covering the full R range like for as-welded data (Section 3.3.1), extends the parameter vector to: $\Phi = \{\log(C_I), S_r, \gamma_{I,SR}, m_I, \sigma_N\}$. The SR data fit in the reference AW data scatter band improved indeed with respect to strength and mechanism: $\log(C)$ and m (Fig. 3.10). The most likely residual stress S_r proved to be compressive (Section 3.3.1), confirming the (average) residual stress for the AW data is highly tensile indeed. Mean residual stress coefficient $\gamma_{I,SR} \sim 0.6$ reflects an almost balanced contribution from stress range and mean residual stress, like for $\gamma = 0.5$ [14]. Since $\gamma_{I,SR} \neq 0$ in case $R < 0$ for the SR joints and $\gamma_{I,SR}$ applies for the full R range, suggests some residual stress is still present. However, the residual stress consists of an equilibrium equivalent and self-equilibrium part as well [18]. A stress-relieving heat treatment could very well eliminate the equilibrium equivalent part, but the self-equilibrium part – highly tensile in the notch affected region, – may still exist. The lifetime standard deviation σ_N has reduced, but is still larger than the original reference data value as the data scatter indicates, suggesting another modelling step is required. Because of the differences in material crystallography for AW and SR data (Section 3.3.1), a dedicated material characteristic strength parameter can be introduced, meaning: $\Phi = \{\log(C_I), S_r, \gamma_{I,SR}, m_I, \rho^*_{I,SR}, \sigma_N\}$. The $\rho^*_{I,SR} \sim 3.86$ estimate
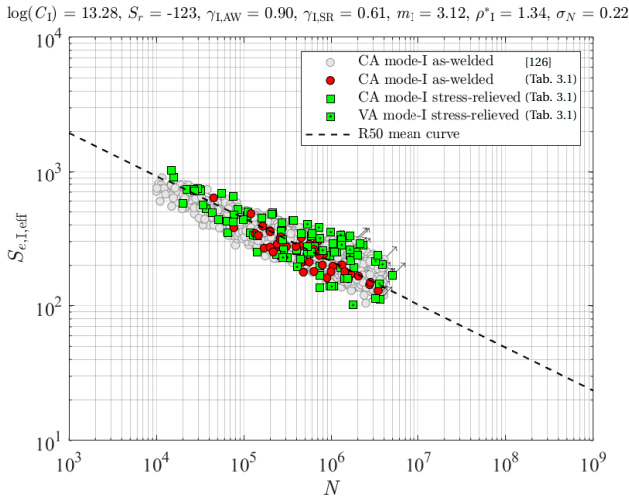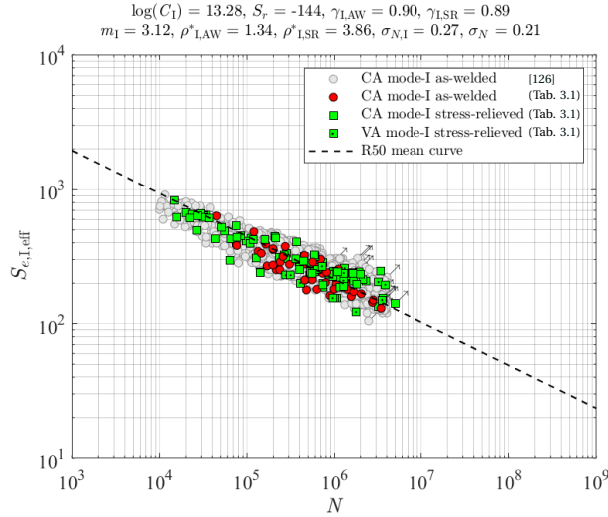

Figure 3.11.: Mode-I data effective notch stress based fatigue resistance, including mean and residual stress correction with dedicated $\rho^*_{I,AW}$ and $\rho^*_{I,SR}$.

turns out to be larger than the AW value: $\rho^*_{I,AW} \sim 1.34$ (Fig. 3.11). Since a stress relieving heat treatment in general decreases the hardness, the initiation resistance decreases and the growth resistance increases (Section 3.3.1), suggesting a decreased

fatigue resistance. However, the positive effect of eliminated residual mean stress consequences exceeds the negative influences of the ρ^* decrease, still providing an increased fatigue resistance when a stress relieving heat treatment is applied. The most likely residual stress estimate S_r changed somewhat, but surprisingly the residual mean stress coefficient $\gamma_{I,SR}$ has become about equal to the AW value $\gamma_{I,AW}$, meaning the stress range contribution dominates anyway. Yet, the most important result seems the reduced lifetime data scatter σ_N, principally the same value as obtained for just the reference data. At the same time, $\sigma_N \sim 0.27$ for the considered data (Fig. 3.7 and Tables 3.1 and 3.2) only; at least a matter of data size as reflected in the parameter confidence (Table 3.3). The corresponding strength scatter band index $T_{\sigma S_e} = 1:1.67$ and turns out to be larger than a typical value of $1:1.50$ [20]. At first glance, the VA data fits the CA data scatter band for $D = 1$, supporting the hypothesis that advanced fatigue damage criteria – including the mean stress as an important sequence parameter in terms of R and γ – contributes to the (linear) damage accumulation model performance (Section 3.2.5).

Table 3.3.: Effective notch stress based parameter estimates and 75[%] lower and upper confidence bounds for mode-I and mode-III.

parameter	mode-I		mode-III	
$\log(C)$	13.28	[13.20, 13.36]	18.91	[18.17, 19.64]
m	3.12	[3.08, 3.15]	5.12	[4.85, 5.37]
ρ^*	/	/	0.12	[0.07, 0.21]
ρ^*_{AW}	1.34	[1.22, 1.45]	/	/
ρ^*_{SR}	3.85	[3.56 4.16]	/	/
γ	/	/	1.00	[0.98, 1.00]
γ_{AW}	0.90	[0.88, 0.91]	/	/
γ_{SR}	0.89	[0.87, 0.91]	/	/
S_r	-144	[-144, -143]	/	/
σ_N	0.27	[0.25, 0.29]	0.21	[0.18, 0.24]
σ_N incl.[126]	0.21	[0.19, 0.23]	/	/

The S_e based mode-III mid-cycle fatigue resistance parameter estimates and confidence (Fig. 3.12 and Table 3.3) for tubular structures in steel (maritime) structures, principally involving hot spots type C and a DS welded T-joint geometry only (Fig. 3.7 and Tables 3.1 and 3.2), have already been established for CA data [29]. The data size is ~ 50. Excellent performance has been obtained, as reflected in the lifetime standard deviation: $\sigma_{N,III} \sim 0.21$; basically the same value as obtained for the mode-I reference data, but way smaller than the value for the considered data: $\sigma_{N,I} \sim 0.27$. The difference in lifetime scatter between mode-I and mode-III could partially be related to the type of loading and the geometry, reflecting a volume (i.e. weld seam length) effect. For the mode-I data on the one hand, most specimens are subjected to a bending moment M_b and have a tubular, circular hollow cross-section (Fig. 3.7). The governing hot spot and most likely fatigue failure position is observed at one location along the weld seam, principally independent of the fabrication aspects induced weakest link; a matter of production tolerances and welding induced defects. On the other hand, for the mode-III data a torsion moment M_t is typically

applied and for tubular, circular hollow cross-sections all locations along the weld seam are identified as hot spot. Fatigue failure develops at the position of the fabrication defined weakest link, like the location of the welding induced extreme defect. The mode-III fatigue strength scatter band index $T_{\sigma S_e} = 1 : 1.27$ is smaller than a typical value of $1 : 1.50$ [20]. Intercept $\log(C_{III}) \sim 18.91$ and slope $m_{III} \sim 5.12$ have been obtained as most likely values. Note that the slope is close to the typical design value $m = 5$ [33, 34]. The real weld notch radius has been required to be included in order to obtain $\rho_{III}^* \sim 0.12$. Since $m_{III} > m_I$ and $\rho_{III}^* < \rho_I^*$, the mode-III damage process seems in comparison to mode-I even more an initiation related near-(notch) surface phenomenon [29]. The response ratio coefficient $\gamma_{III} \sim 1$, meaning (residual) stress hardly affects the mode-III fatigue resistance and distinguishing different thermal conditions seems not relevant (Fig. 3.12). Like for the uniaxial mode-I assessment, the linear damage accumulation up to $D = 1$ shows VA data fitting the CA data scatter band.
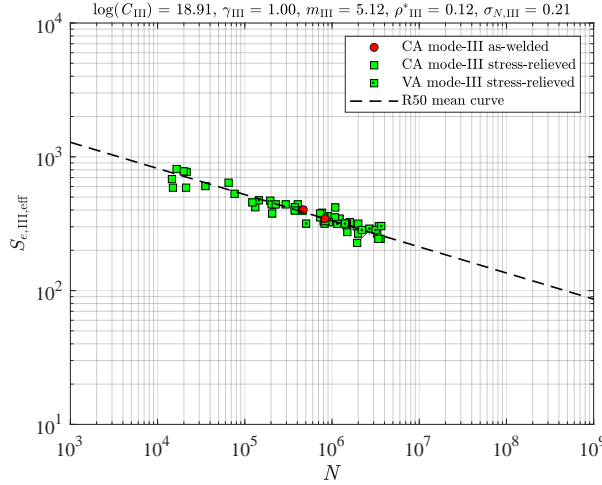
Figure 3.12.: Mode-III data effective notch stress based fatigue resistance, including mean stress correction.

A comparison of mode-I and -III data and mean (i.e. 50 [%] reliability) $S_e - N$ curves clearly shows differences in both strength and mechanism (Fig. 3.13), i.e. in $\{\log(C), \gamma\}$ and $\{m, \rho^*\}$, implying a lifetime dependent shear strength coefficient $\beta(N)$ rather than a constant one is required for multiaxial fatigue assessment (Section 3.3.1).

MULTIAXIAL FATIGUE RESISTANCE

Involving the multiaxial fatigue data (Fig. 3.7 and Tables 3.1 and 3.2), the normal stress equivalent von Mises type of failure criterion is adopted (Eq. 3.12):
$S_e = \sqrt{\left[S_{e,I,eff}(\gamma_I, \rho_I^*)^2 + \beta(N) \cdot S_{e,III,eff}(\gamma_{III}, \rho_{III}^*)^2\right]}$. Note that for the single side (SS)

$\log(C_I) = 13.26$, $S_r = -144$, $\gamma_{I,AW} = 0.90$, $\gamma_{I,SR} = 0.89$, $m_I = 3.12$, $\rho^*_{I,AW} = 1.34$, $\rho^*_{I,SR} = 3.85$
$\sigma_{N,I} = 0.27$, $\log(C_{III}) = 18.91$, $\gamma_{III} = 1.00$, $m_{III} = 5.12$, $\rho^*_{III} = 0.12$, $\sigma_{N,III} = 0.21$

Figure 3.13.: Uniaxial mode-I and mode-III data effective notch stress based fatigue resistance.

welded butt joints the $S_{e,III}$ related C_{tw} estimate (Eq. 3.6) is obtained using the formulation as principally established for DS welded T-joints, assuming $t_c = 0$ [29]. For constant amplitude mixed mode-{I, III} data involving asynchronous behaviour and/or different frequencies, as well as for VA multiaxial data, cycle counting in the von Mises plane is initially adopted without any material characteristic non-proportionality effects: $c_m = C_{np} = 0$ (Eq. 3.13).   In order to illustrate the importance of strength and mechanism contributions, reflected in the $\beta(N)$ related $\{\log(C), m\}$ and the S_e based mode-I and material crystallography dependent $\{\gamma, \rho^*\}$ parameters, regression analysis results for $\beta = \sqrt{3}$ as well as for $\gamma_I = \gamma_{III}$ and $\rho^*_I = \rho^*_{III}$ are provided for reference purposes (Figs. 3.14 and 3.15).   The parameter vectors have been $\Phi = \{\log(C), S_r, \gamma_{I,AW}, \gamma_{I,SR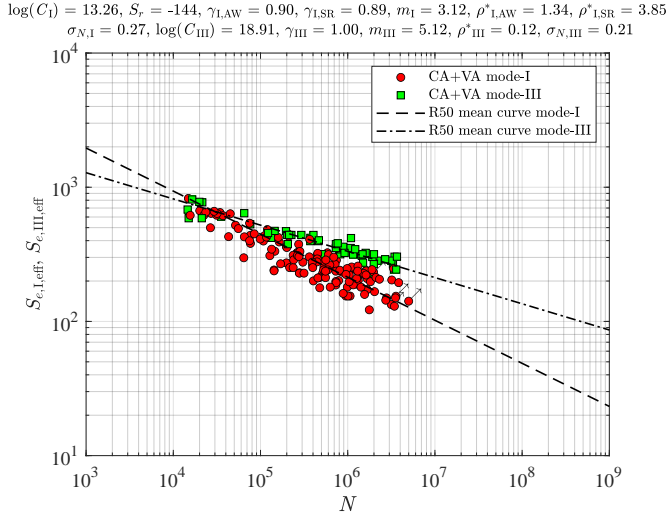}, \gamma_{III}, m, \rho^*_{I,AW}, \rho^*_{I,SR}, \rho^*_{III}, \sigma_N\}$ and $\Phi = \{\log(C), S_r, \gamma, m, \rho^*, \sigma_N\}$ respectively.

In comparison to the structural stress based results (Fig. 3.8), it is clear that adopting the effective notch stress as strength criterion and cycle counting allows to enclose in the same scatter band CA and VA data. At the same time, the overall lifetime standard deviation is significantly reduced.

The different strength and mechanism for the uniaxial mode-I and mode-III as well as the multiaxial P and NP data can clearly be observed in the separate data scatter bands for $\beta = \sqrt{3}$, reflected in the imaginary intercept and slope for each data group (Fig. 3.14).   The lifetime scatter parameter $\sigma_N \sim 0.46$ and corresponding strength index $T_{\sigma S_e} = 1:4.24$ illustrate in comparison to the uniaxial values: $\sigma_{N,I} \sim 0.27$, $\sigma_{N,III} \sim 0.21$, $T_{\sigma S_e,I} = 1:1.67$ and $T_{\sigma S_e,III} = 1:1.27$ (Section 3.3.3) a much worse fit. Eliminating in addition the S_e related mode and material sensitive strength and mechanism contributions changes the imaginary intercept and slope

Figure 3.14.: Effective notch stress based fatigue resistance for uniaxial and multiaxial data; $\rho_I^* \neq \rho_{III}^*$ and $\beta = \sqrt{3}$.
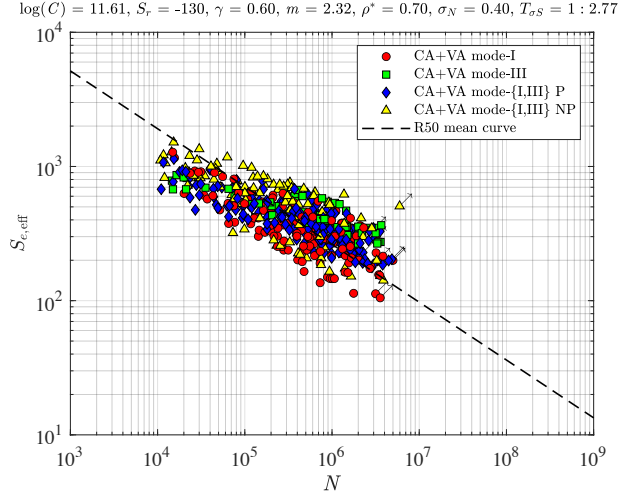
Figure 3.15.: Effective notch stress based fatigue resistance for uniaxial and multiaxial data; $\rho_I^* = \rho_{III}^*$ and $\beta = \sqrt{3}$.

for each data group (Fig. 3.15), but improves the overall performance: $\sigma_N \sim 0.40$ and $T_{\sigma S_e} = 1 : 2.77$. However, the data scatter of the individual data groups even increased, suggesting the equivalent shear strength and effective notch stress based strength and mechanism contributions are important. Overall, the uniaxial mode-I

and multiaxial mode-{I, III} P data shows a reasonable fit, but the uniaxial mode-III and mode-{I, III} NP data are way out of range (Figs. 3.14 and 3.15), illustrating at the same time the consequences of data imbalance (Section 3.3.2). Without affecting the global performance lifetime and strength parameters σ_N and $T_{\sigma S_e}$, the relative position of groups of data can change significantly and may cause wrong conclusions regarding the importance of strength and mechanism contributions as observed before [55, 79, 80]. Adopting the mode specific and material characteristic strength and mechanism contributions; $\{\log(C), m\}$ in terms of $\beta(N)$ – for an iteratively obtained N value (Section 3.3.1) – and $\{\gamma, \rho^*\}$, significantly improves the model performance (Fig. 3.16). The lifetime scatter and strength scatter band index reduced to a value about equal to that of the uniaxial mode-I data: $\sigma_N \sim 0.28$ (Section 3.3.3) and $T_{\sigma S_e} = 1 : 1.70$. However, the multiaxial NP data group still shows room for improvement. Adopting a 0th, 1st or 2nd order moment approach
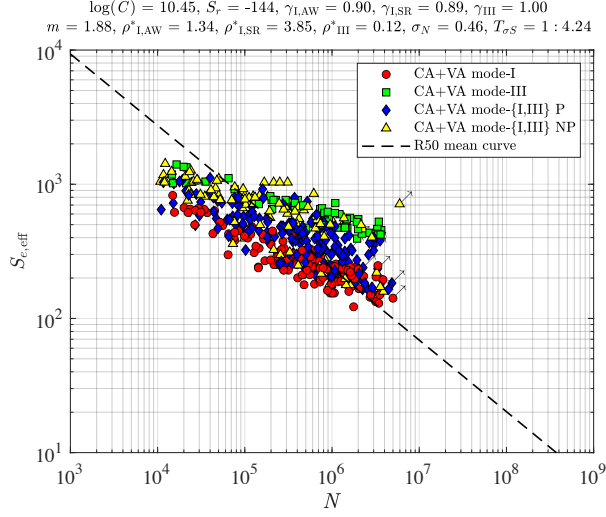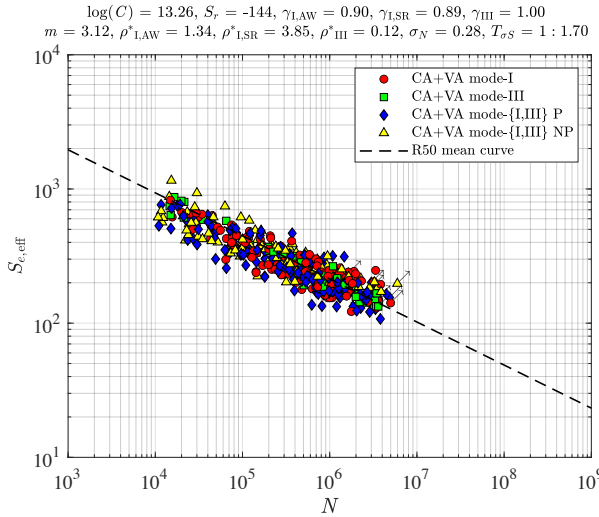

Figure 3.16.: Effective notch stress based fatigue resistance for uniaxial and multiaxial data; $\rho_{\text{I}}^* \neq \rho_{\text{III}}^*$ and $\beta = f(N)$.

(Section 3.3.1), differences between the actual response path and the (straight) range have been used to incorporate non-proportionality cycle-by-cycle in terms of C_{np} (Eq. 3.14), including a material characteristic contribution c_m (Eq. 3.13). The $c_m - \sigma_N$ sensitivity has been investigated for the C_{np} defined 0th, 1st and 2nd order moment approaches to evaluate the model performance. At the same time, the influence of ρ^* has been explored up to some extent, running the sensitivity analysis for the most likely mode-I and mode-III ρ^* estimate, as well as a smaller and larger value (Figs. 3.17 and 3.18). Since data is unbalanced, i.e. the multiaxial NP data size is relatively small, the performance for the multiaxial NP data only as well as all data has been considered. Looking at the $c_m - \sigma_N$ sensitivity for varying ρ_{III}^* (Fig. 3.18), the trendlines do not change much. However, in contrast to the results
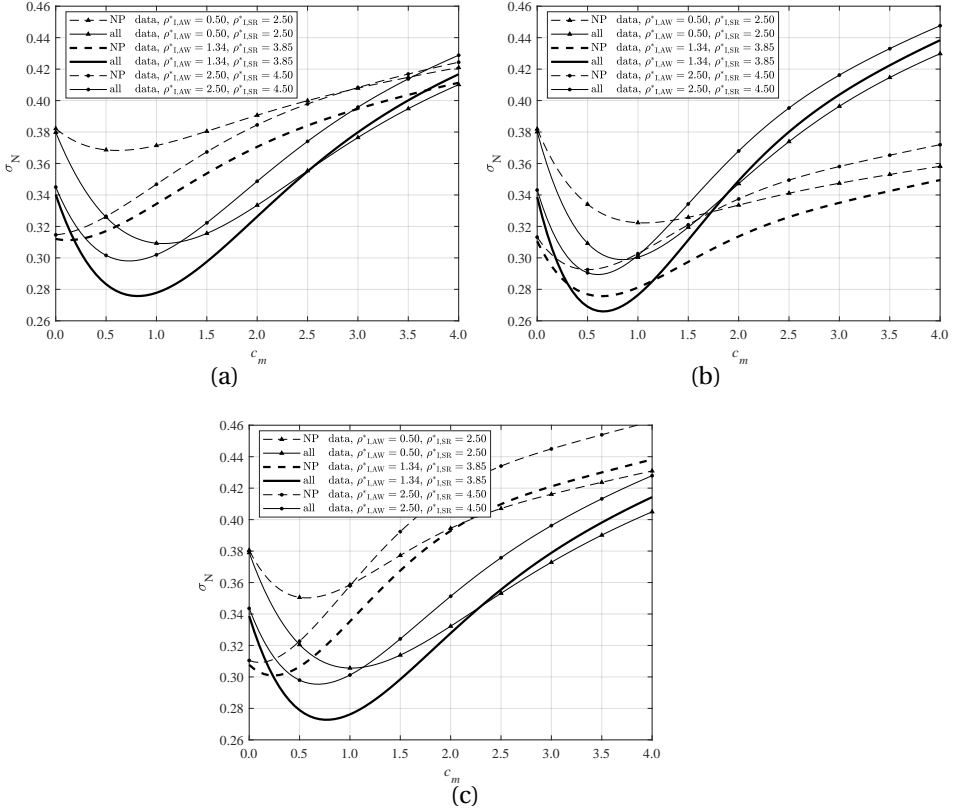
Figure 3.17.: Most likely σ_N for a range of c_m in case of three different ρ_I^* values and $\rho_{III}^* = 0.12$. Path dependent non-proportionality: 0th moment (a), 1st moment (b) and 2nd moment (c).

for varying ρ_I^*, the sensitivity is approximately ρ_{III}^* independent considering all data, since the governing scatter contribution is mode-I related (Figs. 3.10 and 3.11). An optimum c_m still exists for the 0th, 1st and 2nd order approach. Again, the best performance is obtained for a 1st order approach and a coinciding optimum for both the multiaxial NP data only and all data is observed. However, for a smaller ρ_{III}^* an even better performance – still for $c_m \sim 0.65$ – is obtained, basically confirming that c_m corrects in addition for any cycle counting and/or non-proportionality related model deficiency indeed. Assessing all data (Fig. 3.7 and Tables 3.1 and 3.2) using the most likely mode and material specific strength contributions, $\{\log(C), m\}$ and $\{\gamma, \rho^*\}$ respectively represented in $\beta(N)$ and S_e, as well as the 1st order approach to obtain C_{np} cycle by cycle for $c_m \sim 0.65$ in case of non-proportionality, an even better performance is obtained. The lifetime scatter has reduced to $\sigma_N \sim 0.26$ and the strength scatter band to $T_{\sigma S_e} = 1 : 1.65$. (Figs. 3.16 and 3.19). Principally all data
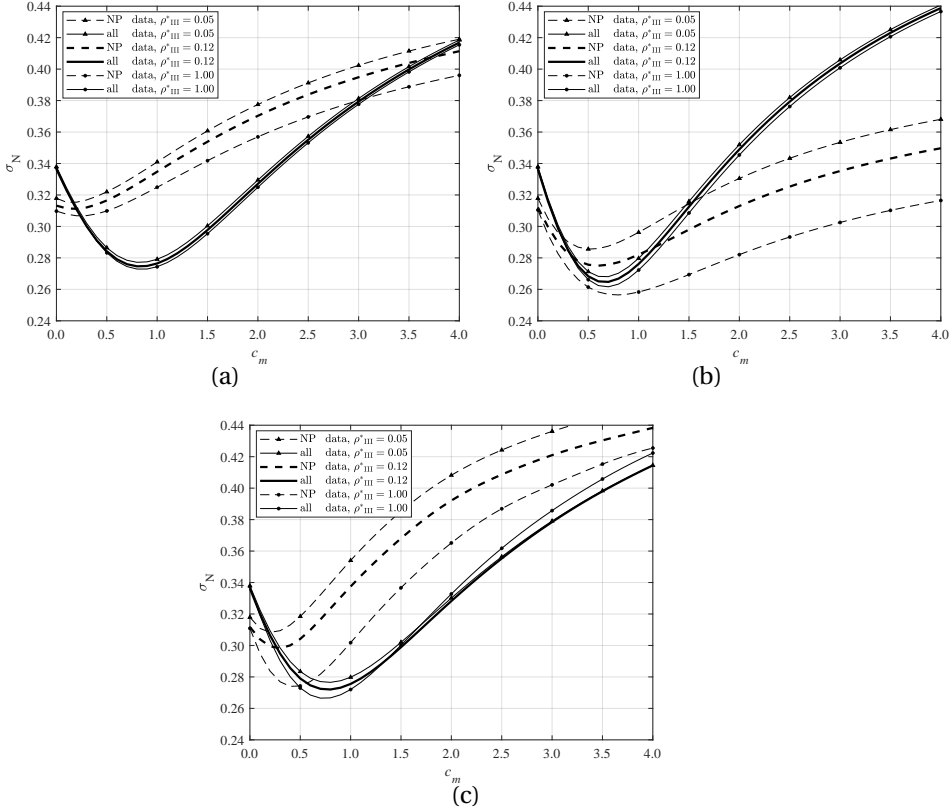
Figure 3.18.: Most likely σ_N for a range of c_m in case of three different ρ^*_{III} values and $\rho^*_{I,AW} = 1.34$ and $\rho^*_{I,SR} = 3.85$. Path dependent non-proportionality: 0th moment (a), 1st moment (b) and 2nd moment (c).

fits the mode-I reference data scatter band, i.e. the interval in between 5 and 95 [%] reliability for 75 [%] confidence (Figs. 3.19 and 3.20). Note that an increased data size: currently ~ 500 for the assessed data (Fig. 3.7 and Tables 3.1 and 3.2) and ~ 2500 for the mode-I reference data, can contribute to another σ_N reduction.

The multiaxial mode-{I, III} P data appears to show the largest scatter. However, the uniaxial mode-I and mode-III resistance (material) characteristics have been explicitly incorporated, as well as multiaxial mode-{I, III} non-proportionality measures, meaning that only for the multiaxial mode-{I, III} P data no specific resistance aspects have been considered; an obvious requirement to continue the improvement of the fatigue resistance formulation. Aside from improved damage plane selections, cycle counting algorithms and/or non-proportionality measures, failure criterion aspects could be reconsidered as well. One possible research

3
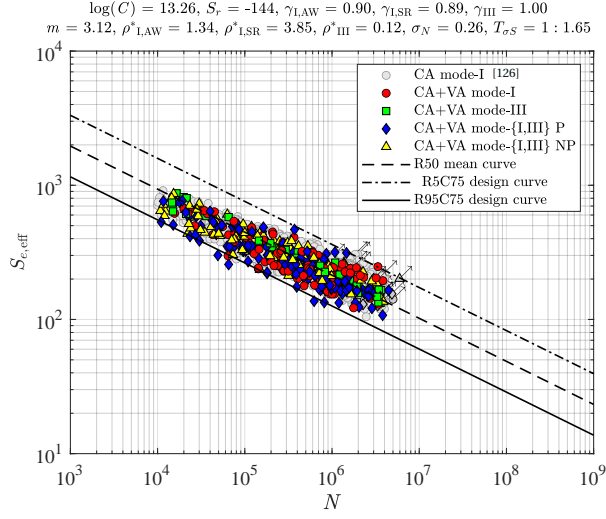
Figure 3.19.: Effective notch stress based fatigue resistance for uniaxial and multiaxial data; $\rho_{\mathrm{I}}^* \neq \rho_{\mathrm{III}}^*$, $\beta(N)$, 1$^{\mathrm{st}}$ order path dependent non-proportionality with $c_m = 0.65$.
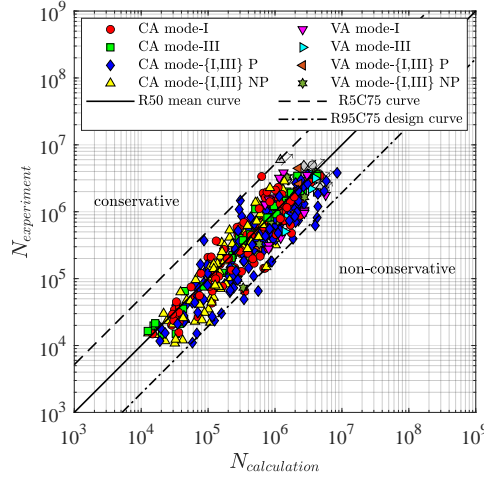
Figure 3.20.: Lifetime ratio plot of effective notch stress based fatigue resistance for uniaxial and multiaxial data; $\rho_{\mathrm{I}}^* \neq \rho_{\mathrm{III}}^*$, $\beta(N)$, 1$^{\mathrm{st}}$ order path dependent non-proportionality with $c_m = 0.65$.

direction could be to incorporate a shear strength coefficient based on times series rather than a peak-valley sequence analysis, i.e. instantaneous rather than

cycle-by-cycle; $\beta(t)$ rather than $\beta(N)$, implying even the multiaxial P data would show NP behaviour in the von Mises stress plane. However, a redefinition of the failure criterion may be required as well, since the S_e formulation is currently based on a cycle characteristic parameter: the (effective) stress range. Another direction might be the introduction of coupling terms, for example like $S_e = \sqrt{C_1 \cdot S_{e,I}^2 + C_2 \cdot S_{e,I} \cdot S_{e,III} + C_3 \cdot S_{e,III}^2}$. To illustrate: mean (residual) stress effects for uniaxial mode-III fatigue might be negligible, but may be relevant if a mode-I contribution is involved as well [e.g. 127]. Mode and material specific uniaxial $\{\log(C), \gamma, m, \rho^*\}$ parameters have been established to assess multiaxial data, but missing mode-{I, III} interaction could explain the multiaxial proportional data scatter. The variable amplitude data fits the constant amplitude data scatter band for $D = 1$ (Fig. 3.21), supporting the hypothesis that an advanced fatigue failure criterion like S_e contributes to the (linear) damage accumulation model performance. However, most variable amplitude data involves a random sequence reflected in a Normal distributed narrow-band spectrum (Fig. 3.22), meaning the data contains at maximum an averaged sequence effect. A response based non-linear damage model (Section 3.2.5) may still be required if data for different types of random sequence (e.g. broad-band spectra) or even for a determined sequence will be incorporated.

$$\log(C) = 13.26,\ S_r = \text{-}144,\ \gamma_{\text{I,AW}} = 0.90,\ \gamma_{\text{I,SR}} = 0.89,\ \gamma_{\text{III}} = 1.00$$
$$m = 3.12,\ \rho^*_{\text{I,AW}} = 1.34,\ \rho^*_{\text{I,SR}} = 3.85,\ \rho^*_{\text{III}} = 0.12,\ \sigma_N = 0.26,\ T_{\sigma S} = 1:1.65$$
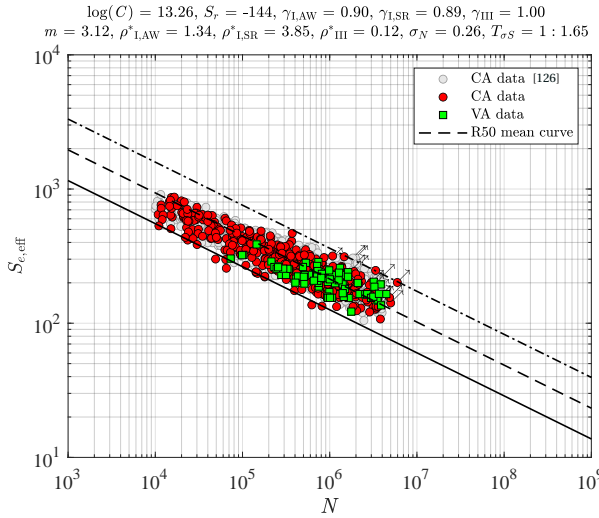
Figure 3.21.: Effective notch stress based fatigue resistance for uniaxial and multiaxial, constant and variable amplitude data.

In comparison to the assessment for other combinations of failure criterion, damage plane, cycle counting algorithm, non-proportionality measure and damage accumulation model in terms of lifetime and strength scatter; i.e. σ_N and $T_{\sigma S_e}$, the outperformance is impressive (Table 3.4). In principle only the effective notch stress is considered for the sake of fair judgement, although one mode and material
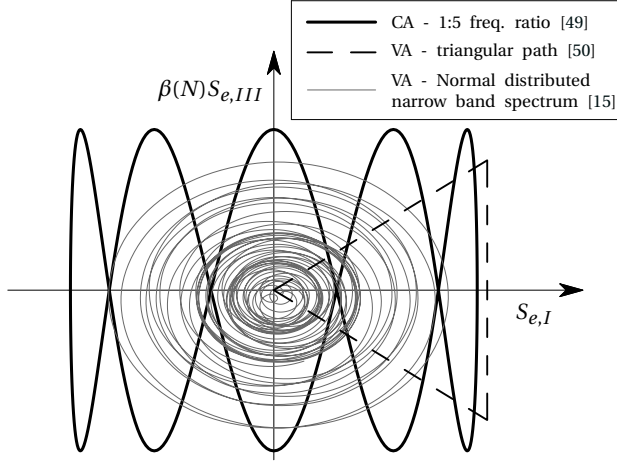
Figure 3.22.: Different stress histories in the von Mises stress plane.

invariant fictitious notch radius is adopted to obtain an S_e estimate at once, rather than averaging the stress distribution over a material characteristic length to obtain the actual S_e [33, 87, 109–111, 128, 129]. One exception is the equivalent traction based structural stress; a cracked rather than intact geometry based parameter, considered because a similar cycle counting algorithm is involved. Results from other sources (Table 3.4) do not consider all the data available (Fig. 3.7 and Tables 3.1 and 3.2), meaning in general a better fit than when all data is involved and emphasizing at the same time the quality of the obtained performance criteria: $\sigma_N \sim 0.26$ and $T_{\sigma S_e} = 1 : 1.65$. Using not the same data sets partially explains the differences for the multiple IIW and Eurocode results as well. Note that the lifetime scatter parameter σ_N is not proportional to the corresponding strength scatter band index (Table 3.4), since $T_{\sigma S_e}$ is slope dependent: $T_{\sigma S} = 1 : (S_{e,10}/S_{e,90})$ with $S_{e p_s} = \left\{ N \cdot \left(C \cdot 10^{\Phi^{-1}(1-p_s) \cdot \sigma_N} \right)^{-1} \right\}^{-1/m}$ and $\Phi^{-1}(1-p_s)$ the inverse of the adopted Normal distributed probability density function for probability of survival p_s, meaning $(S_{e,10}/S_{e,90}) = \left\{ 10^{\sigma_N (\Phi^{-1}(1-0.10) - \Phi^{-1}(1-0.90))} \right\}^{1/m}$. Anyway, both the lifetime scatter and strength scatter band index are not yet similar to the reference mode-I data values [126]: $\sigma_N = 0.21$ and $T_{\sigma S_e} = 1 : 1.49$, suggesting room for improvement of effective notch stress assessment is still left.

3

Table 3.4.: Lifetime standard deviation σ_N and strength scatter band index $T_{\sigma S}$ for different multiaxial fatigue assessment concepts.

source	developer	failure criterion	damage plane	cycle counting algorithm	non-prop. measure	damage acc. model	σ_N	$T_{\sigma S}$
Eq. 3.12	Bufalari et al.	[a] non-linear eq. stress (von Mises type with $\beta(N)$)	critical	multiaxial: von Mises plane	path: 1st order (cycle-by-cycle)	linear	0.26	1:1.65
[66]	IIW (guidelines)	[b] non-linear eq. stress (von Mises type)	critical	uniaxial	damage down grade	linear	0.46	1:2.69
[55]	IIW (guidelines)	[b] non-linear eq. stress (von Mises type)	critical	uniaxial	damage down grade	linear	0.42	1:2.28
[66]	CEN (Eurocode)	[b] non-linear eq. stress based on linear damage mode superposition	critical	uniaxial	/	linear	0.40	1:2.65
[55]	CEN (Eurocode)	[b] non-linear eq. stress based on linear damage mode superposition	critical	uniaxial	/	linear	0.49	1:2.62
[66]	Sonsino	[b] non-linear eq. stress (von Mises type)	integral	uniaxial	implicitly in failure criterion	linear	0.58	1:6.04
/		[b] von Mises stress	critical	uniaxial	/	linear	0.44	1:2.41
[66]		[b] max principal stress	critical	uniaxial	/	linear	0.51	1:3.45
[66]	Carpinteri et al.	[b] non-linear eq. stress (von Mises type with $\beta(N)$)	critical	multiaxial main+aux. channel	implicitly in failure criterion (cycle-by-cycle)	non-linear	0.47	1:2.81
[66]	Findley	[b] linear eq. stress	critical	uniaxial	/ (cycle-by-cycle)	linear	0.46	1:2.40
[66]	Susmel	[b] shear stress	invariant	uniaxial	implicitly in resistance curve (time series VAR)	linear	0.48	/
[55]	Dong et al.	[c] non-linear eq. stress (von Mises type with $\beta = \sqrt{3}$)	critical	multiaxial: von Mises plane	path: 1st order (cycle-by-cycle)	linear	0.36	1:2.03

Fatigue strength parameter:
(a) effective notch stress using material characteristic length
(b) effective notch stress using fictitious notch radius
(c) traction equivalent structural stress

3.4. CONCLUSIONS AND OUTLOOK

The fatigue lifetime of arc-welded joints is predominantly spent in the notch affected region, explaining why the effective notch stress S_e has been adopted as intact geometry fatigue strength parameter. A formulation has been established taking advantage of semi-analytical weld notch stress distribution expressions. Uniaxial mode-I and mode-III investigations [14, 16, 29] already revealed distinguished material dependent strength and mechanism contributions in terms of {log(C), γ} and {m, ρ^*}, i.e. respectively the resistance curve intercept and mean stress induced response ratio coefficient, resistance curve slope and material characteristic length. Since for mixed mode-{I, III} multiaxial response conditions of planar and tubular maritime structures the mode-I contribution is governing and at the same time the fatigue lifetime of arc-welded joints is growth defined rather than initiation controlled (i.e. a shear induced process) because of the welding induced defects, an equivalent normal stress based von Mises type of failure criterion at the critical fracture plane has been selected for fatigue assessment purposes. Cycles are counted in the von Mises plane, incorporating non-proportionality cycle-by-cycle (*research sub-question 4*) and accumulating damage using a linear model.

In comparison to the assessment for other combinations of failure criterion, damage plane, cycle counting algorithm, non-proportionality measure and damage accumulation model in terms of lifetime and strength scatter; i.e. σ_N and $T_{\sigma S_e}$, the outperformance is impressive. Rather than a constant, a lifetime dependent shear strength coefficient $\beta(N)$ has been introduced to cover the mode specific and material characteristic {log(C), m}, whereas S_e explicitly contains {γ, ρ^*}. The cycle-by-cycle non-proportionality measure includes a response path and material contribution. A 1st order response approach shows the best performance. Judgement is based on the affected data rather than all data, since balance between the non-proportional and other data does not exist. If non-proportionality involves a material aspect indeed seems impossible to prove, as the material fitting coefficient c_m behaves at the same time as a cycle counting and non-proportionality modelling deficiency correction factor. The multiaxial proportional data appears to show the largest scatter. However, the uniaxial mode-I and mode-III resistance (material) characteristics have been explicitly incorporated, as well as multiaxial mode-{I, III} non-proportionality measures, meaning that only for the multiaxial proportional data no specific resistance aspects have been considered; an obvious requirement to continue the improvement of the fatigue resistance formulation, for example incorporating a shear strength coefficient based on times series rather than a peak-valley sequence analysis – implying even the multiaxial proportional data would show non-proportional behaviour in the von Mises stress plane – or introducing coupling terms to the failure criterion (*research sub-questions 2a and 4*).

The VA data fits the CA data scatter band for $D = 1$, supporting the hypothesis that an advanced fatigue strength parameter like S_e contributes to the (linear) damage accumulation model performance. However, most VA data involves a random sequence reflected in a Normal distributed narrow-band spectrum, meaning the data contains at maximum an averaged sequence effect. A response based non-linear damage model may still be required if data for different types of random sequence

(e.g. broad-band spectra) or even for a determined sequence will be incorporated. A resistance induced non-linearity becomes relevant if both mid- and high- cycle fatigue become involved.

Although the obtained lifetime scatter parameter σ_N is still relatively large, the assessed uniaxial and multiaxial mode-{I, III} data fits the uniaxial mode-I reference data scatter band and a single $S_e - N$ resistance curve can be used for fatigue assessment in engineering applications (*research sub-question 5a*). However, the aim for high accuracy may impose high engineer qualifications in order to satisfy the balance with model complexity and computational (programming) efforts (*research sub-question 3a*).

3

4

S_T BASED MIXED MODE-{I, III} MULTIAXIAL FATIGUE RESISTANCE

There is a crack in everything.

Leonard Cohen, singer

4.1. INTRODUCTION

Despite the impressive outperformance of S_e (Chapter 3) in comparison to other combinations of failure criterion, damage plane, cycle counting algorithm, non-proportionality measure and damage accumulation model, the P data shows a relatively large data scatter. Multiaxial mode-{I, III} coupling seems incomplete and involving the mode specific and material characteristic parameters only is likely insufficient. Adopting a von Mises type of failure criterion – without mode-{I, III} coupling by definition – and corresponding cycle counting plane and algorithm could be an explanation, as well as the involved intact geometry parameter S_e rather than a cracked geometry one. Since the notches inevitably contain welding induced defects, adopting a notch characteristic cracked geometry parameter like the total stress S_T [6, 14, 16, 18] to establish the fatigue strength seems as justified as an intact one (Chapter 3). The actual initiation (i.e. nucleation) contribution to the total fatigue life time is virtually eliminated and growth is governing. The intact geometry related semi-analytical weld notch stress distribution formulations can be turned into cracked geometry ones, introducing the weld notch stress intensity factor (SIF) K. Cyclic loading & response conditions turn K into a crack growth driving force ΔK and defects may develop into cracks. Since the growth rate initially shows

elastoplastic wake field affected anomalies [18], a modified Paris' equation has been established, including the weld notch- and far field characteristic contributions: a generalised two-stage crack growth relation. Applying an integral operator provides a log-log linear resistance relation of the Basquin type, correlating the fatigue life time N and an equivalent fatigue strength parameter: the total stress S_T [6, 18]. Uniaxial mode-I intercept $\log(C_I)$ and slope m_I, as well as response ratio coefficient γ_I and elastoplasticity coefficient n_I estimates have already been obtained for welded joints in steel (maritime) structures [14, 16]. The S_T and S_e performance in terms of life time scatter σ_N and strength scatter band index $T_{\sigma S}$ proved to be similar.

Whereas ρ^* is a mode specific and material characteristic length defining S_e to incorporate the notch stress gradient, S_T includes the stress (intensity) gradient along the full plate thickness t_p defined final crack length a_f, suggesting ρ^* and a_f serve the same purpose. However, S_T contains an additional mechanism related parameter n and may increase insight in the mode specific and material characteristic behaviour. The uniaxial mode-III and multiaxial mode-{I, III} S_T performance have not been established before and a key question is if the mode coupling is equally important for S_T as for S_e. At the same time, a cracked geometry parameter seems one step closer to the actual damage process than an intact one, hypothesising a fatigue strength parameter S_T may outperform S_e for multiaxial fatigue.

The intact geometry related weld notch stress distribution will be translated first to a cracked geometry equivalent weld notch stress intensity distribution (Section 4.2), providing input for S_T. Considering all relevant assessment aspects for a time domain approach, including type of criterion, damage plane selection, cycle counting aspects including ways to deal with non-proportionality and damage accumulation [130], the S_T performance will be evaluated for multiaxial fatigue resistance data of welded joints in steel maritime structures (Section 4.3). Mode specific and material characteristic strength and mechanism contributions, $\{\log(C), \gamma\}$ and $\{m, n\}$ respectively, will be established. A comparison to S_e as well as another cracked geometry parameter: the traction equivalent structural stress S_t [41, 55, 113, 128, 131], will be provided for reference purposes.

The conclusions and outlook (Section 4.4) provide answers to research sub-questions 1, 2 and 5 (Section 1.3).

4.2. WELD NOTCH STRESS (INTENSITY) DISTRIBUTIONS

Although mode-I and mode-III through-thickness weld notch stress distribution formulations along the expected (2D) crack path $\{\sigma_I(r/t_p), \tau_{III}(r/t_p)\}$ – key elements for a fatigue design criterion – are separately established before [14, 16, 18, 29], a short recapitulation is provided (Section 4.2.1) in order to discuss the differences, as well as to present a comparison to bi-linear approximations [132]. At the same time, the intact geometry related $\{\sigma_I(r/t_p), \tau_{III}(r/t_p)\}$ are used to obtain the cracked geometry equivalent weld notch stress intensity distributions (Section 4.2.2): $\{K_I(a/t_p), K_{III}(a/t_p)\}$. Mode-I formulations for planar structures are already available

[16, 18], but modifications turned out to be required for tubular ones. Sufficiently accurate mode-III formulations seem to be still lacking in literature and have been derived for both planar and tubular structure configurations [29]. Last but not least, a comparison to the bi-linear approximation based $\{K_I(a/t_p),\ K_{III}(a/t_p)\}$ formulations [132] is provided.

4.2.1. WELD NOTCH STRESS DISTRIBUTIONS

Adopting a linear superposition principle [18], equilibrium equivalent and self-equilibrium parts $\{\sigma_{fe}, \sigma_{se}; \tau_{fe}, \tau_{se}\}$ have been distinguished (Fig. 4.1) in order to formulate $\{\sigma_I(r/t_p),\ \tau_{III}(r/t_p)\}$. Three components are involved: the notch stress, the weld-load carrying stress and the far field stress. Typically three zones can be identified in all distributions: the zone 1 peak stress value, the zone 2 notch-affected stress gradient and the zone 3 far-field dominated stress gradient, demonstrating stress field similarity.
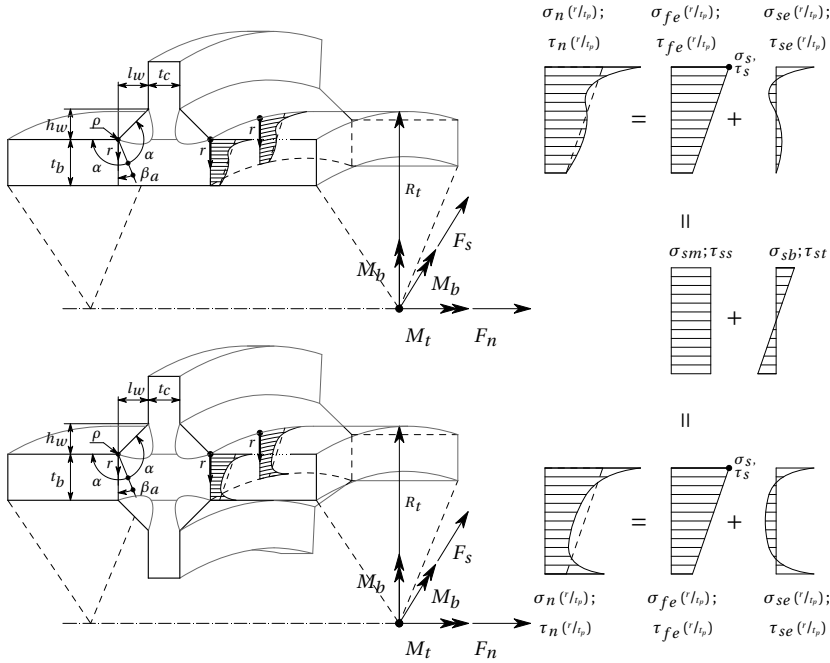
Figure 4.1.: Linear superposition of an equilibrium equivalent and self-equilibrium part for the mode-{I, III} weld toe notch stress distributions of a DS welded T-joint and DS welded cruciform joint in a tubular structure.

The V-shaped notch angle characteristic stress component applies to both groove and fillet welds and represents the (near) singular contribution defining the hot spot [16, 18, 29].

Since the weld geometry causes a local change in stiffness, the notch becomes load carrying up to some extent, depending on the joint dimensions including

welding penetration level as well as loading conditions. Weld notch load carrying stress component estimates can be obtained using beam finite element (FE) models, but polynomial fitting functions turned out to be more useful from engineering perspective [16, 29].

The equilibrium equivalent far field stress components $\{\sigma_{fe}, \tau_{fe}\}$ in the cross-section at a weld toe (Fig. 4.1) is in compliance with the fracture mechanics definition [40, 41]. Estimates are naturally obtained using through-thickness linearisation rather than surface extrapolation [133] adopting a relatively coarse meshed shell/plate FE model (Figs. 4.2a and 4.2b) [43, 44]. Transforming the nodal normal and shear forces $\{F_{n,i}, F_{s,i}\}$ as well as bending and torsion moments $\{M_{b,i}, M_{t,i}\}$ along the weld seam to line forces and moments $\{f_{n,i}, f_{s,i}\}$ and $\{m_{b,i}, m_{t,i}\}$, four systems of equations have to be solved for: $\{F_n\} = [T]\{f_n\}$, $\{F_s\} = [T]\{f_s\}$, $\{M_b\} = [T]\{m_b\}$ and $\{M_t\} = [T]\{m_t\}$ [41, 112, 113], the constant membrane and linear bending terms $\{\sigma_{sm}, \sigma_{sb}\}$, as well as the constant shear and linear torsion ones $\{\tau_{ss}, \tau_{st}\}$ for respectively mode-I and mode-III [44] can be calculated to acquire the structural stresses $\{\sigma_s = \sigma_{sm} + \sigma_{sb}, \tau_s = \tau_{ss} + \tau_{st}\}$ and structural stress ratios $\{r_{\sigma s} = \sigma_{sb}/\sigma_s, r_{\tau s} = \tau_{st}/\tau_s\}$ as characteristic far field stress parameters.
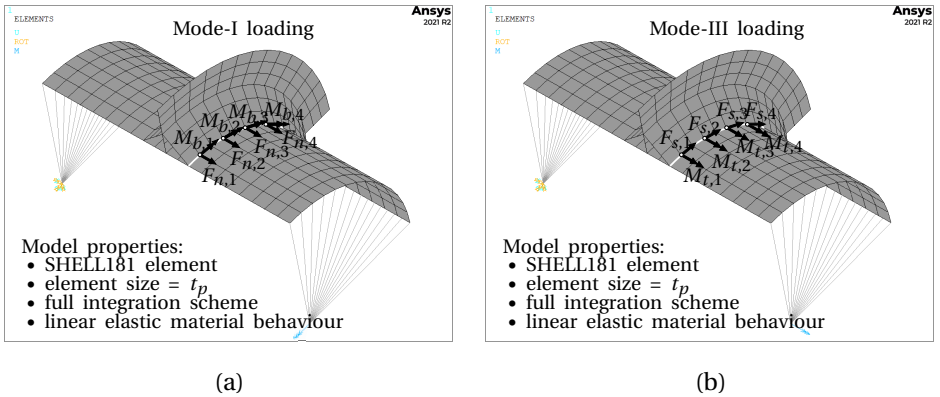
Figure 4.2.: Part of a shell FE model of a (non-symmetric) T-joint in a tubular structure for a mode-I (a) and mode-III (b) response.

If the welded joint structural stiffness – either in planar or tubular structures – does not significantly affect the stress distribution, like in general for groove welds (e.g. in butt joints), the weld does not need to be modelled and the far field stress information can be obtained at the intersection line of the connected structural members [29, 40]. However, fillet weld modelling is typically required (e.g. in T-joints and cruciform joints) for more accurate far field stress estimates – although avoided in some guide lines for engineering purposes [34] –, in particular if a structural response contains superimposed contributions from different levels of stiffness hierarchy, like often applies to maritime structures. Considering for example a stiffener-frame connection as a critical fatigue sensitive location in the bottom structure of a ship sailing in quartering seas, the mode-{I, III} far field stress consists
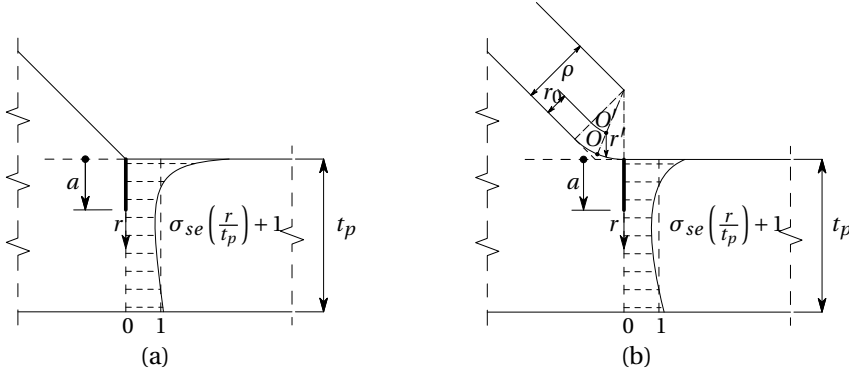
Figure 4.3.: Self-equilibrium stress part for a mode-I response applied as unit crack face traction at weld toe notches for $\rho = 0$ (a) and $\rho > 0$ (b).

at least of a local water pressure and shear force induced response at plate-stiffener level, as well as a bending moment and torsion moment induced one at global hull girder level [134, 135]. Inclined shell elements have been used (Fig. 4.2), rather than inclined rigid ones or shell elements with increased local thickness at the joint location [44, 46].

MODE-I FORMULATION

For non-symmetry with respect to half the plate thickness ($t_p/2$) and notch radius $\rho = 0$, the mode-I weld toe notch formulation yields [130]:

$$\sigma_n \left(\frac{r}{t_p} \right) = \sigma_s \left[\sigma_{se} \left(\frac{r}{t_p} \right) - 2r_{\sigma_s} \left(\frac{r}{t_p} \right) \right] \tag{4.1}$$

with σ_{se} being the self equilibrium stress part (Eq. D.1). Similar formulations are available for symmetry with respect to ($t_p/2$) as well as for the $\rho > 0$ cases [18].

A non-monotonic and monotonically increasing weld notch stress distribution at the weld toe of a double sided (DS) T-joint are shown for illustration purposes (Fig. 4.4a and 4.4b). Load cases are respectively a normal force F_n ($r_{\sigma s} = 0$) and a combined one involving an additional bending moment M_b ($r_{\sigma s} = 0.25$). Note that at the same time the geometry has changed from approximately a planar ($R_t = 5000$) to a tubular one ($R_t = 36$), implying that the weld notch stress distribution formulations hold in general. The joint dimensions are arbitrary, but realistic for steel maritime structures and the weld notch load carrying level is relatively low: $C_{bw} = \{0.16, 0.15\}$. Comparing the weld toe notch stress and far field stress distributions indicate that equilibrium is satisfied indeed. Converged FE solutions show the accuracy of the formulation.

The bi-linear approximation involves a predefined notch to far field transition location at $0.1(r/t_p)$ and is – in contrast to the semi-analytical formulation (Eqs. (4.1) and (D.1)), reflected in C_{bw} – only loading dependent [132], meaning any local notch

geometry information is not explicitly taken into account. Note that for $(r/t_p) \to 0$ the notch stress is finite, even for $\rho = 0$; the singular case. If the weld notch load carrying level increases, a notch affected zone size of $0.1(r/t_p)$ turns out to be too small [16, 18].

MODE-III FORMULATION

Similar to mode-I, weld toe notch formulations for mode-III are obtained. For non-symmetry with respect to $(t_p/2)$ and $\rho = 0$ [29]:

$$\tau_n\left(\frac{r}{t_p}\right) = \tau_s\left[\tau_{se}\left(\frac{r}{t_p}\right) - 2r_{\tau_s}\left(\frac{r}{t_p}\right)\right] \tag{4.2}$$

with the self-equilibrium stress part $\tau_{se}(r/t_p)$:

$$\tau_{se}\left(\frac{r}{t_p}\right) = \left(\frac{r}{t_p}\right)^{\lambda_\tau - 1} \mu_{\tau F} \cos(\lambda_\tau \beta_a) - (C_{tw} + \mu_{\tau M})\left\{2\left(\frac{r}{t_p}\right) - 1\right\}. \tag{4.3}$$

Formulations are available for symmetry with respect to $(t_p/2)$ as well, including the $\rho > 0$ cases (Section 2.2).

A non-monotonic and monotonically increasing weld notch stress distribution at the weld toe of a DS T-joint (Fig. 4.5a and 4.5b) illustrate the performance of the developed formulations in comparison to the converged FE solutions. The applied load is a torsion moment M_t. Changing the geometry from an approximately planar ($R_t = 5000$) to a tubular one ($R_t = 36$) is responsible for the different structural shear stress ratio, $r_{\tau s} = \{0, 0.25\}$, basically representing an approximately applied shear force F_s load case and a combined one involving an additional torsion moment M_t. In comparison to the mode-I results, for the same geometry the weld notch load carrying level has increased: $C_{tw} = \{0.18, 0.19\}$, as reflected in the increased notch affected region (Figs. 4.4 and 4.5).

The bi-linear approximation as originally developed for mode-I has been extended to mode-III applications [79, 128, 136, 137]. Despite the increased notch affected region, the transition location is still fixed at $0.1(r/t_p)$ and the fit seems not to be perfect. Anyway, even for different C_{tw} values providing a better fit, a predefined and geometry independent transition location remains a modelling limitation for an accurate joint specific weld notch stress distribution representation.

4.2.2. WELD NOTCH STRESS INTENSITY DISTRIBUTIONS

Scaling of welded joint fatigue damage requires a total stress parameter taking all zone {1, 2, 3} contributions into account; a criterion the stress intensity (similarity) factor K seems to meet. Turning the intact geometry related weld toe notch stress distributions into crack damaged equivalents, the zone {1, 2} self-equilibrium and zone 3 equilibrium equivalent stress parts $\{\sigma_{fe}(r/t_p), \sigma_{se}(r/t_p); \tau_{fe}(r/t_p), \tau_{se}(r/t_p)\}$ have been used to introduce respectively a notch factor $Y_n(a/t_p)$ and a far field factor $Y_f(a/t_p)$, defining the weld toe notch stress intensity factor for respectively

mode-I and mode-III:

$$K_I = \sigma_s \sqrt{t_p} Y_{n,I}(a/t_p) Y_{f,I}(a/t_p) \sqrt{\pi(a/t_p)} \tag{4.4}$$

$$K_{III} = \tau_s \sqrt{t_p} Y_{n,III}(a/t_p) Y_{f,III}(a/t_p) \sqrt{\pi(a/t_p)} \tag{4.5}$$

The stress intensity magnitude is characterised using the structural stress $\{\sigma_s, \tau_s\}$. Assuming the crack tip is infinitely sharp explains the square root behaviour $\sqrt{\pi(a/t_p)}$ for $(a/t_p) \to 0$.

Mode-I formulation

Aiming for a $Y_n Y_f$ rather than $(Y_n + Y_f)$ formulation, $\sigma_{se}(r/t_p)$; the self-equilibrium stress part (Eq. D.1) has been applied as unit crack face traction along the assumed virtual crack path (Fig. 4.3) using the weight function approach [138]. For non-symmetry with respect to $(t_p/2)$ and $\rho = 0$ [16, 18] the notch factor yields:

$$
\begin{aligned}
Y_n &= \left(\frac{2}{\pi}\right) \int_0^1 \frac{\sigma_{se}\left(\frac{r}{a} \cdot \frac{a}{t_p}\right) + 1}{\sqrt{1 - \left(\frac{r}{a}\right)^2}} \, d\left(\frac{r}{a}\right) \\
&= \left(\frac{2}{\pi}\right) \left[\left(\frac{a}{t_p}\right)^{\lambda_{\sigma s} - 1} \mu_{\sigma s} \left(\frac{\sqrt{\pi}}{2}\right) \frac{\Gamma\left(\frac{\lambda_{\sigma s}}{2}\right)}{\Gamma\left(\frac{\lambda_{\sigma s}+1}{2}\right)} \lambda_{\sigma s}(\lambda_{\sigma s}+1) \cdot \right. \\
&\quad [\cos\{(\lambda_{\sigma s}+1)\beta_a\} - \chi_{\sigma s}\cos\{(\lambda_{\sigma s}-1)\beta_a\} + \\
&\quad \left(\frac{a}{t_p}\right)^{\lambda_{\sigma a}-1} \mu_{\sigma a} \left(\frac{\sqrt{\pi}}{2}\right) \frac{\Gamma\left(\frac{\lambda_{\sigma a}}{2}\right)}{\Gamma\left(\frac{\lambda_{\sigma a}+1}{2}\right)} \lambda_{\sigma a}(\lambda_{\sigma a}+1) \cdot \\
&\quad \left. [\sin\{(\lambda_{\sigma a}+1)\beta_a\} - \chi_{\sigma a}\sin\{(\lambda_{\sigma a}-1)\beta_a\} + C_{bw}\left\{2\left(\frac{a}{t_p}\right) - \frac{\pi}{2}\right\} \right].
\end{aligned}
\tag{4.6}
$$

The through-thickness crack coordinate (a/t_p) naturally replaced the corresponding through-thickness stress coordinate (r/t_p). The primitives introduce $\Gamma(\cdot)$; the complete gamma function. Formulations for symmetry with respect to $(t_p/2)$ and $\rho > 0$ have been established as well [16, 18]. The linear far field stress distribution $\sigma_{fe}(r/t_p) = \sigma_s\{1 - 2r_{\sigma s}(r/t_p)\}$ in the fracture mechanics context with $\sigma_s = \sigma_{sm} + \sigma_{sb}$ and $r_{\sigma s} = \sigma_{sb}/\sigma_s$ is consistent with the one defined for the welded joint. A superposition of the involved constant membrane and linear bending component applies to the far field factor as well [16, 18]:

$$Y_{f,I}\left(\frac{a}{t_b}, r_{\sigma s}\right) = Y_{fm} - r_{\sigma s}(Y_{fm} - Y_{fb}) \tag{4.7}$$

For a single edge crack configuration in planar structures, $\{Y_{fm}, Y_{fb}\}$ handbook solutions are available [16, 18]. However, for tubular ones, results proved to be not sufficiently accurate. Redefining the structural normal stress ratio: $r_{\sigma s} = t_b/(2R_t)$, new formulations have been established, fitting FE results:

$$Y_{fm} = \eta^{-1} \cdot \left\{ A_1 \left(\frac{a}{t_b} \right)^4 + A_2 \left(\frac{a}{t_b} \right)^3 + A_3 \left(\frac{a}{t_b} \right)^2 + A_4 \left(\frac{a}{t_b} \right) + A_5 \right\} \qquad (4.8)$$

with

$$A_1 = -0.4102\eta^5 + 5.9416\eta^4 - 31.2763\eta^3 + 74.7289\eta^2 - 76.6080\eta + 32.5525$$
$$A_2 = 0.3159\eta^5 - 4.7704\eta^4 + 26.4878\eta^3 - 66.1652\eta^2 + 65.8295\eta - 26.0822$$
$$A_3 = -0.0914\eta^5 + 1.4008\eta^4 - 8.1841\eta^3 + 23.0032\eta^2 - 24.1433\eta + 10.8140$$
$$A_4 = 0.0072\eta^5 - 0.1105\eta^4 + 0.6432\eta^3 - 1.7606\eta^2 + 2.1383\eta - 0.8209$$
$$A_5 = 1.0122\eta + 0.0157$$

and

$$Y_{fb} = \eta^{-1} \cdot \left\{ B_1 \left(\frac{a}{t_b} \right)^4 + B_2 \left(\frac{a}{t_b} \right)^3 + B_3 \left(\frac{a}{t_b} \right)^2 + B_4 \left(\frac{a}{t_b} \right) + B_5 \right\} \qquad (4.9)$$

with

$$B_1 = -1.2609\eta^5 + 18.5324\eta^4 - 103.4794\eta^3 + 274.5174\eta^2 - 341.9945\eta + 167.7979$$
$$B_2 = 0.9786\eta^5 - 14.5248\eta^4 + 82.2228\eta^3 - 220.5391\eta^2 + 272.6368\eta - 132.8441$$
$$B_3 = -0.2529\eta^5 + 3.8114\eta^4 - 22.2233\eta^3 + 63.1152\eta^2 - 81.0820\eta + 43.6888$$
$$B_4 = 0.0255\eta^5 - 0.3747\eta^4 + 2.1096\eta^3 - 5.6774\eta^2 + 7.2997\eta - 3.8365$$
$$B_5 = 1.0123\eta + 0.0164.$$

Since the relative membrane and bending contributions are not just loading dependent, a geometry parameter has been introduced: $\eta = -\log\left(\frac{t_b}{2R_t}\right)$. The formulations are applicable for $\{1/2 \le (t_b/2R_t) \le 1/200\}$ and $\{0 \le (a/t_b) \le 1\}$.

Considering the same geometry and loading conditions as for the weld notch stress distributions (Fig. 4.4a and 4.4b), the weld notch stress intensity weight functions $\{Y_{n,I}, Y_{f,I}\}$ are obtained (Fig. 4.4c and 4.4d). If the weld notch load carrying level as reflected in C_{bw} is relatively small, $Y_{n,I}$ turns to be governing for $\{0 < (a/t_p) \le 0.2\}$; a zone {1,2} affected (technical) short crack region, divided into a respectively a notch dominated and a weld load carrying controlled part. Far field factor $Y_{f,I}$ controls the zone 3 contribution in a long-crack region $\{0.2 < (a/t_p) \le 1\}$, meaning all 3 stress components are decisive in a certain crack length region. Depending on C_{bw} and $r_{\sigma s}$, the $Y_{n,I} - Y_{f,I}$ transition may shift left or right. The FE solutions, obtained for plane strain conditions, proved to be rather good $Y_{n,I} Y_{f,I}$ estimates. Using the bi-linear weld notch stress distribution approximation (Fig. 4.4a and 4.4b) to obtain a K_I estimate is one of the traction equivalent structural stress concept features [112, 132]; a robust procedure [139]. Although the notch stress intensities are in agreement with the FE solutions (Fig. 4.4c and 4.4d) for short cracks, $M_{kn} Y_{f,I}$ seems consistently overestimated for $\{a/(t_p/2)\} < 0.1$. Modifying $Y_{f,I}$ to incorporate the notch characteristic behaviour and establish the notch magnification factor M_{kn} – a Y_n equivalent parameter, rather than adopting the crack face traction definition (Eq. 4.6), seems the explanation [18, 126]. Differences in the long crack region

for the tubular structure (Fig. 4.4 d) are a result of a planar geometry based $Y_{f,I}$ formulation.

The normalised SIF's (K_I/σ_s) for the considered examples perfectly match the FE solution (Fig. 4.4e and 4.4f) and hold in general (Fig. 4.6). Regardless the non-monotonic $Y_{n,I}Y_{f,I}$ behaviour, (K_I/σ_s) remains monotonically increasing because of $\sqrt{\pi(a/t_p)}$ being involved. However, $K_I(M_{kn}Y_{f,I})/\sigma_s$ shows non-monotonic behaviour and includes even a singularity for $\{(a/t_p) \to 0\}$. Despite being explained as an higher order effect [112, 132], the contribution should be finite at most [114], suggesting fictitious behaviour.

4

MODE-III FORMULATION

Applying $\tau_{se}(r/t_p)$, the self-equilibrium stress part (Eq. 4.3), as unit crack face traction along the assumed virtual crack path using the weight function approach [138] provides for non-symmetry with respect to ($t_p/2$) and $\rho = 0$:

$$
Y_n = \left(\frac{2}{\pi}\right) \int_0^1 \frac{\tau_{se}\left(\frac{r}{a} \cdot \frac{a}{t_p}\right)}{\sqrt{1 - \left(\frac{r}{a}\right)^2}} \, d\left(\frac{r}{a}\right)
$$

$$
= \left(\frac{2}{\pi}\right) \left[\frac{\left(\frac{a}{t_p}\right)^{\lambda_\tau} \mu_{\tau F} \cos(\lambda_\tau \beta_a) \sqrt{\pi} \Gamma\left(\frac{\lambda_\tau}{2}\right)}{2\left(\frac{a}{t_p}\right) \Gamma\left(\frac{\lambda_\tau + 1}{2}\right)} - \frac{\left(\frac{C_{tw}}{2} + \mu_{\tau M}\right)\left(\frac{a}{t_p}\right)\left[\pi - 4\left(\frac{a}{t_p}\right)\right] \Gamma\left(\frac{\lambda_\tau + 1}{2}\right)}{2\left(\frac{a}{t_p}\right) \Gamma\left(\frac{\lambda_\tau + 1}{2}\right)} \right].
$$

(4.10)

Note that only half the C_{tw} value of the stress distribution (Eq. 4.10) is involved for the sake of fitting both the stress as well as the stress intensity. Formulations for symmetry with respect to ($t_p/2$) and $\rho > 0$ have been established as well (Appendix E). The far field stress distribution $\tau_{fe}(r/t_p) = \tau_s\{1 - 2r_{\tau s}(r/t_p)\}$ with $\tau_s = \tau_{ss} + \tau_{st}$ and $r_{\tau s} = \tau_{st}/\tau_s$ involves a superposition of a constant shear force and linear torsion moment induced component and applies principally to the far field factor as well:

$$
Y_{f,III}\left(\frac{a}{t_b}, r_{\tau s}\right) = Y_{fs} - r_{\tau s}(Y_{fs} - Y_{ft})
$$

(4.11)

with

$$
Y_{fs}\left(\frac{a}{t_b}\right) = \sqrt{\frac{2t_b}{\pi a} \tan\left(\frac{\pi a}{2t_b}\right)}
$$

(4.12)

being a handbook solution [140] and

$$
Y_{ft}\left(\frac{a}{t_b}\right) = \left(C_1\left(\frac{a}{t_b}\right)^4 + C_2\left(\frac{a}{t_b}\right)^3 + C_3\left(\frac{a}{t_b}\right)^2 + C_4\left(\frac{a}{t_b}\right) + C_5\right)
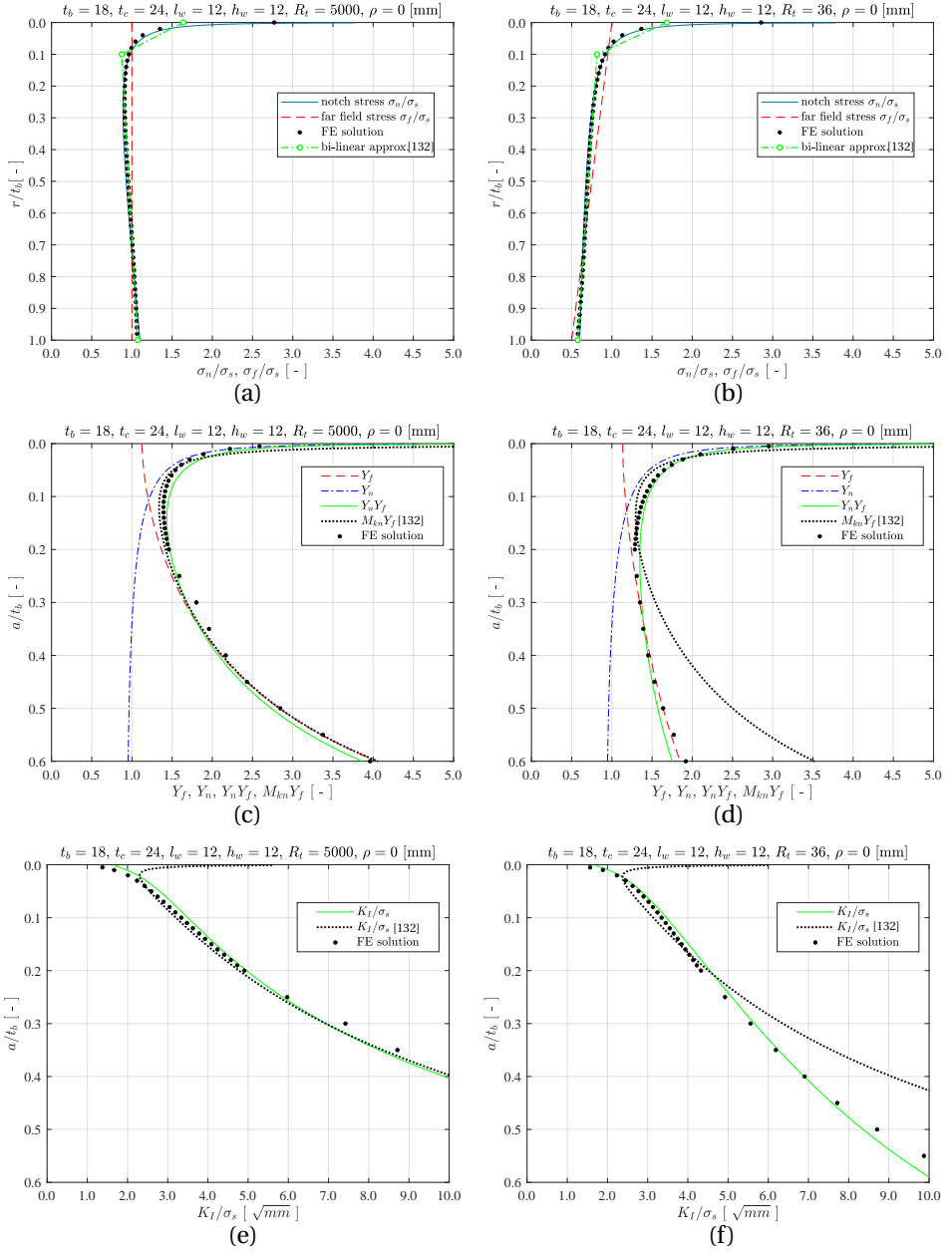$$

(4.13)

4

Figure 4.4.: Mode-I weld toe notch stress distribution (a, b), SIF far field- and notch distribution (c, d) and K_I distribution (e, f) for a DS welded T-joint; $r_{\sigma_s} = 0$ (a, c, e), $r_{\sigma_s} = 0.25$ (b, d, f).

including

$$C_1 = 9.6071\eta^4 - 67.0441\eta^3 + 197.6515\eta^2 - 212.0015\eta + 98.4731$$
$$C_2 = -15.5960\eta^4 + 108.8379\eta^3 - 320.8629\eta^2 + 344.1559\eta - 131.7393$$
$$C_3 = 8.8200\eta^4 - 63.3751\eta^3 + 196.7602\eta^2 - 244.8683\eta + 111.5116$$
$$C_4 = -1.6428\eta^4 + 11.0064\eta^3 - 32.5305\eta^2 + 41.1094\eta - 17.5662$$
$$C_5 = 0.0522\eta^4 - 0.2881\eta^3 + 0.7159\eta^2 - 0.9626\eta + 1.4579$$

a FE fitted formulation. Structural shear stress ratio $r_{\tau s} = t_b/(2R_t)$. The $Y_{f,III}(a/t_p, r_{\tau s})$ formulation is applicable for $\{1/2 \le (t_b/2R_t) \le 1/200\}$ and $\{0 \le (a/t_b) \le 1\}$ and hold asymptotically for planar structures.

For the same geometry and loading conditions, the increased weld notch stress affected region for mode-III in comparison to mode-I translates (Figs. 4.4 and 4.5a and 4.5b) one-to-one to the $Y_{n,III}Y_{f,III}$ distribution (Figs. 4.4 and 4.5c and 4.5d). The $Y_{n,III}$ controlled zone $\{1,2\}$ short crack region has increased to $\{0 < (a/t_p) \le 0.3\}$, meaning the $Y_{f,III}$ defined zone 3 long-crack region has decreased to $\{0.3 < (a/t_p) \le 1\}$. Different C_{tw} and $r_{\tau s}$ values shift the $Y_{n,III} - Y_{f,III}$ transition left or right. A good agreement with FE solutions is obtained.

Assuming the mode-{I, III} weld notch stress distribution characteristics are similar, the bi-linear approximation – including the transition location at $0.1(r/t_p)$ – does not change and the traction equivalent structural stress concept $M_{kn}(a/t_p)$ formulation is pretended to be the same as well. Handbook solutions are used to define the far field factor $Y_{f,III}$ [128]. However, comparing the mode-{I, III} results (Figs. 4.4 and 4.5c and 4.5d), the notch stress intensity has turned from a small $M_{kn}Y_{f,I}$ – into a significant $M_{kn}Y_{f,III}$ overestimate. Whereas for the stress distribution the transition location should change to a larger value, reflecting an enlarged short crack region, a smaller – contradictory – one seems required to provide a better intensity estimate; a consequence of the M_{kn} definition [16, 18, 132]. The overestimates in the long crack region are a consequence of the solid shaft $Y_{f,III}$ solution, being insufficient for hollow shafts; tubular structures, or even planar ones. Adopting $Y_{f,III}$ (Eq. 4.11) improves the far field estimate.

The (K_{III}/τ_s) solutions for the considered examples perfectly match the FE results (Fig. 4.5e and 4.5f), and hold in general (Fig. 4.6). Fictitious non-monotonic $K_{III}(M_{kn}Y_{f,III})/\tau_s$ behaviour for $\{(a/t_p) \to 0\}$ is observed up to a relatively large extent in comparison to the mode-I results, in particular for an unchanged transition location at $0.1(r/t_p)$.

4.3. Total stress assessment

For mixed mode-{I, III} multiaxial response conditions of planar and tubular maritime structures, the mode-I contribution is governing, meaning the normal stress is predominant (Chapter 1). At the same time, the fatigue lifetime of arc-welded joints is growth – rather than shear induced initiation – controlled because of the welding induced defects, explaining why a cracked geometry based fatigue strength parameter
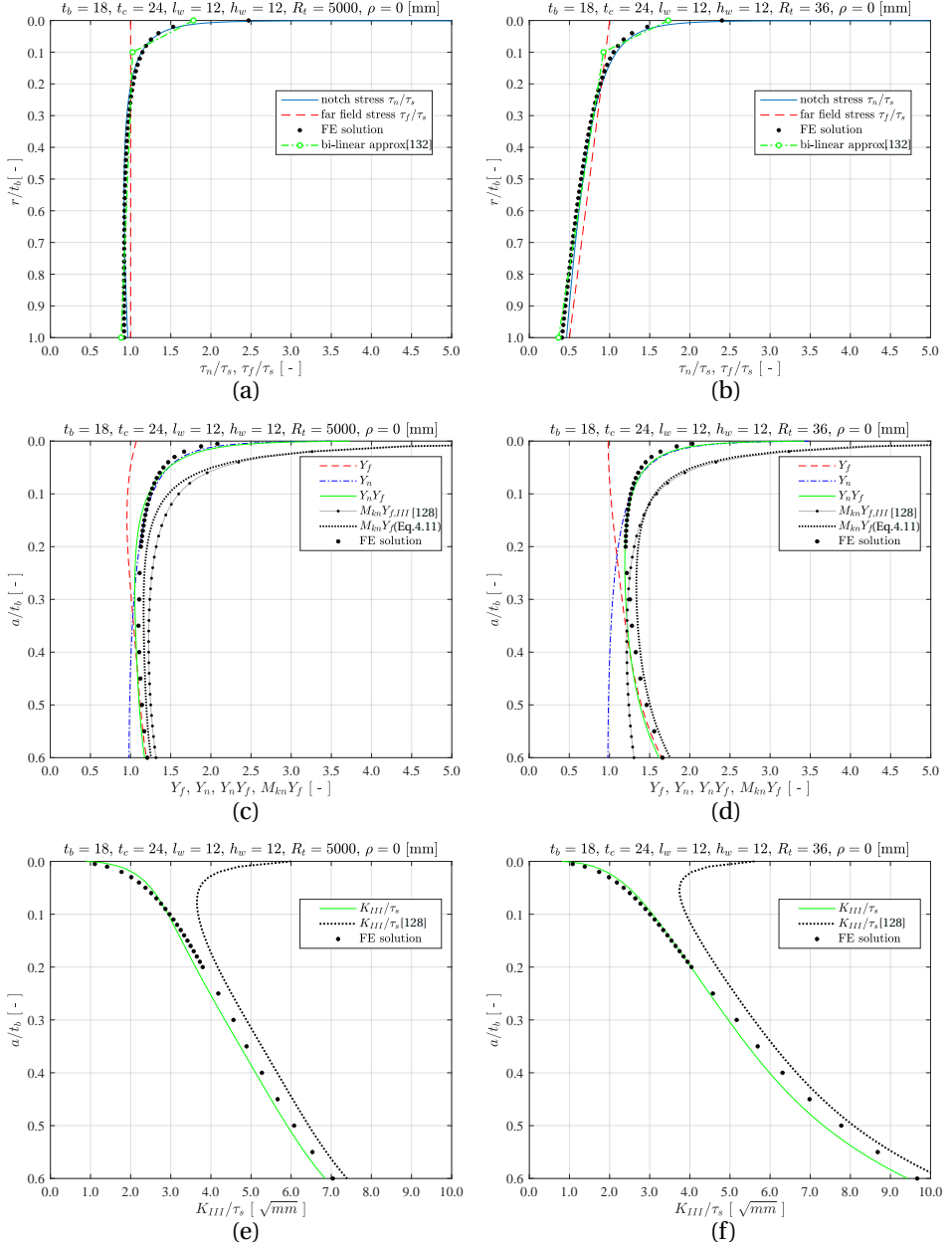
4

Figure 4.5.: Mode-III weld toe notch stress distribution (a, b), SIF far field- and notch distribution (c, d) and K_{III} distribution (e, f) for a DS welded T-joint; $r_{\tau_s} = 0$ (a, c, e), $r_{\tau_s} = 0.25$ (b, d, f).
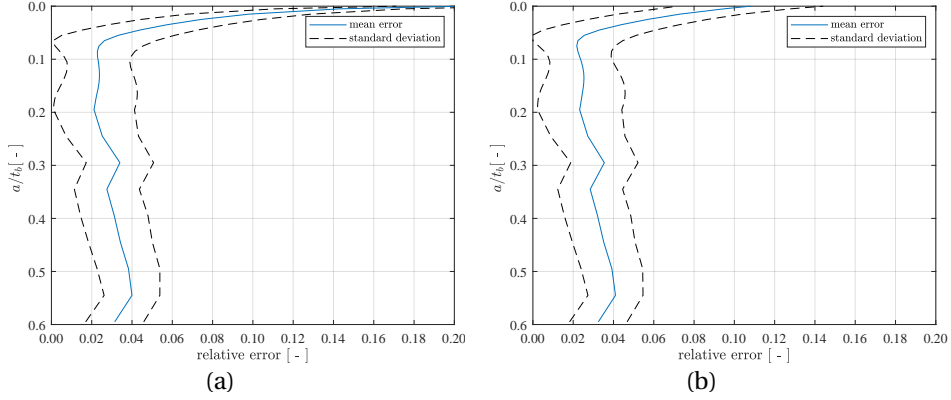
Figure 4.6.: Relative K_I (a) and K_{III} (b) error for DS welded T-joint, comparing the FE solutions and the analytical results for the full parameter application range.

will be adopted to establish a normal stress equivalent von Mises type of failure criterion [130]. Involving the stress intensity distributions at the critical fracture plane (Section 4.2), the total stress parameter $S = S_T = \sqrt{S_{T,I}^2 + \beta(N)S_{T,III}^2}$ will be established first (Section 4.3.1), including a lifetime dependent shear stress coefficient $\beta(N)$. Cycles will be counted – because of the time domain approach – in the von Mises plane, in order to be able to incorporate non-proportionality cycle-by-cycle. The linear damage accumulation model will be used, since good performance has been shown for advanced fatigue strength criteria [18]. Using mid-cycle fatigue test data from literature (Section 4.3.2) the strength and mechanism contributions, reflected in respectively mode specific $\{\log(C), \gamma\}$ and $\{m, n\}$ coefficients, will be investigated (Section 4.3.3).

4.3.1. FATIGUE STRENGTH PARAMETER

Cyclic loading induced response conditions turn the SIF's $\{K_I, K_{III}\}$ into crack growth driving forces $\{\Delta K_I, \Delta K_{III}\}$ and defects may develop into cracks. The crack growth rate $(\mathrm{d}a/\mathrm{d}n)$ of short-cracks emanating at notches show elastoplastic wake field affected anomalies [18]. Modifying Paris' equation, a generalised two-stage model has been established containing a transition; a natural pivot rather than a mathematical one [141, 142] from a short to a long crack growth region meant to incorporate all relevant crack growth driving force components [143–145]; i.e. to include both the weld notch- and far field characteristic mode-I response contributions: $(\mathrm{d}a/\mathrm{d}n)_I = C_I \cdot Y_{n,I}^{n_I} \cdot \{\Delta\sigma_{s,eff} \cdot Y_{f,I} \cdot \sqrt{(\pi a)}\}^{m_I}$. Notch elastoplasticity coefficient n_I is response dependent and defines the level of monotonically increasing or non-monotonic crack growth behaviour (Fig. 4.7), in contrast to a fixed value in a similar model: $(\mathrm{d}a/\mathrm{d}n)_I' = C \cdot M_{kn}^n \cdot \{\Delta\sigma_{s,eff'} \cdot Y_{f,I} \cdot \sqrt{(\pi a)}\}^m$ with $n = 2$, assuming response invariant non-monotonic behaviour [6, 132, 146, 147].

Since welding induced residual stress affects n_I, as-welded (AW) joint fatigue resistance data is typically used to obtain an average estimate, rather than crack growth data obtained using standard specimens geometries like the compact tension configuration [14]. Recognising that a spatial description of a loading induced response cycle requires two parameters, e.g. range $\Delta\sigma_s$ and ratio $R_I = (\sigma_{s,min}/\sigma_{s,max})$ reflecting a mean stress effect, Walker's model has been adopted [14, 16, 58]. The stress range becomes an effective one: $\Delta\sigma_{s,eff} = \Delta\sigma_s / \{(1-R_I)\}^{1-\gamma}$ with $0 \le \gamma \le 1$. For $\gamma \to 1$, the nominal stress range $\Delta\sigma_s$ dominates the fatigue resistance; the mean stress becomes governing for $\gamma \to 0$. Assuming mean stress affects predominantly the notch region [146, 147], $\Delta\sigma_{s,eff'} = \Delta\sigma_s / \{(1-R_I)\}^{n(1-\gamma)/m}$. Mean stress coefficient $\gamma = 0.5$ for $R_\sigma \le 0$ and reflects an equal contribution of the stress range $\Delta\sigma_s$ and max stress $\sigma_{s,max} = \Delta\sigma_s/(1-R_I)$; $\gamma = 0$ for $R_\sigma < 0$ meaning only $\Delta\sigma_s^+$ is considered to contribute effectively. Incorporating the welding induced residual (mean) stress distribution as well – if available, a different interpretation seems to apply and R_I turned into a crack length dependent far field stress intensity contribution: $\Delta\sigma_{s,eff'} = \Delta\sigma_s / \{1 - R_{Ir}(a/t_p)\}^{1-\gamma}$ with $R_{Ir}(a/t_p) = [K_I(\sigma_{s,max}, a/t_p) + K_I\{\sigma_r(a/t_p), a/t_p\}] / [K_I(\sigma_{s,min}, a/t_p) + K_I\{\sigma_r(a/t_p), a/t_p\}]$ and $\gamma = 0.5$ for any $R_{Ir}(a/t_p)$ [148].

Crack growth behaviour at notches for a mode-III response as often observed is monotonically increasing [127, 149–154]. However, some evidence for non-monotonic crack growth is available as well [155–157], principally justifying a mode-I model similarity: $(da/dn)_{III} = C_{III} \cdot Y_{n,III}^{n_{III}} \cdot \{\Delta\tau_{s,eff} \cdot Y_{f,III} \cdot \sqrt{(\pi a)}\}^{m_{III}}$. Non-monotonicity becomes more pronounced for a small notch radius ($\rho \to 0$), a large amplitude – negative ratio characterised response $\{\tau_s \to \tau_y, R_{III} < 0\}$ and a plane stress condition, supporting large scale yielding [18].

For crack growth in mixed mode-{I, III} conditions an equivalent stress intensity can be adopted, typically similar to equivalent stress formulations [130], either a linear one of the Tresca type: $\Delta K_{eq} = C_I \cdot K_I + C_{III} \cdot K_{III}$ or a non-linear one of the von Mises type: $\Delta K_{eq} = \sqrt{(C_I \cdot K_I)^2 + (C_{III} \cdot K_{III})^2}$ [127, 137, 152–154, 157–165]. Even higher order non-linear formulations haven been proposed and some contain coupling terms to incorporate interaction effects [137, 161, 162]. However, because of the $S_{eq} - \Delta K_{eq}$ formulation similarity, an equivalent stress S_{eq} [130] rather than an equivalent stress intensity ΔK_{eq} will be adopted as fatigue strength parameter, aiming for a mixed mode-{I, III} $S_{eq} - N$ fatigue resistance – rather than a $\Delta K_{eq} - (da/dn)$ crack growth relation.

Applying an integral operator on the individual mode-{I, III} crack growth models provides mid-cycle fatigue related resistance relations of the Basquin type: $\log(N_j) = \log(C_j) - m_j \log(S_{T,j})$ with $j = \{I, III\}$, correlating the fatigue life time N_i and a total stress fatigue strength parameter [6, 14, 16, 18]:

$$S_{T,j} = \frac{S_j}{\left(1 - R_j\right)^{1-\gamma} \cdot I_{N,j}^{\frac{1}{m_j}} \cdot t_p^{\frac{2-m_j}{2m_j}}} \tag{4.14}$$
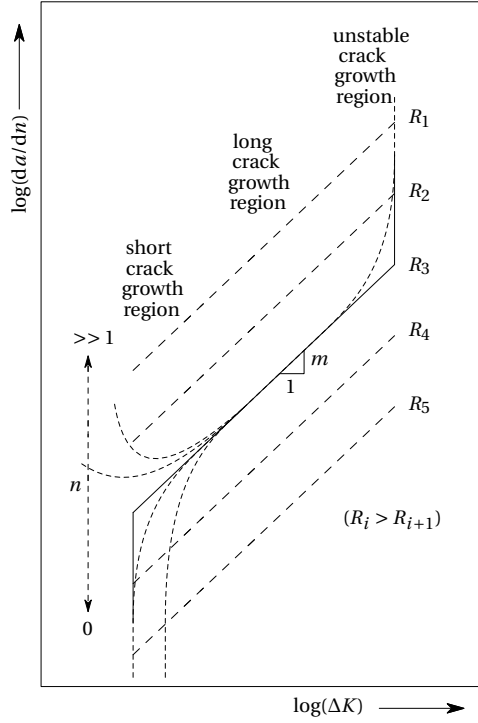
Figure 4.7.: Elastoplasticity and mean stress effects in the short and long crack growth region.

with

$$I_{N,j} = \int\limits_{\frac{a_i}{t_p}}^{\frac{a_f}{t_p}} \frac{1}{\left\{Y_{n,j}\left(\frac{a}{t_p}\right)\right\}_j^n \cdot \left\{Y_{f,j}\left(\frac{a}{t_p}\right)\right\}_j^m \cdot \left(\frac{a}{t_p}\right)^{\frac{m_j}{2}}} \, \mathrm{d}\left(\frac{a}{t_p}\right),$$

$S_1 = \Delta\sigma_s$ and $S_2 = \Delta\tau_s$. Scaling parameter $t_p^{(2-m_j)/2m_j}$ takes the response gradient induced size effects into account. Rather than a sufficiently small (a_i/t_p) providing a converged notch crack growth integral solution $I_{N,j}$, an arc-welding induced most likely material characteristic defect size estimate has been established; $(a_f/t_p) = 1$ is based on a through-thickness crack criterion.

An environment and service loading induced mean stress component as reflected in $\{R_I, R_{III}\}$ is in general not the only one, since arc-welding adds a thermal loading induced – typically high-tensile – quasi-constant residual (mean) stress, affecting the fatigue strength. An explicit residual stress measure is typically not included, since

for fatigue design in general only joints in AW condition are considered [33, 34, 114], meaning any residual stress affecting the fatigue resistance is just implicitly incorporated in the most likely fatigue resistance parameter estimates. A stress relieving heat treatment can be applied, being one way to virtually eliminate residual stress and improve the fatigue strength. If both AW and stress-relieved (SR) test data are jointly considered, an explicit residual stress measure S_r – an average estimate, since the actual distribution is typically unknown – will be introduced to represent the thermal condition, meaning a re-formulation of the response ratio is required:

$$R_{Ir} = \frac{S_{T,I,min} + S_r}{S_{T,I,max} + S_r} = \frac{R_I \cdot S_{T,I} + S_r(1 - R_I)}{S_{T,I} + S_r(1 - R_I)} \tag{4.15}$$

$$R_{IIIr} = \frac{S_{T,III,min} + S_r}{S_{T,III,max} + S_r} = \frac{R_{III} \cdot S_{T,III} + S_r(1 - R_{III})}{S_{T,III} + S_r(1 - R_{III})}. \tag{4.16}$$

Since a stress relieving heat treatment affects the grain size and local yielding properties [130], a dedicated elastoplasticity coefficient n will be needed for the AW and SR conditions.

Because of the mode-I and mode-III finite life time specific strength and mechanism fatigue resistance characteristics, a response level dependent shear strength coefficient $\beta(N)$ – rather than a constant one – can be defined for a single-slope resistance relation $N = C \cdot S_T^m$ in the mid-cycle fatigue region [130]:

$$\beta(N) = \frac{S_{T,I}(N)}{S_{T,III}(N)} = C_\beta \cdot N^{M_\beta} \tag{4.17}$$

with

$$C_\beta = 10^{\frac{\log(C_I)m_{III} - \log(C_{III})m_I}{m_I \cdot m_{III}}}$$

and

$$M_\beta = \frac{m_I - m_{III}}{m_I \cdot m_{III}}.$$

Since only the uniaxial mode-{I, III} number of cycles $\{N_I, N_{III}\}$ are known in advance, the actual $\beta(N)$ value has to be obtained in an iterative cycle counting process in order to capture N for the equivalent normal stress based von Mises type of criterion:

$$S_T = \sqrt{\left\{ S_{T,I}^2 + \beta(N) \cdot S_{T,III}^2 \right\}}. \tag{4.18}$$

Counting iteratively the effective von Mises notch stress (Fig. 4.8) at the critical fracture plane (Section 4.2), the range $S_{T,i}$ including the normal and equivalent shear stress projections $\{S_{T,I,i}, \beta(N) \cdot S_{T,III,i}\}$ and corresponding ratios $\{R_I = S_{T,I,min,i}/S_{T,I,max,i}, R_{III} = \beta(N) \cdot S_{T,III,min,i}/\beta(N) \cdot S_{T,III,max,i}\}$ can be obtained for each cycle i. Adopting a 0th, 1st or 2nd order moment approach, differences between the actual response path and the (straight) range have been used to incorporate a non-proportionality effect cycle-by-cycle in terms of C_{np}, including a material characteristic contribution in terms of c_m [79, 80, 85, 94, 130]:

$$S_{T,eff,i} = S_{T,i} \left(1 + c_m \cdot C_{np,i}\right) \tag{4.19}$$

with

$$C_{np,i} = \frac{\int_{\tilde{S}} (r \cdot |\sin(\theta)|)^n \mathrm{d}p}{\int_{S} (R \cdot |\sin(\theta)|)^n \mathrm{d}p} \quad \text{for } n = 0, 1 \text{ or } 2. \tag{4.20}$$
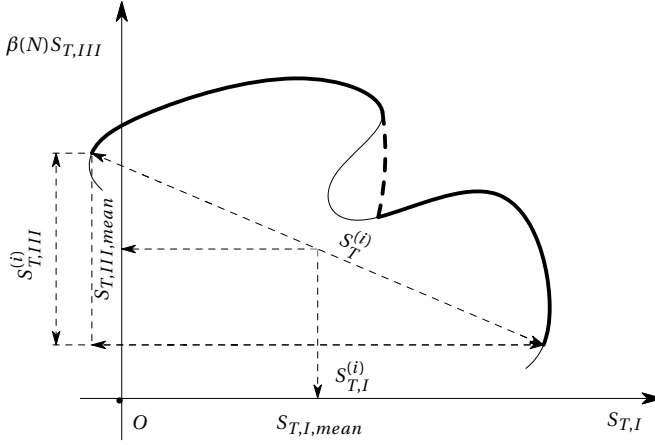
Figure 4.8.: Total stress cycle characteristics in the von Mises plane.

Although $C_{np,i}$ and c_m are meant to reflect respectively the path and material characteristic part, c_m may correct for any cycle counting and/or non-proportionality related model deficiency as well, since data fitting is used to obtain an estimate. A compromised value may be acquired, meaning interpretation becomes more difficult. In order to obtain a mid-cycle fatigue related equivalent total stress parameter $S_{T,eq}$ for variable amplitude (VA) data fitting the constant amplitude (CA) data scatter band; i.e. $N(S_T) = C \cdot S_T^{-m}$ with $S_T = S_{T,eq}$, the linear damage model is adopted: $D = \sum \{n_i(S_{T,i})/N_i(S_{T,i})\} \le 1$ with $N_i(S_{T,i}) = C \cdot S_{T,i}^{-m}$. For $D = 1$, reflecting failure, the formulation becomes:

$$S_{T,eq} = \left[\frac{\sum \{n_i(S_{T,eff,i}) \cdot S_{T,eff,i}^m\}}{N} \right]^{1/m}. \tag{4.21}$$

Similarly, applying an integral operator to the $(\mathrm{d}a/\mathrm{d}n)_{I'} = C \cdot M_{kn}^2 \cdot \{\Delta\sigma_{s,eff'} \cdot Y_{f,I} \cdot \sqrt{(\pi a)}\}^m$ mode-I crack growth relation [132, 146, 147] provides a master curve formulation: $\log(N_I) = \log(C_I) - m_I \log(S_{t,I})$ with $S_{t,I} = \Delta\sigma_s/\{(1 - R_\sigma)^{2(1-\gamma)/m} \cdot I_{N,I'}(r_{\sigma s})^{1/m_I} \cdot t_p^{(2-m_I)/2m_I}\}$. The crack growth integral $I_{N,I'}(r_{\sigma s})^{1/m_I} = \left[\int 1/M_{kn}^2(a/t_p) \cdot Y_{f,I}(a/t_p, r_{\sigma s})^{m_I} \cdot (a/t_p)^{m_I/2} \mathrm{d}(a/t_p)\right]^{(1/m_I)}$ is approximated using a 6th order polynomial for engineering purposes [131]. Provided $r_{\sigma s} = |\Delta\sigma_{sb}|/(|\Delta\sigma_{sm}| + |\Delta\sigma_{sb}|)$ [131, 166, 167], non-monotonic weld notch stress dis-

tributions [14, 16] are not considered since the formulation provides only $r_{\sigma s} \geq 0$ values. Because of the fixed notch governing to far field dominated transition location, the considered weld notch load carrying level is the same for all. Rather than an arc-welding induced most likely material characteristic defect size estimate, $(a_i/t_p) = 10^{-3}$ has been adopted providing a converged $I_{n,I'}(r_{\sigma s})^{1/m_I}$ solution; $(a_f/t_p) = 1$ is based on a through-thickness crack criterion. Whereas for SR welded joints in steel structures $\Delta\sigma_{s,eff'}$ is considered, for AW ones mean stress effects are not taken into account and $\Delta\sigma_{s,eff'} \rightarrow \Delta\sigma_s$, reducing the mode-I traction equivalent structural stress to $S_{t,I} = \Delta\sigma_s/\{I_{N,I'}(r_{\sigma s})^{1/m} \cdot t_p^{(2-m)/2m}\}$ [131, 137].

Mode-III crack growth at notched geometries seems not investigated. However, a traction equivalent structural shear stress formulation has been established, assuming the non-monotonic behaviour as identified for mode-I still holds: $S_{t,III} = \Delta\tau_s/\{I_{N,III'}(r_{\tau s})^{1/m_{III}} \cdot t_p^{(2-m_{III})/2m_{III}}\}$. A 4th order polynomial has been established [128, 136] to approximate the notch crack growth integral $I_{N,III'}(r_{\tau s})^{1/m_{III}} = [\int 1/\{M_{kn}^2(a/t_p) \cdot Y_{f,III}(a/t_p, r_{\tau s})^{m_{III}} \cdot (a/t_p)^{m_{III}/2}d(a/t_p)\}]^{1/m_{III}}$ involving the solid shaft $Y_{f,III}$ solution (Section 4.2.2) [128, 136] and is applicable for monotonic weld notch shear stress distributions only: $r_{\tau s} = |\Delta\tau_{st}|/(|\Delta\tau_{ss}| + |\Delta\tau_{st}|)$. Slope $m_{III} = 5$ has been postulated. Using the improved far field factor $Y_{f,III}$ formulation (Eq. 4.11), $I_{N,III'}(r_{\tau s})^{1/m_{III}}$ has been re-established and a revised polynomial approximation is proposed. The notch characteristics (Section 4.2) have not been changed, meaning the transition size is assumed to be the same as for mode-I.

For mixed mode-{I, III} multiaxial fatigue, a von Mises type of equivalent stress formulation has been adopted, defined at the critical fracture plane (Section 4.2):

$$S_t = \sqrt{(S_{t,I}^2 + \beta \cdot S_{t,III}^2)} \tag{4.22}$$

with

$$S_{t,I} = \Delta\sigma_s/\{(1 - R_\sigma)^{2(1-\gamma)/m} \cdot I_{N,I'}(r_{\sigma s})^{1/m_I} \cdot t_p^{(2-m_I)/2m_I}\},$$

$$I_{N,I'}(r_{\sigma s})^{1/m_I} \approx 0.0011 \cdot r_{\sigma s}^6 + 0.0767 \cdot r_{\sigma s}^5 - 0.0988 \cdot r_{\sigma s}^4 + 0.0946 \cdot r_{\sigma s}^3 q + 0.0221 \cdot r_{\sigma s}^2 +$$
$$0.014 \cdot r_{\sigma s} + 1.2223,$$

$$S_{t,III} = \Delta\tau_s/I_{N,III'}(r_{\tau s})^{1/m_{III}} \cdot t_p^{(2-m_{III})/2m_{III}},$$

$$I_{N,III'}(r_{\tau s})^{1/m_{III}} \approx 1.4131 \cdot r_{\tau s}^4 - 1.0448 \cdot r_{\tau s}^3 + 1.0264 \cdot r_{\tau s}^2 + 0.7087 \cdot r_{\tau s} + 1.4244$$

and $\beta = 3$; a constant rather than a response level dependent one, explaining why fatigue resistance data analysis for welded joints in steel structures provided an average slope value $m \sim 4$ [79, 128, 168, 169] in between $m_I \sim 3$ and $m_{III} \sim 5$. Another track has been developed as well. Because well-established mode-III short and long crack growth data is lacking, $S_t = \Delta\sigma_{s,vM}/\{I_{N,I'}(r_{s,vM})^{1/m_I} \cdot t_p^{(2-m_I)/2m_I}\}$ with $\Delta\sigma_{s,vM} = \sqrt{(\Delta\sigma_s^2 + \beta \cdot \Delta\tau_s^2)}$, $r_{s,vM} = \sqrt{(\Delta\sigma_{sb}^2 + \beta \cdot \Delta\tau_{st}^2)}/\{\sqrt{(\Delta\sigma_{sm}^2 + \beta \cdot \Delta\tau_{ss}^2)} + |\Delta\sigma_{sb}|\}$ and $\beta = 3$ has been proposed, assuming the crack growth behaviour is mode-I dominated [55, 137]. If mode-III contributions become more important, deviations can be expected.

Cycles are counted in the $S_{t,I} - \beta S_{t,III}$ or $\sigma_s - \beta \tau_s$ plane [55, 79, 128, 137] for the proposed S_t formulations – respectively incorporating full- or just partial far field fatigue strength information and includes cycle-by-cycle non-proportionality measures [79, 80, 85, 94].

In order to obtain an equivalent stress parameter $S_{t,eq}$ for VA data fitting the CA data scatter band, the linear damage model is adopted: $D = \sum \{n_i(S_{t,i}) \cdot S_{t,i}^m / N_i(S_{t,i})\}$. For $D = 1$, the formulation becomes: $S_{t,eq} = [\sum \{n_i(S_{t,i})/N\}]^{1/m}$ with $N = \sum \{n_i(S_{t,i})\}$ the total number of counted von Mises cycles.

4.3.2. TEST DATA

Data series containing steel specimens with both tubular and planar structural joints have been considered (Fig. 3.7 and Tables 3.1 and 3.2) – the same as used to investigate the effective notch stress performance [130], involving respectively circular/square hollow and plate cross-sections with specified joint dimensions (Fig. 4.1). Most data is obtained for CA loading conditions, but some VA data is included as well. Uniaxial mode-I, uniaxial mode-III and multiaxial mode-{I, III} response conditions – both P and NP – have been introduced at the governing fatigue sensitive locations: single sided (SS) welded butt joints and DS welded T-joints, as well as DS welded cruciform joints showing respectively non-symmetry and symmetry with respect to $(t_p/2)$ [16, 18, 29]. The governing hot spot is typically of the type C along the weld seam, although some of the type A at the weld end exist as well. Only specimens showing weld toe induced fatigue damage are included, involving predominantly failures and some run-outs. The data size is ~ 500.

The external loading consists of a normal force F_n or bending moment M_b for the mode-I response and a shear force F_s or torsion moment M_t for the mode-III response, obtained using FE shell models (Section 4.2.1). Multiaxiality is often either loading [15, 49–51, 53, 54, 56, 82, 119, 120, 122] or geometry [121, 123–125] induced. In case a mode-I and mode-III response related external loading component (e.g. M_b and M_t) are applied and at the same time the specimen contains a non-circular cross-section and warping constraints, multiaxiality includes even both a loading and geometry contribution [54, 56]. The response is proportional by definition if multiaxiality is a result of geometry only. The response ratio $R = 0$ for the majority of the data series, reflecting a pulsating loading induced response condition with non-zero mean. For a significant amount of data $R = -1$, meaning the response condition is fully reversed and the mean component is zero. For the remaining data series, $R \neq \{0; -1\}$. Since data with both AW and SR thermal conditions are considered, the influence of (mean) residual stress has to be addressed as well. A von Mises based structural stress fatigue assessment of the adopted test data (Fig. 3.7 and Tables 3.1 and 3.2) shows the initial data scatter and the clear distinction between CA and (maximum range) VA results [130].

4.3.3. STRENGTH AND MECHANISM CONTRIBUTIONS

The life time range of the considered data (Fig. 3.7 and Tables 3.1 and 3.2) virtually reflects mid-cycle fatigue characteristics only: $N = (10^4 \sim 5 \cdot 10^6)$ cycles. A log-log

linear resistance formulation of the Basquin type typically relates N to a fatigue strength parameter S [14]: $\log(N) = \log(C) - m \cdot \log(S)$. Linear regression on life time is adopted to estimate the single-slope curve parameters: intercept $\log(C)$ and slope m, respectively reflecting a strength and mechanism contribution, introducing the life time scatter (i.e. performance) parameter σ_N. For strength performance evaluation purposes, the scatter band index $T_{\sigma S} = 1 : (S_{10}/S_{90})$ will be used: the fatigue strength ratio for 10[%] and 90[%] probability of survival [111]. Maximum likelihood based regression [18, 57] will be employed to obtain the most likely parameter vector estimate $\Phi : \max \mathscr{L}(\Phi; N|S)$ with $\Phi = \{\log(C), m, \sigma_N\}$, assuming fatigue lifetime N is most likely log-Normal distributed [16, 29]. For $S = S_{T,eff}$ (Section 4.3.1), the response ratio coefficient and material characteristic elastoplasticity coefficient providing respectively another strength and mechanism contribution are introduced, principally extending the parameter vector to: $\Phi = \{\log(C), \gamma, m, n, \sigma_N\}$. Note that ideally the uniaxial mode-I and mode-III, as well as the multiaxial P and NP mode-{I, III} data (Fig. 3.7 and Tables 3.1 and 3.2) would have been balanced for appropriate $S_{T,eff}$ performance evaluation, meaning that except the σ_N and $T_{\sigma S}$ parameters as global indicators for all data, the individual data groups behaviour have to be carefully considered as well. Starting with the uniaxial reference fatigue resistance in terms of $S_{T,eff}$, the mode specific strength and mechanism coefficients will be established first (Section 4.3.3) in order to obtain $\beta(N)$. The $S_{T,eff}$ performance for multiaxial fatigue resistance data will be investigated accordingly (Section 4.3.3), in comparison to $S_{e,eff}$ and S_t. Particular attention will be paid to the consequences of mode specific strength and mechanism for mixed mode-{I, III} fatigue and the influence of non-proportionality. Since $S_{T,eff}$ is an equivalent normal stress von Mises type of parameter, the fitting of the multiaxial data in the mode-I uniaxial data scatter band will be verified, as well as the fitting of VA data in the CA data scatter band in order to establish the performance of the adopted linear damage accumulation model for a $S_{T,eff}$ based fatigue assessment.

UNIAXIAL REFERENCE FATIGUE DATA

The $S_{T,eff}$ based mode-I mid-cycle fatigue resistance formulation for planar structures in steel (maritime) structures, involving hot spots type {A, B, C} and various AW joint geometries, has already been established for CA data [126] and shows excellent performance as reflected in the life time standard deviation: $\sigma_N = 0.21$. The intercept and slope as strength and mechanism parameters are: $\log(C_I) \sim 13.05$ and slope $m_I \sim 3.15$. Note that the slope is close to the typical design value $m = 3$ [33, 34]. Response ratio coefficient $\gamma_{I,AW} \sim 0.89$ for the full R_I range implies a predominant contribution of stress range over mean stress. For an average most likely initial crack size $(a_i/t_p) = 0.006$ and final crack size $(a_f/t_p) = 1$ – representing a through-thickness crack (Section 4.2) – and real notch radius $\rho = 0$ (Fig. 4.7), a most likely $n_{I,AW} \sim 3.48$ has been obtained, reflecting notch and/or crack tip elastoplasticity induced non-monotonic crack growth behaviour (Fig. 4.7). Both $\gamma_{I,AW}$ and $n_{I,AW}$ are welding induced high-tensile residual stress affected. Since the data size of the considered (predominant) tubular and (some) planar mode-I data (Fig. 3.7 and Tables 3.1 and 3.2) is ~ 140, relatively small in comparison to

Table 4.1.: Total stress based parameter estimates and 75[%] lower and upper parameter confidence bounds for mode-I and mode-III.

parameter	mode-I		mode-III			
			$\rho = 0$		$\rho > 0$	
$\log(C)$	13.05	[12.97, 13.13]	17.77	[17.11, 18.43]	16.46	[15.90, 17.02]
m	3.15	[3.11, 3.18]	4.82	[4.46, 5.18]	5.02	[4.67, 5.37]
n	/	/	9.00	[4.17, 13.83]	3.12	[1.14, 5.09]
n_{AW}	3.48	[3.28, 3.68]	/	/	/	/
n_{SR}	0.09	[0.01, 0.17]	/	/	/	/
γ	/	/	1.00	[0.98, 1.00]	1.00	[0.98, 1.00]
γ_{AW}	0.89	[0.88, 0.91]	/	/	/	/
γ_{SR}	0.95	[0.93, 0.98]	/	/	/	/
S_r	-113	[-115, -110]	/	/	/	/
σ_N	0.30	[0.26, 0.33]	0.25	[0.22, 0.28]	0.21	[0.18, 0.24]
σ_N incl.[126]	0.22	[0.19, 0.24]	/	/	/	/

the ~ 2500 assessed before [126], enforcing $\log(C_I) \sim 13.05$, $m_I \sim 3.15$, $\gamma_{I,AW} \sim 0.89$ and $n_{I,AW} \sim 3.48$ seems straightforward from parameter confidence perspective. A previous fatigue resistance investigation based on the effective notch stress S_e [130]; an intact geometry fatigue strength parameter, revealed that distinguished material dependent strength and mechanism contributions for AW and SR thermal conditions are required, suggesting dedicated $\{\gamma_{I,SR}, n_{I,SR}\}$ estimates should be assigned. At the same time, an explicit residual stress measure S_r is introduced for the SR data since AW and SR data are jointly considered, meaning the response ratio R_{Ir} rather than R_I should be adopted (Section 4.3.1). The parameter vector becomes: $\Phi = \{S_{r,I}, \gamma_{I,SR}, n_{I,SR}, \sigma_{N,I}\}$. Regression analysis shows the AW and SR data (Fig. 3.7 and Tables 3.1 and 3.2) turns out to fit in the reference AW data scatter band (Fig. 4.9), suggesting strength and mechanism contributions are sufficiently covered. The most likely residual stress estimate S_r (Fig. 4.9 and Table 4.1) proved to be compressive (Section 4.3.1), confirming the (average) residual stress for the AW data is highly tensile indeed. Note $S_{r,I}$ is a total stress rather than a structural stress value (Section 4.3.1), meaning a one-to-one comparison to the S_e based $S_{r,I}$ value [130] is not possible. Surprisingly, the residual mean stress coefficient $\gamma_{I,SR}$ has become about equal to the AW value $\gamma_{I,AW}$ – although for the S_e based fatigue resistance assessment the same behaviour is observed, meaning the stress range contribution dominates anyway. The $n_{I,SR} \sim 0.09$ estimate (Fig. 4.9 and Table 4.1) turns out to be smaller than the AW value as expected and reflects soft monotonically increasing crack growth behaviour (Fig. 4.7) – close to log-log-linear behaviour in the Paris defined long-crack growth region and correlates to a predominant elastic notch and/or crack tip response as a consequence of eliminated residual (mean) stress. At the same time, a stress-relieving heat treatment decreases the hardness and supports ductile material behaviour, improving the elastic material capacity. However, since the amount of SR data is just ~ 3 [%] of the total size, data balance is lost, meaning $n_{I,SR}$ is likely compromised up to some extent in order to enforce an AW data fit. The life time scatter of the considered data (Fig. 3.7 and Tables 3.1 and 3.2) in

terms of $\sigma_{N,I}$ is somewhat large and seems at least partially a matter of data size as reflected in the parameter confidence (Table 4.1). The corresponding strength scatter band index $T_{\sigma_{S_T}} = 1 : 1.77$ and turns out to be larger than a typical value of $1 : 1.50$ [20]. In comparison to S_e [130], the S_T performance is slightly worse.

At first glance, the VA data fits the CA data scatter band for $D = 1$, supporting the hypothesis that advanced fatigue damage criteria – including the mean stress as an important sequence parameter in terms of R and γ – contributes to the (linear) damage accumulation model performance.

The mode-III mid-cycle fatigue resistance for (predominantly) tubular steel (maritime) structures principally involves hot spots type C and a DS welded T-joint geometry only (Fig. 3.7 and Tables 3.1 and 3.2). The data size is ∼ 50. Since the (as) weld(ed) toe notch radius is a stochastic variable along the weld seam and quite small [82], $\rho = 0$ is typically adopted. However, S_e based investigations [130] suggest that the actual ρ value is important, explaining why regression analysis will be performed for the the $\rho > 0$ case. For reference purposes, $\rho = 0$ results will be provided as well. Since notch radius information is often not available (Tables 3.1 and 3.2), $\rho \sim 1.3$ [mm] has been selected as most likely – average – estimate for the data sets with unknown ρ, following previous investigations [29]. Mean stress effects are hardly observed [130], implying differences in fatigue resistance for AW and SR test data is not expected and the parameter vector $\Phi = \{\log(C_{III}), m_{III}, n_{III}, \sigma_{N,III}\}$ is considered to be sufficient.

The obtained most likely intercept and slope, $\log(C_{III}) \sim 16.46$ and $m_{III} \sim 5.02$, are different from the mode-I values (Fig. 4.9 and Table 4.1), proving different strength and mechanism contributions. Note m_{III} is similar for the $\rho = 0$ and $\rho > 0$ case and close to a typical design value of 5 [33, 34]. Elastoplasticity coefficient n_{III} for $\rho = 0$ is relatively large – even unrealistic – in comparison to the $\rho > 0$ value since notch elastoplasticity increases for decreasing ρ. An interesting observation is that $n_{III} \sim 3.12$ for $\rho > 0$; close to the mode-I value for $\rho = 0$, although the parameter confidence interval is relatively large (Table 4.1). The parameter confidence bounds suggest that crack growth behaviour can still range from monotonically increasing to non-monotonic (Fig. 4.7). Most likely the limited variation in data properties as well as the data size are the main reasons. Similar to the S_e based assessment [29], the life time scatter parameter values for $\rho = 0$ and $\rho > 0$ illustrate why the actual notch radius (at the surface) should be included: $\sigma_{N,III}$ reduces from ∼ 0.25 to ∼ 0.21, supporting the hypothesis that the mode-III fatigue damage process might even be more a near-surface phenomenon than for mode-I. Considering the type of loading and geometry reveals a volume (i.e. weld seam length) effect and could partially explain why $\sigma_{N,III}$ turns out to be relatively small in comparison to $\sigma_{N,I}$ [130]. For the mode-I data on the one hand, most specimens are subjected to a bending moment M_b and have a tubular, circular hollow cross-section (Fig. 3.7). The governing hot spot and most likely fatigue failure position is observed at one location along the weld seam, principally independent of the fabrication aspects induced weakest link; a matter of production tolerances and welding induced defects. On the other hand, for the mode-III data a torsion moment M_t is typically applied and for tubular, circular hollow cross-sections all locations along the weld seam are

identified as hot spot. Fatigue failure develops at the position of the fabrication defined weakest link, like the location of the welding induced extreme defect. The mode-III fatigue strength scatter band index $T_{\sigma S_T} = 1 : 1.28$ is smaller than a typical value of $1 : 1.50$ [20].
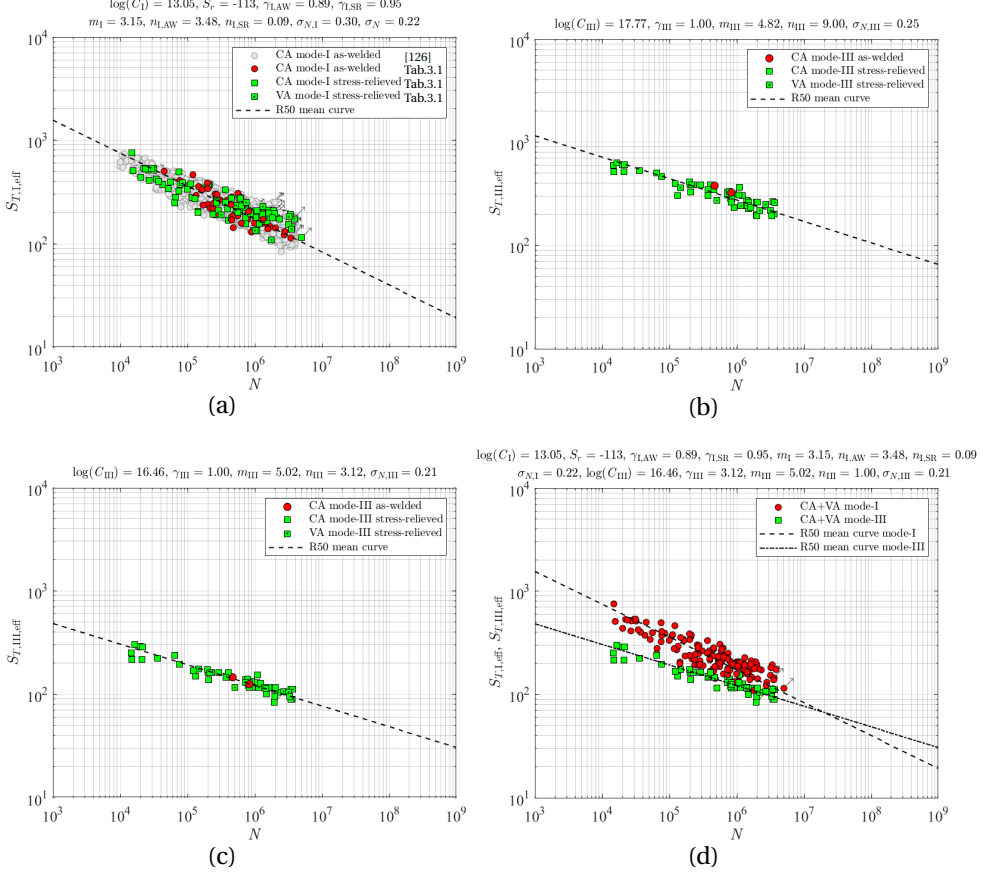
Figure 4.9.: Uniaxial reference fatigue resistance. Mode-I data total stress based fatigue resistance, including mean and residual stress correction with dedicated $n_{I,AW}$ and $n_{I,SR}$ (a); Mode-III data total stress based fatigue resistance; $\rho = 0$ (b) and $\rho > 0$ (c). Uniaxial mode-I and mode-III data total stress based fatigue resistance (d). Note: $c_m = C_{np,i} = 0$.

Like for the uniaxial mode-I assessment, the linear damage accumulation up to $D = 1$ shows VA data fitting the CA data scatter band. A comparison of mode-I and -III data and mean (i.e. 50 [%] reliability) $S_{T,eff} - N$ curves clearly shows differences in both strength and mechanism (Fig. 4.9), i.e. in $\{\log(C), \gamma\}$ and $\{m, n\}$, implying a lifetime dependent shear strength coefficient $\beta(N)$ rather than a constant one is required for multiaxial fatigue assessment (Section 4.3.1).

Multiaxial fatigue resistance

Involving the multiaxial fatigue data (Fig. 3.7 and Tables 3.1 and 3.2), the normal stress equivalent von Mises type of failure criterion is adopted (Eq. 4.18): $S_T = \sqrt{[S_{T,I}(\gamma_I, n_I)^2 + S_{T,III}(\gamma_{III}, n_{III})^2]}$. Note that for the SS welded butt joints the $S_{T,III}$ related C_{tw} estimate is obtained using the formulation as principally established for double sided (DS) welded T-joints, assuming $t_c = 0$ [29]. For CA mixed mode-{I, III} data involving asynchronous behaviour and/or different frequencies, as well as for VA multiaxial data, cycle counting in the von Mises plane is initially adopted without any material characteristic non-proportionality effects: $c_m = C_{np} = 0$ (Eq. 4.19). In order to illustrate the importance of strength and mechanism contributions, reflected in the $\beta(N)$ related {$\log(C), m$} and the mode and material dependent $S_{T,eff}$ parameters {γ, n}, regression analysis results for $\beta = \sqrt{3}$ as well as for $n_I = n_{III}$ are provided for reference purposes (Fig. 4.10 a and b). The parameter vectors have been $\Phi = \{\log(C), S_r, \gamma_{I,AW}, \gamma_{I,SR}, m, n_{I,AW}, n_{I,SR}, n_{III}, \sigma_N\}$ and $\Phi = \{\log(C), S_r, \gamma, m, n, \sigma_N\}$ respectively.

The different strength and mechanism for the uniaxial mode-I and mode-III as well as the multiaxial mode-{I, III} P and NP data can clearly be observed in the separate data scatter bands for $\beta = \sqrt{3}$, reflected in the imaginary intercept and slope for each data group (Fig. 4.10a). The lifetime scatter parameter $\sigma_N \sim 0.42$ and corresponding strength index $T_{\sigma S_T} = 1 : 2.72$ illustrate in comparison to the uniaxial values: $\sigma_{N,I} \sim 0.30$, $\sigma_{N,III} \sim 0.21$, $T_{\sigma S_T,I} = 1 : 1.75$ and $T_{\sigma S_T,III} = 1 : 1.28$ (Section 4.3.3) a much worse fit. Eliminating in addition the $S_{T,eff}$ related mode and material sensitive strength and mechanism contributions changes the imaginary intercept and slope for each data group (Fig. 4.10b), although the overall performance basically did not improve: $\sigma_N \sim 0.42$ and $T_{\sigma S_T} = 1 : 2.52$.

However, the scatter of the individual data groups did change. For the uniaxial mode-I and multiaxial mode-{I, III} P data in particular a significant increase and decrease are respectively observed, suggesting the equivalent shear strength and total stress based strength and mechanism contributions are important. The different consequences for uniaxial and multiaxial response conditions even indicate that mode-coupling; an interaction effect, might be involved indeed (Chapter 1). Overall, the uniaxial mode-I and mode-III as well as the multiaxial mode-{I, III} P data shows a reasonable fit, but the multiaxial mode-{I, III} NP data remains out of range up to a large extent (Fig. 4.10a and 4.10b), illustrating at the same time the consequences of data imbalance (Section 4.3.2). Without affecting the global performance lifetime and strength parameters σ_N and $T_{\sigma S_T}$, the relative position of data groups can change significantly and may cause wrong conclusions regarding the importance of strength and mechanism contributions as observed before [55, 79, 80].

Adopting the mode specific and material characteristic strength and mechanism contributions; {$\log(C), m$} in terms of $\beta(N)$ – for an iteratively obtained N value (Section 4.3.1) – and {γ, n}, improves the model performance just up to some extend (Fig. 4.10c). The lifetime scatter and strength scatter band index reduced a bit: $\sigma_N \sim 0.39$ and $T_{\sigma S_T} = 1 : 2.09$, but are still relatively large in comparison to the uniaxial mode-I data values (Section 4.3.3). At the same time, the multiaxial P and NP data groups still show room for improvement. One reason seems that
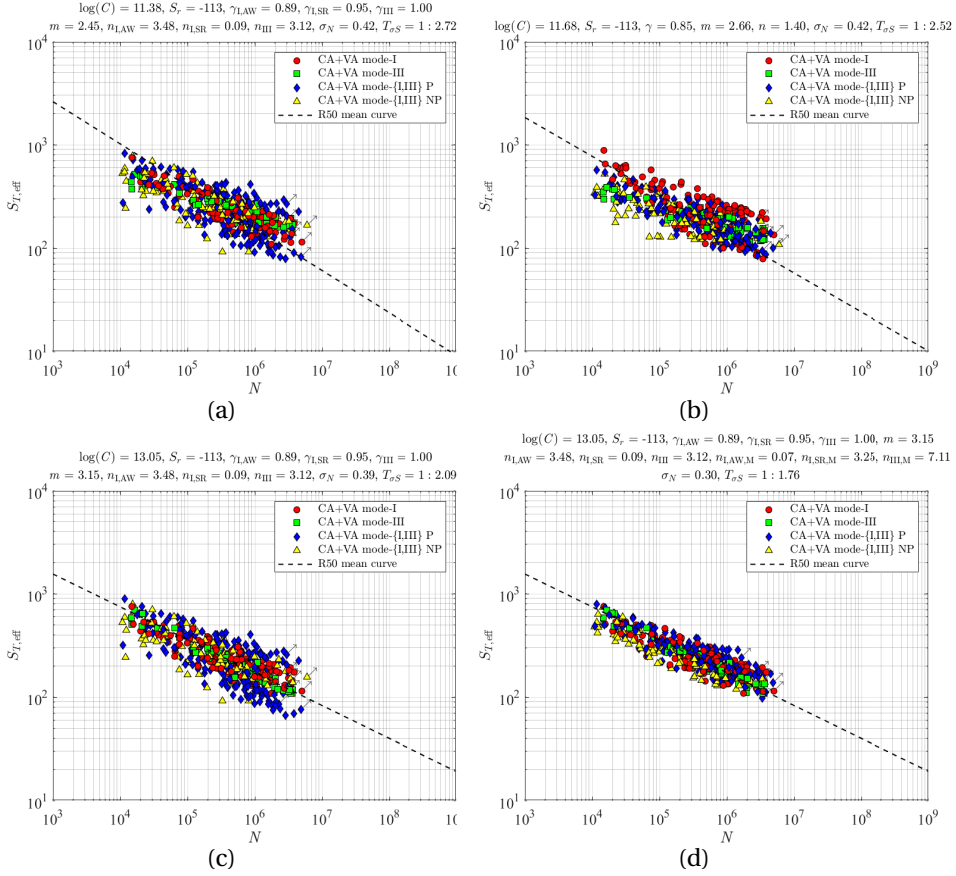
Figure 4.10.: Total stress based fatigue resistance for uniaxial and multiaxial data adopting: $\beta = \sqrt{3}$ and $\{n_I, \gamma_I\} \neq \{n_{III}, \gamma_{III}\}$ (a); $\beta = \sqrt{3}$ and $\{n_I, \gamma_I\} = \{n_{III}, \gamma_{III}\}$ (b); $\beta = f(N)$ and $n_I \neq n_{III}$ for 3 n approach (c) and 6 n approach (d). Note: $c_m = C_{np,i} = 0$.

$\beta(N)$ is not very effective in aligning the scatter bands of the different data groups. For the mid-cycle fatigue range $\beta(N)$ is varying from ~ 1.2 to ~ 1.4 and the mean value is ~ 1.8; quite close to $\beta = \sqrt{3}$ like used for the reference results (Fig. 4.10a). A similar observation has been made before [79], but seems no argument for a general conclusion since $\beta(N)$ is varying from ~ 0.5 to ~ 1.1 for S_e as fatigue strength parameter [130] and performance parameters similar to the mode-I data values are already obtained, whereas for $S_{T,eff}$ a next step is required.

Observing one more time the change in data scatter bands for the reference results from different to similar elastoplasticity coefficients (Fig. 4.10a and 4.10b), dedicated ones $\{n_{I,AW,M}, n_{I,SR,M}, n_{III,M}\}$ will be introduced for the mode-{I, III} multiaxial response conditions, reflecting a mechanism in-

teraction effect.   For regression analysis, the parameter vector becomes: $\Phi = \{\gamma_{I,AW}, \gamma_{I,SR}, \gamma_{III}, n_{I,AW}, n_{I,SR}, n_{III}, n_{I,AW,M}, n_{I,SR,M}, n_{III,M}, \sigma_N\}$.   Although – in addition to the previously investigated uniaxial mode-I two-stage crack growth characteristics (Section 4.3.1) – uniaxial mode-III and mixed mode-{I, III} crack growth testing (e.g. using CT specimens) is required to obtain the short crack growth related elastoplasticity coefficients n in order to prove interaction effects, still, most likely n estimates for welded joint fatigue test data are required for verification purposes.   Applying one-to-one crack growth based n estimates for welded joint fatigue life time estimates would imply similarity, and proof should be provided. A reversed engineering approach is adopted and most likely n estimates for multiaxial fatigue test data are obtained first in order to reveal the consequences of ignoring interaction effects.   Mode-I and mixed mode-{I, III} crack growth tests will be the next step. In case long crack growth mode-{I, III} interaction effects should be incorporated as well, the SIF has to be reformulated including coupling terms (Section 4.3.1).

The most likely multiaxial n estimates are quite different from the uniaxial counterparts and an interpretation of the values seems not straightforward, keeping in mind that the different data groups are not in balance (Section 4.3.2) and $\{n_{I,AW,M}, n_{I,SR,M}, n_{III,M}\}$ may serve at the same time the purpose of model deficiency correction factor. For mode-I the crack growth behaviour would change from non-monotonic to monotonically increasing and the other way around for respectively the AW and SR data; $\{n_{I,AW} = 3.48, n_{I,AW,M} = 0.07\}$ and $\{n_{I,SR} = 0.09, n_{I,SR,M} = 3.25\}$. Multiaxial response conditions would increase the level of elastoplasticity; for mode-III $n_{III,M} > n_{III}$.   The parameters confidence does not look unrealistic (Table 4.2) and even similar to the uniaxial ones (Table 4.1). A major achievement is that the life time scatter and strength scatter band index significantly reduced to $\sigma_N \sim 0.30$ and $T_{\sigma S_T} = 1:1.76$, supporting the hypothesis of involved interaction effects.

Table 4.2.: Total stress and Effective notch stress based $\{n, \rho^*\}$ parameter estimates for multiaxial response conditions, including 75[%] parameter confidence bounds.

	parameter	estimate	75[%] confidence
S_T	$n_{I,AW,M}$	0.07	[0.03, 0.19]
	$n_{I,SR,M}$	3.25	[3.01, 3.59]
	$n_{III,M}$	7.11	[5.07, 9.27]
S_e	$\rho^*_{I,AW,M}$	1.02	[0.17, 2.29]
	$\rho^*_{I,SR,M}$	3.95	[2.77, 5.10]
	$\rho^*_{III,M}$	0.09	[0.01, 1.27]

So far, the most likely initial and final crack size values as obtained for the mode-I fatigue resistance of AW joints in planar steel structures are adopted: respectively $(a_i/t_p) \sim 6 \cdot 10^{-3}$ as characteristic defect size and $(a_f/t_p) = 1$ reflecting a through-thickness crack [14].   However, the majority of the considered fatigue

resistance data is about welded joints in tubular steel structures (Section 4.3.2) and welding procedures can be different, explaining why the most likely (a_i/t_p) will be verified with respect to σ_N. Since ρ^* and a_f for respectively $S_{e,eff}$ and $S_{T,eff}$ serve the same purpose (Chapter 1), (a_f/t_p) will be reconsidered as well. The most likely defect size (a_i/t_p) is still $\sim 6 \cdot 10^{-3}$ (Fig. 4.11). For the considered fatigue resistance data (Tables 3.1 and 3.2) t_p is in between 3.2 and 12.5 [mm], meaning a_i would range from 0.02 to 0.08 [mm], in agreement with typical defect size measurement results [170–172]. Varying (a_f/t_p) for $(a_i/t_p) \sim 6 \cdot 10^{-3}$, $(a_f/t_p) = 1$ still provides the best result, suggesting the stress (intensity) gradient is important for any crack size up to t_p.
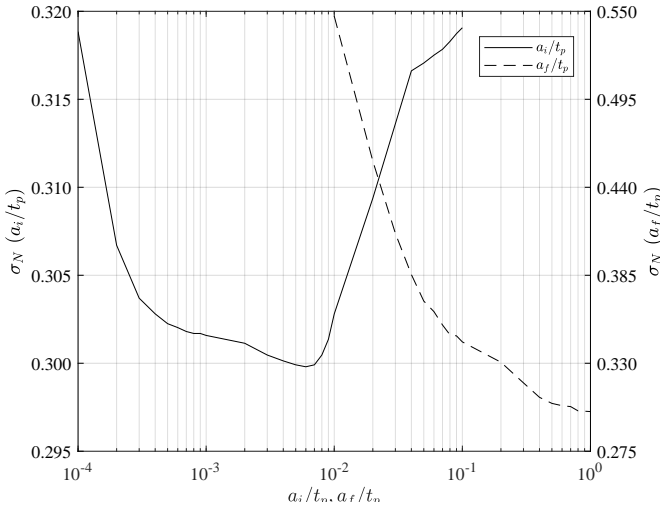

Figure 4.11.: Most likely σ_N for a range of $a_i/t_p|_{a_f/t_p=1}$ and $a_f/t_p|_{a_i/t_p=0.006}$.

Adopting a 0th, 1st or 2nd order moment approach (Section 4.3.1), differences between the actual response path and the (straight) range have been used to incorporate non-proportionality cycle-by-cycle in terms of C_{np} (Eq. 4.20), including a material characteristic contribution c_m (Eq. 4.19). The $c_m - \sigma_N$ sensitivity has been investigated for the C_{np} defined 0th, 1st and 2nd order moment approaches to evaluate the model performance, using the most likely $\{\log(C), S_{r,I}, \gamma_{I,AW}, \gamma_{I,SR}, m, n_{I,AW}, n_{I,AW,M}, n_{I,SR}, n_{I,SR,M}, n_{III}, n_{III,M}\}$ estimates (Fig. 4.10c and 4.10d, Tables 4.1 and 4.2), $(a_i/t_p) \sim 6 \cdot 10^{-3}$ and $(a_f/t_p) = 1$. Since data is unbalanced, i.e. the multiaxial NP data size is relatively small, the performance for the multiaxial NP data only as well as for all data has been considered. An optimum c_m exists for all approaches and the 1st order one provides the best result (Fig. 4.12), like for $S_{e,eff}$ [130]. Comparing the total stress and effective notch stress plots, obviously the $S_{T,eff}$ based optimum $c_m \sim 0.40$ is different from the $S_{e,eff}$ related one: $c_m \sim 0.65$, because the fatigue strength parameter is not the same. In contrast to $S_{e,eff}$, the $S_{T,eff}$ optimum for the multiaxial NP data

only and all data is not aligned, neither for the 1st order approach nor another one, basically confirming that – like $\{n_{I,AW,M}, n_{I,SR,M}, n_{III,M}\}$ – c_m corrects in addition for any cycle counting and/or non-proportionality related model deficiency. However, $c_m = 1$, suggesting non-proportionality is material invariant, would provide a deficient formulation. Different from $S_{e,eff}$ considering the uniaxial mode and material specific characteristic lengths only (i.e. involving 3 ρ^* parameters), the $S_{T,eff}$ performance for the multiaxial NP data only is even better than for all data, suggesting the distinct elastoplasticity coefficients for multiaxial mode-{I, III} response conditions (i.e. 6 n parameters in total) improves the model performance indeed.
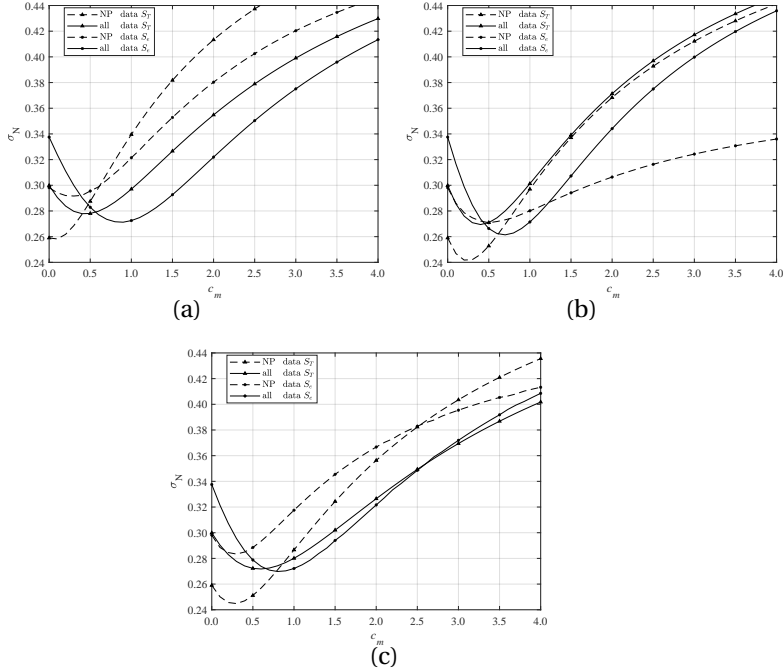
Figure 4.12.: Most likely σ_N for a range of c_m. Path dependent non-proportionality: 0th moment (a), 1st moment (b) and 2nd moment (c) for the $S_{T,eff}$ related 6 n approach and the $S_{e,eff}$ related 6 ρ^* approach.

Assessing all data (Fig. 3.7 and Tables 3.1 and 3.2) using the most likely mode and material specific strength contributions, $\{\log(C), m\}$ and $\{\gamma, n\}$ respectively represented in $\beta(N)$ and $S_{T,eff}$, as well as the 1st order approach to obtain C_{np} cycle by cycle for $c_m \sim 0.40$ in case of non-proportionality, an even better performance is obtained. The lifetime scatter has reduced to $\sigma_N \sim 0.27$ and the strength scatter band to $T_{\sigma S_T} = 1 : 1.66$ (Fig. 4.13). Principally all data fits the mode-I reference data scatter band, i.e. the interval in between 5 and 95 [%] reliability for 75 [%] confidence. Note that an increased data size: currently ~ 500 for the assessed data (Fig. 3.7 and

Tables 3.1 and 3.2) and ~ 2500 for the mode-I reference data, can contribute to another σ_N reduction.

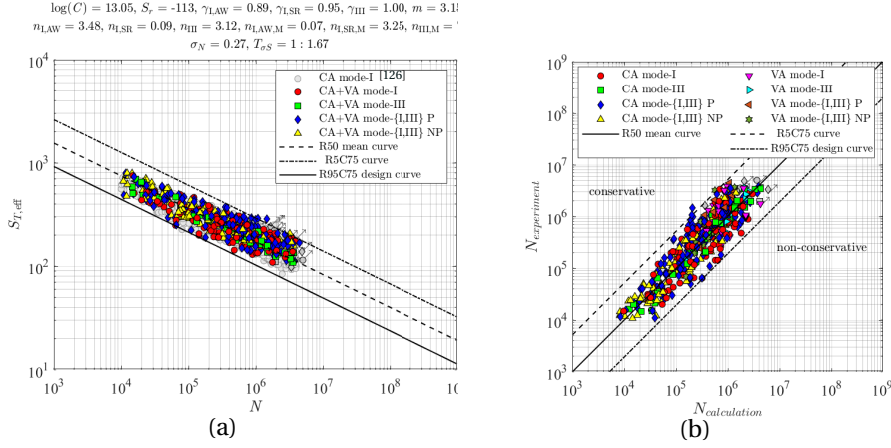Figure 4.13.: Total stress based fatigue resistance (a) and lifetime ratio plot (b) for uniaxial and multiaxial data; $n_I \neq n_{III}$, $\beta(N)$, 1$^{\text{st}}$ order path dependent non-proportionality with $c_m = 0.40$.

The scatter of the uniaxial mode-I and multiaxial mode-{I, III} P data is about the same and relatively large in comparison to the one of the uniaxial mode-III and multiaxial mode-{I, III} NP data. Although the $S_{T,eff}$ performance is just not equal to that of $S_{e,eff}$ with $\sigma_N \sim 0.26$ and $T_{\sigma S_T} = 1 : 1.65$ [130], the multiaxial mode-{I, III} P data shows a reduced number of outliers and seems a result of the introduced elastoplasticity coefficients $\{n_{I,AW,M}, n_{I,SR,M}, n_{III,M}\}$ for the multiaxial response conditions.

Similarly introducing $\{\rho^*_{I,AW,M}, \rho^*_{I,SR,M}, \rho^*_{III,M}\}$ to incorporate a mechanism interaction effect provides a 6 parameter formulation for $S_{e,eff}$ as well, but hardly improves the performance (Fig. 4.14a). Whereas $\{n_{I,AW,M}, n_{I,SR,M}, n_{III,M}\}$ and $\{n_{I,AW}, n_{I,SR}, n_{III}\}$ for $S_{T,eff}$ are quite different, the multiaxial $\{\rho^*_{I,AW,M}, \rho^*_{I,SR,M}, \rho^*_{III,M}\}$ estimates are approximately equal to the uniaxial counter parts $\{\rho^*_{I,AW}, \rho^*_{I,SR}, \rho^*_{III}\}$, implying $c_m \sim 0.65$ hardly changes either (Fig. 4.12). A part of the explanation of ρ^* being less sensitive to mechanism interaction, mode-{I, III} coupling, might be that ρ^* seems to be a more implicit measure; an averaged parameter reflecting a (mixed) mode and material characteristic length in which the majority of the life time has been spent. The (mixed) mode affected elastoplasticity parameter n changes the crack growth behaviour directly (Fig. 4.7), suggesting n is a more explicit mechanism measure able to provide a better representation of the multiaxial response conditions.

Using S_t (Eq. 4.22), the improved $I_{N,III'}(r_{\tau s})^{1/m_{III}}$ formulation reduces the life time scatter σ_N from 0.36 to 0.32 (Fig. 4.14 b) and scatter band index $T_{\sigma S_t}$ from 1 : 1.63 to 1 : 1.54. In comparison to $S_{T,eff}$ and $S_{e,eff}$, the S_t performance is a result of the adopted modelling steps with respect to the stress (intensity)

distribution (Section 4.2), the crack growth behaviour and the traction equivalent stress formulation (Section 4.3.1). The performance of the related S_t based on predominant mode-I crack growth behaviour (Section 4.3.1), currently $\sigma_N = 0.36$ and $T_{\sigma S_t} = 1 : 2.03$ [55], cannot be improved accordingly, since the mode-III stress intensity formulation is not involved. Note that only a selection of the resistance data (Section 4.3.2) is included, i.e. the same ∼ 180 SR data points as used before [128, 136]. The constant shear strength coefficient $\beta = 3$ explains the average slope value $m \sim 4$ in between $m_I \sim 3$ and $m_{III} \sim 5$, meaning for uniaxial and multiaxial fatigue assessment different resistance curves are used. Since the scatter band index $T_{\sigma S}$ is slope dependent [130], $m \sim 4$ explains at the same time the smaller value for S_t and the larger ones for the mode-I equivalent $S_{T,eff}$ and $S_{e,eff}$.

4
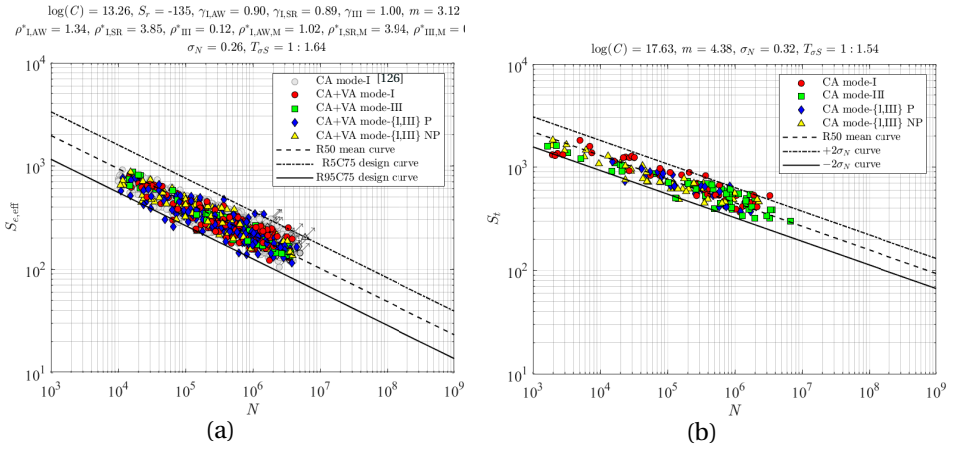
Figure 4.14.: Effective notch stress based fatigue resistance for uniaxial and multiaxial data and $\rho_I^* \neq \rho_{III}^*$, $\beta(N)$, 1st order path dependent non-proportionality with $c_m = 0.65$ (a) and traction equivalent structural stress based fatigue resistance (b).

Overall, the cracked geometry parameter $S_{T,eff}$ and intact geometry parameter $S_{e,eff}$ are able to achieve a similar performance. Looking in particular at the multiaxial P data scatter, an improved multiaxial fatigue strength parameter $S_{T,eff}$ seems still possible, although mode-I formulation advances seems to be a first step since the uniaxial mode-I data scatter is in control (Fig. 4.9 a). However, $S_{T,eff}$ is computationally more expensive because of the $I_N(a/t_p)$ calculation (Section 4.3.1), whereas $S_{e,eff}$ can be straightforward obtained using an explicit formulation [16, 18, 29, 130].

The VA data fits the CA data scatter band for $D = 1$ (Fig. 4.15), supporting the hypothesis that an advanced fatigue failure criterion like $S_{T,eff}$ contributes to an improved (linear) damage accumulation model performance [130].

$\log(C) = 13.05$, $S_r = -113$, $\gamma_{I,AW} = 0.89$, $\gamma_{I,SR} = 0.95$, $\gamma_{III} = 1.00$, $m = 3.15$
$n_{I,AW} = 3.48$, $n_{I,SR} = 0.09$, $n_{III} = 3.12$, $n_{I,AW,M} = 0.07$, $n_{I,SR,M} = 3.25$, $n_{III,M} = 7.11$
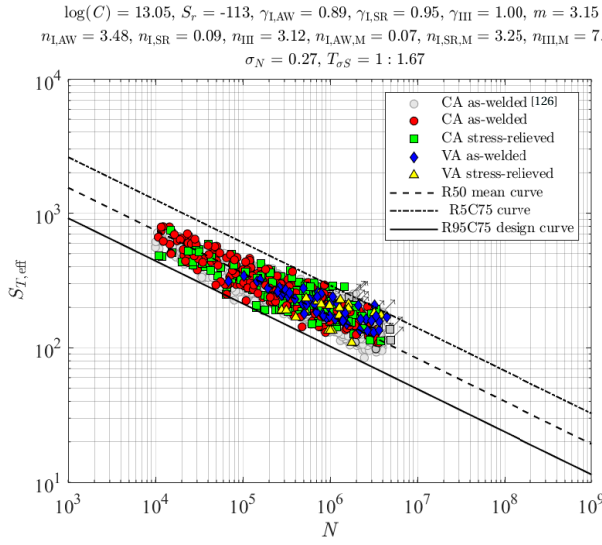$\sigma_N = 0.27$, $T_{\sigma S} = 1 : 1.67$

Figure 4.15.: Total stress based fatigue resistance for uniaxial and multiaxial, constant and variable amplitude, as-welded and stress-relieved data.

4.4. CONCLUSIONS AND OUTLOOK

Adopting the total stress S_T as SIF based fatigue strength parameter to assess arc-welded joints, dedicated mode-{I, III} far field factor formulations $\{Y_{f,I}, Y_{f,III}\}$ have been established for tubular structures, principally holding for planar ones as an extreme case $(R_t \rightarrow \infty)$. Good agreement with FE solutions have been obtained.

Uniaxial mode-I and mode-III MCF resistance investigations revealed distinguished material dependent strength and mechanism contributions in terms of $\{\log(C), \gamma\}$ and $\{m, n\}$, i.e. respectively the resistance curve intercept and mean stress induced response ratio coefficient, resistance curve slope and notch and crack tip elastoplasticity coefficient. For mode-III, the most likely n implicitly suggests (welding residual stress induced) non-monotonic crack growth behaviour, like for mode-I, although the parameter confidence bounds reflects quite some uncertainty and monotonically increasing behaviour could be involved as well. Explicit proof is not available and dedicated mode-III crack growth testing at notches – in particular at different mean stress levels – is recommended.

A von Mises type of failure criterion at the critical fracture plane has been adopted, and a lifetime dependent shear strength coefficient $\beta(N)$ has been introduced to cover the mode specific and material characteristic $\{\log(C), m\}$, whereas S_T explicitly contains $\{\gamma, n\}$. To improve the S_T performance, except 3 uniaxial n parameters, 3 multiaxial ones are introduced, reflecting mixed mode-{I, III} behaviour; an interaction mechanism. Although the most likely multiaxial n estimates are not straightforward to interpret, the significantly reduced data scatter suggests an interaction effect should be taken into account (*research sub-question 2*). Long crack growth mode-{I, III} interaction effects could be incorporated as well and requires

a SIF reformulation containing coupling terms. However, the short crack growth contribution seems more important, as reflected in the current S_T performance, because the fatigue life time is predominantly spent in the notch affected region. Mixed mode-{I, III} crack growth testing is required to investigate the two-stage crack growth behaviour and corresponding n values, as well as to address crack growth and fatigue resistance similarity. Embedded in the critical distance theory, the elastoplasticity coefficients are principally response level dependent. Although for MCF resistance data only the obtained average estimates already provide a constant scatter over the full range, this may change when HCF resistance data will be considered as well. Incorporating a cycle-by-cycle non-proportionality measure with a response path and material contribution, a 1st order response approach shows the best result. The VA data fits the CA data scatter band for $D = 1$.

In comparison to S_e, the S_T performance is similar (*research sub-question 1*). The multiaxial P data scatter turns out to be smaller; a consequence of the multiaxial n parameters. Introducing multiaxial ρ^* values for S_e, however, hardly improves the performance, revealing an insensitivity. Whereas n seems to be a more explicit measure directly affecting the crack growth behaviour, ρ^* seems a more implicit measure reflecting the material characteristic length for (mixed) mode and (multiaxial) response conditions. In this respect, S_T can be considered one step closer to the actual physics of the fatigue damage process. In fact, S_T contains with n one more parameter to characterise multiaxiality, since ρ^* for S_e principally serves the same purpose as a_f for S_T. Life time scatter investigations showed that $a_f \rightarrow t_p$ rather than $a_f \rightarrow \rho^*$ should be used in order to maximise the incorporated stress (intensity) gradient effects and minimise the resistance data scatter. For S_e, a different way to incorporate mixed mode-{I, III} behaviour has to be provided [130].

In order to continue the improvement of the multiaxial fatigue strength parameters S_T or S_e, the mode-I formulation should be re-investigated since the predominantly tubular joint defined uniaxial mode-I data scatter is in control, significantly exceeding the planar joint σ_N value. However, the assessed uniaxial and multiaxial mode-{I, III} data fits the uniaxial mode-I reference data scatter band and a single $S_T - N$ resistance curve can be used for fatigue assessment in engineering applications (*research sub-question 5*).

Aiming to incorporate the mode specific characteristics for the traction equivalent stress S_t, the notch to far field transition size should be different for mode-I and mode-III. Fitting the bi-linearised stress distribution approximations suggests $0.1 t_p$ to be a good one for mode-III; a smaller notch affected region seems to provide a better fit for mode-I. However, the stress intensity $M_{kn} Y_{f,III}$ requires the opposite in order to obtain a good fit with FE results, suggesting the maximum possible is to incorporate the proposed $Y_{f,III}$ formulation. Improved S_t performance has been obtained accordingly.

5

MULTIAXIAL FATIGUE TESTING OF HIGH-QUALITY WELDS USING A HEXAPOD

The laws of science do not distinguish between past and future (fatigue test results).

Stephen Hawking, physicist

5.1. INTRODUCTION

In order to validate the performance of multiaxial fatigue strength parameters, test data is required. However, to introduce multiaxial structural response conditions into specimens – either loading, geometry and/or even material induced (Chapter 2) – can be challenging and may explain the limited availability of multiaxial fatigue data for welded joints [74, 78, 110, 173]. For geometry [121, 123–125] or material [174] induced multiaxiality, uniaxial test rigs can still be used. In case of ultrasonic capabilities, testing is not limited to the mid-cycle fatigue range and even high-cycle fatigue data can be obtained [175, 176]. Non-proportionality, though, cannot be investigated – at least for metals like steel – and requires loading induced multiaxiality; i.e. multiple actuators [177] controlling different degrees of freedom (DoF's).

Biaxial test rigs, involving either two translational DoF's or a combination of one translational and one rotational DoF, are nowadays standardised equipment, allowing respectively for mixed mode-{I, II} and mixed mode-{I, III} testing [e.g. 178–180]. For

---

DoF's up to six, available test rigs are typically custom built for a particular purpose [e.g. 181–183].

Aiming for a wide application range and freedom with respect to specimen size and material strength, a high loading capacity six DoF multiaxial fatigue test rig, a hexapod (i.e. a Steward platform), has been developed. Whereas the typically available configurations with six linear actuators provide a combination of large motions and relatively small forces [e.g. 184, 185], this one offers unparalleled performance in terms of loading combinations, accuracy, and system stability, allowing to investigate multiaxial fatigue of maritime structures [e.g. 2, 3, 186].

Available fatigue test data from literature, i.e. fatigue life time information N for a particular fatigue strength S, can be used to obtain average quality based parameter coefficient estimates in order to establish one $S - N$ relation for general engineering applications. Depending on the specimen quality – reflected in strength, geometry and material aspects; respectively welding induced residual stress, weld dimensions, as well as material microstructure composition and hardness distribution [e.g. 187–190], a particular data set may be on the scatter band lower or upper bound. For high-performance welds, the average quality based $S - N$ relation may provide overconservative fatigue strength and life time estimates. A dedicated one with representative parameter coefficient estimates might be a better option, reflecting the actual quality.

In order to assess the multiaxial mid-cycle fatigue resistance of high-performance welds for maritime applications, test results obtained using the TU Delft hexapod will be evaluated. Test rig properties as well as specimens information will be provided first (Section 5.2). Fitting in the average quality data scatter band will be investigated for both the effective notch stress S_e (Chapter 3) and total stress S_T (Chapter 4), including a parameter confidence bound analysis (Section 5.3) in order to evaluate if quality dependent $\{S_e - N, S_T - N\}$ relations would be preferred, rather than one for all data.

The conclusions and outlook (Section 5.4) provide answers to research sub-questions 3 and 6 (Section 1.3).

5.2. Multiaxial fatigue tests

Since the TU Delft hexapod is quite different from existing ones, design requirements and capabilities will be revealed first (Section 5.2.1). The specimens were developed for mixed mode-{I, III} fatigue investigations and will be discussed with respect to geometry aspects, material properties, welding procedure and parameters, as well as metallurgical analysis results including macro and micro observations and hardness measurement data in order to verify the high-performance at materials level (Section 5.2.2). Last but not least, the mid-cycle fatigue test results will be provided, including (mixed) mode-specific fracture surface characteristics (Section 5.2.3).

5.2.1. Hexapod description

Parallel manipulators offer a high loading capacity, excellent dynamic response characteristics and accurate positioning capabilities [191]. Using 6 linear actuators

in pairs; i.e. in parallel, attached to a base and crossing over to a platform at 3 equidistant positions, introduces a hexapod (Fig. 5.1), able to apply (coupled, multiaxial) motions and loads in 6 DoF: 3 translations/forces and 3 rotations/moments, varying over time. All 12 connections are principally universal joints. Depending on the operation requirements the actuators are either electric or hydraulic controlled, based on inverse kinematics equations.
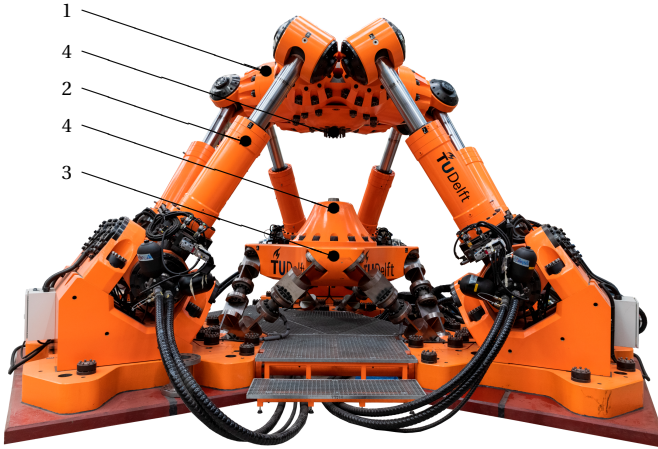

Figure 5.1.: TU Delft Hexapod. 1 = platform; 2 = actuator; 3 = pedestal with 6-DoF load cell; 4 = specimen grips.

Hexapods used for simulation purposes of ship, car or airplane dynamics typically involve relatively large motions and smaller loads. However, mechanical testing comes along with relatively large loads and smaller motions, meaning the system requirements will be completely different. For ultimate and fatigue limit state as well as structural dynamics testing at Delft University of Technology, a custom-built hydraulically controlled hexapod has been developed [32]; one of the largest ever built (Table 5.1).

Table 5.1.: TU Delft hexapod dimensions and weight.

item	value
diameter platform	2550 [mm]
diameter cylinder lower attachment	4070 [mm]
total height (neutral position)	3000 [mm]
pedestal - platform distance (neutral position)	1200 [mm]
pedestal - platform distance (max.)	1700 [mm]
cylinder length (neutral position)	2080 [mm]
cylinder stroke	± 300 [mm]
approximate platform weight	13 [tonnes]
approximate total weight	60 [tonnes]

In order to be able to apply relative large loads (Table 5.2), i.e. forces up to 1

Table 5.2.: TU Delft hexapod maximum load capacity.

description	capacity
shear force	±400 [kN]
shear displacement	±300 [mm]
axial force	±1000 [kN]
axial displacement	±450 [mm]
bending moment	±400 [kNm]
bending rotation	±11 [deg]
torsion moment	±1000 [kNm]
torsion rotation	±20 [deg]
test frequency	0 - 30 [Hz]

[MN] and moments up to 1 [MNm], the system is operated using hydraulics with a max. oil flow capacity of 1500 [L/min] at 280 [bar]. Cyclic loading conditions up to 30 [Hz] can be both constant and variable (i.e. random). All DoF's can be individually controlled with respect to amplitude, frequency and phase. For measurement purposes, an advanced load cell in hexapod configuration has been developed, rather than a box type one. The 6 legs with predominant axial stiffness contain each an uniaxial load cell and the output is used to reconstruct the 6 DoF loads: 3 forces and 3 moments. The load cell deck is the pedestal the specimens can be mounted on. To fix the specimens, custom grips at the pedestal and/or platform are required.

For specimens in between the pedestal and platform, the maximum volume is about 1 [m^3], allowing for larger sizes than typically fit in biaxial test rigs. Long slender specimens like pipe sections can be put through the platform and even through the pedestal, provided dedicated grips are used to enable mounting. Last but not least, specimens can be mounted on top of the platform, providing the possibility to investigate structural dynamics experimentally, like sloshing in LNG tanks or earth quake vibrations of buildings.

5.2.2. Specimen details

To investigate mode-{I, III} multiaxial fatigue of arc-welded DS T-joints, a tubular geometry rather than a planar one has been adopted (Fig. 5.2) to ensure the hot spot type C along the weld seam is governing. The selected base- and cross-plate thickness of 10 [mm] is representative for maritime structures. Flanges have been introduced to support bolt connections for specimen mounting purposes. In order to avoid a fatigue critical flange-tube transition, the curvature is semi-elliptical.

Aiming for fixed boundary conditions, the specimens are fastened at each flange using 16 M20 double end threaded studs and super nuts with jack bolts for accurate pre-load control – up to 90 [%] of the yield strength – without hydraulic tensioner. The stud normal strength and shear strength accommodate respectively the mode-I and mode-III specimen loading components. A diamond coated friction shim has been put in between the specimen flanges and the grips in order to prevent for mode-III torsion induced slip.
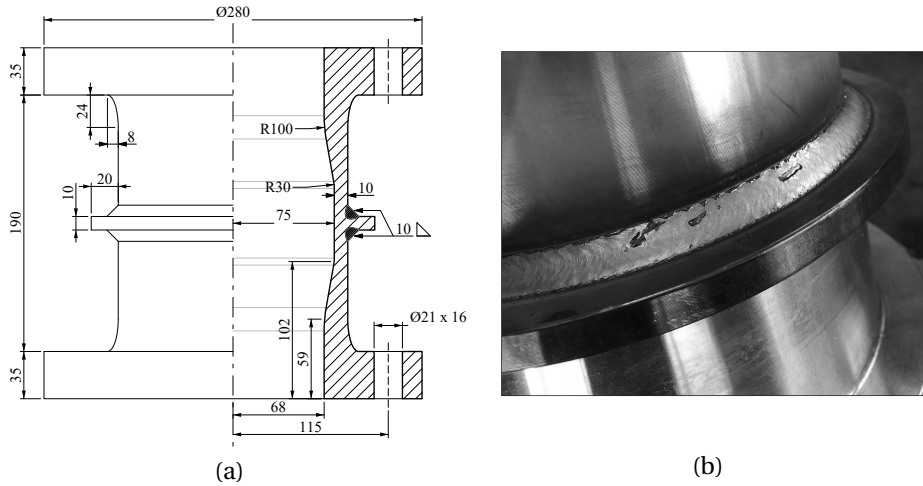
(a)   (b)

Figure 5.2.: Specimen geometry dimensions in [mm] (a) and weld detail (b).

To make sure fatigue cracks will develop at the weld toe rather than the weld root, each specimen – consisting of a tube, two flanges and a circumferential attachment (Fig. 5.2) – is machined in one piece from a round bar of a commonly used alloy in steel maritime structures: S355J2G3+N (Table 5.3). For reference purposes, the composition and properties of a similar type of alloy; EH36, are provided as well. The yield strength for S355 is smaller than the tabular value and is likely a consequence of the bar manufacturing process, since the sample is taken from the representative pipe diameter location; i.e. away from the surface of the original round bar.

Table 5.3.: Chemical composition information and mechanical properties of S355J2G3+N and EH36, obtained using X-ray diffraction, combustion analysis and a tensile test.

material	C [%]	Si [%]	Mn [%]	P [%]	Cr [%]	Mo [%]	Ni [%]	Al [%]	Cu [%]
S355	0.17	0.33	1.43	0.016	0.06	0.03	0.17	0.05	0.09
EH36	0.12	0.42	1.39	0.011	0.03	-	-	-	-

material	yield strength [MPa]	tensile strength [MPa]	Young's modulus [GPa]
S355	340	506	206
EH36	406	548	206

A partially penetrated fillet weld has been added at each side of the attachment to obtain the DS welded T-joint, with the weld starts ∼ 180 [deg] away one

from the other to make sure the two start and stop positions are not aligned. Although no thermal analysis has been performed, this precautionary measure is expected to prevent for concentration of thermal effects on a single side of each specimen. Welding a separate attachment to a tube would impose a full penetration requirement, meaning a significantly increased heat input, welding induced deformations as well as residual stresses and has been prevented for. The welds are fabricated using a robot, involving a turning manipulator and a fixed welding torch (Fig. 5.3).

Figure 5.3.: Specimen welding using a robot with a turning manipulator and a fixed torch.

The welding procedure has been certified according to offshore quality standards (EN 10204-2004) and the welds are inspected visually (standard: NEN-EN-ISO 17637, acceptance criteria: NEN-EN-ISO 5817) as well as using magnetic particle inspection (standard: NEN-EN-ISO 17638, acceptance criteria: NEN-EN-ISO 23278). A few specimens have been thermally stress-relieved at $560 - 600$ $[°C]$ for a minimum of 2 hours to be able to get an impression of welding induced residual stress affecting the fatigue performance in comparison to the as-welded specimen data.

Optical microscopy at macro and micro scale, as well as hardness measurement data are compared for the hexapod specimen welds with respect to reference welds to illustrate the high-performance properties. For both welds, two samples were extracted from different specimens at different locations along the weld seam. The samples were cold mounted in a two-part acrylic resin and a range of P180 to P4000 grit sandpaper as well as 3 to 1 $[\mu m]$ diamond polishing suspensions were used to prepare the metallurgical investigations. Nital 5% etchant was used for 5 $[s]$ in order

to reveal the microstructure.

Macro images were taken at 40x magnification using a microscope and stitched together to an image containing the complete weld. For both the reference and hexapod welds, the base metal (BM); respectively EH36 and S355J2G3+N, fusion zone (FZ) and heat affected zone (HAZ) can be distinguished (Fig. 5.4). The weld dimensions were measured; i.e. weld leg length l_w, weld leg height h_w and notch radius ρ, using 10 samples (Table 5.4). The reference weld notch radius turned out to be similar to previous observations [192–194] and the hexapod one seems relatively large at a slightly deeper penetration level. The larger notch radius reduces the stress concentration, whereas the penetration induced small undercut increases the far field stress up to a minor extent.
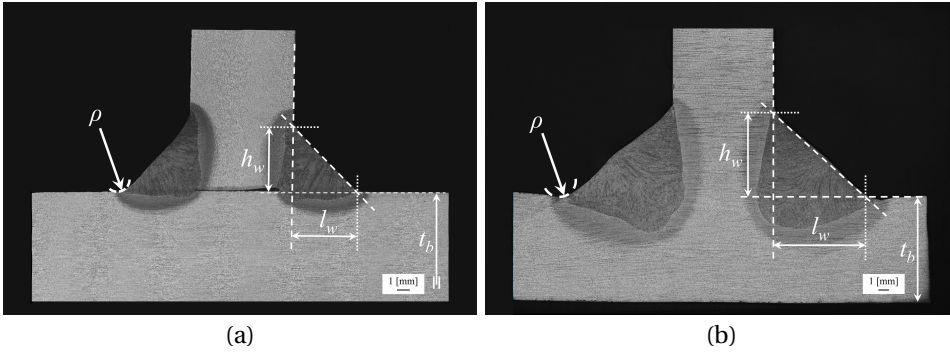

(a)   (b)

Figure 5.4.: Macro images for the reference (a) and hexapod (b) welds.

Table 5.4.: Measured weld dimensions.

weld dimensions	l_w		h_w		ρ	
	μ	σ	μ	σ	μ	σ
reference weld	4.88	0.49	5.20	0.23	1.27	0.43
hexapod weld	9.16	0.44	9.06	0.44	3.12	0.99

Vickers hardness measurements were conducted using a DuraScan Microhardness Tester applying 2 [kgf]; HV2, rather than 5 [kgf]; HV5, or 10 [kgf]; HV10, in order to obtain sufficient spatial resolution (Fig. 5.5). Although in general the material zones of a perfect welded joint would have an homogeneous hardness distribution of similar magnitude as the base metal, the actual distribution varies since the arc-welding induced heat input and cooling down process changes the material microstructure. Hardness distributions can be used to identify peak locations, reflecting brittle – weak – spots and to provide information about fatigue influence factors like residual stress [e.g. 188].

The BM hardness for both welds is similar as expected, in average respectively 159 HV2 and 170 HV2. Increased hardness is observed in the FZ. For the hexapod weld 222±4.0 HV2 left and 226±3.9 HV2 right (Fig. 5.5a), with a relatively low standard

deviation suggesting a homogenous material structure. However, the reference weld hardness of 284±14 and 328±15 (Fig. 5.5b) is significantly higher and much more scattered, implying a rather inhomogeneous one. The HAZ contains the highest hardness for both the reference and hexapod weld, respectively 413 HV2 (Fig. 5.5a) and 343 HV2 (Fig. 5.5b). Note that the reference weld value exceeds the allowed maximum of 380 HV10 (NEN-EN-ISO 9015-1:2011), keeping in mind that a HV2 maximum would be higher.

(a)   (b)
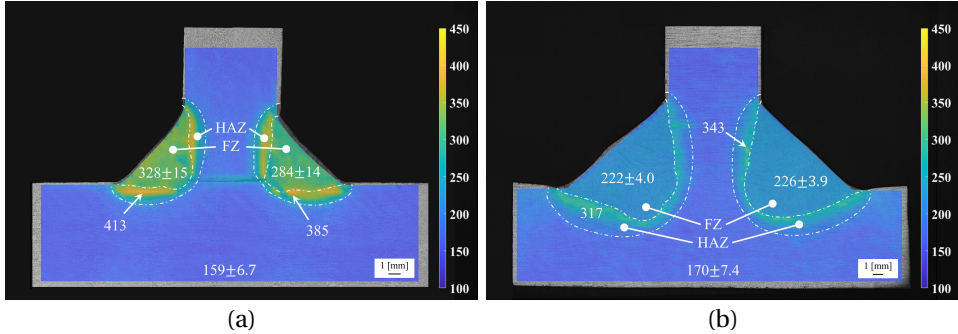
Figure 5.5.: Vickers hardness maps for the reference (a) and hexapod (b) welds.

The hexapod weld is more sensitive to the formation of hard brittle phases because of the relatively large {C, Mn, Si} content [195] of both the filler wire (Table 5.5) and the BM (Table 5.3). Since the same shielding gas ($80\% Ar + 20\% CO_2$) was used for both welds as well, the weld dimensions and (welding parameter induced) penetration level are the most reasonable explanation for the obtained hardness maps. For a larger weld and deeper penetration level, more thermal energy needs to dissipate into the surrounding material, suggesting a slower cooling rate and a more gradual transition from one material zone to another (Figs. 5.4 and 5.5), typically responsible for reduced residual stress levels as well as smaller welding induced defects.

Table 5.5.: Chemical composition of filler materials.

filler composition	C [%]	Mn [%]	Si [%]
reference weld	0.06	1.20	0.40
hexapod weld	0.08	1.47	0.83

Optical microscopy observations at high magnification (Fig. 5.7) and hardness map interpretations revealed that for the reference weld the BM consists of ferrite (α) with a grain size of approximately 10 [μm] and pearlite (P) in a banded structure, typical for rolled plates (Fig. 5.7a), whereas for the hexapod weld ferrite with a grain size of approximately 20 [μm] and pearlite in a homogeneous structure is identified (Fig. 5.7b). The larger BM hardness of the hexapod weld with respect to the reference

one is a result of the increased carbon content (Table 5.3). Characterising the refence weld FZ, predominantly acicular ferrite (AF) with proeutectoid ferrite (α_{pro}) and islands of martensite (M) are observed (Fig. 5.7c), while for the hexapod weld FZ acicular ferrite, allotriomorphic ferrite (α_{allo}), Widmanstätten ferrite (WF) and limited formations of martensite (Fig. 5.7d) are identified. The peak hardness in the HAZ of the reference weld shows mostly martensite with proeutectoid ferrite grains (Fig. 5.7e) and the one of the hexapod weld consists of martensite, upper bainite (UB), acicular ferrite, proeutectoid ferrite and Widmanstätten ferrite forming directly from the prior austenite grain boundaries (Fig. 5.7f). The near-surface microstructure at the notch of the reference weld (Fig. 5.7g) is very inhomogeneous as a result of the sharp FZ to BM transition, whereas for the hexapod weld a more gradual change in microstructure is observed as a consequence of the thermal history (Fig. 5.7h). Although the near-surface hardness at the notch of the reference weld is relatively large in comparison to the one of the hexapod (Fig. 5.5) – suggesting an increased fatigue crack initiation performance [e.g. 196], crack growth is in charge because of the welding induced defects and a one-to-one relation between hardness and a growth dominated fatigue life time for welded joints does not exist. However, hardness can still provide information about fatigue influence factors like residual stress.

5

5.2.3. TEST PROGRAM INFORMATION AND RESULTS

The 72 available specimens were used to generate uniaxial mode-I and mode-III as well as mixed mode-{I, III} data for both CA and VA loading in as-welded (AW) and in stress-relieved (SR) conditions, aiming to investigate multiaxial fatigue resistance including damage accumulation and mean (residual) stress aspects (Appendix F).

The acquired uniaxial mode-I and mode-III CA data is for reference purposes. Because of the tubular specimen geometry with a circumferential weld, mode-III data (15 specimens) were obtained (Fig. 5.9) applying a cyclic (sinusoidal) torsion

(a)

(b)

(c)

(d)

(e)

(f)

(g) (h)
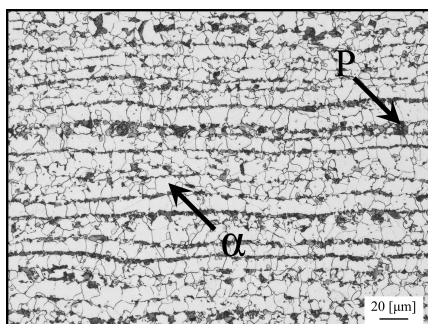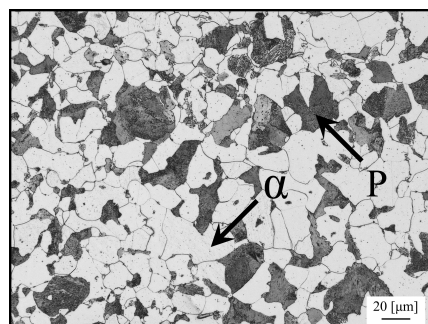
Figure 5.7.: Reference (left column) and hexapod (right column) weld material microstructure for the BM (a and b), the HAZ (c and d), the FZ (e and f) and notch detail (g and h), showing ferrite (α), pearlite (P), proeutectoid ferrite ($\alp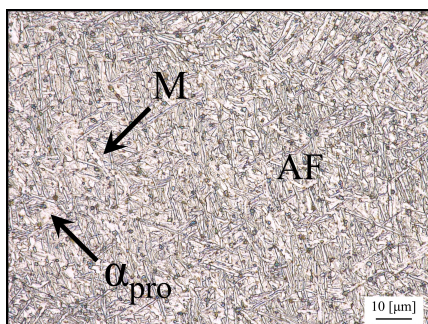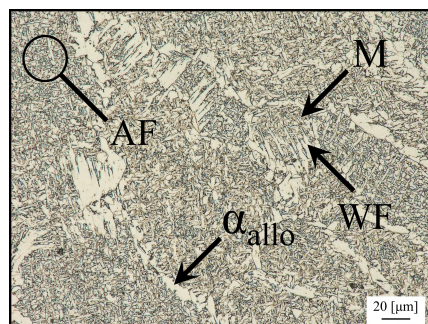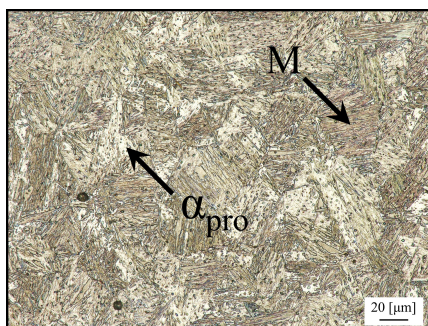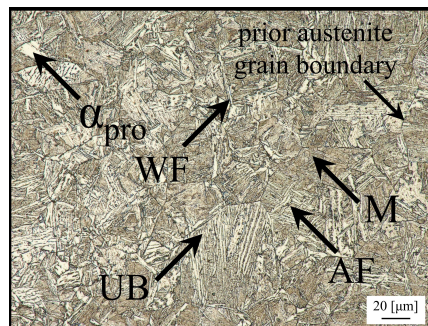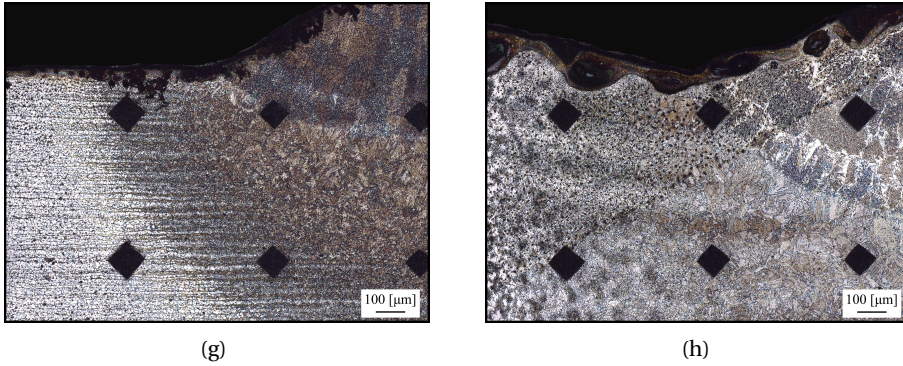ha_{pro}$), allotriomorphic ferrite (α_{allo}), Widmanstätten ferrite (WF), acicular ferrite (AF), upper bainite (UB) and martensite (M).

moment M_t rather than a shear force F_s. Although fatigue induced failure may appear at the start/stop location, affecting the hot spot type C fatigue resistance, the actual locations were observed along the weld seam. The structural stress concentration factor $K_s = \tau_s/\tau_n = 1.05$. Loading and response ratio $R_{III} = M_{t,min}/M_{t,max} = \tau_{min}/\tau_{max} = -1$ to obtain a sufficiently high far field response range (below yielding) for life times in the mid-cycle fatigue (MCF) region: $N = O(10^4...5 \cdot 10^6)$ cycles. Mode-I data (22 specimens) is obtained (Fig. 5.9) applying for the first few specimens a normal force F_n and for the remaining ones a bending moment M_b. Although F_n was preferred in order to avoid a weld volume effect [e.g. 8] and allow for a one-to-one comparison to the mode-III data, fatigue induced failures were obtained at the start/stop location. A M_b type of load with the start/stop location around the neutral axis turned out to be a solution, accepting that a possible weld volume effect may have to be taken care of. The structural stress concentration factor for F_n and M_b: $K_s = \sigma_s/\sigma_n = \{1.15, 1.20\}$. Loading and response ratio $R_I = F_{n,min}/F_{n,max} = M_{b,min}/M_{b,max} = \sigma_{min}/\sigma_{max} = 0.1$ to obtain at least a fully effective far field response cycle as far as the applied $\{F_n, M_b\}$ is concerned, assuming that mode-III mean stress effects are typically negligible [29, 130, 197] and a mode-I to mode-IIII data comparison is still feasible. To indicate any mean (residual) stress effect, some tests have been conducted with $R_I = -1$, involving both AW and SR specimens (Fig. 5.9).

Mixed mode-{I, III} CA data is obtained applying $\{M_b|R_I = 0.1, M_t|R_{III} = 0.1\}$ simultaneously, either proportional (i.e. in-phase), non-proportional (i.e. 90 [deg] out-of-phase) or with a frequency ratio of 1 : 3 (i.e. for 1 cycle in bending, 3 cycles in torsion are applied at the same time). Based on the von Mises type of criterion [130, 197], $\tau = \sqrt{3}\sigma$ has been adopted to ensure equal shear and normal stress contributions to failure [32].

For both the uniaxial and multiaxial random VA loading and response conditions,

the generated time traces are based a on Gauss distributed frequency spectrum (Fig. 5.8): $G(\omega) = (\Delta S_{n,max}/6)^2 \cdot \exp\{-(\omega - \mu_\omega)^2/(2 \cdot \lambda_\omega^2)\}/\{\sqrt{2\pi}\lambda_\omega$, with $\Delta S_{n,max}$ a normal or shear stress range scaling parameter, the spectrum width $\lambda_\omega = 1.4$ and the spectrum mean value $\mu_\omega = 5$. For the uniaxial mode-{I, III} VA conditions the time trace global mean $\{R_I, R_{III}\} = \{0.1, -1\}$, similar to the CA values. The $\tau(t)$ and $\sigma(t)$ time series for the mixed mode-{I, III} VA conditions are the same, except for the von Mises based scaling of the magnitude and the 90 [deg] phase shift for the NP conditions. Like for the CA case, the time trace global mean $\{R_I, R_{III}\} = \{0.1, -1\}$.

To make sure sufficient statistical variability is accounted for [49], the time trace length is $5 \cdot 10^4$ cycles. However, the length is relatively large and the time trace may contain extremes at a very small probability of occurrence exceeding 3 times the time trace standard deviation, but should be prevented for to avoid yielding. A clipping ratio corresponding to 3 time the time trace standard deviation has been introduced to cut off the extremes; both the maxima and the minima (Fig. 5.8). Since the global mean value of the generated time traces is zero; i.e. $R = -1$, a shift is applied if $R = 0.1$ is required. The time trace irregularity factor I_r, defined as the ratio of the number of zero up-crossings and the number of peaks, a bandwidth measure, has been set to $I_r = 0.88$ and resembles a typical wave irregularity encountered by maritime structures

A von Mises based structural stress $S_s - N$ plot (Fig. 5.9) of the obtained test results (Tables F.1 and F.2) shows the initial fatigue resistance data scatter. Distinct strength and mechanism contributions can be observed comparing uniaxial mode-I and mode-III results for both CA and (maximum range $S_{s,max}$ signed) VA loading conditions. The mode-I F_n and M_b results are not very well aligned and might be a consequence of volume effects and/or failures at the start/stop location. Even the different notch stress gradients could provide a contribution. At first glance, the uniaxial AW and SR mode-{I, III} data does not show a significantly different fatigue strength, suggesting residual stress might not be involved at all in support of the hardness distribution maps (Section 5.2.2). The uniaxial mode-I and mixed mode-{I, III} test data seems to align; similar to literature data [130]. Note that N for the multiaxial data is based on the mode-I contribution only, since no multiaxial cycle counting is involved. Mean stress effects are not incorporated and may partially explain why the mode-III data tested at $R = -1$ shows a relatively large fatigue strength in comparison to the other data obtained at $R = 0.1$. The $S_{s,max}$ value for the mode-III VA data exceeds the yield strength. Avoiding far field stress cycles with an elastoplastic response was preferred, but turned out to be inevitable because of the aim to obtain failures in the MCF region.

As soon as a through-thickness crack has developed at the position of the fabrication defined weakest link along the weld seam (Fig. 5.10), the adopted failure criterion, the fracture surfaces can be observed and distinct patterns can be distinguished (Fig. 5.11). Some highlights will be addressed.

The fracture surfaces for the mode-I CA and VA data turned out to be relatively smooth, similar, as well as loading and response level invariant. A semi-elliptical shape has grown in through-thickness direction (Fig. 5.11a and 5.11b). For the mode-III CA and VA data, the fracture surface characteristic pattern appeared to be
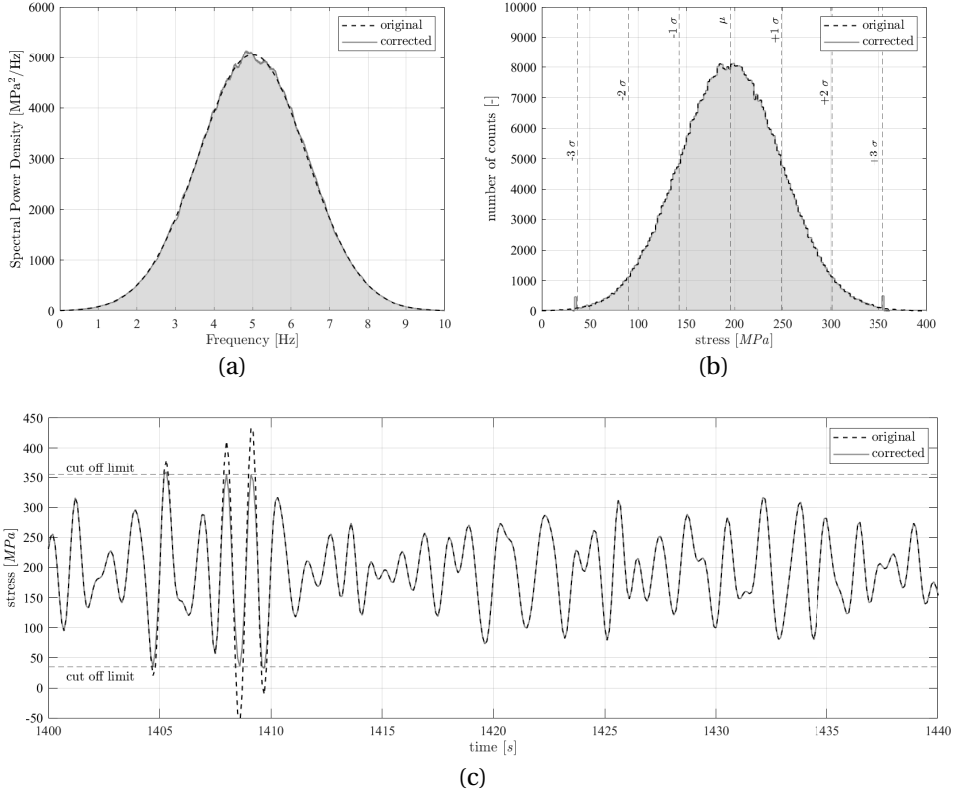
Figure 5.8.: Description of the Gaussian load sequence for the VA mode-I bending moment M_b test with $\Delta\sigma_{n,max} = 320$ [MPa]. Gauss distributed frequency spectrum (a), histogram of counted cycles (b) and time trace (c). Original and after extreme values cut off.

loading and response level dependent. At higher load level (Fig. 5.11c), the crack developed straight along the weld seam and looks similar to the mode-I equivalent. Reducing the load level (Fig. 5.11d), the characteristic V (for $R_{III} > 0$) or X ($R_{III} < 0$) shapes tend to become more apparent [e.g. 198, 199]. Differences for CA and VA did not seem significant. Mixed mode-{I, III} P CA and VA loading and response conditions come along with mixed fracture characteristic contributions. Comparing the crack surfaces for higher (Fig. 5.11e) and lower (Fig. 5.11f) load levels, a mode-III induced load level dependency is observed and the V or X shapes can be distinguished more and more clearly. Although mixed mode-{I, III} characteristic fracture contributions can still be distinguished for the NP CA and VA loading and response conditions, including a mode-III induced load level dependency (Fig. 5.11g and 5.11h), the mode-I contribution is more dominant than observed for the mixed mode-{I, III} P crack surfaces (Fig. 5.11e and 5.11f). The fracture surfaces for
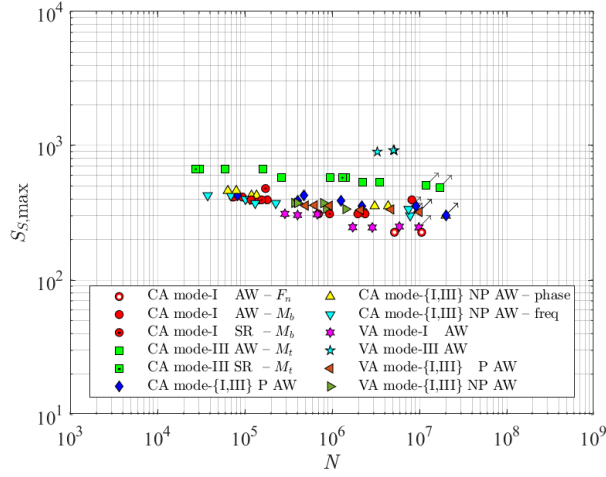
Figure 5.9.: Hexapod fatigue test data.
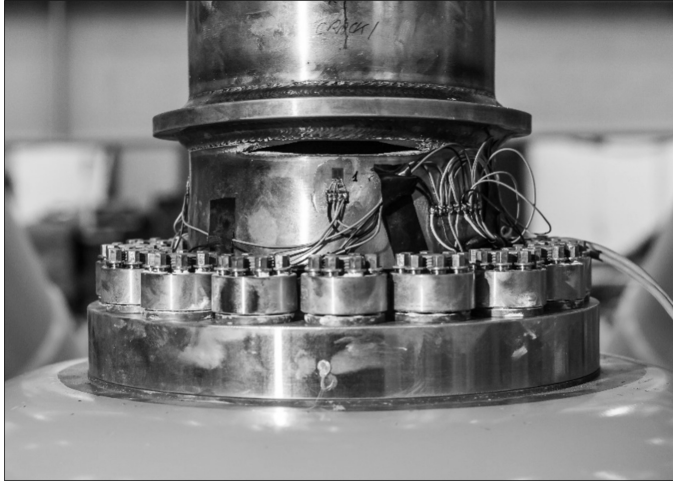
Figure 5.10.: Specimen in hexapod after fatigue failure with through-thickness crack.

the mixed-mode-{I, III} P $\sigma : \tau = 1 : 3$ ratio shows the mode-III induced load level dependent characteristics as well (Fig. 5.11i and 5.11j). Note that the extent of the V or X shaped pattern is observed to be in between the ones of the uniaxial mode-III and multiaxial mode-{I, III} P conditions (Fig. 5.11d, 5.11f and 5.11i); a frequency effect.

Last but not least, the life time scatter σ_N of the individual uniaxial and multiaxial $S_{s,max} - N$ data series (Fig. 5.9) correlates roughly speaking to the contribution of
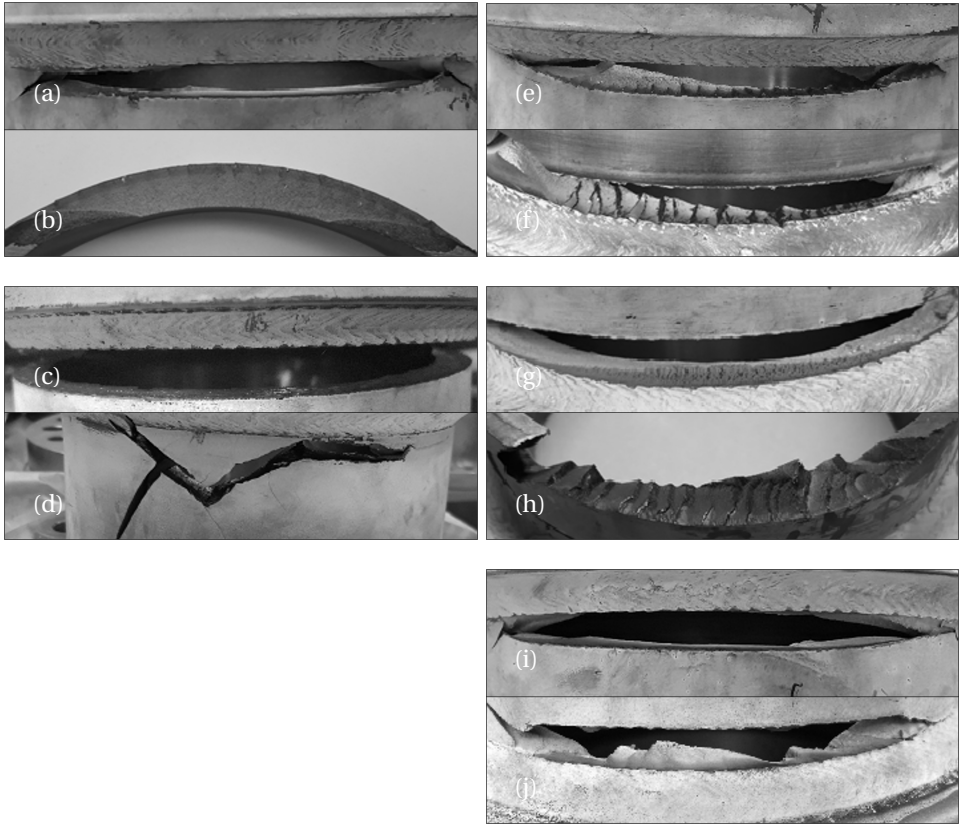
Figure 5.11.: Fracture surface characteristics for mode-I (a, b), mode-III (c, d), mixed
mode-{I, III} P (e, f), mixed mode-{I, III} NP (g, h), mixed mode-{I, III}
P with frequency ratio $\sigma : \tau = 1 : 3$ (i, j).

the mode-III induced X or V shaped characteristic to the fracture surface pattern
(Fig. 5.11); i.e. the more pronounced, the larger σ_N Table 5.6.

Table 5.6.: σ_N for individual $S_{s,max} - N$ data series.

load case	σ_N
mode-I	0.15
mode-III	0.33
mode-{I, III} P	0.32
mode-{I, III} NP – phase	0.13
mode-{I, III} NP – frequency	0.13

5.3. Multiaxial fatigue resistance

The fatigue damage process involves an initiation and growth contribution [1] and can be modelled using a fatigue strength parameter S in order to obtain a life time estimate N [6]. Since far field response spectra of welded joints in steel maritime structures reflect predominantly linear elastic behaviour, S is typically of the stress – rather than strain or energy – type, in particular for mid- and high-cycle fatigue [14]. Correlation of S and N in the mid-cycle fatigue range often reveals a log–log linear relation and a Basquin type of formulation is naturally adopted: $\log(N) = \log(C) - m \cdot \log(S)$; a resistance curve. Intercept $\log(C)$ and slope m are respectively mode specific and material characteristic strength and damage mechanism coefficients. Using maximum likelihood based regression on life time, $\max\{\mathscr{L}(\Phi; N|S); \Phi\}$, introduces a life time scatter (i.e. performance) parameter σ_N [18, 57] and the most likely parameter vector estimate $\Phi = \{\log(C), m, \sigma_N\}$ can be obtained. The lifetime N in the mid-cycle fatigue range is assumed to be log(Normal) distributed [16, 29]. Scatter band index $T_{\sigma S} = 1 : (S_{10}/S_{90})$, the fatigue strength ratio for 10 [%] and 90 [%] probability of survival [200] is adopted for strength performance evaluation purposes.

A major part of the fatigue life time N is predominantly spent in the weld notch affected region, suggesting the fatigue strength parameter S could be a notch characteristic intact geometry parameter like the effective notch stress S_e [130]. At the same time, the notches inevitably contain welding induced defects. The actual initiation (i.e. nucleation) contribution to the total fatigue life time is virtually eliminated and growth is governing, suggesting a cracked geometry parameter like the total stress S_T incorporating the notch characteristics seems justified as well [197].

For mixed mode-{I, III} multiaxial response conditions of planar and tubular (maritime) structures, the mode-I contribution is governing [130, 197]. The normal stress is predominant, explaining why a mode-I equivalent normal stress based von Mises type of failure criterion:

$$S_e = \sqrt{S_{e,I}^2 + \beta(N) S_{e,III}^2} \tag{5.1}$$

or

$$S_T = \sqrt{S_{T,I}^2 + \beta(N) S_{T,III}^2} \,, \tag{5.2}$$

is adopted. Rather than a constant shear strength coefficient, a life time dependent one:

$$\beta(N) = C_\beta \cdot N^{M\beta} \tag{5.3}$$

with

$$C_\beta = 10^{[\log(C_I) \cdot m_{III} - \log(C_{III}) \cdot mI]/[m_I \cdot m_{III}]}$$

and

$$M_\beta = (m_I - m_{III})/(m_I \cdot m_{III}),$$

has been introduced to cover the mode-{I, III} strength and mechanism contributions $\{\log(C_I), \log(C_{III}), m_I, m_{III}\}$ for welded joints in steel structures [130, 197].

Since cracks at weld notches typically develop first in plate thickness direction, the fracture plane is identified as the decisive one and is selected for criterion evaluation. Cycles are counted – adopting a time domain approach – in the von Mises plane. Using a 1st order moment formulation, differences between the actual response path and the (straight) range for each cycle i have been used to incorporate a cycle-by-cycle non-proportionality effect in terms of C_{np}, including a material characteristic contribution c_m:

$$S_{e,eff} = S_{e,i}(1 + c_m \cdot C_{np,i}) \tag{5.4}$$

or

$$S_{T,eff} = S_{T,i}(1 + c_m \cdot C_{np,i}). \tag{5.5}$$

In order to obtain an equivalent fatigue strength parameter for VA data fitting the mode-I CA data scatter band, a linear damage accumulation model is adopted. For damage $D = 1$ rather than a smaller value [15, 130, 201], reflecting failure:

$$S_{e,eq} = \left[\sum \{n_i(S_{e,eff,i}) \cdot S_{e,eff,i}^{m_I}\}/N \right]^{1/m_I} \tag{5.6}$$

or

$$S_{T,eq} = \left[\sum \{n_i(S_{T,eff,i}) \cdot S_{T,eff,i}^{m_I}\}/N \right]^{1/m_I}. \tag{5.7}$$

Using S_e (Section 5.3.1) and S_T (Section 5.3.2), the uniaxial mode-I and mode-III resistance (Section 5.3.3) will be investigated first for reference purposes, before the mixed-mode-{I, III} fatigue characteristics will be established (Section 5.3.4). Particular attention will be paid to the strength and mechanism contributions, as well as the parameter coefficient confidence [e.g. 202] to be able to evaluate if quality dependent resistance curves or just one for all data would be preferred.

5.3.1. FATIGUE STRENGTH PARAMETER S_e

The through-thickness weld notch stress distributions along the expected (2D) crack path – defining the fracture plane – are assumed to be a key element for an appropriate fatigue design and detectable repair criterion [16]. Semi-analytical mode-{I, III} formulations $\{\sigma_n(r/t_p, \sigma_s), \tau_n(r/t_p, \tau_s)\}$, with plate thickness t_p either the base plate or cross plate value, t_b or t_c, have been developed for both non-symmetry and symmetry with respect to half the plate thickness $(t_p/2)$, in case of both zero and finite notch radius ρ [16, 29]. Adopting a linear superposition principle, far field related equilibrium equivalent and self-equilibrium parts $\{\sigma_{fe}, \sigma_{se}; \tau_{fe}, \tau_{se}\}$ have been distinguished, involving three components: the notch stress, the weld-load carrying stress and the far field stress. Typically three zones can be identified in all distributions: the zone 1 peak stress value, the zone 2 notch-affected stress gradient and the zone 3 far-field dominated stress gradient. Excellent performance is proven in comparison to finite element (FE) solutions, like illustrated (Fig. 5.12a and 5.12b, Fig. 5.13a and 5.13b) for the fatigue specimen geometry (Section 5.2.2), meaning numerical modelling [e.g. 203] is not required to estimate the effective notch stress S_e.

Taking advantage of $\{\sigma_n(r/t_p, \sigma_s), \tau_n(r/t_p, \tau_s)\}$, S_e can be calculated averaging the notch stress distribution along the expected crack path over a material characteristic length ρ^*; another mechanism parameter. Uniaxial mode-I and mode-III investigations for welded joints in steel (maritime) structures revealed distinguished $\{\rho_I^*, \rho_{III}^*\}$ as well as $\{\log(C_I), \log(C_{III})\}$ and $\{m_I, m_{III}\}$ values [14, 16, 29]. Since a response cycle needs two parameters for a complete spatial description, e.g. range $S = (S_{max} - S_{min})$ and ratio $R = (S_{min}/S_{max})$, mode specific response ratio coefficients $\{\gamma_I, \gamma_{III}\}$; additional strength parameters, have been discovered as well to obtain an effective formulation [130]: $S_{e,eff} = S_e/(1-R)^{1-\gamma}$. If both AW and SR test data are jointly considered, an explicit residual stress measure S_r has been introduced to cover the thermal condition, turning the ratio into: $R_r = (S_{e,min} + S_r)/(S_{e,max} + S_r) = \{R \cdot S_e + S_r(1-R)\}/\{S_e + S_r(1-R)\}$. Dedicated $\{\rho_{I,AW}^*, \rho_{I,SR}^*\}$ and $\{\gamma_{I,AW}, \gamma_{I,SR}\}$ mode-I contributions are established. The mean (residual) stress – reflected in R_r – hardly affects the mode-III fatigue resistance [130], explaining why no ratio contribution is involved. Coefficient $\gamma_{III} = 1$, regardless the thermal condition. For $S = S_e$, regression analysis provides the most likely extended parameter vector estimates $\Phi = \{\log(C), S_r, \gamma_{I,AW}, \gamma_{I,SR}, m_I, \rho_{I,AW}^*, \rho_{I,SR}^*, \rho_{III}^*, \sigma_N\}$ to obtain the mode-{I, III} effective notch stress contributions:

$$S_{e,I} = \frac{S_{e,I}}{(1-R_{r,I})^{1-\gamma_I}} = \int_0^{\frac{\rho_I^*}{t_p}} \frac{\sigma_n\left(\frac{r}{t_p}, \Delta\sigma_s\right)}{(1-R_{r,I})^{1-\gamma_I}} \mathrm{d}\left(\frac{r}{t_p}\right) \tag{5.8}$$

and

$$S_{e,III} = \int_0^{\frac{\rho_{III}^*}{t_p}} \tau_n\left(\frac{r}{t_p}, \Delta\tau_s\right) \mathrm{d}\left(\frac{r}{t_p}\right). \tag{5.9}$$

The involved far field stress information $\{\Delta\sigma_s, r_{\sigma s}; \Delta\tau_s, r_{\tau s}\}$ is calculated using nodal force output of relatively coarse meshed shell/plate FE models [41, 47, 113], providing the structural normal stress range: a superposition of a constant membrane and linear bending contribution: $\Delta\sigma_s = \Delta\sigma_{sm} + \Delta\sigma_{sb}$, as well as the structural shear stress range: $\Delta\tau_s = \Delta\tau_{ss} + \Delta\tau_{st}$, involving a constant shear and linear torsion contribution. The structural normal and shear stress ratios: $r_{\sigma s} = (\Delta\sigma_{sb}/\Delta\sigma_s)$ and $r_{\tau s} = (\Delta\tau_{st}/\Delta\tau_s)$ reflect the far field stress gradients [16, 29].

Figure 5.12.: Mode-I weld toe notch stress distributions (a, b), SIF far field- and notch distributions (c, d) and K_I distributions (e, f) for the specimen geometry (Fig. 5.2) with respectively $\rho = 0$ (a, c, e) in a worst case scenario and the measured $\rho = 3.0$ (b, d, f).
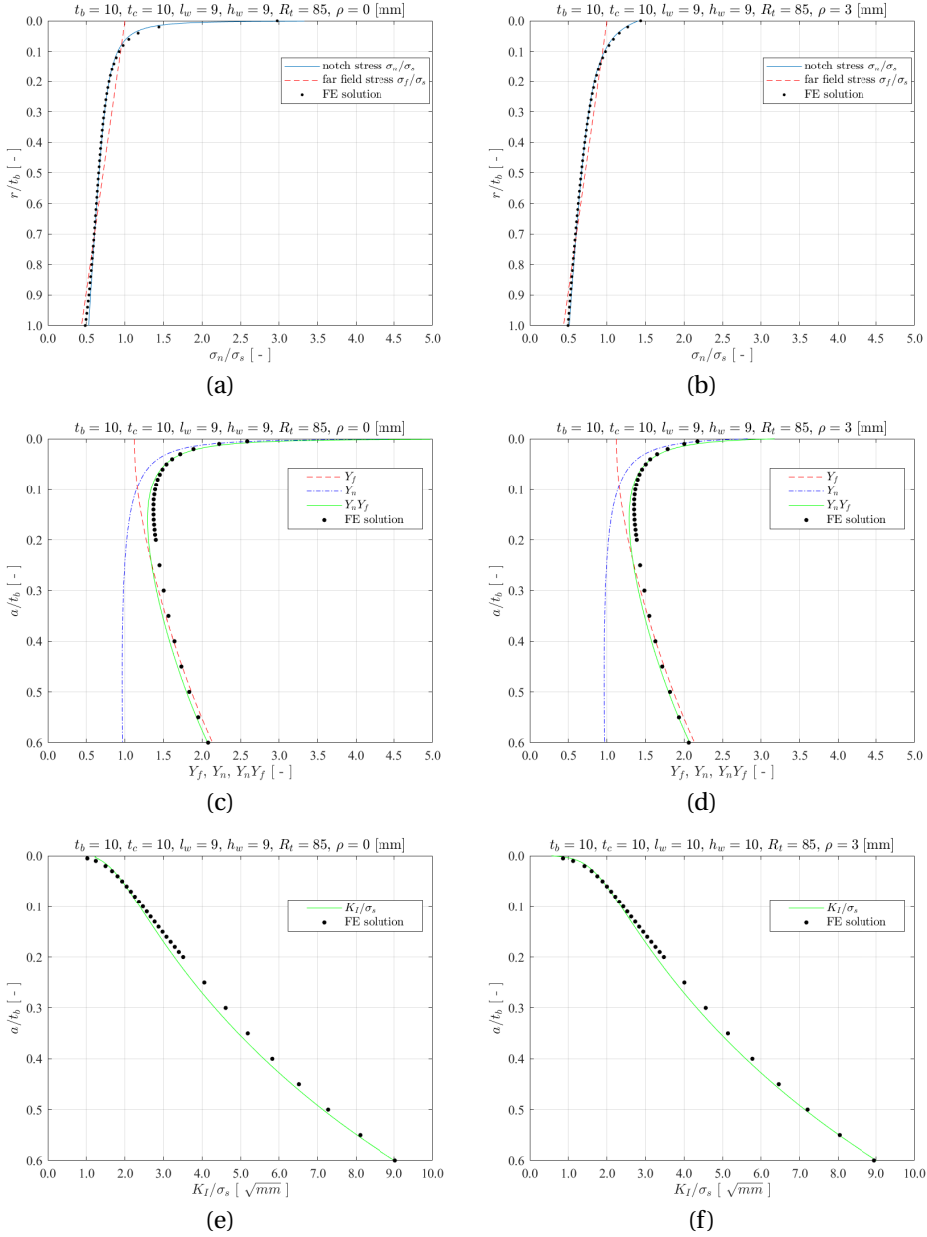
Figure 5.13.: Mode-III weld toe notch stress distributions (a, b), SIF far field- and notch distributions (c, d) and K_{III} distributions (e,f) for the specimen geometry (Fig. 5.2) with respectively $\rho = 0$ (a, c, e) in a worst case scenario and the measured $\rho = 3.0$ (b, d, f).
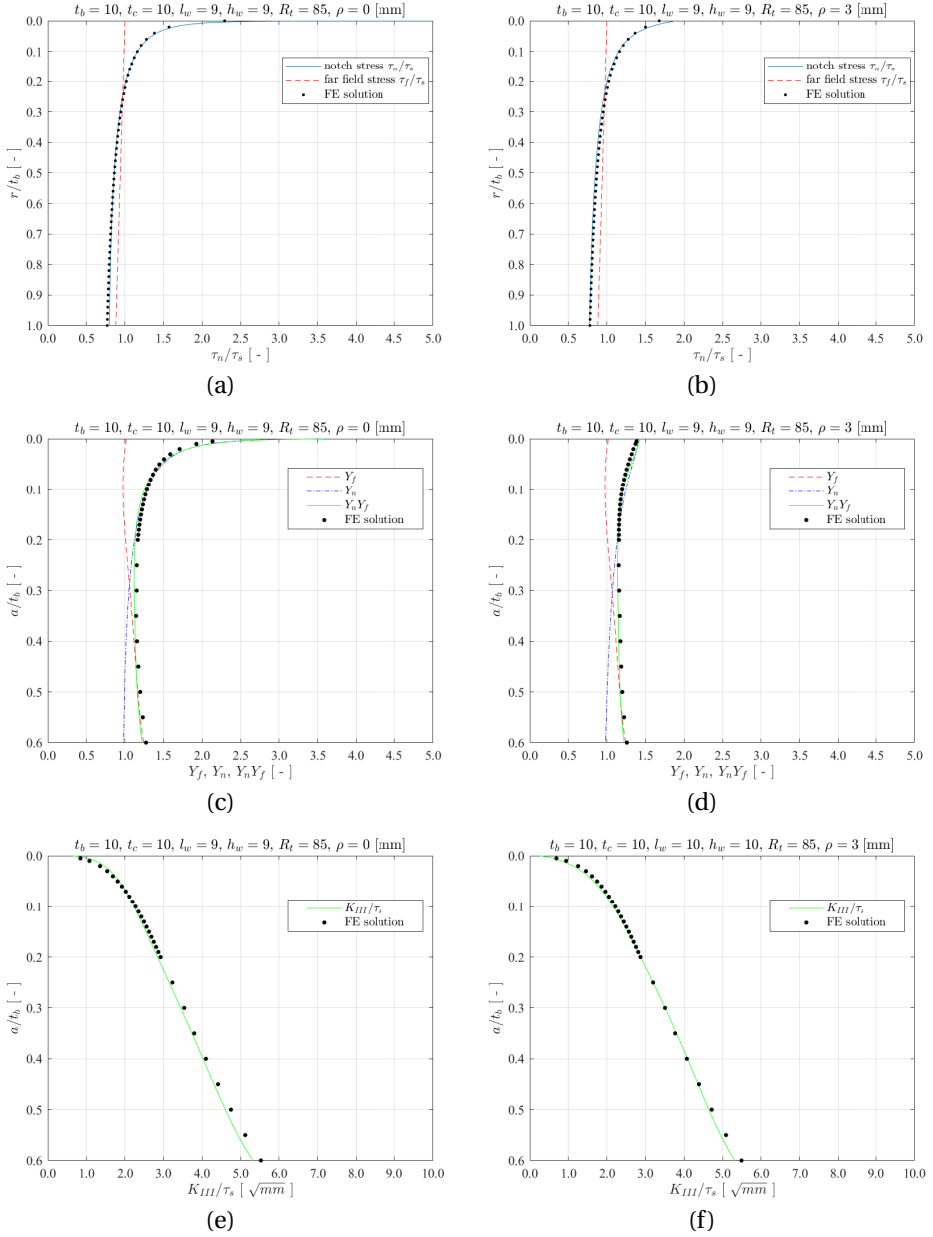
5.3.2. Fatigue strength parameter S_T

Converting the intact geometry related weld toe notch stress distribution expressions into crack damaged equivalents [197], the zone {1, 2} self-equilibrium and zone 3 equilibrium equivalent stress parts $\{\sigma_{fe}(r/t_p), \sigma_{se}(r/t_p); \tau_{fe}(r/t_p), \tau_{se}(r/t_p)\}$ have been used to obtain respectively a notch factor $Y_n(a/t_p)$ and a far field factor $Y_f(a/t_p)$, defining the weld toe notch stress intensity factor (SIF) for respectively mode-I and mode-III: $K_I = \sigma_s \sqrt{t_p} Y_{n,I}(a/t_p) Y_{f,I}(a/t_p) \sqrt{\pi(a/t_p)}$ and $K_{III} = \tau_s \sqrt{t_p} Y_{n,III}(a/t_p) Y_{f,III}(a/t_p) \sqrt{\pi(a/t_p)}$. In comparison to FE solutions, excellent performance is proven for the semi-analytical stress intensity $\{Y_{n,I} Y_{f,I}, Y_{n,III} Y_{f,III}\}$ as well as the SIF $\{K_I, K_{III}\}$ formulations, like illustrated (Fig. 5.12c and 5.12d, 5.12e and 5.12f; Fig. 5.13c and 5.13d, 5.13e and 5.13f) for the fatigue specimen geometry (Section 5.2.2). Numerical modelling [164, 204] is not required.

Cyclic loading induced response conditions turn the SIF's $\{K_I, K_{III}\}$ into crack growth driving forces $\{\Delta K_I, \Delta K_{III}\}$ and defects may develop into cracks. The crack growth rate (da/dn) of short-cracks emanating at notches show elastoplastic wake field affected anomalies [18]. Modifying Paris' equation, a generalised two-stage model has been established containing a transition from a short to a long crack growth region meant to incorporate all relevant crack growth driving force components [143–145]; i.e. to include both the weld notch- and far field characteristic mode-{I, III} response contributions: $(da/dn)_I = C_I \cdot Y_{n,I}^{n,I} \cdot \{\Delta\sigma_s \cdot Y_{f,I} \cdot \sqrt{\pi a}\}^{m_I}$ and $(da/dn)_{III} = C_I \cdot Y_{n,III}^{n,III} \cdot \{\Delta\tau_s \cdot Y_{f,III} \cdot \sqrt{\pi a}\}^{m_I II}$. Notch elastoplasticity coefficients $\{n_I, n_{III}\}$; mechanism parameters, are response dependent and define the level of monotonically increasing or non-monotonic crack growth behaviour. For a complete spatial description, R_r has been introduced like for S_e, adding $\{\gamma_I, \gamma_{III}\}$ as strength parameters. Applying an integral operator on the individual mode-{I, III} crack growth models provides mid-cycle fatigue related resistance relations of the Basquin type: $\log(N_I) = \log(C_I) - m_I \log(S_{T,I})$ and $\log(N_{III}) = \log(C_{III}) - m_{III} \log(S_{T,III})$, with the mode-{I, III} total stress contributions [197]:

$$S_{T,I} = \frac{S_{T,I}}{(1 - R_{r,I})^{1-\gamma_I}} = \frac{\Delta\sigma_s}{\left(1 - R_{r,I}\right)^{1-\gamma_I} \cdot I_{N,I}^{\frac{1}{m_I}} \cdot t_p^{\frac{2-m_I}{2m_I}}} \tag{5.10}$$

with

$$I_{N,I} = \int_{\frac{a_i}{t_p}}^{\frac{a_f}{t_p}} \frac{1}{\left\{Y_{n,I}\left(\frac{a}{t_p}\right)\right\}_I^n \cdot \left\{Y_{f,I}\left(\frac{a}{t_p}\right)\right\}_I^m \cdot \left(\frac{a}{t_p}\right)^{\frac{m_I}{2}}} \, d\left(\frac{a}{t_p}\right)$$

and

$$S_{T,III} = \frac{S_{T,III}}{(1 - R_{r,III})^{1-\gamma_{III}}} = \frac{\Delta\sigma_s}{\left(1 - R_{r,III}\right)^{1-\gamma_{III}} \cdot I_{N,III}^{\frac{1}{m_{III}}} \cdot t_p^{\frac{2-m_{III}}{2m_{III}}}} \tag{5.11}$$

with

$$I_{N,III} = \int_{\frac{a_i}{t_p}}^{\frac{a_f}{t_p}} \frac{1}{\left\{Y_{n,III}\left(\frac{a}{t_p}\right)\right\}_{III}^{n} \cdot \left\{Y_{f,III}\left(\frac{a}{t_p}\right)\right\}_{III}^{m} \cdot \left(\frac{a}{t_p}\right)^{\frac{m_{III}}{2}}} \, \mathrm{d}\left(\frac{a}{t_p}\right)$$

Regression analysis provides the most likely extended parameter vector estimates: $\Phi = \{\log(C), S_r, \gamma_{I,AW}, \gamma_{I,SR}, m_I, n_{I,AW}, n_{I,SR}, n_{III}, \sigma_N\}$. Thermal conditions require distinguished mode-I elastoplasticity coefficients $\{n_{I,AW}, n_{I,SR}\}$. Mode-III mean (residual) stress effects are insignificant, explaining $\gamma_{III} = 1$. Scaling parameters $\{t_p^{(2-m_I)/(2m_I)}, t_p^{(2-m_{III})/(2m_{III})}\}$ take the response gradient induced size effects into account. Rather than a sufficiently small welding induced defect size (a_i/t_p) providing a converged notch crack growth integral solutions $\{I_{N,I}, I_{N,III}\}$, an arc-welding induced most likely material characteristic estimate has been established; $(a_f/t_p) = 1$ is based on a through-thickness crack criterion.

5.3.3. Uniaxial reference resistance

The S_e based uniaxial mode-I mid-cycle fatigue reference resistance for planar and tubular geometries in steel (maritime) structures, involving hot spot types {A, B, C} and both AW and SR thermal conditions, has already been established for CA and VA literature data [16, 130].

In order to fit for tubular geometries the SR literature data in the AW literature data scatter band, a residual stress component S_r – a strength related quality aspect – has been introduced. Since the AW thermal condition is considered to be the reference case for fatigue design, S_r is applied to the SR data explaining the compressive value [130]. However, in contrast to the literature data, the fatigue strength of the AW and SR hexapod data is similar (Fig. 5.9), suggesting that no residual stress is involved at all. To fit the mid-cycle fatigue hexapod data into the literature data scatter band, S_r should apply for both the AW and SR thermal conditions. Adopting the most likely reference parameter estimates for regression analysis of both the literature and hexapod tubular data, though, reduces the S_e performance as reflected in the data touching the lower and upper bound of the literature data scatter band (Fig. 5.14a). The life time scatter parameter σ_N increased from 0.27 [130] to 0.29, obtained for $\Phi = \{\sigma_N\}$. Regression of the hexapod data only provides $\sigma_{N,I} \sim 0.38$; quite worse. Note that the high-cycle fatigue hexapod data $(N > 5 \cdot 10^6)$ is not assessed since no literature data is available for reference purposes. The average weld quality reference data (Section 5.2.2) is added for convenience and illustrates the fit in the literature data scatter band.

Using the actual notch radius ρ (Table 5.4) – a geometry related quality aspect, rather than a conservative lower bound $\rho = 0$ like adopted for the literature data [14, 130] affects S_e (Eq. 5.1) of the hexapod data just up to a minor extent, since $\{\rho_{I,AW}^*, \rho_{I,SR}^*\}$ is relatively large. The S_e performance did not change (Fig. 5.14a).

An important observation is that the VA and CA hexapod data is not well aligned – although the data fits in the literature data scatter band – and seems a result of inaccurate strength and mechanism contributions; i.e. inaccurate intercept $\log(C_I)$

and slope m_I. The welding quality of the reference and hexapod data at materials level as reflected in the micro-structure composition is not significantly different (Fig. 5.7), explaining why the mode and material characteristic ρ^* is reasonably assumed to be similar for both data sets. However, the imaginary slope of the hexapod data (Fig. 5.9 and 5.14a) seems relatively large in comparison to the literature data, suggesting another mechanism contribution. Observing the hardness distributions (Fig. 5.5), smaller values are obtained for the HAZ and FZ in the hexapod welds – relative to the reference ones, implying a lower cooling rate being typically responsible for reduced residual stress levels as well as decreased number and size of welding induced defects. A larger contribution of crack initiation (i.e. short crack growth) to the total life time as a result of residual stress not being involved and a smaller welding induced defect size seems a reasonable explanation, justifying a regression analysis of the hexapod only in order to establish the S_e performance and dedicated most likely parameter estimates. For $\Phi = \{\log(C_I), S_r, \gamma_{I,AW}, \gamma_{I,SR}, m_I, \rho^*_{I,AW}, \rho^*_{I,SR}, \sigma_{N,I}\}$, slope $m_I \sim 7.5$, a most likely estimate in between the typical $m_I = 3$ for arc-welded joints and base material value $m_I \sim 13$ [205]. The material characteristic length estimates $\{\rho^*_{I,AW}, \rho^*_{I,SR}\}$ are similar and comparable to the literature data based values, confirming that heat treatment did not affect the hexapod data fatigue resistance as well as that based on the micro-structure composition (Fig. 5.7) the quality of the hexapod and literature data at materials level is comparable indeed. Intercept $\log(C_I)$, reflecting the fatigue strength, naturally increased because of the $\log(C)$-m correlation for a log-log linear $S_e - N$ MCF Basquin type of relation [14]. The $S_r \sim 0$ estimate basically confirms that residual stress does not affect the hexapod fatigue strength quality. Since the (mean) residual stress affects $\{\gamma_{I,AW}, \gamma_{I,SR}\}$, the most likely estimates are different from the literature data based values. As the hexapod mode-I data size is relatively small and the specimen geometry and loading conditions do not contain sufficient variability, the AW data became the reference for the SR ones. The life time scatter parameter reduced to $\sigma_{N,I} = 0.21$; way below the reference data value, suggesting at first glance that an exclusive high quality hexapod data resistance curve makes sense (Fig. 5.14b). The fatigue strength scatter band index $T_{\sigma e, I} = 1 : 1.36$. Note that the VA hexapod data fits the CA data scatter band for the representative $\log(C_I)$ and m_I.

Because of the relatively small hexapod data size, the parameter confidence intervals are relatively large in comparison to the ones of the reference data, like illustrated for the 75 [%] bounds (Table 5.7). Comparing the mode-I R95C75 quantiles reflecting a probability of survival $p_s = 0.95$ (Fig. 5.14a and 5.14b), a dedicated resistance curve for the high-quality hexapod mode-I data seems to provide more accurate life time estimates for fatigue design purposes indeed. For general applicability the reference data curve should still be used in order to obtain conservative N values.

Principally, the (mean) residual stress quality aspect does not affect the mode-III welded joint fatigue resistance [29, 130], meaning S_r is not involved nor dedicated AW and SR γ parameters are distinguished. The actual notch radius (Table 5.4); a geometry quality aspect, has to be incorporated since the mode-III damage accumulation is in comparison to mode-I a (near) surface phenomenon to an even

Table 5.7.: Mode-{I, III} resistance S_e parameter likelihood estimates and 75 [%] lower and upper confidence bounds.

parameter	reference data		hexapod data	
$\log(C_I)$	13.28	[13.20, 13.36]	25.45	[22.59, 28.32]
m_I	3.12	[3.08, 3.15]	7.55	[6.47, 8.64]
$\rho^*_{I,AW}$	1.34	[1.22, 1.45]	/	/
$\rho^*_{I,SR}$	3.85	[3.56, 4.16]	/	/
$\gamma_{I,AW}$	0.90	[0.88, 0.91]	/	/
$\gamma_{I,SR}$	0.89	[0.87, 0.91]	/	/
S_r	-144	[-144, -143]	0	[-1, 1]
$\sigma_{N,I}$	0.21	[0.19, 0.23]	0.21	[0.16, 0.25]
$\log(C_{III})$	18.91	[18.17, 19.64]	52.00	[46.05, 57.96]
m_{III}	5.12	[4.85, 5.37]	17.87	[15.58, 20.15]
$\rho^* III$	0.12	[0.07, 0.21]	/	/
γ_{III}	1.00	[0.98, 1.00]	/	/
$\sigma_{N,III}$	0.21	[0.19, 0.23]	0.25	[0.20 0.31]

5

greater extent, as reflected in $\rho^*_{III} < \rho^*_I$. Using the most likely reference parameter estimates for regression analysis of both the literature and hexapod tubular data significantly reduces the S_e performance (Fig. 5.14c): σ_N increased from 0.21 [29] to 0.31, obtained for $\Phi = \{\sigma_N\}$. Regression of the hexapod data only provides $\sigma_{N,III} \sim 0.30$. Because of similar micro-structure composition for the reference and hexapod welds (Fig. 5.7), ρ^*_{III} is not expected to be responsible for the reduced performance. Like for mode-I (Fig. 5.14a), the imaginary slope is relatively large in comparison to the literature data (Fig. 5.14c). Based on the comparison of the hardness distributions for the reference and hexapod welds (Fig. 5.5), an increased contribution of crack initiation to the total life time explains the change in mechanism, in slope m_{III}. Regression analysis for $\Phi = \{\log(C_{III}), \gamma_{III}, m_{III}, \sigma_{N,III}\}$ provides slope $m_{III} \sim 17.9$, a most likely estimate close to the base material value $m_{III} \sim 18$ [205]. Except a similar micro-structure composition, the specimen geometry and loading conditions variability is insufficient nor different thermal conditions are involved, explaining why the reference material characteristic length is adopted: $\rho^*_{III} \sim 0.12$. Intercept $\log(C_{III})$, reflecting the fatigue strength, naturally increased because of the $\log(C) - m$ correlation. Mean (residual) stress does not affect the hexapod fatigue strength quality, as reflected in the $\gamma_{III} \sim 1$ estimate. The life time scatter parameter reduced to $\sigma_{N,III} = 0.25$; an improvement in comparison to the $\sigma_{N,III} \sim 0.30$ estimate as obtained for using the reference parameter values (Fig. 5.14d). The fatigue strength scatter band index $T_{\sigma S_e,III} = 1 : 1.14$.

Like for mode-I, the parameter confidence intervals are relatively large in comparison to the ones of the reference data, as illustrated for the 75 [%] bounds (Table 5.7). Comparing the mode-III R95C75 quantiles (Fig. 5.14c and 5.14d), a dedicated resistance curve for the high-quality hexapod mode-III data seems to provide more accurate life time estimates. Non-conservative N values at the mid-cycle fatigue region lower bound can even be obtained when applying the reference data curve.

Figure 5.14.: Mode-I S_e resistance with enforced reference strength and mechanism parameters (a), as well as dedicated strength and mechanism parameters (b); mode-III S_e resistance with enforced (c) and dedicated (d) reference strength and mechanism parameters.

For the total stress S_T as fatigue strength parameter (Eq. 5.2), uniaxial mode-I mid-cycle fatigue reference resistance for planar and tubular geometries in steel (maritime) structures has already been established for CA and VA literature data as well [197]. To fit the mid-cycle fatigue hexapod data into the $S_T - N$ literature data scatter band, S_r will be applied for both the AW and SR thermal conditions, since no significant residual stress is involved. At the same time, S_r affects the notch and crack tip elastoplastic behaviour, explaining why $n_{I,AW}$ has been used for all the hexapod data. Adopting the most likely reference parameter estimates, regression analysis of both the literature and hexapod tubular data for $\Phi = \{\sigma_N\}$ reduces the S_T performance as reflected in the hexapod data touching the bounds of the literature data scatter band (Fig. 5.15a), like for S_e (Fig. 5.14a): σ_N increased from 0.30 [197]

to 0.31. Regression of the mid-cycle fatigue hexapod data only provides $\sigma_{N,I} \sim 0.39$; quite worse. The average quality reference data (Section 5.2.2) is added for convenience and illustrates the fit in the literature data scatter band. Using the actual notch radius ρ (Table 5.4) – a geometry related quality aspect – affects the notch factor Y_n (Eqs. (5.10) and (5.11)) for $(a/t_p) \to 0$, but the square root singularity for small cracks close to the notch surface (radius) controls the crack growth integral I_N (Eqs. (5.10) and (5.11)); i.e. S_T, meaning the performance hardly changed (Fig. 5.15a). Like observed for S_e (Fig. 5.14a), the damage mechanism seems responsible for the different imaginary slope of the hexapod data in comparison to the literature data. The hardness distribution; a welding quality measure at materials level, supports principally the hypothesis of a larger contribution of crack initiation to the total life time because of no residual stress and a decreased number and size of welding induced defects. Regression analysis of all the hexapod data only; i.e. uniaxial and multiaxial, for $\Phi = \{\log(C_I), m_I, \sigma_{N,I}\}$ and varying defect size shows that that with respect to the life time scatter parameter $\sigma_{N,I}$ still $(a_i/t_p) \sim 6 \cdot 10^{-3}$ is the most likely estimate (Fig. 5.16). An import note, however, is that the parameters affecting (a_i/t_p) the most; in particular the mean stress and elastoplasticity coefficients $\{\gamma, n\}$, are the same as for the literature data, meaning proof of a smaller welding induced defect size would require additional test data, obtained for different geometry – in particular wall thickness t_p – and different R levels. Slope $m_I \sim 7.5$ is more than double the typical $m_I = 3$ value for arc-welded joints, confirming the change in mechanism. The elastoplasticity coefficients estimates $\{n_{I,AW}, n_{I,SR}\}$ are similar and comparable to the literature data based values, confirming that S_r did not affect the hexapod data fatigue resistance indeed as well as that notch and crack tip elastoplasticity affected short crack growth behaviour for the AW and SR data is about the same. Explanations for $\log(C_I)$, S_r and $\{\gamma_{I,AW}, \gamma_{I,SR}\}$ as provided for S_e still hold for S_T (Fig. 5.15b): respectively a natural increase because of the $\log(C) - m$ correlation, a confirmation that (mean) residual stress does not affect the hexapod data fatigue strength and the AW data being reference for the SR ones since the data size is relatively small and sufficient specimen geometry and loading condition variability is lacking. The life time scatter parameter reduced to $\sigma_{N,I} = 0.21$; way below the reference data value, suggesting an exclusive hexapod data resistance curve makes sense (Fig. 5.15b). The fatigue strength scatter band index $T_{\sigma S_{T,I}} = 1 : 1.36$. Dedicated $\log(C_I)$ and m_I parameters ensure the VA hexapod data fits the CA data scatter band. Note that the S_e and S_T performance is similar, like observed before [197].

The parameter confidence intervals are relatively large in comparison to the ones of the reference data because of the relatively small hexapod data size, like illustrated for the 75 [%] bounds (Table 5.8). The mode-I R95C75 quantiles reflect a probability of survival $p_s = 0.95$ (Fig. 5.15a and 5.15b) and suggest that a dedicated resistance curve for the high-quality hexapod mode-I data provides more accurate life time estimates for fatigue design purposes. Applying the reference data curve for general purposes provides conservative N values.

Since the residual stress hardly affects the mode-III welded joint fatigue resistance [29, 130], S_r is not involved nor dedicated AW and SR γ parameters are distinguished. The actual notch radius (Table 5.4) is incorporated since mode-III damage
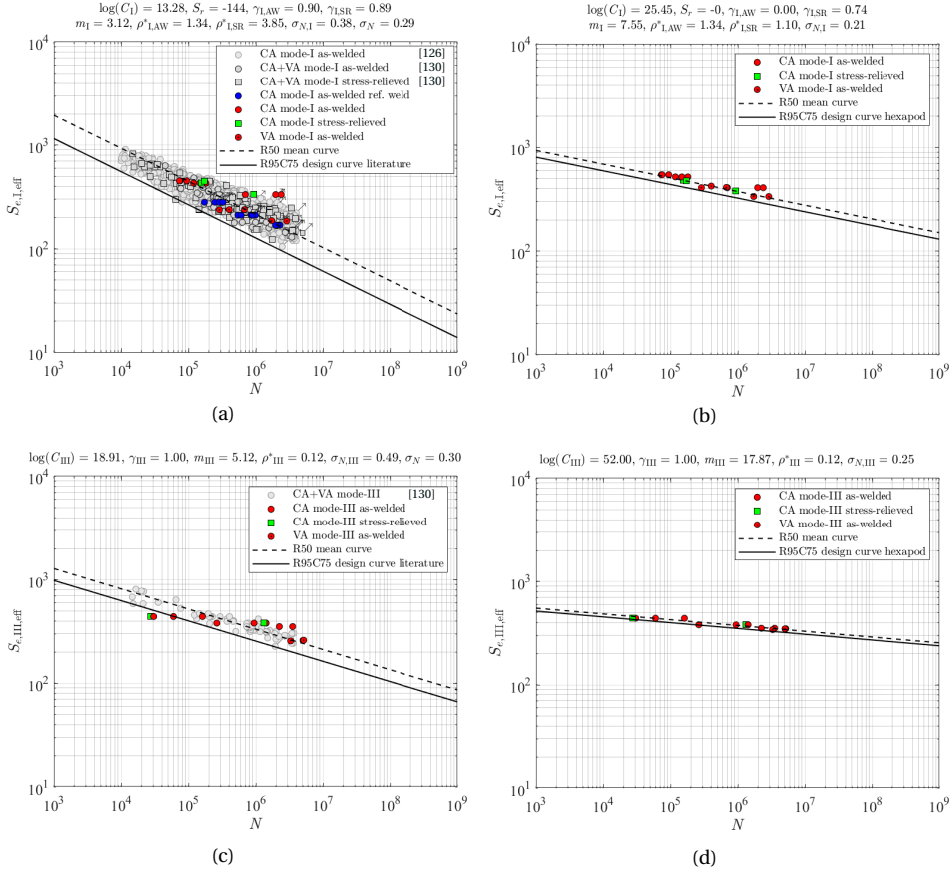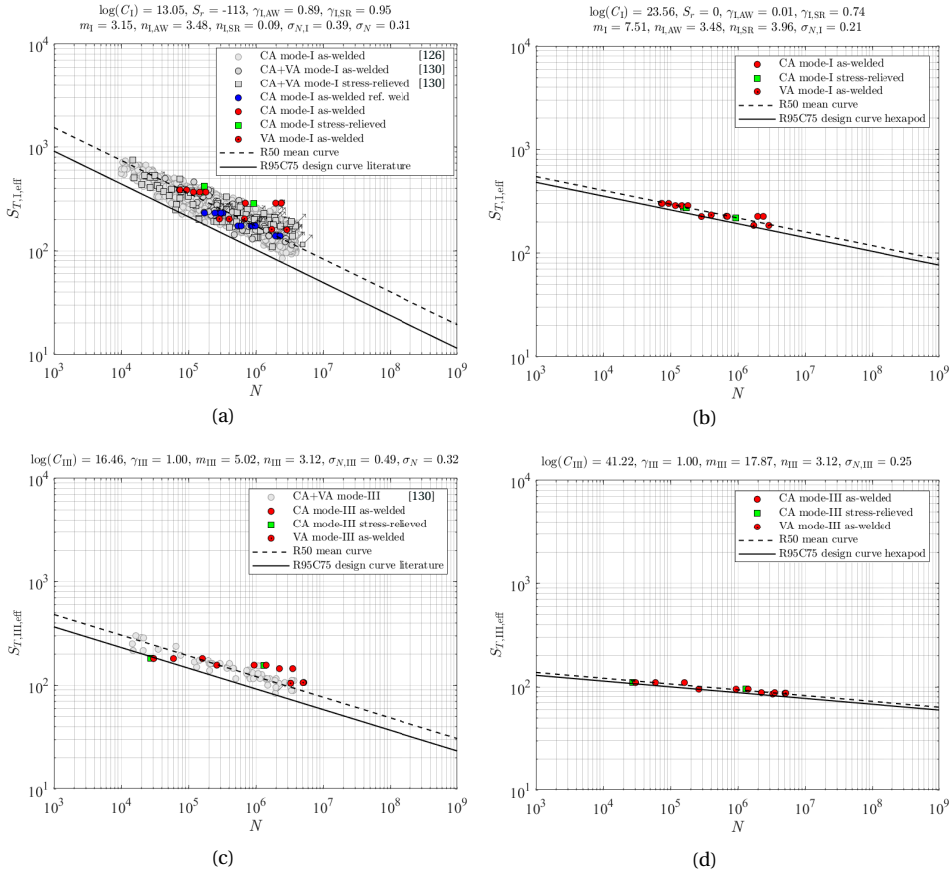
Figure 5.15.: Mode-I S_T resistance with enforced reference strength and mechanism parameters (a), as well as dedicated strength and mechanism parameters (b); mode-III S_T resistance with enforced (c) and dedicated (d) reference strength and mechanism parameters.

accumulation is a (near) surface phenomenon up to a large extent. Using the most likely reference parameter estimates for regression analysis of both the literature and hexapod tubular data significantly reduces the S_T performance (Fig. 5.15c): σ_N increased from 0.21 [197] to 0.32, obtained for $\Phi = \{\sigma_N\}$. Regression of the hexapod data only provides $\sigma_{N,III} \sim 0.49$. Since the microstructure composition for the reference and hexapod welds are similar (Fig. 5.7) and at the same time S_r – affecting the notch and crack tip elastoplastic behaviour – does not significantly influence the mode-III fatigue resistance, n_{III} is not expected to be responsible for the reduced performance. As for mode-I (Fig. 5.15a), the imaginary slope is relatively large in comparison to the literature data (Fig. 5.15c) and likely a result of an increased contribution of crack initiation to the total life time, as reflected in the hardness

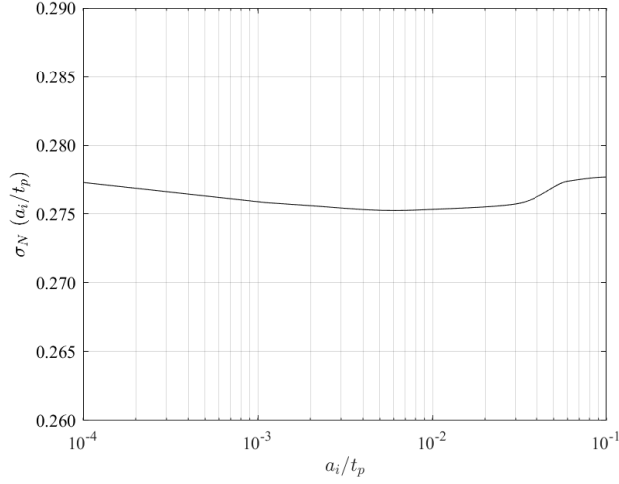Figure 5.16.: Most likely σ_N for a range of $a_i/t_p|_{a_f/t_p=1}$.

Table 5.8.: Mode-{I, III} resistance S_T parameter likelihood estimates and 75 [%] lower and upper confidence bounds.

parameter	reference data		hexapod data	
$\log(C_I)$	13.05	[12.97, 13.13]	23.56	[21.55, 25.77]
m_I	3.15	[3.11, 3.18]	7.51	[6.58, 8.53]
$n_{I,AW}$	3.48	[3.28, 3.68]	/	/
$n_{I,SR}$	0.09	[0.01, 0.17]	/	/
$\gamma_{I,AW}$	0.89	[0.88, 0.91]	/	/
$\gamma_{I,SR}$	0.95	[0.93, 0.98]	/	/
S_r	-113	[-115, -110]	0	[-1, 1]
$\sigma_{N,I}$	0.22	[0.19, 0.24]	0.21	[0.16, 0.25]
$\log(C_{III})$	16.46	[15.90, 17.02]	41.42	[36.17, 46.67]
m_{III}	5.02	[4.67, 5.37]	17.87	[15.74, 20.11]
n_{III}	3.12	[1.14, 5.09]	/	/
γ_{III}	1.00	[0.98, 1.00]	/	/
$\sigma_{N,III}$	0.21	[0.18, 0.24]	0.25	[0.20, 0.30]

distributions for the reference and hexapod welds (Fig. 5.5). Regression analysis for $\Phi = \{\log(C_{III}), \gamma_{III}, m_{III}, \sigma_{N,III}\}$ provides slope $m_{III} \sim 17.9$, a most likely estimate close to the base material value $m_{III} \sim 18$ [205]. Except a similar micro-structure composition, the specimen geometry and loading conditions variability is insufficient nor thermal conditions are involved, explaining why the reference elastoplasticity coefficient is adopted: $n_{III} \sim 3.12$. Intercept $\log(C_{III})$, reflecting the fatigue strength, naturally increased because of the $\log(C) - m$ correlation. Mean (residual) stress does not affect the hexapod fatigue strength quality, as reflected in the $\gamma_{III} \sim 1$ estimate. The life time scatter parameter reduced to $\sigma_{N,III} = 0.25$; an

improvement in comparison to the $\sigma_{N,III} \sim 0.32$ estimate as obtained for using the reference parameter values (Fig. 5.15d). The fatigue strength scatter band index $T_{\sigma S_{T,III}} = 1:1.14$.

Like for mode-I, the parameter confidence intervals are relatively large in comparison to the ones of the reference data, as illustrated for the 75 [%] bounds (Table 5.8). Comparing the mode-III R95C75 quantiles (Fig. 5.15c and 5.15d), a dedicated resistance curve for the high-quality hexapod mode-III data seems to provide more accurate life time estimates. The literature data curve may provide non-conservative N estimates.

Comparing the uniaxial mode-{I, III} MCF resistance (Fig. 5.17), σ_N illustrates a similar performance for S_e and S_T; respectively an intact and cracked geometry parameter. Linear damage accumulation up to $D = 1$ shows VA data fitting the CA data scatter band. The different strength and mechanism as reflected in $\{\log(C), \gamma\}$, as well as $\{m, \rho^*\}$ or $\{m, n\}$ for S_e and S_T respectively, suggesting a life time dependent shear strength coefficient $\beta(N)$ rather than a constant one β is required for multiaxial fatigue assessment. Note that the strength and mechanism contributions for the high-quality hexapod data is quite different from the average-quality literature data [130, 197], affecting $\beta(N)$.
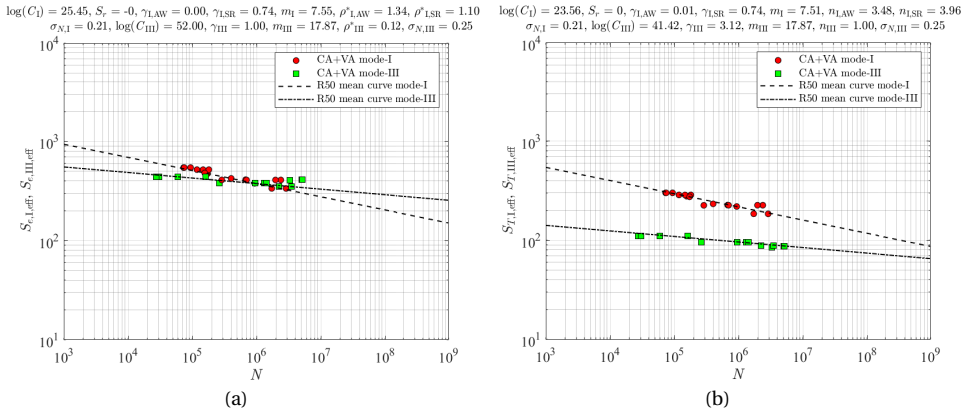
Figure 5.17.: Uniaxial mode-{I, III} hexapod data fatigue resistance for S_e (a) and S_T (b).

5.3.4. MULTIAXIAL RESISTANCE

Adopting the von Mises criterion S_e (Eq. 5.1), the reference data uniaxial mode-{I, III} strength and mechanism parameters $\{\gamma_{I,AW}, \rho^*_{I,AW}, \rho^*_{III}\}$ as well as the optimum 1st order non-proportionality coefficients (Eq. 5.4) C_{np} and c_m [130], the multiaxial hexapod data fits the data scatter band (Fig. 5.18a). Conservative design life time estimates can be obtained, but the data is quite scattered as reflected in $\sigma_N = 0.38$; relative large with respect to $\sigma_N = 0.29$ of the reference data. For the uniaxial

mode-{I, III} strength and mechanism estimates of the hexapod data (Fig. 5.17a), the optimum non-proportionality measure turned out to be still 1st order. The possibility of c_m being a material characteristic holds [130] since the value hardly changed (Fig. 5.18b) – recalling the similar material micro-structure for the hexapod and reference welds (Fig. 5.7), but proof is not conclusive. The life time scatter, however, reduced to $\sigma_N = 0.29$, equal to the reference data value and reflecting a narrow scatter band (Fig. 5.18b). For the reference data, mode-{I, III} coupling is introduced in order to explain the multiaxial fatigue resistance characteristics [197], reflected in the introduced mechanism parameters $\{\rho^*_{I,AW,M}, \rho^*_{III,M}\}$. Dedicated hexapod data values are obtained as well, but are quite close to the reference ones. The scatter of the individual multiaxial data groups, P and NP, did change, but the similar σ_N may suggest any possible influence of mode-{I, III} coupling might be limited. However, the hexapod data geometry and loading variations are too limited to provide a conclusive answer. Only a small S_e improvement is gained (Fig. 5.18c and 5.18d), knowing that the concept of stress averaging implies a relatively small ρ^* sensitivity anyway. The life time scatter reduced to $\sigma_N = 0.28$ and relatively accurate life time estimates can be obtained.

Assessment of the hexapod data using the total stress S_T (Eq. 5.2) provides similar results. For the average quality reference data parameters a fit in the scatter band is obtained (Fig. 5.19a), although the high-quality hexapod data is clearly at the upper bound. Dedicated hexapod data parameters including the non-proportionality coefficients $\{C_{np}, c_m\}$ provide a much better fit (Fig. 5.19b): σ_N reduced from 0.38 to 0.24, even smaller than the S_e value (Fig. 5.18b). The optimum material characteristic c_m reduced a bit, but is still similar to the reference data value. Although mode-{I, III} coupling improved the S_T reference data formulation up to some extent [197], for the hexapod data no obvious differences are observed (Fig. 5.19c and 5.19d). The elastoplasticity coefficients $\{n_{I,AW,M}, n_{III,M}\}$ are similar to the uniaxial values, explaining the unaffected σ_N. Like for S_e, the scatter of the individual multiaxial data groups did change, but geometry and loading limitations prevent for conclusive evidence of coupling effects. In general, the small crack size singularity dominates the crack growth integral (Section 5.3.2) and is quite sensitive to the involved elastoplasticity coefficient n – in contrast to the ρ^* sensitivity for S_e. Accurate design life time estimates can be obtained.

5.4. Conclusions and Outlook

The custom-built TU Delft hexapod for mechanical testing purposes, allowing for relatively large loads and smaller motions at all 6 individually controlled DoF's, turned out to be an excellent test rig for multiaxial CA and VA fatigue testing.

Tubular arc-welded DS T-joints are manufactured according to offshore standards and proved to be of high-quality in terms of strength, geometry and material aspects, as respectively reflected in a negligible residual stress, a relatively large notch radius, a homogeneous micro-structure in the WM and HAZ and a gradual hardness distribution at a relatively low level. Taking all aspects into account fits the (mixed) mode-{I, III} hexapod test data in the average quality fatigue literature data
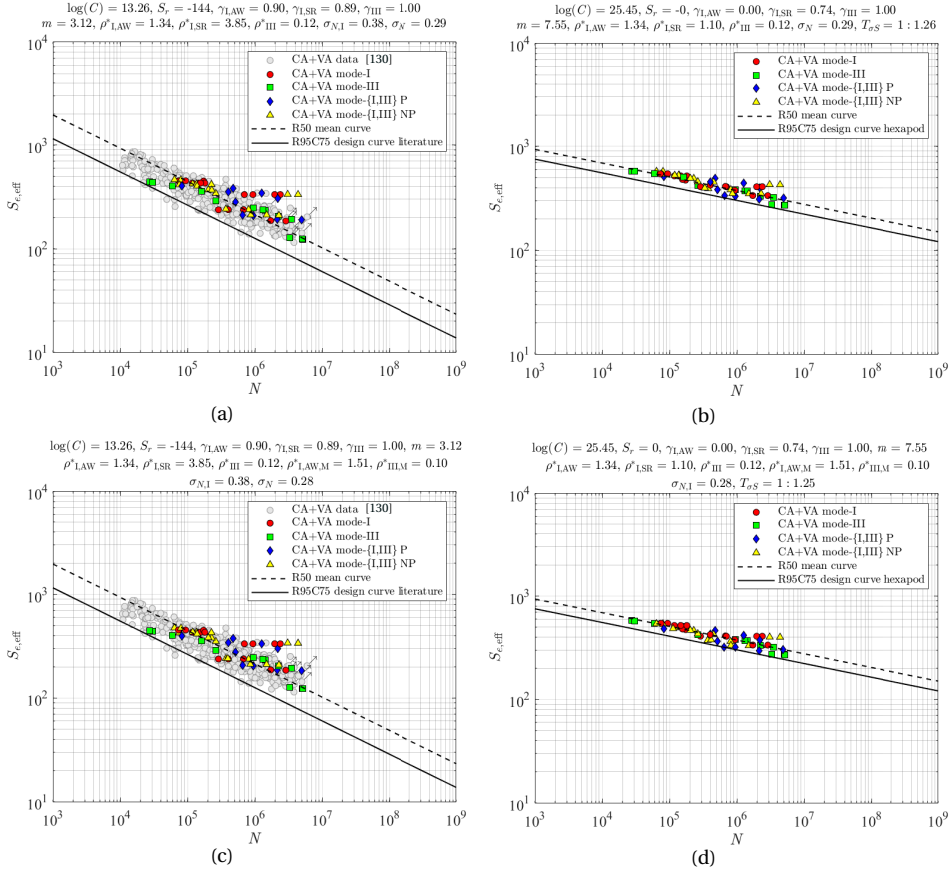
$\log(C) = 13.26,\ S_r = -144,\ \gamma_{\text{I,AW}} = 0.90,\ \gamma_{\text{I,SR}} = 0.89,\ \gamma_{\text{III}} = 1.00$
$m = 3.12,\ \rho^*_{\text{I,AW}} = 1.34,\ \rho^*_{\text{I,SR}} = 3.85,\ \rho^*_{\text{III}} = 0.12,\ \sigma_{N,I} = 0.38,\ \sigma_N = 0.29$

$\log(C) = 25.45,\ S_r = -0,\ \gamma_{\text{I,AW}} = 0.00,\ \gamma_{\text{I,SR}} = 0.74,\ \gamma_{\text{III}} = 1.00$
$m = 7.55,\ \rho^*_{\text{I,AW}} = 1.34,\ \rho^*_{\text{I,SR}} = 1.10,\ \rho^*_{\text{III}} = 0.12,\ \sigma_N = 0.29,\ T_{\sigma S} = 1 : 1.26$

(a)

(b)

$\log(C) = 13.26,\ S_r = -144,\ \gamma_{\text{I,AW}} = 0.90,\ \gamma_{\text{I,SR}} = 0.89,\ \gamma_{\text{III}} = 1.00,\ m = 3.12$
$\rho^*_{\text{I,AW}} = 1.34,\ \rho^*_{\text{I,SR}} = 3.85,\ \rho^*_{\text{III}} = 0.12,\ \rho^*_{\text{I,AW,M}} = 1.51,\ \rho^*_{\text{III,M}} = 0.10$
$\sigma_{N,I} = 0.38,\ \sigma_N = 0.28$

$\log(C) = 25.45,\ S_r = 0,\ \gamma_{\text{I,AW}} = 0.00,\ \gamma_{\text{I,SR}} = 0.74,\ \gamma_{\text{III}} = 1.00,\ m = 7.55$
$\rho^*_{\text{I,AW}} = 1.34,\ \rho^*_{\text{I,SR}} = 1.10,\ \rho^*_{\text{III}} = 0.12,\ \rho^*_{\text{I,AW,M}} = 1.51,\ \rho^*_{\text{III,M}} = 0.10$
$\sigma_{N,I} = 0.28,\ T_{\sigma S} = 1 : 1.25$

(c)

(d)

Figure 5.18.: Effective notch stress based hexapod multiaxial fatigue resistance for uniaxial ρ^* values and reference parameters; $c_m = 0.40$ (a), uniaxial ρ^* values and dedicated parameters; $c_m = 0.45$ (b), multiaxial ρ^* values and reference parameters; $c_m = 0.50$ (c), multiaxial ρ^* values and dedicated parameters; $c_m = 0.45$ (d).

scatter band for advanced multiaxial criteria: the effective notch stress S_e and the total stress S_T; an intact and cracked geometry parameter. Support for the residual $S_r = 0$ is observed in the hardness distribution as well as the AW and SR fatigue test data; in particular the mode-I resistance (contribution) is affected for both S_e and S_T. Mode-III resistance is hardly (mean) residual stress sensitive. The real notch radius ρ hardly affects the mode-I fatigue resistance for S_e and S_T, respectively because of the relatively large ρ^*_I and the square root singularity for small cracks close to the notch surface (radius) being governing. However, for mode-III ρ has to be incorporated considering S_e, because of the relatively small ρ^*_{III} reflecting a near surface phenomenon. For S_T, on the other hand, ρ is less important for the same
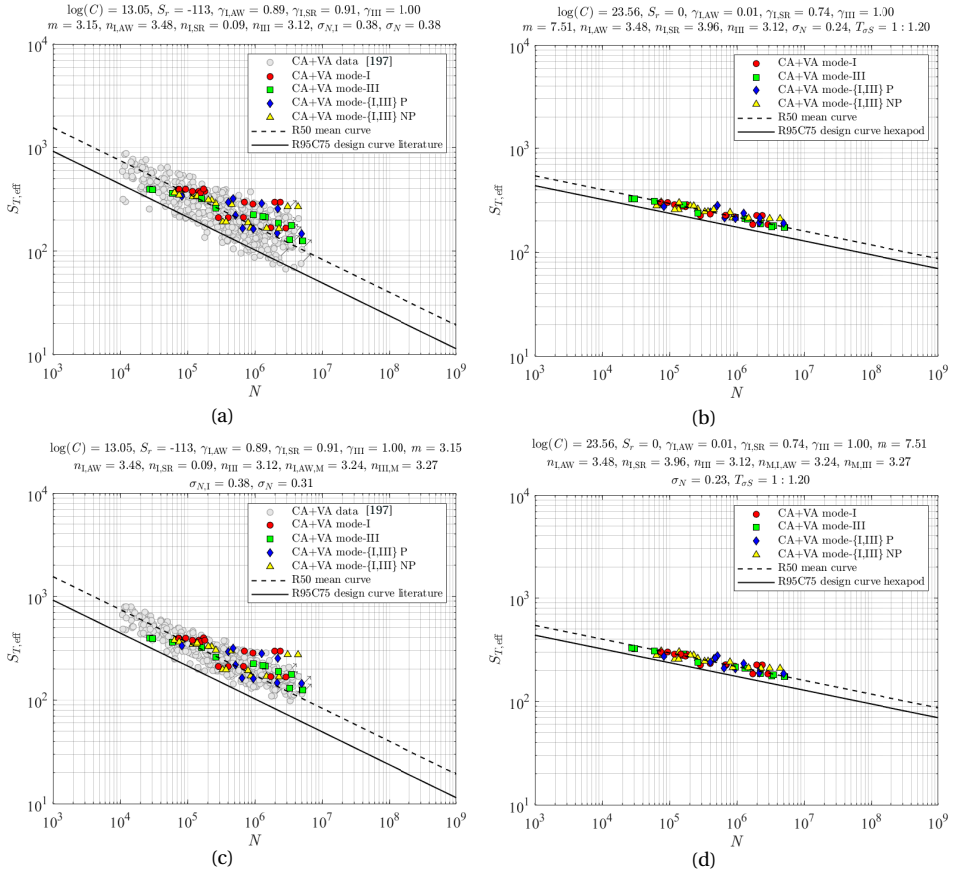
Figure 5.19.: Total stress based hexapod multiaxial fatigue resistance for uniaxial n values and reference parameters; $c_m = 0.45$ (a), uniaxial n values and dedicated parameters; $c_m = 0.40$ (b), multiaxial n values and reference parameters; $c_m = 0.60$ (c), multiaxial n values and dedicated parameters; $c_m = 0.45$ (d).

reason as mentioned for mode-I. Similar material micro-structure compositions for the (literature) reference and hexapod weld suggest that the fatigue mechanism parameters ρ^* and n for respectively S_e and S_T are not very different, as confirmed in the hexapod data likelihood regression results. Although the hardness distribution supports a smaller welding induced defect size (a_i/t_p) for the high quality hexapod data, the variation in geometry and loading conditions – mean stress in particular – is insufficient and conclusive proof cannot be provided, since the literature data based strength and mechanism parameter estimates $\{\gamma, n\}$ rather than dedicated ones had to be adopted for S_T; the same ones as used to obtain the most likely (a_i/t_p) for the average quality literature fatigue test data.

Since the multiaxial hexapod fatigue test data fits the reference data scatter band, conservative life time estimates can be obtained adopting S_e and S_T with the reference data strength and mechanism parameters. However, dedicated hexapod data parameters significantly improve the accuracy, distinguishing the high-quality welded joints from the average ones. Like observed for the reference data, the performance of S_T is better than of S_e, as reflected in σ_N. Whereas the S_e related ρ^* equivalent for S_T is the final crack size (a_f/t_p), S_T has one more mechanism parameter in terms of the elastoplasticity coefficient n to model the fatigue (crack growth) behaviour, providing more accurate life time estimates. Mode-{I, III} coupling improves the individual multiaxial data set performance with respect to (non-) proportionality for S_e and S_T, but hardly affects the overall performance defining the resistance curve. For particular multiaxial loading and response conditions, coupling can be important, although conclusive proof for the hexapod data cannot be provided because of limited geometry and loading variations.

High-quality welded joint fatigue resistance is predominantly reflected in the larger resistance curve intercept $\log(C)$ and slope m; a strength and a mechanism parameter, implying a larger initiation (i.e. short crack growth) contribution to the total life time. Still adopting the average quality related reference curve {$\log(C), m$} for high-quality hexapod data means, however, for VA loading and response conditions that damage equivalence is lost. Despite the smaller parameter confidence for the high-quality welded joint fatigue resistance because of the smaller hexapod data size, the design life estimates are more accurate in comparison to the conservative average quality reference data based estimates (*research sub-question 6*). In order to improve the basis for a high quality hexapod data fatigue resistance curve, more tests are required with different geometry and mean (residual) stress conditions to obtain dedicated strength and mechanism parameters, i.e. {γ, ρ^*} for S_e and {γ, n} as well as (a_i/t_p) for S_T.

For general fatigue assessment applications, an average quality based resistance curve is recommended from design perspective. If high-quality resistance can be guaranteed, a dedicated curve can be used. For the most accurate life time estimates S_T is preferred as fatigue strength parameter. However, balancing computational efforts, parameter complexity and accuracy, S_e can be adopted as well (*research sub-question 3*).

6

EVALUATION AND DISCUSSION

Reasoning draws a conclusion, but does not make the conclusion certain.

Roger Bacon, philosopher

6.1. CONCLUSIONS

Main objective of the research as presented (Chapter 2-5) was to incorporate adequate (mixed) mode-I, III strength and mechanism contributions to improve the multiaxial fatigu elife time estimates for arc-welded joints in steel (maritime) structures.

Based on an excellent mode-I performance, two parameters, the effective notch stress S_e and total stress S_T as respectively an intact and cracked geometry parameter have been adopted, aiming for one resistance curve for uniaxial as well as multiaxial fatigue. Introducing a von Mises type of criterion, a multiaxial $\{S_e, S_T\}$ formulation has been established and in comparison to other existing parameters an excellent performance is obtained. An experimental campaign, the first-ever involving a 6 DoF test rig; the TU Delft hexapod, offered insight in the significance of weld quality affecting the fatigue resistance and data for validation of S_e and S_T.

The first research step involved the derivation of a novel mode-III weld notch stress distribution formulation $\tau_n(r/t_p)$ for weld notch geometries, distinguishing non-symmetry and symmetry with respect to half the plate thickness, as well as a zero and finite notch radius configuration. Provided a geometry description and far field stress information is available, $\tau_n(r/t_p)$ can be obtained for structures ranging from tubular (with finite radius R) to planar (with infinite R) ones. Using $\tau_n(r/t_p)$, the intact geometry parameter $S_{e,III}$ has been established, involving notch and far field contributions. Assessment of mode-III arc-welded joint fatigue test data from the literature revealed the superior performance of $S_{e,III}$ in comparison to the nominal stress S_n, showing that incorporating local notch information provides more accurate fatigue strength and life time estimates. Adopting the real weld notch radius $\rho^* > 0$ statistics improved the accuracy. At the same time the most likely ρ^*_{III} value of ~0.1 [mm] is relatively small in comparison to the typical mode-I value: ρ^*_I

~1.0 [mm] obtained for $\rho = 0$. Both observations suggest that the mode-III fatigue damage process is more initiation than growth related, like reflected in the resistance curve slopes: $m_{III} \sim 5 > m_I \sim 3$, explaining why the local geometry is important. Walker's model has been used to investigate the influence of mean stress, either mechanical (loading) or thermal (welding residual stress) induced, but the mode-III fatigue resistance turned out to be rather mean stress insensitive. In contrast to opening mode-I, sliding mode-III seems to suffer from friction between the fracture surfaces suppressing any possible mean stress effect. Since mode-III arc-welded joint fatigue resistance data is relatively scarce, the $\{\log(C_{III}), \gamma_{III}, m_{III}, \rho^*_{III}\}$ parameter confidence interval is quite large.

In order to be able to deal with random multiaxial response conditions, failure criterion options, damage plane selection, cycle counting aspects including ways to deal with non-proportionality, as well as fatigue damage accumulation model considerations have been reviewed. Since for mixed mode-I, III multiaxial response conditions of planar and tubular (maritime) structures the mode-I contribution is governing and at the same time the fatigue lifetime of arc-welded joints is growth defined rather than initiation controlled (i.e. a shear induced process) because of the welding induced defects, an equivalent normal stress based von Mises type of failure criterion at the critical fracture plane has been selected for fatigue assessment purposes. In particular, a lifetime dependent shear strength coefficient $\beta(N)$ has been introduced to cover the mode specific and material characteristic $\log(C)$, m mechanism and strength contributions. Cycles are counted in the equivalent von Mises plane, incorporating non-proportionality cycle-by-cycle and accumulating damage using a linear model. S_e explicitly involves a mean stress coefficient γ and material characteristic length ρ^*, reflecting respectively a strength and mechanism contribution. Fatigue test data assessment showed that γ, ρ^* are not only mode specific, but thermal condition – i.e. as-welded or stress-relieved – dependent as well. The best performing non-proportionality measure is a 1$^{\text{st}}$ order formulation containing a response path and material contribution. In comparison to the assessment for other combinations of failure criterion, damage plane, cycle counting algorithm, non-proportionality measure and damage accumulation model in terms of lifetime and strength scatter, the outperformance is impressive. The VA data aligns with the CA data scatter band for $D = 1$. All evaluated uniaxial and multiaxial mode-I, III data aligns with the uniaxial mode-I reference data scatter band, allowing for a single $S_e - N$ fatigue resistance curve in engineering applications.

Because of the welding induced defects at the governing fatigue sensitive locations; the notches, a cracked geometry parameter like the total stress S_T rather than an intact one, can be justified as well. The mode-III weld notch stress distribution formulations have been turned into an equivalent weld notch stress intensity $Y_n(a/t_p)Y_f(a/t_p)$ applicable for both tubular and planar structures. Introducing a two-stage crack growth model with a notch and far field dominated region, as reflected in respectively $Y_n(a/t_p)$ and $Y_f(a/t_p)$, the equivalent stress parameter S_T has been established. Like S_e, S_T contains with γ, n a strength and mechanism parameter as well. Since ρ^* serves the same purpose as the final crack length

a_f, S_T contains with n an additional (short crack) mechanism related parameter, able to turn crack growth in the notch affected region to either non-monotonic or monotonically increasing behaviour, different from the far field controlled Paris region. For S_T, the parameter estimates turned out to be mode and welding condition dependent as well, whereas the confidence interval is relatively large because available data in literature is limited. As already observed for S_e, the mode-III fatigue resistance seems to be mean stress insensitive. However, for a cyclic mode-I response with a static mode-III component mean stress can be important. The currently used (von Mises) failure criterion would require an additional coupling term to take that into account. Assessment of multiaxial fatigue test data clearly indicated an interaction effect, explaining why except uniaxial and thermal condition dependent coefficients n, mixed mode-I, III counterparts have been introduced as well, significantly improving the S_T performance. Interpretation of the n values for mode-coupling seems not straight forward and mixed-mode crack growth testing is required, both to validate the involved crack growth model well as to address crack growth and fatigue resistance similarity. Similar to S_e, a 1st order non-proportionality measure with a response path and material contribution provides the best results. In comparison to S_e, the S_T performance is similar. The multiaxial P data scatter turns out to be smaller; a consequence of the multiaxial n parameters. Introducing multiaxial ρ^* values for S_e, however, hardly improves the performance, revealing an insensitivity. Whereas n seems to be a more explicit measure directly affecting the crack growth behaviour, ρ^* seems a more implicit one reflecting the material characteristic length for (mixed) mode and (multiaxial) response conditions. In this respect, S_T can be considered one step closer to the actual physics of the fatigue damage process. However, balancing life time estimate accuracy, parameter complexity and computational efforts, S_e seems more effective at the moment.

Using the TU Delft hexapod, a 6 DoF test rig, uniaxial mode-I and mode-III as well as mixed mode-{I,III} fatigue test results have been obtained for arc-welded joints in steel (maritime) structures in constant and variable amplitude conditions. A welding procedure certified to offshore quality standards ensured high-performance welds, as confirmed by metallurgical analysis. Regression analysis shows that the fatigue strength and mechanism contributions are quite close to base material level, as reflected in the intercept $\log(C)$ and the slope m, implying a larger initiation (i.e. short crack growth) contribution to the total life time. Using S_e and S_T (Chapter 3 and 4), the hexapod data has been used to verify a fit in the average quality based literature resistance data scatter in terms of strength, geometry and material aspects, as respectively reflected in a negligible residual stress, a relatively large notch radius, a homogeneous micro-structure in the weld material and heat affected zone and a gradual hardness distribution at a relatively low level. However, a separate hexapod data analysis – introducing dedicated ρ^* and n parameter estimates reflecting different strength and mechanism, significantly reduced the fatigue strength scatter band and life time standard deviation, allowing for more accurate estimates. Individual data set performance at the possible cost of losing general applicability depends on the production quality as well as the individual data set size, defining the parameter confidence bounds.

6.2. OUTLOOK

Reflecting on the completed research path with the focus on S_e and S_T as respectively the best performing intact and cracked fatigue parameters, as well as multiaxial fatigue testing using a hexapod, some suggestions for future work will be provided, meant to provide additional insights and enhanced understanding with respect to multiaxial fatigue of arc-welded joints.

Assuming a Basquin type of relation: $\log(N) = \log(C) - m \cdot \log(S)$, distinguished strength and mechanism coefficients {log(C), m} have been obtained for mode-I and mode-III. The life time dependent shear strength coefficient $\beta(N, C_I, C_{III}, m_I, m_{III})$ has been introduced to account for mixed mode contributions (Chapter 3). However, S – either S_e or S_T, is typically a cycle characteristic; i.e. a (n effective) stress range, but does not account for the actual time history. In fact, $S(t)$ is reduced to a peak-valley sequence $S(N)$ for the sake of cycle counting. Aim of β is to translate the mode-III τ component to an equivalent σ mode-I value, meaning that for $\tau(t)$ and $\sigma(t)$, the shear strength coefficient would be time dependent as well; i.e. $\beta(t)$. The stress path would scale non-uniform in the $\sigma - \beta\tau$ plane (Fig. 6.1) and even multiaxial proportional loading would generate a non-proportional response. Since strength and mechanism contributions turned out to be crucial for multiaxial fatigue assessment, $\beta(t)$ reflects another source of non-proportionality, expected to increase insight and understanding. Whereas $\beta(N)$ is obtained as a ratio of resistance curves related to the cycle characteristic $S(N)$, $S(t)$ value should be converted to an equivalent $S(N)$, or vice versa.

For both S_e and S_T, mode-{I, III} coupling improved the correlation for proportional and non-proportional multiaxial fatigue test data, particularly reflected in dedicated mechanism parameters, i.e. respectively ρ^* and n. However, conclusive proof could not be provided because of limited test data variations with respect to geometry and multiaxial loading conditions (Chapters 2 to 5) and a dedicated test campaign is recommended.

The total stress parameter S_T is based on a two-stage crack growth model, incorporating notch affected short crack- and far field dominated long crack growth contributions. Because of mode-{I, III} interaction effects, mixed-mode elastoplasticity coefficients n have been introduced, predominantly affecting the short crack growth characteristics. Most likely n estimates have been obtained using welded joint fatigue test data in a reversed engineering approach (Chapter 4). However, mixed mode-{I, III} crack growth testing is highly recommended to prove the two-stage crack growth behaviour and validate the corresponding n values, as well as to address crack growth and fatigue resistance similarity. For long crack mixed-mode characteristics, the adopted von Mises criterion could be extended with a coupling term, but will complicate the adopted cycle counting algorithm.

The test data in literature as well as the data obtained using the TU Delft hexapod is related to multiaxial mid-cycle fatigue; i.e. $N = O(10^4...10^6)$. Crack growth typically controls the fatigue damage process. The strength and mechanism
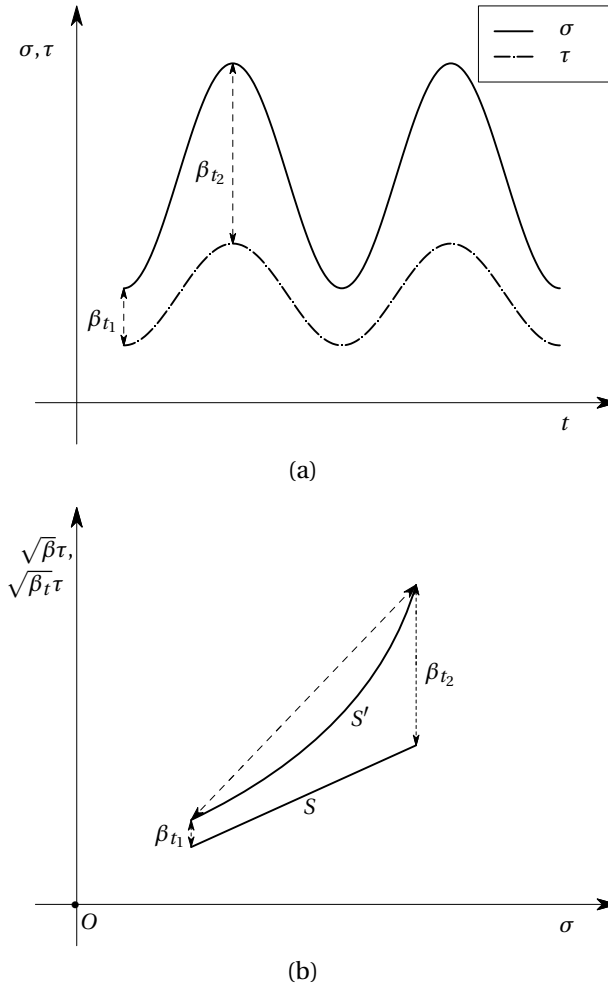
Figure 6.1.: Time trace of proportional normal and shear stress components with varying β values (a) and representation in the $\sigma - \sqrt{\beta}\tau$ stress plane (b). The proportional load path S in the $\sigma - \sqrt{\beta}\tau$ stress plane is transformed in the non-proportional load path S' in the $\sigma - \sqrt{\beta_t}\tau$ plane.

parameters like ρ^* for S_e and n for S_T are mid-cycle fatigue related average values. In order to improve the parameter confidence – like for mode-I, still more uniaxial mode-III and mixed mode-{I, III} mid-cycle fatigue test data is required. For high-cycle fatigue; $N > O(10^6)$, initiation becomes more dominant, meaning the fatigue strength and mechanism parameters $\{\log(C), m\}$ will change and ρ^* as well n are expected to become response level dependent, introducing at the same time a resistance induced damage accumulation non-linearity. Since (maritime) structures

are typically exposed to (stochastic) variable amplitude loading conditions, both mid-cycle and high-cycle multiaxial fatigue resistance information is considered to be important and high-cycle fatigue investigations are considered to be a crucial next step. Response induced damage accumulation non-linearities may be introduced – including mixed mode-{I, III} sequence effects – and should be investigated for different type of spectral distributions.

For more advanced fatigue strength parameters like S_e and S_T, typically more input is required. The exact weld geometry dimensions, for example. However, welding induced residual stress seems to be another important parameter – in particular fur tubular structures like often used for mixed mode-{I, III} testing and seems to be responsible for significant part of the data scatter. At the same time, a comparison of the data from literature and the data obtained using the TU Delft hexapod suggests that the residual stress is responsible for the difference between average quality or high-performance welds, implying that residual stress measurements are considered to indispensable for new tests (Chapter 5).

For the adopted time domain formulation, cycle counting has been used to incorporate the mode-{I, III} non-proportionality aspects (Chapters 3 and 4). However, if the loading and response conditions are linear, stationary and can be considered as random Gaussian processes [e.g. 206], a more cost effective frequency domain formulation can be used, improving the balance between accuracy, efforts and complexity (Chapter 1). Several efforts have already been taken [e.g. 207–209], but should be re-addressed in view of the S_e and S_T results. Particular attention should be paid to mean stress and interaction effects; i.e. mode-{I, III} coupling contributions (Chapters 3 and 4), as well as wide band process implications.

Whereas strength and mechanism effects for multiaxial mid-cycle fatigue of arc-welded joints have been observed and incorporated, including mixed-mode effects, the research was limited to steel structures (Chapters 2 to 5). In order to verify if the obtained parameter coefficient estimates are material characteristic as well, investigations for different metals like aluminium, magnesium and titanium are recommended.

Although the developed multiaxial fatigue parameters and corresponding resistance curves define the capacity part, the demand; i.e. the loading and response conditions, should be investigated for multiaxiality in the first place. Introducing screening criteria with respect to level of multiaxiality, level of non-proportionality, response magnitude and damage magnitude [e.g. 186] can improve insight. In particular for relatively new type of structures like floating offshore wind turbines in different configurations or ships with wind assisted propulsion systems involving two important load components: wind and waves, since the governing fatigue loading and response conditions are not well-established yet.

A

MODE-III NOTCH SHEAR STRESS COMPONENT FORMULATION

Adopting a complex potential, identically satisfying equilibrium (body forces are assumed to be zero) and compatibility requirements – deformations without any gaps or overlaps, the characteristic stress distribution singularity at a V-shaped notch for a fillet weld geometry with $\rho = 0$ (Fig. 2.2) can be obtained [35–39]:

$$\tau_{xr}(r,\theta) = C_1 r^{\lambda-1} \sin(\lambda\theta) - C_2 r^{-\lambda-1} \sin(\lambda\theta)$$
$$\tau_{x\theta}(r,\theta) = C_1 r^{\lambda-1} \cos(\lambda\theta) + C_2 r^{-\lambda-1} \cos(\lambda\theta). \tag{A.1}$$

The transformation from Cartesian (Eq. A.1) to Polar coordinates has been obtained using [36]:

$$\tau_{xr} = \tau_{xz} \cos(\theta) + \tau_{xy} \sin(\theta)$$
$$\tau_{x\theta} = \tau_{xy} \cos(\theta) - \tau_{xz} \sin(\theta). \tag{A.2}$$

Boundary conditions to be satisfied at the free surface denote:

$$\tau_{xr}(r,\theta = \alpha) = 0 \tag{A.3a}$$
$$\tau_{x\theta}(r,\theta = \alpha) = 0. \tag{A.3b}$$

Because of symmetry, $\tau_{x\theta}(r,\theta = \alpha) = \tau_{x\theta}(r,\theta = -\alpha) = 0$ is identically satisfied. Substitution of the stress components (Eq. A.1) in the boundary conditions (Eq. A.3) yield:

$$(C_1 r^{\lambda-1} - C_2 r^{-\lambda-1}) \sin(\lambda\alpha) = 0 \tag{A.4a}$$
$$(C_1 r^{\lambda-1} + C_2 r^{-\lambda-1}) \cos(\lambda\alpha) = 0. \tag{A.4b}$$

Since $(C_1 r^{\lambda-1} + C_2 r^{-\lambda-1}) \neq 0$, the $\tau_{x\theta}$ boundary condition (Eqs. (A.3b) and (A.4b))

provides the eigenvalue solution λ:

$$\cos(\lambda\alpha) = 0$$
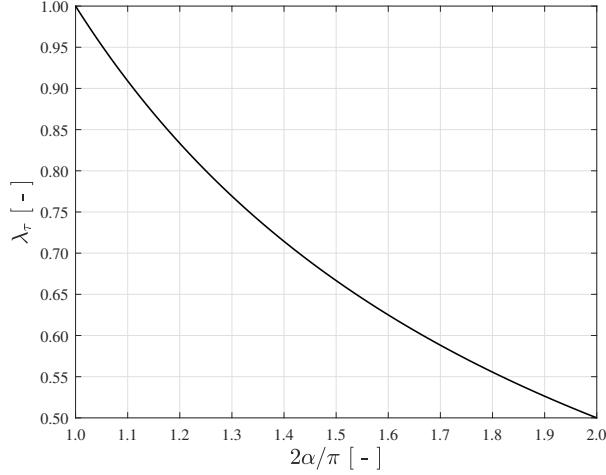$$\lambda = \lambda_\tau = \frac{\pi}{2\alpha}. \tag{A.5}$$

Figure A.1.: Eigenvalue solutions $\lambda_\tau(2\alpha)$.

Only the first governing notch angle dependent λ_τ, defining the degree of weld notch stress field singularity, will be considered (Fig. A.1). To satisfy the τ_{xr} boundary condition (Eqs. (A.3a) and (A.4a)) as well: $\sin(\lambda\alpha) = 0 \rightarrow \lambda = \lambda_\tau = \pi/(2\alpha)$ cannot be satisfied at the same time, meaning:

$$C_2 = C_1 r^{2\lambda}. \tag{A.6}$$

Substitution of C_2 (Eq. A.6) into the stress components $\tau_{xr}(r,\theta)$ and $\tau_{x\theta}(r,\theta)$ (Eq. A.1) yields:

$$\tau_{xr}(r,\theta) = 0$$
$$\tau_{x\theta}(r,\theta) = C_1' r^{\lambda-1} \cos(\lambda\theta). \tag{A.7}$$

Introducing the dimensionless coordinate (r/t_p) as well as τ_s in order to establish a relation to the far field stress (Section 2.2.3) provides for a weld notch angle dependent stress angle $\theta = \beta$:

$$\tau_{x\theta}\left(\frac{r}{t_p}\right) = \tau_s \left(\frac{r}{t_p}\right)^{\lambda_\tau-1} \mu_{\tau F} \cos(\lambda_\tau\beta) \tag{A.8}$$

with

$$\mu_{\tau F} = \frac{C_1' t_p^{\lambda_\tau - 1}}{\tau_s}. \tag{A.9}$$

For $\rho > 0$ (Fig. 2.3), the stress distribution is assumed to be affected for $r \to 0$ only, suggesting the same complex potential as for $\rho = 0$ can be adopted, but the boundary conditions (Eq. A.3) have to be changed into [39]:

$$\tau_{xr}(r = \rho, \theta) = 0 \tag{A.10a}$$

$$\tau_{x\theta}(r, \theta = \alpha) = 0. \tag{A.10b}$$

Because of symmetry, $\tau_{x\theta}(r, \theta = \alpha) = \tau_{x\theta}(r, \theta = -\alpha) = 0$ is identically satisfied, like for $\rho = 0$. Substitution of the stress components (Eq. A.1) in the boundary conditions (Eq. A.10) yield [39]:

$$(C_1 \rho^{\lambda-1} - C_2 \rho^{-\lambda-1}) \sin(\lambda\theta) = 0. \tag{A.11}$$

Since the $\tau_{x\theta}$ boundary condition (Eq. A.10b) for ($\rho = 0$) and ($\rho > 0$) is the same, the eigenvalue solution does not change: $\lambda = \lambda_\tau = \pi/(2\alpha)$. However, to satisfy τ_{xr} (Eq. A.10a) requires:

$$C_2 = C_1 \rho^{2\lambda}. \tag{A.12}$$

Substitution of C_2 (Eq. A.12) into the stress components $\tau_{xr}(r, \theta)$ and $\tau_{x\theta}(r, \theta)$ (Eq. A.1) denotes:

$$\begin{aligned}
\tau_{xr}(r, \theta) &= C_1' r'^{\lambda_\tau - 1} \sin(\lambda_\tau \theta) \left(1 - (r_0/r')^{2\lambda_\tau}\right) \\
\tau_{x\theta}(r, \theta) &= C_1' r'^{\lambda_\tau - 1} \cos(\lambda_\tau \theta) \left(1 + (r_0/r')^{2\lambda_\tau}\right).
\end{aligned} \tag{A.13}$$

Introducing the dimensionless coordinate (r/t_p) as well as τ_s in order to establish a relation to the far field stress (Section 2.2.3), like for $\rho = 0$, provides for a weld notch angle dependent stress angle $\theta = \beta$:

$$\begin{aligned}
\tau_{xr}\left(\frac{r}{t_p}\right) &= \tau_s \left(\frac{r'}{t_p}\right)^{\lambda_\tau - 1} \mu_{\tau F} \sin(\lambda_\tau \beta) \quad \left\{1 - \left(\frac{r_0}{t_p}\right)^{2\lambda_\tau} \left(\frac{r'}{t_p}\right)^{-2\lambda_\tau}\right\} \\
\tau_{x\theta}\left(\frac{r}{t_p}\right) &= \tau_s \left(\frac{r'}{t_p}\right)^{\lambda_\tau - 1} \mu_{\tau F} \cos(\lambda_\tau \beta) \quad \left\{1 + \left(\frac{r_0}{t_p}\right)^{2\lambda_\tau} \left(\frac{r'}{t_p}\right)^{-2\lambda_\tau}\right\}
\end{aligned} \tag{A.14}$$

with

$$\mu_{\tau F} = \frac{C_1' t_p^{\lambda_\tau - 1}}{\tau_s}. \tag{A.15}$$

B

MODE-III WELD LOAD CARRYING SHEAR STRESS COEFFICIENT

To capture C_{tw} estimates, 4th order polynomial fitting functions have been established. In case of non-symmetry:

$$
\begin{aligned}
C_{tw} = \\
0.166 &+ 0.078Q^3P + 0.037WQ^2 - 0.003TWQ^2 - \\
0.372P &- 0.758QP - 1.517QP^2 + 0.020WQP + \\
0.908P^2 &+ 0.436Q^2P + 0.355Q^2P^2 - 0.024TW^2P - \\
2.309P^3 &- 0.168WP^3 + 0.004WP + 0.001WQ^2P + \\
0.536Q &- 0.079WQ + 2.487QP^3 - 0.051WQP^2 - \\
0.398Q^2 &+ 0.179WP^2 - 0.003WQ^3 + 0.012TWQ + \\
0.127Q^3 &+ 0.002W^2P^2 - 0.003W^2Q + 0.016W^2QP - \\
0.015Q^4 &- 0.019W^2P + 0.003W^3Q + 0.028TQ^2P - \\
0.225W &+ 0.087TP^3 - 0.015TQ - 0.179TQP + \\
0.095W^2 &+ 0.013TQ^2 + 0.271TP + 0.024TWP^2 - \\
0.014W^3 &- 0.006TW - 0.003TQ^3 + 0.062TWP - \\
0.027TWQP &- 0.003W^2Q^2 - 0.402TP^2 + 0.301TQP^2
\end{aligned}
\tag{B.1}
$$

and in case of symmetry:

$$
\begin{aligned}
C_{tw} = \\
-0.036 &- 0.049QP &- 0.018Q^2P &+ 0.087TQP &+ \\
0.257P &- 0.035QP^2 &+ 0.235QP^3 &- 0.024T^2WP &- \\
0.159P^2 &+ 0.038Q^2P^2 &+ 0.008T^2Q &- 0.004T^2WQ &+ \\
0.599P^3 &+ 0.047WP^3 &- 0.036WQ &- 0.022WQP &- \\
1.619P^4 &+ 0.006WQ^2 &+ 0.004T^2Q^2 &- 0.036TWP &- \\
0.012Q &- 0.012W^2P^2 &- 0.003W^2Q^2 &+ 0.004TQ^2P &+ \\
0.016Q^2 &- 0.084WP &+ 0.0189W^2P &+ 0.028WQP^2 &+ \\
0.006T &+ 0.093TP &- 0.102TP^2 &+ 0.013TQP^2 &- \\
0.016T^2 &+ 0.022TQ &+ 0.016WP^2 &+ 0.038TWP^2 &+ \\
0.056W &- 0.278TP^3 &- 0.024TQ^2 &+ 0.005TWQ &- \\
0.012W^2 &+ 0.005T^2P &- 0.058T^2P^2 &- 0.036T^2QP &+ \\
0.028TWQP &- 0.002TW^2 &+ 0.002T^2W &- 0.004TW^2P
\end{aligned}
\tag{B.2}
$$

with

$$
\begin{aligned}
T &= \log(t_c/2 + l_w)/t_b \\
W &= l_w/h_w \\
Q &= l_w/t_b \\
P &= t_b/R_t.
\end{aligned}
\tag{B.3}
$$

Negligible terms are excluded. Fitting function application is not limited to the absolute geometry dimensions as shown (Figs. 2.8 and 2.15), but the range for particular relative ones: (l_w/h_w), (l_w/t_b), $\log((t_c/2 + l_w)/t_b)$, (t_b/R_t), has to be satisfied.

C

MODE-I S_e FORMULATION FOR SYMMETRY WITH RESPECT TO $(t_p/2)$

Taking advantage of the stress distribution formulations for mode-I [18], the effective notch stress criterion $S_{e,I} = \Delta\sigma_e$ (Eq. 3.1) becomes in case of symmetry with respect to $(t_p/2)$ for $\rho = 0$:

$$
S_{e,I} = \Delta\sigma_s \left(\frac{t_p}{\rho_I^*}\right) \left\{ \left[1 - 2r_{\sigma_s}\left(1 - f_{\rho=0}\left(\frac{r}{t_p} = \frac{1}{2}\right)\right)\right] \cdot \right.
$$

$$
\left(\left(\frac{\rho_I^*}{t_p}\right)^{\lambda_{\sigma s}} \frac{\mu_{\sigma s}\lambda_{\sigma s}(\lambda_{\sigma s}+1)}{\lambda_{\sigma s}} \left[\cos\{(\lambda_{\sigma s}+1)\beta_a\} - \chi_{\sigma s}\cos\{(\lambda_{\sigma s}-1)\beta_a\}\right] + \right.
$$

$$
\left(\frac{\rho_I^*}{t_p}\right)^{\lambda_{\sigma a}} \frac{\mu_{\sigma a}\lambda_{\sigma a}(\lambda_{\sigma a}+1)}{\lambda_{\sigma a}} \left[\sin\{(\lambda_{\sigma a}+1)\beta_a\} - \chi_{\sigma a}\sin\{(\lambda_{\sigma a}-1)\beta_a\}\right] + \tag{C.1}
$$

$$
\left. C_{bw}\left\{2\left(\frac{\rho_I^*}{t_p}\right)^2 - \left(\frac{\rho_I^*}{t_p}\right)\right\}\right) + r_{\sigma_s}\left\{2f_{\rho=0}\left(\frac{r}{t_p} = \frac{1}{2}\right) - 1\right\} \cdot
$$

$$
\left. \left[\left\{1 - f_{\rho=0}\left(\frac{r}{t_p} = \frac{1}{2}\right)\right\}\left(\frac{\rho_I^*}{t_p}\right) - \left(\frac{\rho_I^*}{t_p}\right)^2\right]\right\}
$$

with

$$
f_{\rho=0}\left(\frac{r}{t_p} = \frac{1}{2}\right) = \frac{(\lambda_{\sigma a} - \lambda_{\sigma s})\,(\lambda_{\sigma a}\lambda_{\sigma s} - 2C_{bw})}{\lambda_{\sigma a}\,(\lambda_{\sigma a}-1) - \lambda_{\sigma s}\,(\lambda_{\sigma s}-1)} + C_{bw}. \tag{C.2}
$$

For $\rho > 0$:

$$
\begin{aligned}
S_{e,I} = {} & \Delta\sigma_s \left(\frac{t_p}{r_0 + \rho_I^*}\right) \left\{ \left[1 - 2r_{\sigma_s} \left(1 - f_{\rho>0}\left(\frac{r}{t_p} = \frac{1}{2}\right)\right)\right] \cdot \right. \\
& \left(\left[\left(\frac{r_0 + \rho_I^*}{t_p}\right)^{\lambda_{\sigma s}} - \left(\frac{r_0}{t_p}\right)^{\lambda_{\sigma s}} \right] \frac{\mu_{\sigma s} \lambda_{\sigma s}(\lambda_{\sigma s} + 1)}{\lambda_{\sigma s}} \cdot \right. \\
& \left[\cos\{(\lambda_{\sigma s} + 1)\beta_a\} - \chi_{\sigma s} \cos\{(\lambda_{\sigma s} - 1)\beta_a\} \right] + \\
& \left[\left(\frac{r_0 + \rho_I^*}{t_p}\right)^{\zeta_{\sigma s}} - \left(\frac{r_0}{t_p}\right)^{\zeta_{\sigma s}} \right] \left(\frac{r_0}{t_p}\right)^{\lambda_{\sigma s} - \zeta_{\sigma s}} \frac{\lambda_{\sigma s}}{\zeta_{\sigma s}} \frac{\left(\frac{2\alpha}{\pi}\right)}{4\{\left(\frac{2\alpha}{\pi}\right) - 1\}} \cdot \\
& \left[\omega_{\sigma s1} \cos\{(\zeta_{\sigma s} + 1)\beta_a\} + \omega_{\sigma s2}(\zeta_{\sigma s} + 1)\cos\{(\zeta_{\sigma s} - 1)\beta_a\} \right] + \\
& \left[\left(\frac{r_0 + \rho_I^*}{t_p}\right)^{\lambda_{\sigma a}} - \left(\frac{r_0}{t_p}\right)^{\lambda_{\sigma a}} \right] \frac{\mu_{\sigma a} \lambda_{\sigma a}(\lambda_{\sigma a} + 1)}{\lambda_{\sigma a}} \cdot \\
& \left[\sin\{(\lambda_{\sigma a} + 1)\beta_a\} - \chi_{\sigma a} \sin\{(\lambda_{\sigma a} - 1)\beta_a\} \right] + \\
& \left[\left(\frac{r_0 + \rho_I^*}{t_p}\right)^{\zeta_{\sigma a}} - \left(\frac{r_0}{t_p}\right)^{\zeta_{\sigma a}} \right] \left(\frac{r_0}{t_p}\right)^{\lambda_{\sigma a} - \zeta_{\sigma a}} \frac{\lambda_{\sigma a}}{4\zeta_{\sigma a}(\zeta_{\sigma a} - 1)} \cdot \\
& \left[\omega_{\sigma a1} \sin\{(\zeta_{\sigma a} + 1)\beta_a\} + \omega_{\sigma a2}(\zeta_{\sigma a} + 1)\sin\{(\zeta_{\sigma a} - 1)\beta_a\} \right] + \\
& \left. C_{bw} \left\{ \left(\frac{r_0 + \rho_I^*}{t_p}\right)^2 - \left(\frac{r_0}{t_p}\right)^2 - \left(\frac{2r_0 + \rho_I^*}{t_p}\right) \right\} \right\} - \\
& \left. r_{\sigma_s} \left\{ 2f_{\rho>0}\left(\frac{r}{t_p} = \frac{1}{2}\right) - 1 \right\} \left[\left\{ 1 - f_{\rho>0}\left(\frac{r}{t_p} = \frac{1}{2}\right) \right\} \left(\frac{\rho_I^*}{t_p}\right) - \left(\frac{\rho_I^*}{t_p}\right)^2 \right] \right\}.
\end{aligned}
$$

Plate thickness t_p is either the base plate or the cross plate value: $t_p = t_b$ or $t_p = t_c$, respectively (Fig. 4.1). Coefficients $\{\mu_s, \mu_a\}$ are obtained using force and moment equilibrium. The involved eigenvalues $\{\lambda_{\sigma s}, \lambda_{\sigma a}\}$, the eigenvalue coefficients $\{\chi_{\sigma s}, \chi_{\sigma a}\}$ as well as the stress angle β_a are notch angle α dependent. The weld notch load carrying stress coefficient C_{bw} is geometry (t_b, t_c, l_w, h_w) and loading (f_n, m_b) dependent and contains the notch stress distribution specific information.

D

MODE-I WELD NOTCH STRESS DISTRIBUTION

For mode-I the self-equilibrium stress part $\sigma_{se}(r/t_p)$ consisting of the V-shaped notch angle characteristic stress and the weld notch load carrying stress components yields:

$$\sigma_{se}\left(\frac{r}{t_p}\right) = \left(\frac{r}{t_p}\right)^{\lambda_{\sigma s}-1} \mu_{\sigma s}\lambda_{\sigma s}(\lambda_{\sigma s}+1) \cdot \left[\cos\{(\lambda_{\sigma s}+1)\beta_a\} - \chi_{\sigma s}\cos\{(\lambda_{\sigma s}-1)\beta_a\}\right] +$$
$$\left(\frac{r}{t_p}\right)^{\lambda_{\sigma a}-1} \mu_{\sigma a}\lambda_{\sigma a}(\lambda_{\sigma a}+1) \cdot \left[\sin\{(\lambda_{\sigma a}+1)\beta_a\} - \chi_{\sigma a}\sin\{(\lambda_{\sigma a}-1)\beta_a\}\right] + \quad \text{(D.1)}$$
$$C_{bw}\left\{2\left(\frac{r}{t_p}\right)-1\right\}.$$

Plate thickness t_p is either the base plate or the cross plate value: $t_p = t_b$ or $t_p = t_c$, respectively (Fig. 4.1). Coefficients $\{\mu_s, \mu_a\}$ are obtained using force and moment equilibrium. The involved eigenvalues $\{\lambda_{\sigma s}, \lambda_{\sigma a}\}$, the eigenvalue coefficients $\{\chi_{\sigma s}, \chi_{\sigma a}\}$ as well as the stress angle β_a are notch angle α dependent. The weld notch load carrying stress coefficient C_{bw} is geometry (t_b, t_c, l_w, h_w) and loading (f_n, m_b) dependent and contains the notch stress distribution specific information [18]. The weld toe notch stress distribution formulation yields:

$$\sigma_n\left(\frac{r}{t_p}\right) = \sigma_s\left(\sigma_{se}\left(\frac{r}{t_p}\right) - 2r_{\sigma s}\left(\frac{r}{t_p}\right)\right). \qquad \text{(D.2)}$$

E

MODE-III WELD NOTCH STRESS INTENSITY DISTRIBUTION

Although the real weld notch radius ρ is often virtually zero – justifying the $\rho = 0$ assumption, in some cases the influence of $\rho > 0$ (Fig. 4.3b) cannot be neglected. The coordinate system origin will be transformed $(O' \to O)$, keeping the polar axis parallel to the original one:

$$r'^2 = r^2 + 2\cos(\beta_a - \theta)\, r_0 r + r_0^2 \tag{E.1}$$

with

$$r_0 = \rho\left(1 - \frac{\pi}{2\alpha}\right).$$

The weight function approach (Eq. 4.10) should be modified accordingly $(r \to r')$ and the τ_{se} formulation [29] denotes:

$$\tau_{se}\left(\frac{r}{t_p}\right) = \left[\left(\frac{r'}{t_p}\right)^{\lambda_\tau - 1} \mu_{\tau F}\cos(\lambda_\tau\beta_a)\left\{1 + \left(\frac{r_0}{t_p}\right)^{2\lambda_\tau}\left(\frac{r'}{t_p}\right)^{-2\lambda_\tau}\right\} - (C_{tw} + \mu_{\tau M})\left\{2\left(\frac{r'}{t_p}\right) - 1\right\}\right] \tag{E.2}$$

with

$$\mu_{\tau F} = -\frac{\lambda_\tau\left\{\mu_{\tau M}\left[\left(\frac{r_0}{t_p}\right)^2 - \left(\frac{r_0}{t_p}\right)\right] - \left(\frac{r_0}{t_p}\right)^2 r_{\tau_s} - 1\right\}}{\cos(\lambda_\tau\beta_a)\left[1 - \left(\frac{r_0}{t_p}\right)^{2\lambda_\tau}\right]}$$

161

and

$$\mu_{\tau M} = \frac{\begin{matrix} 6\lambda_\tau(\lambda_\tau+1)\left(\frac{r_0}{t_p}\right)^{2\lambda_\tau+1} - 3(\lambda_\tau^2-1)\left(\frac{r_0}{t_p}\right)^{2\lambda_\tau+2} - \\ 12\lambda_\tau\left(\frac{r_0}{t_p}\right)^{\lambda_\tau+2} - 3(\lambda_\tau+1)^2\left(\frac{r_0}{t_p}\right)^{2\lambda_\tau} + 12\lambda_\tau\left(\frac{r_0}{t_p}\right)^{\lambda_\tau+1} + \\ 3\left[\left(\frac{r_0}{t_p}\right)-1\right](\lambda_\tau-1)\left\{\left[\left(\frac{r_0}{t_p}\right)-1\right]\lambda_\tau + \left(\frac{r_0}{t_p}\right)+1\right\} \end{matrix}}{\begin{matrix} 6\lambda_\tau(\lambda_\tau+1)\left(\frac{r_0}{t_p}\right)^{2\lambda_\tau+1} - (9\lambda_\tau^2+6\lambda_\tau-3)\left(\frac{r_0}{t_p}\right)^{2\lambda_\tau+2} - \\ 12\lambda_\tau\left(\frac{r_0}{t_p}\right)^{\lambda_\tau+2} - (\lambda_\tau^2-1)\left(\frac{r_0}{t_p}\right)^{2\lambda_\tau} + 12\lambda_\tau\left(\frac{r_0}{t_p}\right)^{\lambda_\tau+3} + \\ \left\{\left[-4\left(\frac{r_0}{t_p}\right)^3 + 9\left(\frac{r_0}{t_p}\right)^2 + 4\left(\frac{r_0}{t_p}\right)^{2\lambda_\tau+3} - 6\left(\frac{r_0}{t_p}\right)+1\right]\lambda_\tau - \\ 4\left(\frac{r_0}{t_p}\right)^3 + 3\left(\frac{r_0}{t_p}\right)^2 + 4\left(\frac{r_0}{t_p}\right)^{2\lambda_\tau+3} + 1\right\}(\lambda_\tau-1) \end{matrix}}.$$

Although the full self-equilibrium stress distribution $\tau_{se}(r/t_b)$ should be involved in order to obtain Y_n, integrating the complete expression does not provide satisfactory results and a simplification is required. The original coordinate system origin transformation (Eq. E.1) is reduced to:

$$r'^2 = r^2 + r_0^2 \tag{E.3}$$

and the $\left\{1+\left(\frac{r_0}{t_p}\right)^{2\lambda_\tau}\left(\frac{r'}{t_p}\right)^{-2\lambda_\tau}\right\}$ term is excluded. At the same time, for an accurate Y_n definition near the notch, only the exponential term $\left(\frac{r'}{t_p}\right)^{\lambda_\tau-1}$ needs to be evaluated and the bending equilibrium related term $(C_{tw}+\mu_{\tau M})\left\{2\left(\frac{r'}{t_p}\right)-1\right\}$ can be excluded

from integration. Notch factor Y_n becomes:

$$Y_n\left(\frac{a}{t_p}\right) = \left(\frac{2}{\pi}\right)\int\limits_0^1 \frac{\tau_{se}\left(\frac{r'}{a}\cdot\frac{a}{t_p}\right)}{\sqrt{1-\left(\frac{r'}{a}\right)^2}}\mathrm{d}\left(\frac{r'}{a}\right)$$

$$= \left(\frac{2}{\pi}\right)\int\limits_0^1 \frac{\mu_{\tau F}\cos(\lambda_\tau\theta)\left[\left(\frac{r'}{a}\cdot\frac{a}{t_p}\right)^2+\left(\frac{r_0}{t_p}\right)^2\right]^{\frac{\lambda_\tau-1}{2}}}{\sqrt{1-\left(\frac{r'}{a}\right)^2}}\mathrm{d}\left(\frac{r'}{a}\right) - (\mu_{\tau M}+C_{tw})\left\{2\left(\frac{a}{t_p}\right)-\frac{\pi}{2}\right\}$$

$$= \left(\frac{2}{\pi}\right)\left\{\mu_{\tau F}\left(\frac{r_0}{t_b}\right)^{\lambda_\tau-1}\cos(\lambda_\tau\theta)\sqrt{\pi}r_0\cdot\right.$$

$$\left[\Gamma(1-\lambda_\tau)\Gamma\left(\frac{\lambda_\tau}{2}\right)a^{\lambda_\tau}r_0^{-\lambda_\tau}{}_2F_1\left(\left[\frac{1-\lambda_\tau}{2},\frac{1-\lambda_\tau}{2}\right];1-\frac{\lambda_\tau}{2};-\frac{r_0^2}{a^2}\right)+\right.$$

$$\left.\Gamma\left(-\frac{\lambda_\tau}{2}\right)\Gamma\left(\frac{\lambda_\tau+1}{2}\right){}_2F_1\left(\left[\frac{1}{2},\frac{1}{2}\right];1+\frac{\lambda_\tau}{2};-\frac{r_0^2}{a^2}\right)\right]\right\}\cdot$$

$$\left.\left\{2a\Gamma\left(\frac{1-\lambda_\tau}{2}\right)\Gamma\left(\frac{\lambda_\tau+1}{2}\right)\right\}^{-1} - (\mu_{\tau M}+C_{tw})\left\{2\left(\frac{a}{t_p}\right)-\frac{\pi}{2}\right\}\right.$$

(E.4)

with ${}_2F_1(\cdot)$ representing the Hypergeometric function expression. Note that the $\rho=0$ formulation (Eq. 4.10) is still a $\rho>0$ limit case. The notch stress intensity in terms of $Y_{n,III}Y_{f,III}$ and K_{III} for the same geometry and loading conditions as provided for $\rho=0$ (Fig. 4.5) are shown for illustration purposes (Fig. E.1). A good match with the FE results is obtained.

Weld toe notches appear at both sides of a plate/shell if stress distribution symmetry with respect to $(t_p/2)$ is detected, as shown for a DS welded cruciform joint (Fig. 4.1). Any influence of another crack at a weld toe notch in the plane of symmetry at $(t_p/2)$ is assumed to be a long crack effect, i.e. considering one notch at the time is sufficient. For an out-of-plane shear force induced response $(\tau_s=\tau_{ss})$, the self-equilibrium stress part of $\tau_s(r/t_p)$ for $\rho=0$ yields [29]:

$$\tau_{se}\left(\frac{r}{t_p}\right) = \left(\frac{r}{t_p}\right)^{\lambda_\tau-1}\mu_{\tau F}\cos(\lambda_\tau\beta_a) - \mu_{\tau M}\left\{2\left(\frac{r}{t_p}\right)-1\right\} - C_{tw}\left\{4\left(\frac{r}{t_p}\right)-1\right\}.$$

(E.5)

For $\rho>0$, the coordinate system origin must be transformed $(O'\to O)$ like for non-symmetry (Eq. E.1) and becomes:
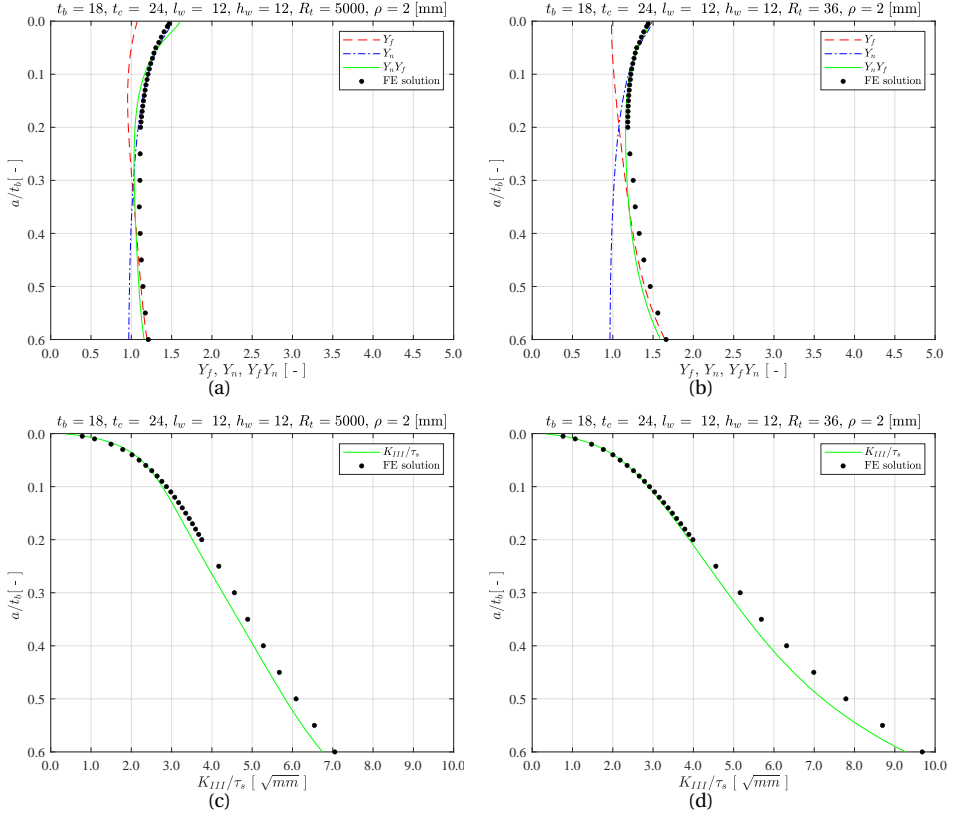
Figure E.1.: Mode-III weld toe notch SIF far field- and notch distribution (a, b) and K_{III} distribution (c, d) for a DS welded T-joint with $\rho > 0$; $r_{\tau_s} = 0$ (a, c), $r_{\tau_s} = 0.25$ (b, d).

$$\tau_{se}\left(\frac{r}{t_p}\right) = \left(\frac{r'}{t_p}\right)^{\lambda_\tau - 1} \mu_{\tau F} \cos(\lambda_\tau \beta_a) \left\{ 1 + \left(\frac{r_0}{t_p}\right)^{2\lambda_\tau} \left(\frac{r'}{t_p}\right)^{-2\lambda_\tau} \right\} - \mu_{\tau M} \left\{ 2\left(\frac{r'}{t_p}\right) - 1 \right\} - C_{tw}\left\{ 4\left(\frac{r'}{t_p}\right) - 1 \right\}. \tag{E.6}$$

To calculate the coefficients $\mu_{\tau F}$ and $\mu_{\tau M}$, half the plate thickness is considered. Using force and moment equilibrium only is principally not sufficient and a symmetry condition has been added as a 3rd equation. However, the system of equations has become over determined, meaning a least squares solution will be obtained. Allowing for some relaxation, i.e. ignoring moment equilibrium, provides quite accurate results – like for mode-I [18]. Force equilibrium in a weak form and

symmetry for $\rho = 0$ provides [130]:

$$\mu_{\tau F} = \frac{\lambda_\tau (C_{tw} + 1)}{\cos(\lambda_\tau \beta_a) 2^{1-\lambda_\tau} \left(1 + \frac{\lambda_\tau}{2}(\lambda_\tau - 1)\right)} \qquad (E.7)$$

and

$$\mu_{\tau M} = \frac{2\lambda_\tau (\lambda_\tau - 1)}{\lambda_\tau^2 - \lambda_\tau + 2} \qquad (E.8)$$

and for $\rho > 0$ [130]:

$$\mu_{\tau F} = \frac{\lambda_\tau \left\{\lambda_\tau \left(\frac{r_0}{t_p}\right)^{2\lambda_\tau} \left(\frac{2r_0+1}{2t_p}\right)\left(\frac{4r_0+1}{4t_p^2}\right)\left\{2^{\lambda_\tau-1} + C_{tw}2^{\lambda_\tau}\left(\frac{1}{2t_p}\right)\right\} - \begin{array}{c} \\ 2^{\lambda_\tau+1}C_{tw}\left[\left(\frac{2r_0+1}{2t_p}\right)^2 \left(\frac{r_0}{t_p}\right)^{\lambda_\tau} - \left(\frac{2r_0+1}{2t_p}\right)\left(\frac{r_0}{t_p}\right)^{\lambda_\tau+1} - \left(\frac{2r_0+1}{2t_p}\right)^{2+\lambda_\tau} + \\ \left(\frac{r_0}{t_p}\right)\left(\frac{2r_0+1}{2t_p}\right)^{\lambda_\tau+1}\right] - 2^{\lambda_\tau}\left[\left(\frac{r_0}{t_p}\right)^{\lambda_\tau}\left(\frac{2r_0+1}{2t_p}\right) - \left(\frac{2r_0+1}{2t_p}\right)^{\lambda_\tau+1}\right]\right\}\end{array}}{\cos(\lambda_\tau \theta)\left(\frac{2r_0+1}{2t_p}\right)\left[\lambda_\tau\left[\left(\frac{4r_0+1}{4t_p^2}\right)\right]\left(\frac{r_0}{t_p}\right)^{2\lambda_\tau} - 2\left(\frac{r_0}{t_p}\right)^{\lambda_\tau} + \begin{array}{c} \\ 2\left(\frac{2r_0+1}{2t_p}\right)^{\lambda_\tau}\right]\left\{\left(\frac{2r_0+1}{2t_p}\right)\lambda_\tau 2^{\lambda_\tau}\left[\left(\frac{1}{2t_p}\right)\right]\left(\frac{r_0}{t_p}\right)^{2\lambda_\tau} + \\ 2^{\lambda_\tau}\left[\left(\frac{2r_0+1}{2t_p}\right)^{\lambda_\tau} - \left(\frac{r_0}{t_p}\right)^{\lambda_\tau}\right] + \frac{\lambda_\tau(\lambda_\tau-1)}{2t_p^2}\right\}\end{array}} \qquad (E.9)$$

and

$$\mu_{\tau M} = \frac{\left(\frac{2r_0+1}{2t_p}\right)^2 \lambda_\tau \left\{2^{\lambda_\tau}\left(\frac{r_0}{t_p}\right)^{2\lambda_\tau} + 4(\lambda_\tau - 1)\right\}}{\left\{\lambda_\tau 2^{\lambda_\tau}\left(\frac{r_0}{t_p}\right)^{2\lambda_\tau}\left(\frac{2r_0+1}{4t_p^2}\right) + 2^{\lambda_\tau}\left[\left(\frac{2r_0+1}{2t_p}\right)^{\lambda_\tau} - \left(\frac{r_0}{t_p}\right)^{\lambda_\tau}\right] + \frac{\lambda_\tau(\lambda_\tau-1)}{2t_p^2}\right\}}. \qquad (E.10)$$

Applying the $\tau_{se}(r/t_p)$ formulation (Eq. E.5) as unit crack face traction along the assumed virtual crack path using the weight function approach (Eq. 4.10) denotes for $\rho = 0$:

$$\begin{aligned} Y_{n,III,s}\left(\frac{a}{t_p}\right) &= f_{\rho=0}\left(\frac{a}{t_p}\right) \\ &= \frac{\left(\frac{a}{t_p}\right)^{\lambda_\tau} \mu_{\tau F} \cos(\lambda_\tau \beta_a)\sqrt{\pi}\Gamma\left(\frac{\lambda_\tau}{2}\right)}{2\left(\frac{a}{t_p}\right)\Gamma\left(\frac{\lambda_\tau+1}{2}\right)} + \\ &\quad \frac{\left[\left(\frac{a}{t_p}\right)(-4\mu_{\tau M} - 8C_{tw}) + \pi\left(\mu_{\tau M} + C_{tw}\right)\right]\left(\frac{a}{t_p}\right)\Gamma\left(\frac{\lambda_\tau+1}{2}\right)}{2\left(\frac{a}{t_p}\right)\Gamma\left(\frac{\lambda_\tau+1}{2}\right)}. \end{aligned} \qquad (E.11)$$

In case of $\rho > 0$, using the complete $\tau_{se}(r/t_p)$ formulation (Eq. E.6) does not provide satisfactory $Y_{n,III,s}(a/tp)$ results, like for non-symmetry with respect to $(t_p/2)$. Similarly modifying the coordinate system transformation, ignoring the

E

notch affecting term $\left\{1+\left(\frac{r_0}{t_p}\right)^{2\lambda_\tau}\left(\frac{r'}{t_p}\right)^{-2\lambda_\tau}\right\}$ and excluding the $\left(\mu_{\tau M}\left\{2\left(\frac{r'}{t_p}\right)-1\right\}\right)$ and $\left(C_{tw}\left\{4\left(\frac{r'}{t_p}\right)-1\right\}\right)$ terms from transformation for the sake of simplification, the notch factor for an out-of-plane shear force becomes:

$$
\begin{aligned}
Y_{n,III,s}\left(\frac{a}{t_p}\right) &= f_{\rho>0}\left(\frac{a}{t_p}\right) \\
&= \left(\frac{2}{\pi}\right)\int_0^1 \frac{\mu_{\tau F}\cos(\lambda_\tau\theta)\left[\left(\frac{r'}{a}\cdot\frac{a}{t_p}\right)^2+\left(\frac{r_0}{t_p}\right)^2\right]^{\frac{\lambda_\tau-1}{2}}}{\sqrt{1-\left(\frac{r'}{a}\right)^2}}\,\mathrm{d}\left(\frac{r'}{a}\right) - \\
&\quad \mu_{\tau M}\left\{2\left(\frac{a}{t_p}\right)-\frac{\pi}{2}\right\} - C_{tw}\left\{4\left(\frac{a}{t_p}\right)-\frac{\pi}{2}\right\} \\
&= \left(\frac{2}{\pi}\right)\left\{\mu_{\tau F}\left(\frac{r_0}{t_b}\right)^{\lambda_\tau-1}\cos\left(\lambda_\tau\theta\right)\sqrt{\pi}r_0\cdot \right.\\
&\quad \left[\Gamma\left(1-\lambda_\tau\right)\Gamma\left(\frac{\lambda_\tau}{2}\right)a^{\lambda_\tau}r_0^{-\lambda_\tau}{}_2F_1\left(\left[\frac{1-\lambda_\tau}{2},\frac{1-\lambda_\tau}{2}\right];1-\frac{\lambda_\tau}{2};-\frac{r_0^2}{a^2}\right)+\right.\\
&\quad \left.\Gamma\left(-\frac{\lambda_\tau}{2}\right)\Gamma\left(\frac{\lambda_\tau+1}{2}\right){}_2F_1\left(\left[\frac{1}{2},\frac{1}{2}\right];1+\frac{\lambda_\tau}{2};-\frac{r_0^2}{a^2}\right)\right]\right\}\cdot \\
&\quad \left.\left\{2a\Gamma\left(\frac{1-\lambda_\tau}{2}\right)\Gamma\left(\frac{\lambda_\tau+1}{2}\right)\right\}^{-1} - \mu_{\tau M}\left\{2\left(\frac{a}{t_p}\right)-\frac{\pi}{2}\right\} - C_{tw}\left\{4\left(\frac{a}{t_p}\right)-\frac{\pi}{2}\right\}.
\end{aligned}
$$
(E.12)

For a torsion moment induced response ($\tau_s = \tau_{st}$) the far field torsion stress projection must be included. Like for the $\tau_{ns}(r/t_p)$ formulation [130], $Y_{n,III,s}(a/t_p)$ needs to be shifted first by either $\{1-f_{\rho=0}(a/t_p = 1/2)\}$ or $\{1-f_{\rho>0}(a/t_p = 1/2)\}$ in order to meet the condition $\tau_{nt}(r/t_p = 1/2) = 0$. To satisfy anti-symmetry, the τ_{nt} gradient at $(r/t_p = 1/2)$ should be equal to the far field torsion value: -2. Subtracting the shift in terms of a torsion stress gradient $-2\{1-f_{\rho=0}(r/t_p = 1/2)\}$ or $-2\{1-f_{\rho>0}(r/t_p = 1/2)\}$ from the unit stress 1, the obtained formulation needs to be scaled using $\{2f_{\rho=0}(r/t_p = 1/2)-1\}$ or $\{2f_{\rho>0}(r/t_p = 1/2)-1\}$. For $\rho = 0$, the notch factor yields:

$$
Y_{n,III,t}\left(\frac{a}{t_p}\right) = \left(\frac{2}{\pi}\right)\left[2f_{\rho=0}\left(\frac{a}{t_p}=\frac{1}{2}\right)-1\right]\left\{f_{\rho=0}\left(\frac{a}{t_p}\right)+\left[1-f_{\rho=0}\left(\frac{a}{t_p}=\frac{1}{2}\right)\right]\right\}
$$
(E.13)

with

$$f_{\rho=0}\left(\frac{a}{t_p}=\frac{1}{2}\right)=\left(\frac{2}{\pi}\right)\left[\frac{2^{-\lambda_\tau}\mu_{\tau F}\cos(\lambda_\tau\beta_a)\sqrt{\pi}\Gamma\left(\frac{\lambda_\tau}{2}\right)}{\Gamma\left(\frac{\lambda_\tau+1}{2}\right)}+\right.$$
$$\left.\frac{[(-2\mu_{\tau M}-4C_{tw})+\pi\left(\mu_{\tau M}+C_{tw}\right)]\Gamma\left(\frac{\lambda_\tau+1}{2}\right)}{2\Gamma\left(\frac{\lambda_\tau+1}{2}\right)}\right].$$

In case $\rho>0$:

$$Y_{n,III,t}\left(\frac{a}{t_p}\right)=\left(\frac{2}{\pi}\right)\left[2f_{\rho>0}\left(\frac{a}{t_p}=\frac{1}{2}\right)-1\right]\left\{f_{\rho>0}\left(\frac{a}{t_p}\right)+\left[1-f_{\rho>0}\left(\frac{a}{t_p}=\frac{1}{2}\right)\right]\right\} \quad\text{(E.14)}$$

with $f_{\rho>0}(a/t_p=1/2)$ being numerically obtained (Eq. E.12). Adopting a linear superposition principle for the shear force and torsion moment contributions provides for $\rho=0$:

$$Y_{n,III}\left(\frac{a}{t_p}\right)=\tau_s\left(\frac{2}{\pi}\right)\left(\left[1-2r_{\tau_s}\left\{1-f_{\rho=0}\left(\frac{a}{t_p}=\frac{1}{2}\right)\right\}\right]f_{\rho=0}\left(\frac{a}{t_p}\right)+\right.$$
$$\left.\left[2f_{\rho=0}\left(\frac{a}{t_p}=\frac{1}{2}\right)-1\right]\left[1-f_{\rho=0}\left(\frac{a}{t_p}=\frac{1}{2}\right)\right]\right). \quad\text{(E.15)}$$

The same formulation applies for $\rho>0$, involving $f_{\rho>0}(a/t_p=1/2)$. Like for non-symmetry with respect to $(t_p/2)$, the $\rho=0$ formulations are a $\rho>0$ limit case. For a tubular structure with attachment involving a DS welded cruciform joint and an applied torsion moment M_t (Fig. 4.1), r_{τ_s} changes for varying R_t. For $R_t\to t_b$ (reflecting a solid shaft) and $R_t\to\infty$ (corresponding to a quasi-planar structure), the ($r_{\tau_s}=1$) and ($r_{\tau_s}=0$) limit cases appear. The performance of the obtained formulations is illustrated (Figs. E.2 and E.3) for both cases as well as for an in between value ($r_{\tau_s}=0.25$). In general, the relative error (Fig. E.4) is within 5 [%] for both $Y_{n,III}Y_{f,III}$ and K_{III}, except for $(a/t_p)\to0$.
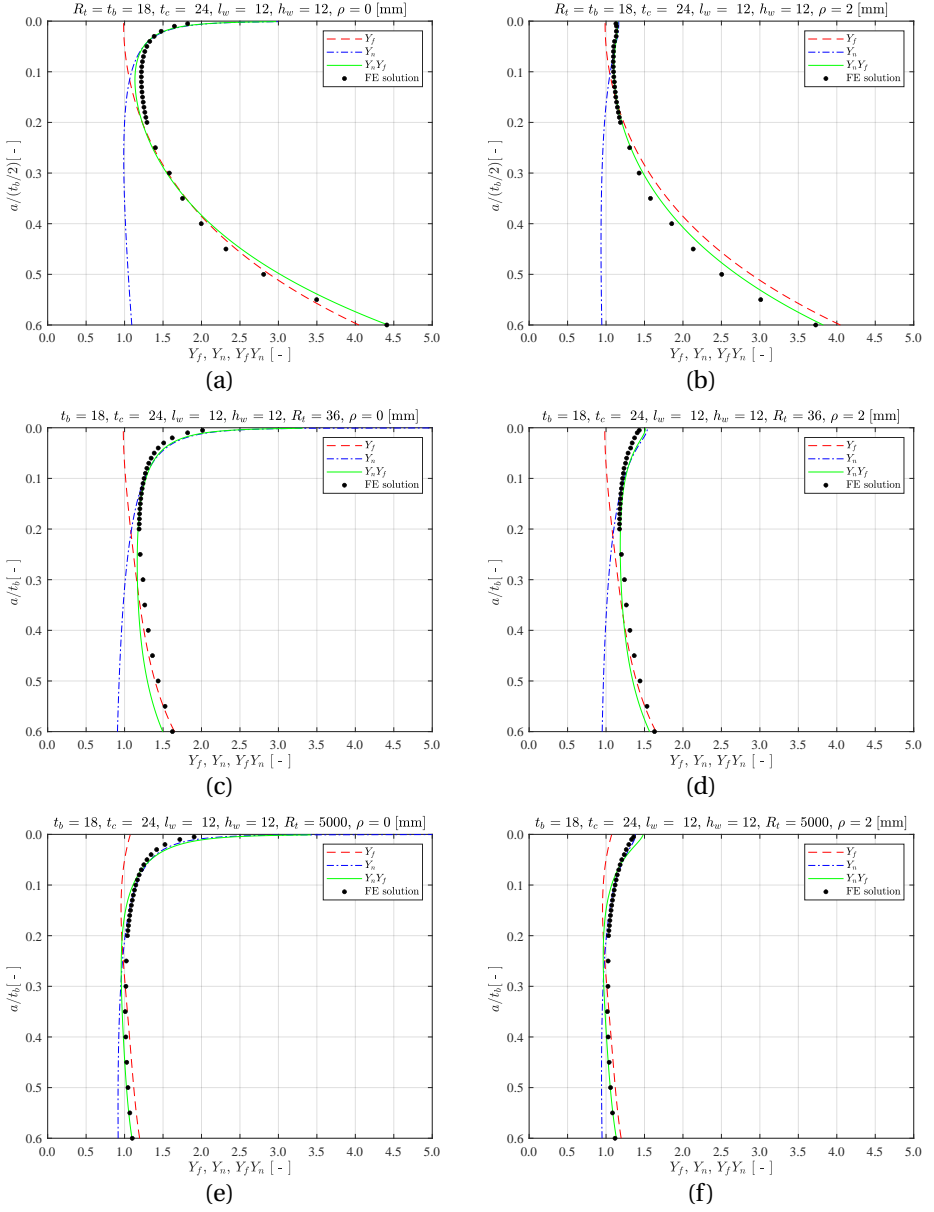
Figure E.2.: Weld toe SIF far field- and notch distribution for $\rho = 0$ (a, c, e) and $\rho > 0$ (b, d, f) for a DS welded cruciform joint; $r_{\tau_s} = 1$ (a, b), $r_{\tau_s} = 0.25$ (c, d), $r_{\tau_s} = 0$ (e, f).
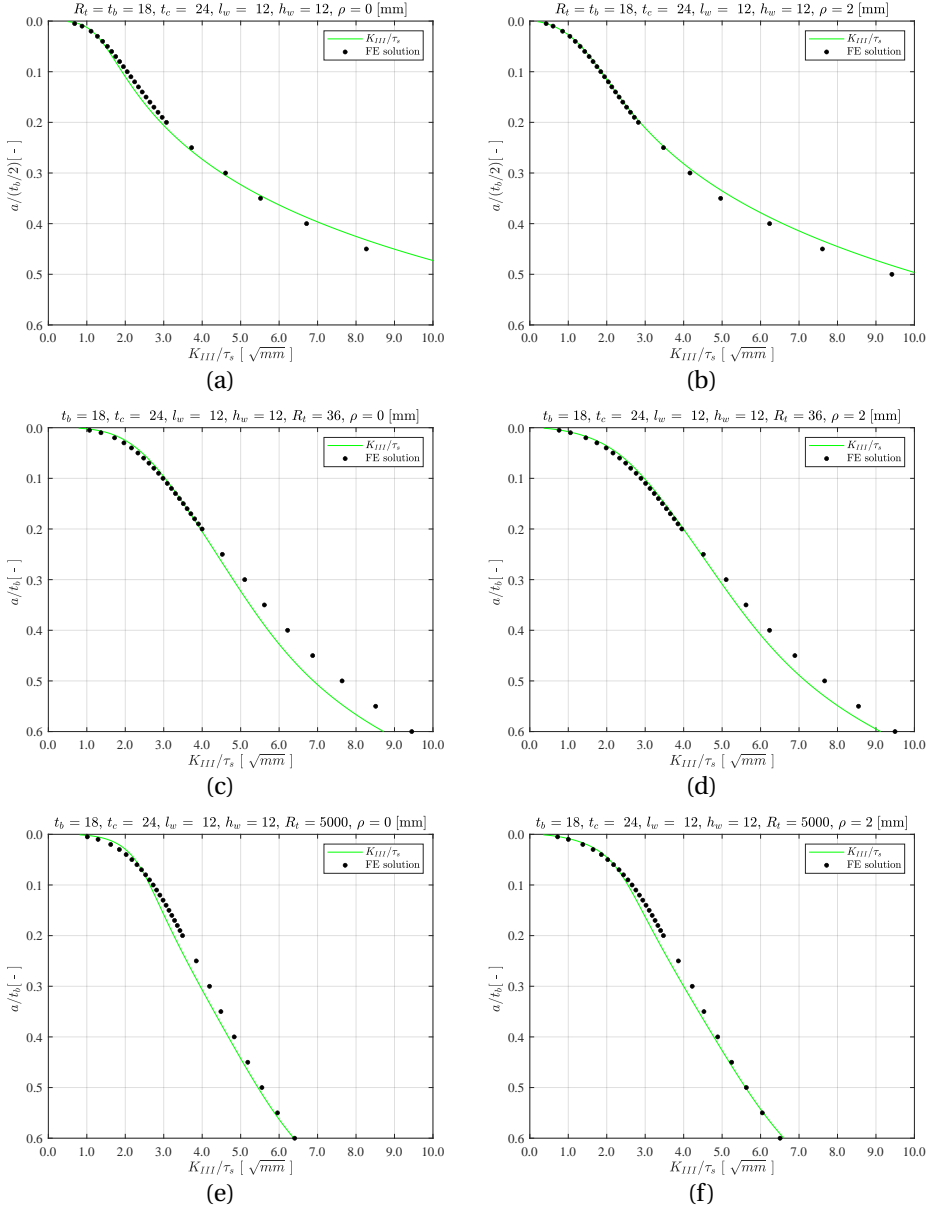
Figure E.3.: Weld toe SIF for $\rho = 0$ (a, c, e) and $\rho > 0$ (b, d, f) for a DS welded cruciform joint; $r_{\tau_s} = 1$ (a, b), $r_{\tau_s} = 0.25$ (c, d), $r_{\tau_s} = 0$ (e, f).

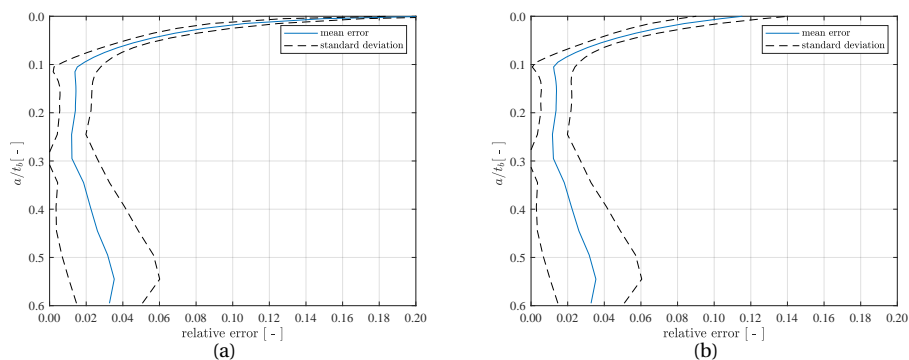**E**

Figure E.4.: Relative $Y_{n,III}Y_{f,III}$ (a) and K_{III} (b) error for DS welded cruciform joint, comparing the FE solutions and the analytical results for the full parameter application range.

F

HEXAPOD FATIGUE TEST DATA

Table F.1.: Constant amplitude loading test results.

load case	$\Delta\sigma_n$ [MPa]	$\Delta\tau_n$ [MPa]	N [-]	R_σ [-]	R_τ [-]	ph.shift [°]	freq.ratio $\sigma:\tau$ [-]	th. cond.
normal force	175		$5.18\cdot10^6$	0.1				AW
F_n	175		$1.06\cdot10^7$	0.1				AW
bending moment	320		$7.32\cdot10^4$	0.1				AW
M_b	320		$7.48\cdot10^4$	0.1				AW
	320		$9.38\cdot10^4$	0.1				AW
	305		$1.18\cdot10^5$	0.1				AW
	305		$1.47\cdot10^5$	0.1				AW
	305		$1.81\cdot10^5$	0.1				AW
	240		$6.98\cdot10^5$	0.1				AW
	240		$1.97\cdot10^6$	0.1				AW
	240		$2.39\cdot10^6$	0.1				AW
	305		$8.19\cdot10^6$	-1				AW
	305		$1.56\cdot10^5$	0.1				SR
	240		$9.36\cdot10^5$	0.1				SR
	370		$1.73\cdot10^5$	-1				SR
torsion moment		318	$3.03\cdot10^4$		-1			AW
M_t		318	$5.97\cdot10^4$		-1			AW
		318	$1.61\cdot10^5$		-1			AW
		274	$2.63\cdot10^5$		-1			AW
		274	$9.41\cdot10^5$		-1			AW
		274	$1.42\cdot10^6$		-1			AW
		254	$3.53\cdot10^6$		-1			AW
		254	$2.24\cdot10^6$		-1			AW
		242	$^*1.19\cdot10^7$		-1			AW
		231	$^*1.71\cdot10^7$		-1			AW
		318	$2.75\cdot10^4$		-1			SR
		274	$1.31\cdot10^6$		-1			SR
M_b and M_t	240	139	$8.32\cdot10^4$	0.1	0.1	0	1	AW
induced multiaxial	240	139	$4.73\cdot10^5$	0.1	0.1	0	1	AW
in-phase	220	127	$4.07\cdot10^5$	0.1	0.1	0	1	AW
	220	127	$1.28\cdot10^6$	0.1	0.1	0	1	AW
	200	115	$2.17\cdot10^6$	0.1	0.1	0	1	AW
	200	115	$9.11\cdot10^6$	0.1	0.1	0	1	AW
	170	98	$^*2.00\cdot10^7$	0.1	0.1	0	1	AW
M_b and M_t	260	150	$6.40\cdot10^4$	0.1	0.1	90	1	AW
induced multiaxial	260	150	$7.99\cdot10^4$	0.1	0.1	90	1	AW
90° out-of-phase	240	139	$1.19\cdot10^5$	0.1	0.1	90	1	AW
	240	139	$1.37\cdot10^5$	0.1	0.1	90	1	AW
	200	115	$3.07\cdot10^6$	0.1	0.1	90	1	AW
	200	115	$4.38\cdot10^6$	0.1	0.1	90	1	AW
	170	98	$^*2.00\cdot10^7$	0.1	0.1	90	1	AW
M_b and M_t	240	139	$3.76\cdot10^4$	0.1	0.1	0	3	AW
induced multiaxial	240	139	$6.94\cdot10^4$	0.1	0.1	0	3	AW
1:3 asynchronous**	225	130	$1.02\cdot10^5$	0.1	0.1	0	3	AW
	225	130	$1.14\cdot10^5$	0.1	0.1	0	3	AW
	210	121	$1.32\cdot10^5$	0.1	0.1	0	3	AW
	210	121	$2.26\cdot10^5$	0.1	0.1	0	3	AW
	190	110	$^*7.49\cdot10^6$	0.1	0.1	0	3	AW
	170	98	$^*7.83\cdot10^6$	0.1	0.1	0	3	AW

$^{(*)}$runout
$^{(**)}$ N correspond to σ cycles

Table F.2.: Variable amplitude loading test results.

load case	$\Delta\sigma_{n,max}$ [MPa]	$\Delta\tau_{n,max}$ [MPa]	N [-]	R_σ [-]	R_τ [-]	ph.shift [°]	freq. ratio $\sigma:\tau$ [-]	th. cond.
bending moment	320		$2.88\cdot10^5$	0.1				AW
M_b	320		$4.02\cdot10^5$	0.1				AW
	320		$6.77\cdot10^5$	0.1				AW
	260		$1.72\cdot10^6$	0.1				AW
	260		$2.88\cdot10^6$	0.1				AW
	260		$5.89\cdot10^6$	0.1				AW
	260		$^*1.00\cdot10^7$	0.1				AW
torsion moment		570	$5.02\cdot10^6$		-1			AW
M_t		570	$5.15\cdot10^6$		-1			AW
		570	$3.29\cdot10^6$		-1			AW
M_b and M_t	267	154	$4.97\cdot10^5$	0.1	0.1	0	1	AW
induced multiaxial	267	154	$6.31\cdot10^5$	0.1	0.1	0	1	AW
in-phase	267	154	$9.36\cdot10^5$	0.1	0.1	0	1	AW
	242	140	$2.12\cdot10^6$	0.1	0.1	0	1	AW
	242	140	$4.75\cdot10^6$	0.1	0.1	0	1	AW
	235	136	$^*1.00\cdot10^7$	0.1	0.1	0	1	AW
	235	136	$^*1.00\cdot10^7$	0.1	0.1	0	1	AW
M_b and M_t	290	167	$3.70\cdot10^5$	0.1	0.1	90	1	AW
induced multiaxial	290	167	$4.00\cdot10^5$	0.1	0.1	90	1	AW
90° out-of-phase	290	167	$7.93\cdot10^5$	0.1	0.1	90	1	AW
	267	154	$8.55\cdot10^5$	0.1	0.1	90	1	AW
	267	154	$1.43\cdot10^6$	0.1	0.1	90	1	AW
	267	154	$2.17\cdot10^6$	0.1	0.1	90	1	AW

$^{(*)}$runout

F

BIBLIOGRAPHY

[1] J. Schijve. *Fatigue of Structures and Materials*. Ed. by J. Schijve. Springer Netherlands, 2009. ISBN: 978-1-4020-6807-2.

[2] G. Bufalari, P. S. Van Lieshout, M. L. Kaminski, and J. H. Den Besten. "Numerical comparative study of multiaxial fatigue methods applied to welded joints in a container vessel". In: *5th Symposium on Structural Durability (SoSDiD)* (May 2017).

[3] C. Han, K. Liu, Y. Ma, P. Qin, and T. Zou. "Multiaxial fatigue assessment of jacket-supported offshore wind turbines considering multiple random correlated loads". In: *Renewable Energy* 169 (May 2021), pp. 1252–1264. ISSN: 18790682. DOI: 10.1016/j.renene.2021.01.093.

[4] L. Reis, B. Li, and M. de Freitas. "A multiaxial fatigue approach to Rolling Contact Fatigue in railways". In: *International Journal of Fatigue* 67 (2014). Multiaxial Fatigue 2013, pp. 191–202. ISSN: 0142-1123. DOI: https://doi.org/10.1016/j.ijfatigue.2014.02.001.

[5] B. Zhao, L. Xie, L. Wang, Z. Hu, S. Zhou, and X. Bai. "A new multiaxial fatigue life prediction model for aircraft aluminum alloy". In: *International Journal of Fatigue* 143 (2021), p. 105993. ISSN: 0142-1123. DOI: https://doi.org/10.1016/j.ijfatigue.2020.105993.

[6] J. den Besten. "Fatigue damage criteria classification, modelling developments and trends for welded joints in marine structures". In: *Ships and Offshore Structures* 13.8 (2018), pp. 787–808. ISSN: 17445302. DOI: 10.1080/17445302.2018.1463609.

[7] R. Danzer, P. Supancic, J. Pascual, and T. Lube. "Fracture statistics of ceramics – Weibull statistics and deviations from Weibull statistics". In: *Engineering Fracture Mechanics* 74.18 (Dec. 2007), pp. 2919–2932. ISSN: 0013-7944. DOI: 10.1016/j.engfracmech.2006.05.028.

[8] A. Wormsen, B. Sjödin, G. Härkegard, and A. Fjeldstad. "Non-local stress approach for fatigue assessment based on weakest-link theory and statistics of extremes". In: *Fatigue & Fracture of Engineering Materials & Structures* 30.12 (Nov. 2007), pp. 1214–1227. ISSN: 1460-2695. DOI: 10.1111/j.1460-2695.2007.01190.x.

[9] M. Todinov. "Is Weibull distribution the correct model for predicting probability of failure initiated by non-interacting flaws?" In: *International Journal of Solids and Structures* 46.3–4 (Feb. 2009), pp. 887–901. ISSN: 0020-7683. DOI: 10.1016/j.ijsolstr.2008.09.033.

[10] P. S. Van Lieshout, J. H. Den Besten, and M. L. Kaminski. "Multiaxial fatigue assessment of welded joints in marine structures Literature overview of progress in academia and engineering practice". In: *International Shipbuilding Progress* 65 (2018), pp. 29–71. DOI: 10.3233/ISP-170141.

[11] I. Glen, A. Dinovitzer, R. Paterson, L. Luznik, and C. Bayley. *Fatigue resistant detail Design Guide for Ship - Ship Structure Committee*. U.S. Coast Guard Headquarters., 1999.

[12] C. Guedes Soares and Y. Garbatov. *Proceedings of 19th International Ship and Offshore Structures Congress (ISSC 2015)*. Vol. 74. 2015. ISBN: 978-1-315-64719-7. DOI: 10.1016/j.marstruc.2017.09.001.

[13] T. Lassen and N. Recho. "Proposal for a more accurate physically based S-N curve for welded steel joints". In: *International Journal of Fatigue* 31.1 (Jan. 2009), pp. 70–78. ISSN: 01421123. DOI: 10.1016/j.ijfatigue.2008.03.032.

[14] Y. Qin, J. den Besten, S. Palkar, and M. L. Kaminski. "Mid- and High-Cycle Fatigue of Welded Joints in Steel Marine Structures: Effective Notch Stress and Total Stress Concept Evaluations". In: *International Journal of Fatigue* 142.July 2020 (2021), p. 105822. ISSN: 01421123. DOI: 10.1016/j.ijfatigue.2020.105822.

[15] C. M. Sonsino and M. Kueppers. "Multiaxial fatigue of welded joints under constant and variable amplitude loadings". In: *Fatigue and Fracture of Engineering Materials and Structures* 24.5 (2001), pp. 309–327. DOI: 10.1046/j.1460-2695.2001.00393.x.

[16] Y. Qin, J. H. den Besten, S. Palkar, and M. L. Kaminski. "Fatigue design of welded double-sided T-joints and double-sided cruciform joints in steel marine structures: A total stress concept". In: *Fatigue and Fracture of Engineering Materials and Structures* 42.12 (Dec. 2019), pp. 2674–2693. ISSN: 14602695. DOI: 10.1111/ffe.13089.

[17] D. Radaj, P. Lazzarin, and F. Berto. "Generalised Neuber concept of fictitious notch rounding". In: *International Journal of Fatigue* 51 (June 2013), pp. 105–115. ISSN: 01421123. DOI: 10.1016/j.ijfatigue.2013.01.005.

[18] J. den Besten. "Fatigue resistance of welded joints in aluminium high-speed craft: a total stress concept". PhD thesis. Delft University of Technology, 2015, pp. 1–396. ISBN: 9789462330405.

[19] H. Neuber. *Kerbspannungslehre*. Springer - Verlag, 1937. ISBN: 3-540-67657-0.

[20] G. Zhang, C. M. Sonsino, and R. Sundermeier. "Method of effective stress for fatigue: Part II – Applications to V-notches and seam welds". In: *International Journal of Fatigue* 37 (Apr. 2012), pp. 24–40. ISSN: 01421123. DOI: 10.1016/j.ijfatigue.2011.09.016.

[21] C. M. Sonsino, W. Fricke, F. De Bruyne, A. Hoppe, A. Ahmadi, and G. Zhang. "Notch stress concepts for the fatigue assessment of welded joints - Background and applications". In: *International Journal of Fatigue* 34.1 (Jan. 2012), pp. 2–16. ISSN: 01421123. DOI: 10.1016/j.ijfatigue.2010.04.011.

[22] A. Carpinteri, J. Boaretto, G. Fortese, F. Giordani, I. Iturrioz, C. Ronchei, D. Scorza, and S. Vantadori. "Fatigue life estimation of fillet-welded tubular T-joints subjected to multiaxial loading". In: *International Journal of Fatigue* 101 (Aug. 2017), pp. 263–270. ISSN: 01421123. DOI: `10.1016/j.ijfatigue.2016.10.012`.

[23] S. Vantadori, I. Iturrioz, A. Carpinteri, F. Greco, and C. Ronchei. "A novel procedure for damage evaluation of fillet-welded joints". In: *International Journal of Fatigue* 136 (July 2020). ISSN: 01421123. DOI: `10.1016/j.ijfatigue.2020.105599`.

[24] D. Taylor. *The theory of critical distances*. Elsevier Science & Technology, May 2014.

[25] O. Ezeh and L. Susmel. "On the notch fatigue strength of additively manufactured polylactide (PLA)". In: *International Journal of Fatigue* 136 (2020), p. 105583. ISSN: 0142-1123. DOI: `https://doi.org/10.1016/j.ijfatigue.2020.105583`.

[26] B. Gillham, A. Yankin, F. McNamara, C. Tomonto, D. Taylor, and R. Lupoi. "Application of the Theory of Critical Distances to predict the effect of induced and process inherent defects for SLM Ti-6Al-4V in high cycle fatigue". In: *CIRP Annals* 70.1 (2021), pp. 171–174. ISSN: 0007-8506. DOI: `https://doi.org/10.1016/j.cirp.2021.03.004`.

[27] B. Gillham, A. Yankin, F. McNamara, C. Tomonto, C. Huang, J. Soete, G. O'Donnell, D. Trimble, S. Yin, D. Taylor, and R. Lupoi. "Tailoring the theory of critical distances to better assess the combined effect of complex geometries and process-inherent defects during the fatigue assessment of SLM Ti-6Al-4V". In: *International Journal of Fatigue* 172 (2023), p. 107602. ISSN: 0142-1123. DOI: `https://doi.org/10.1016/j.ijfatigue.2023.107602`.

[28] H. Bartsch, S. Citarelli, and M. Feldmann. "Generalisation of the effective notch stress concept for the fatigue assessment of arbitrary steel structures". In: *Journal of Constructional Steel Research* 201 (2023), p. 107715. ISSN: 0143-974X. DOI: `https://doi.org/10.1016/j.jcsr.2022.107715`.

[29] G. Bufalari, J. H. Den Besten, and M. L. Kaminski. "Mode-III fatigue of welded joints in steel maritime structures: Weld notch shear stress distributions and effective notch stress based resistance". In: *International Journal of Fatigue* (Aug. 2022), p. 107210. ISSN: 0142-1123. DOI: `10.1016/J.IJFATIGUE.2022.107210`.

[30] P. van Lieshout, J. den Besten, and M. Kaminski. "Validation of the corrected Dang Van multiaxial fatigue criterion applied to turret bearings of FPSO offloading buoys". In: *Ships and Offshore Structures* 12.4 (June 2016), pp. 521–529. ISSN: 1754-212X. DOI: `10.1080/17445302.2016.1182461`.

[31] P. van Lieshout, J. den Besten, and M. Kaminski. "Comparative study of multiaxial fatigue methods applied to welded joints in marine structures". In: *Frattura ed Integrità Strutturale* 10.37 (June 2016), pp. 173–192. ISSN: 1971-8993. DOI: `10.3221/igf-esis.37.24`.

[32]   P. van Lieshout. "On the assessment of multiaxial fatigue resistance of welded steel joints in marine structures when exposed to non-proportional constant amplitude loading". PhD thesis. TU Delft, 2019. DOI: 10.4233/UUID: AFD39F40-7569-4CC6-AC1A-659342B45F9A.

[33]   A. F. Hobbacher. "Recommendations for Fatigue Design of Welded Joints and Components". In: IIW Collection. Springer International, 2016. ISBN: 978-3-319-23756-5.

[34]   CEN. *EN 1993-1-9: Eurocode 3: Design of steel structures - Part 1-9: Fatigue.* 2005.

[35]   P. Lazzarin and S. Filippi. "A generalized stress intensity factor to be applied to rounded V-shaped notches". In: *International Journal of Solids and Structures* 43.9 (2006), pp. 2461–2478. ISSN: 00207683. DOI: 10.1016/j.ijsolstr.2005.03.007.

[36]   P. Lazzarin, M. Zappalorto, and J. Yates. "Analytical study of stress distributions due to semi-elliptic notches in shafts under torsion loading". In: *International Journal of Engineering Science* 45.2-8 (Feb. 2007), pp. 308–328. ISSN: 00207225. DOI: 10.1016/j.ijengsci.2007.04.007.

[37]   M. Zappalorto, P. Lazzarin, and J. R. Yates. "Elastic stress distributions for hyperbolic and parabolic notches in round shafts under torsion and uniform antiplane shear loadings". In: *International Journal of Solids and Structures* 45.18-19 (2008), pp. 4879–4901. ISSN: 00207683. DOI: 10.1016/j.ijsolstr.2008.04.020.

[38]   M. Zappalorto, P. Lazzarin, and F. Berto. "Elastic notch stress intensity factors for sharply V-notched rounded bars under torsion". In: *Engineering Fracture Mechanics* 76.3 (2009), pp. 439–453. ISSN: 00137944. DOI: 10.1016/j.engfracmech.2008.11.008.

[39]   M. Zappalorto and P. Lazzarin. "Stress fields due to inclined notches and shoulder fillets in shafts under torsion". In: *Journal of Strain Analysis for Engineering Design* 46.3 (2011), pp. 187–199. ISSN: 03093247. DOI: 10.1177/0309324710396019.

[40]   E. Niemi. "Stress determination for fatigue analysis of welded components". In: *Stress Determination for Fatigue Analysis of Welded Components*. Abington in association with the International Institute of Welding, 1995. ISBN: 978-1-85573-213-1.

[41]   P. Dong. "A structural stress definition and numerical implementation for fatigue analysis of welded joints". In: *International Journal of Fatigue* 23.10 (Nov. 2001), pp. 865–876. ISSN: 01421123. DOI: 10.1016/S0142-1123(01)00055-X.

[42]   DNV GL. "Class Guideline DNVGL-CG-0127: "Finite element analysis"". In: Oslo, 2016.

[43] J. Rörup, B. Maciolowski, and I. Darie. "FE-based strength analysis of ship structures for a more advanced class approval". In: *PRADS 2016 - Proceedings of the 13th International Symposium on PRActical Design of Ships and Other Floating Structures* August 2016 (2016).

[44] A. Chattopadhyay, G. Glinka, M. El-Zein, J. Qian, and R. Formas. "Stress analysis and fatigue of welded structures". In: *Welding in the World* 55.7-8 (2011), pp. 2–21. ISSN: 00432288. DOI: 10.1007/BF03321303.

[45] E. Niemi, W. Fricke, and S. J. Maddox. *Fatigue Analysis of Welded Components: Designer's Guide to the Structural Hot-Spot Stress Approach.* 2006, pp. 1–49. ISBN: 9781845691240. DOI: 10.1533/9781845696665.

[46] M. Aygul. *Fatigue analysis of welded structures using the Finite Element method.* S.l: Lap Lambert academic publ, 2012. ISBN: 9783659125935.

[47] P. Dong and J. K. Hong. "The Master S-N Curve Approach to Fatigue Evaluation of Offshore and Marine Structures". In: *23rd International Conference on Offshore Mechanics and Arctic Engineering, Volume 2.* Vol. 2. ASMEDC, Jan. 2004, pp. 847–855. ISBN: 0-7918-3744-0. DOI: 10.1115/OMAE2004-51324.

[48] P. Dong. "A robust structural stress method for fatigue analysis of ship structures". In: *Proceedings of the International Conference on Offshore Mechanics and Arctic Engineering - OMAE.* Vol. 3. American Society of Mechanical Engineers Digital Collection, Jan. 2003, pp. 199–211. DOI: 10.1115/OMAE2003-37313.

[49] F. Yousefi, M. Witt, and H. Zenner. "Fatigue strength of welded joints under multiaxial loading: Experiments and calculations". In: *Fatigue and Fracture of Engineering Materials and Structures* 24.5 (2001), pp. 339–355. ISSN: 8756758X. DOI: 10.1046/j.1460-2695.2001.00397.x.

[50] A. Siljander, P. Kurath, and F. V. Lawrence. "Non proportional fatigue of welded structures". In: *ASTM Special Technical Publication* 1122 (1992), pp. 319–338. ISSN: 00660558. DOI: 10.1520/stp24166s.

[51] M. Witt and H. Zenner. "Multiaxial fatigue behavior of welded flange-tube connections under combined loading. Experiments and lifetime prediction". In: *5th International Conference on Biaxial/Multiaxial Fatigue and Fracture.* 1997, pp. 421–434.

[52] T. Seeger and R. Olivier. *Ertragbare und zulaessige Schubspanunngen schingbeanspruchter.* 1987.

[53] Yung and F. Lawrence. "Predicting the fatigue life of welds under combined bending and torsion". In: *Mechanical Engineering Publications, Biaxial and Multiaxial Fatigue* (1986), pp. 53–69.

[54] M. Bäckström. "Multiaxial fatigue life assessment of welds based on nominal and hot spot stresses". PhD thesis. Laapeenranta University, Finland, 2003.

[55] J. Mei, P. Dong, S. Xing, A. Vasu, A. Ganamet, J. Chung, and Y. Mehta. "An overview and comparative assessment of approaches to multi-axial fatigue of welded components in codes and standards". In: *International Journal of Fatigue* 146.November 2020 (2021), p. 106144. ISSN: 01421123. DOI: 10.1016/j.ijfatigue.2021.106144.

[56] R. Archer. "Fatigue of a welded steel attachment under combined direct stress and shear stress". In: *International Conference of Fatigue of Welded Constructions*. Brighton, England, 1987, pp. 63–72.

[57] F. M. Dekking, C. Kraaikamp, H. P. Lopuhaä, and L. E. Meester. "A Modern Introduction to Probability and Statistics: Understanding why and how". In: (). ISSN: 0040-1706. DOI: 10.1198/tech.2007.s502.

[58] K. Walker. "The Effect of Stress Ratio During Crack Propagation and Fatigue for 2024-T3 and 7075-T6 Aluminum". In: *ASTM International* (1970). DOI: 10.1520/stp32032s.

[59] J. Klassen, N. Friedrich, W. Fricke, T. Nitschke-Pagel, and K. Dilger. "Influence of residual stresses on fatigue strength of large-scale welded assembly joints". In: *Welding in the World* 61.2 (2017), pp. 361–374. ISSN: 00432288. DOI: 10.1007/s40194-016-0407-8.

[60] W. N. Findley. "A Theory for the Effect of Mean Stress on Fatigue of Metals Under Combined Torsion and Axial Load or Bending". In: *Journal of Engineering for Industry* 81.4 (Nov. 1959), pp. 301–305. ISSN: 0022-0817. DOI: 10.1115/1.4008327.

[61] A. Nasr, Y. Nadot, C. Bouraoui, and R. Fathallah. "Effect of Artificial Defect and Mean Shear Stress on Torsional Fatigue Behaviour". In: *Applied Mechanics and Materials* 146 (Dec. 2011), pp. 74–82. ISSN: 1662-7482. DOI: 10.4028/www.scientific.net/AMM.146.74.

[62] L. Pallarés-Santasmartas, J. Albizuri, N. Leguinagoicoa, N. Saintier, and J. Merzeau. "The effect of mean axial and torsional stresses on the fatigue strength of 34CrNiMo6 high strength steel". In: *MATEC Web of Conferences* 300 (2019), p. 16004. DOI: 10.1051/matecconf/201930016004.

[63] R. Pawliczek and D. Rozumek. "Cyclic tests of smooth and notched specimens subjected to bending and torsion taking into account the effect of mean stress". In: *Materials* 13.9 (2020). ISSN: 19961944. DOI: 10.3390/ma13092141.

[64] Y. Nishimura, K. Yanase, Y. Tanaka, N. Miyamoto, S. Miyakawa, and M. Endo. "Effects of mean shear stress on the torsional fatigue strength of a spring steel with small scratches". In: *International Journal of Damage Mechanics* 29.1 (2020), pp. 4–18. ISSN: 15307921. DOI: 10.1177/1056789519831434.

[65] L. Susmel. "The theory of critical distances: a review of its applications in fatigue". In: *Engineering Fracture Mechanics* 75.7 (May 2008), pp. 1706–1724. ISSN: 0013-7944. DOI: 10.1016/J.ENGFRACMECH.2006.12.004.

[66] M. M. Pedersen. "Multiaxial fatigue assessment of welded joints using the notch stress approach". In: *International Journal of Fatigue* 83 (2016), pp. 269–279. ISSN: 01421123. DOI: 10.1016/j.ijfatigue.2015.10.021.

[67] M. L. Larsen, J. Baumgartner, H. B. Clausen, and V. Arora. "Multiaxial fatigue assessment of welded joints using a principal component-based measure for non-proportionality". In: *International Journal of Fatigue* 158 (May 2022). ISSN: 01421123. DOI: 10.1016/j.ijfatigue.2022.106731.

[68] A. Fatemi and N. Shamsaei. "Multiaxial fatigue: An overview and some approximation models for life estimation". In: *International Journal of Fatigue* 33 (8 Aug. 2011), pp. 948–958. ISSN: 01421123. DOI: 10.1016/j.ijfatigue.2011.01.003.

[69] R. Hibbeler and K. Yap. *Mechanics of Materials*. Pearson, 2018. ISBN: 9781292178202.

[70] J. Papuga and M. Růžička. "Two new multiaxial criteria for high cycle fatigue computation". In: *International Journal of Fatigue* 30 (1 Jan. 2008), pp. 58–66. ISSN: 01421123. DOI: 10.1016/J.IJFATIGUE.2007.02.015.

[71] J. Papuga. "A survey on evaluating the fatigue limit under multiaxial loading". In: *International Journal of Fatigue* 33 (2 2011), pp. 153–165. ISSN: 01421123. DOI: 10.1016/j.ijfatigue.2010.08.001.

[72] J. Papuga, M. Nesládek, J. Kuželka, and J. Jurenka. "Differences in the response to in-phase and out-of-phase multiaxial high-cycle fatigue loading". In: *Frattura ed Integrita Strutturale* 13 (50 2019), pp. 163–183. ISSN: 19718993. DOI: 10.3221/IGF-ESIS.50.15.

[73] A. Carpinteri, A. Spagnoli, S. Vantadori, and C. Bagni. "Structural integrity assessment of metallic components under multiaxial fatigue: The C-S criterion and its evolution". In: *Fatigue and Fracture of Engineering Materials and Structures* 36 (9 2013), pp. 870–883. ISSN: 14602695. DOI: 10.1111/ffe.12037.

[74] L. Susmel. "A simple and efficient numerical algorithm to determine the orientation of the critical plane in multiaxial fatigue problems". In: *International Journal of Fatigue* 32 (11 Nov. 2010), pp. 1875–1883. ISSN: 0142-1123. DOI: 10.1016/J.IJFATIGUE.2010.05.004.

[75] L. Susmel and H. Askes. "Modified Wöhler Curve Method and multiaxial fatigue assessment of thin welded joints". In: *International Journal of Fatigue* 43 (Oct. 2012), pp. 30–42. ISSN: 01421123. DOI: 10.1016/j.ijfatigue.2012.01.026.

[76] L. Susmel. "Four stress analysis strategies to use the Modified Wöhler Curve Method to perform the fatigue assessment of weldments subjected to constant and variable amplitude multiaxial fatigue loading". In: *International Journal of Fatigue* 67 (2014), pp. 38–54. ISSN: 01421123. DOI: 10.1016/j.ijfatigue.2013.12.001.

[77]   L. Susmel and D. Taylor. "The modified Wöhler curve method applied along with the theory of critical distances to estimate finite life of notched components subjected to complex multiaxial loading paths". In: *Fatigue and Fracture of Engineering Materials and Structures* 31 (12 2008), pp. 1047–1064. ISSN: 8756758X. DOI: 10.1111/j.1460-2695.2008.01296.x.

[78]   V. Anes, L. Reis, B. Li, M. Fonte, and M. De Freitas. "New approach for analysis of complex multiaxial loading paths". In: *International Journal of Fatigue* 62 (2014), pp. 21–33. ISSN: 01421123. DOI: 10.1016/j.ijfatigue.2013.05.004.

[79]   P. Dong, Z. Wei, and J. K. Hong. "A path-dependent cycle counting method for variable-amplitude multi-axial loading". In: *International Journal of Fatigue* 32 (4 Apr. 2010), pp. 720–734. ISSN: 01421123. DOI: 10.1016/j.ijfatigue.2009.10.010.

[80]   Z. Wei, P. Dong, J. Mei, X. Pei, and S. K. Ravi. "A moment of load path-based parameter for modeling multiaxial fatigue damage of welded structures". In: *International Journal of Fatigue* 171 (June 2023), p. 107575. ISSN: 0142-1123. DOI: 10.1016/J.IJFATIGUE.2023.107575.

[81]   J.-S. Kim, C. Kim, T.-E. Jin, and P. Dong. *Mean load effect on fatigue of welded joints using structural stress and fracture mechanics approach*. 2006.

[82]   C. M. Sonsino. "Multiaxial fatigue of welded joints under in-phase and out-of-phase local strains and stresses". In: *International Journal of Fatigue* 17 (1 1995), pp. 55–70. ISSN: 01421123. DOI: 10.1016/0142-1123(95)93051-3.

[83]   A. Bolchoun, C. M. Sonsino, H. Kaufmann, and T. Melz. "Multiaxial random fatigue of magnesium laserbeam-welded joints-Experimental results and numerical fatigue life evaluation". In: *Procedia Engineering*. Vol. 101. Elsevier Ltd, 2015, pp. 61–68. DOI: 10.1016/j.proeng.2015.02.009.

[84]   I. V. Papadopoulos, P. Davoli, C. Gorla, M. Filippini, and A. Bernasconi. "A comparative study of multiaxial high-cycle fatigue criteria for metals". In: *International Journal of Fatigue* 19 (3 1997), pp. 219–235. ISSN: 01421123. DOI: 10.1016/S0142-1123(96)00064-3.

[85]   M. A. Meggiolaro and J. T. P. De Castro. "An improved multiaxial rainflow algorithm for non-proportional stress or strain histories - Part I: Enclosing surface methods". In: *International Journal of Fatigue* 42 (Sept. 2012), pp. 217–226. ISSN: 01421123. DOI: 10.1016/j.ijfatigue.2011.10.014.

[86]   C. Jiang, Z. C. Liu, X. G. Wang, Z. Zhang, and X. Y. Long. "A structural stress-based critical plane method for multiaxial fatigue life estimation in welded joints". In: *Fatigue and Fracture of Engineering Materials and Structures* 39 (3 Mar. 2016), pp. 372–383. ISSN: 1460-2695. DOI: 10.1111/FFE.12369.

[87]   A. Cristofori, L. Susmel, and R. Tovo. "A stress invariant based criterion to estimate fatigue damage under multiaxial loading". In: *International Journal of Fatigue* 30 (9 2008), pp. 1646–1658. ISSN: 01421123. DOI: 10.1016/j.ijfatigue.2007.11.006.

[88] V. Anes, L. Reis, B. Li, and M. De Freitas. "New cycle counting method for multiaxial fatigue". In: *International Journal of Fatigue* 67 (2014), pp. 78–94. ISSN: 01421123. DOI: 10.1016/j.ijfatigue.2014.02.010.

[89] N. Bishop and F. Sherratt. *Finite Element Based Fatigue Calculations*. NAFEMS, Jan. 2000. ISBN: 9781839790089. DOI: 10.59972/TA5H05JD.

[90] J. Papuga, M. Vargas, and M. Hronek. "Evaluation of uniaxial fatigue criteria applied to multiaxially loaded unnotched samples". In: *Engineering Mechanics* 19 (3 2012), pp. 99–111.

[91] A. Carpinteri, A. Spagnoli, and S. Vantadori. "A multiaxial fatigue criterion for random loading". In: *Fatigue and Fracture of Engineering Materials and Structures* 26 (6 June 2003), pp. 515–522. ISSN: 8756758X. DOI: 10.1046/j.1460-2695.2003.00620.x.

[92] C. H. Wang and M. W. Brown. "Life prediction techniques for variable amplitude multiaxial fatigue — Part 1 : Theories". In: *Engineering Materials and Technology* 118 (3 1996), pp. 367–370.

[93] M. A. Meggiolaro and J. T. P. De Castro. "An improved multiaxial rainflow algorithm for non-proportional stress or strain histories - Part II: The Modified Wang-Brown method". In: *International Journal of Fatigue* 42 (2012), pp. 194–206. ISSN: 01421123. DOI: 10.1016/j.ijfatigue.2011.10.012.

[94] J. Mei and P. Dong. "A new path-dependent fatigue damage model for non-proportional multi-axial loading". In: *International Journal of Fatigue* 90 (2016), pp. 210–221. ISSN: 01421123. DOI: 10.1016/j.ijfatigue.2016.05.010.

[95] A. Fatemi and L. Yang. "Cumulative fatigue damage and life prediction theories: a survey of the state of the art for homogeneous materials". In: *International Journal of Fatigue* 20 (1 Jan. 1998), pp. 9–34. ISSN: 0142-1123. DOI: 10.1016/S0142-1123(97)00081-9.

[96] K. Hectors and W. De Waele. "Cumulative damage and life prediction models for high-cycle fatigue of metals: A review". In: *Metals* 11 (2 Feb. 2021), pp. 1–32. ISSN: 20754701. DOI: 10.3390/met11020204.

[97] A. Palmgren. "Die Lebensdauer von Kugellagern (Life Length of Roller Bearings or Durability of Ball Bearings)". In: *Zeitschrift des Vereines Deutscher Ingenieure* 14 (1924), pp. 339–341.

[98] M. A. Miner. "Cumulative Damage in Fatigue". In: *Journal of Applied Mechanics* 12 (3 Sept. 1945), A159–A164. ISSN: 0021-8936. DOI: 10.1115/1.4009458.

[99] M. Deul. *Fatigue damage accumulation in steel welded joints, subject to (random) variable amplitude loading conditions: An improved fatigue-life model for naval ship structural design.* (Master Thesis). 2021.

[100] W. Fricke and H. Paetzold. "Effect of whipping stresses on the fatigue damage of ship structures". In: *Welding in the World* 58 (2 2014), pp. 261–268. ISSN: 00432288. DOI: 10.1007/s40194-014-0111-5.

[101] T. R. Gurney. *Cumulative damage of welded joints*. Woodhead Publishing, 2006, p. 442. ISBN: 9781855739383.

[102] C. M. Sonsino and T. Łagoda. "Assessment of multiaxial fatigue behaviour of welded joints under combined bending and torsion by application of a fictitious notch radius". In: *International Journal of Fatigue* 26 (3 2004), pp. 265–279. ISSN: 01421123. DOI: 10.1016/S0142-1123(03)00143-9.

[103] H. Agerskov. "Fatigue in steel structures under random loading". In: *Journal of Constructional Steel Research* 53 (3 2000), pp. 283–305. ISSN: 0143974X. DOI: 10.1016/S0143-974X(99)00042-5.

[104] L. Xi and Z. Songlin. "Strengthening and damaging under low-amplitude loads below the fatigue limit". In: *International Journal of Fatigue* 31 (2 Feb. 2009), pp. 341–345. ISSN: 01421123. DOI: 10.1016/j.ijfatigue.2008.08.004.

[105] E. Haibach. "The allowable stresses under variable amplitude loading of welded joints". In: *Proceedings of the Conference of the Fatigue Welded Structures*. Vol. 2. The Welding Institute, 1971, pp. 328–339.

[106] C. M. Sonsino, T. Łagoda, and G. Demofonti. "Damage accumulation under variable amplitude loading of welded medium- and high-strength steels". In: *International Journal of Fatigue* 26 (5 May 2004), pp. 487–495. ISSN: 01421123. DOI: 10.1016/j.ijfatigue.2003.10.001.

[107] D. Leonetti, J. Maljaars, and H. H. Snijder. "Fitting fatigue test data with a novel S-N curve using frequentist and Bayesian inference". In: *International Journal of Fatigue* 105 (Dec. 2017), pp. 128–143. ISSN: 0142-1123. DOI: 10.1016/J.IJFATIGUE.2017.08.024.

[108] DNV-GL. *Fatigue assessment of ship structures. Classification note 30.7.* DNV-GL, 2014.

[109] H. J. Gough and H. V. Pollard. "The Strength of Metals under Combined Alternating Stresses:" in: *Proc Int Mech Eng* 131 (1 Feb. 1935), pp. 3–103. ISSN: 0020-3483.

[110] C. M. Sonsino. "Multiaxial fatigue assessment of welded joints - Recommendations for design codes". In: *International Journal of Fatigue* 31 (1 2009), pp. 173–187. ISSN: 01421123. DOI: 10.1016/j.ijfatigue.2008.06.001.

[111] B. Crossland. "Effect of large hydrostatic stress on the torsional fatigue strength of an alloy steel". In: *International Conference on Fatigue of Metals* (1956), pp. 138–149.

[112] P. Dong and J. K. Hong. "The Master S-N Curve Approach to Fatigue Evaluation of Offshore and Marine Structures". In: *23rd International Conference on Offshore Mechanics and Arctic Engineering, Volume 2*. 2004, pp. 847–855.

[113] P. Dong. "A robust structural stress method for fatigue analysis of ship structures". In: *Proceedings of the International Conference on Offshore Mechanics and Arctic Engineering - OMAE*. Vol. 3. American Society of Mechanical Engineers Digital Collection, Jan. 2003, pp. 199–211. DOI: 10.1115/OMAE2003-37313.

[114] DNV. "RP-C203: Fatigue Design of Offshore Steel Structures". In: *Recommended Practice DNV-RPC203* (October 2014), p. 126.

[115] D. M. Rodrigues, C. Leitão, M. Balakrishnan, H. D. Craveiro, and A. Santiago. "Tensile properties of S355 butt welds after exposure to high temperatures". In: *Construction and Building Materials* 302 (Oct. 2021), p. 124374. ISSN: 0950-0618. DOI: 10.1016/J.CONBUILDMAT.2021.124374.

[116] L. Konat and B. Białobrzeska. "Effect of welding technique and thermal treatment parameters on abrasive wear of steel S355". In: *Tribologia* 301 (3 Nov. 2022), pp. 25–38. ISSN: 0208-7774. DOI: 10.5604/01.3001.0016.1021.

[117] C. Pandey, A. Giri, M. M. Mahapatra, and P. Kumar. "Characterization of Microstructure of HAZs in As-Welded and Service Condition of P91 Pipe Weldments". In: *Met. Mater. Int* 23 (1 2017), pp. 148–162. DOI: 10.1007/s12540-017-6394-5.

[118] A. M. De Jesus, R. Matos, B. F. Fontoura, C. Rebelo, L. S. Da Silva, and M. Veljkovic. "A comparison of the fatigue behavior between S355 and S690 steel grades". In: *Journal of Constructional Steel Research* 79 (Dec. 2012), pp. 140–150. ISSN: 0143-974X. DOI: 10.1016/J.JCSR.2012.07.021.

[119] H. Amstutz, K. Störzel, and T. Seeger. "Fatigue crack growth of a welded tube-flange connection under bending and torsional loading". In: *Fatigue and Fracture of Engineering Materials and Structures* 24 (5 2001), pp. 357–368. ISSN: 8756758X. DOI: 10.1046/j.1460-2695.2001.00408.x.

[120] G. R. Razmjoo. "Fatigue of load-carrying fillet welded joints under multiaxial loading". In: *Fatigue – core research from TWI. European structural integrity society*. 2000, pp. 63–99.

[121] G. Meneghetti, A. Campagnolo, V. Babini, M. Riboli, and A. Spagnoli. "Multiaxial fatigue assessment of welded steel details according to the peak stress method: Industrial case studies". In: *International Journal of Fatigue* 125 (Aug. 2019), pp. 362–380. ISSN: 01421123. DOI: 10.1016/j.ijfatigue.2019.04.014.

[122] I. Takahashi, A. Takada, M. Ushijima, and S. Akiyama. "Fatigue behaviour of a box-welded joint under biaxial cyclic loading: Effects of biaxial load range ratio and cyclic compressive loads in the lateral direction". In: *Fatigue and Fracture of Engineering Materials and Structures* 26 (5 2003), pp. 439–448. ISSN: 8756758X. DOI: 10.1046/j.1460-2695.2003.00645.x.

[123] I. Kim and K. Yamada. "Fatigue behaviour of fillet welded joints inclined to a uniaxial cyclic load". In: *IIW Document XIII-2021-04* (2004).

[124] S. J. Maddox. "Fatigue assessment of welds not oriented either normal or parallel to the direction of loading". In: *IIW Document J WG XIII/ XV-218-10* (2010).

[125] T. Dahle, K. E. Olsson, and J. Samuelsson. "Fatigue design optimisation of welded box beams subjected to combined bending and torsion". In: *European Structural Integrity Society* 23 (C 1999), pp. 103–116. ISSN: 15661369. DOI: 10.1016/S1566-1369(99)80034-X.

[126]   Y. Qin, J. Den Besten, and M. L. Kaminski. "Weld toe and weld root notch induced fatigue of welded joints in steelmarine structures: effective notch stress and total stress concept evaluations". In: *International journal of Fatigue* (2023). (in preparation).

[127]   M. Fonte, L. Reis, F. Romeiro, B. Li, and M. De Freitas. "The effect of steady torsion on fatigue crack growth in shafts". In: *International Journal of Fatigue* 28 (5-6 May 2006), pp. 609–617. ISSN: 0142-1123. DOI: 10.1016/J.IJFATIGUE.2005.06.051.

[128]   J. K. Hong and T. P. Forte. "Fatigue Evaluation Procedures for Multiaxial Loading in Welded Structures Using Battelle Structural Stress Approach". In: *Proceedings of the International Conference on Offshore Mechanics and Arctic Engineering - OMAE* 5 (Oct. 2014). DOI: 10.1115/OMAE2014-23459.

[129]   L. Susmel and P. Lazzarin. "A bi-parametric Wöhler curve for high cycle multiaxial fatigue assessment". In: *Fatigue & Fracture of Engineering Materials & Structures* 25 (1 Jan. 2002), pp. 63–78. ISSN: 1460-2695. DOI: 10.1046/J.1460-2695.2002.00462.X.

[130]   G. Bufalari, J. H. den Besten, and M. L. Kaminski. "Mode-{I, III} multiaxial fatigue of welded joints in steel maritime structures: Effective notch stress based resistance incorporating strength and mechanism contributions". In: *International Journal of Fatigue* 180 (2024), p. 108067. ISSN: 0142-1123. DOI: https://doi.org/10.1016/j.ijfatigue.2023.108067.

[131]   P. Dong, J. K. Hong, and A. M. P. De Jesus. "Analysis of Recent Fatigue Data Using the Structural Stress Procedure in ASME Div 2 Rewrite". In: *Journal of Pressure Vessel Technology* 129.3 (May 2006), pp. 355–362. ISSN: 1528-8978. DOI: 10.1115/1.2748818.

[132]   P. Dong, J. K. Hong, and Z. Cao. "Stresses and stress intensities at notches: 'Anomalous crack growth' revisited". In: *International Journal of Fatigue* 25 (9-11 Sept. 2003), pp. 811–825. ISSN: 01421123. DOI: 10.1016/S0142-1123(03)00130-0.

[133]   W. Fricke, M. Codda, O. Feltz, Y. Garbatov, H. Remes, G. Risso, C. Rizzo, and J. Romanoff. "Round-Robin on Local Stress Determination and Fatigue Assessment of Load-Carrying Fillet-Welded Joints". English. In: *Adavances in marine structures*. United States: CRC Press, Mar. 2011, pp. 295–302. ISBN: 978-0-203-80811-5.

[134]   Z. Li, J. W. Ringsberg, and G. Storhaug. "Time-domain fatigue assessment of ship side-shell structures". In: *International Journal of Fatigue* 55 (Oct. 2013), pp. 276–290. ISSN: 0142-1123. DOI: 10.1016/j.ijfatigue.2013.07.007.

[135]   I. Senjanovic, N. Vladimir, M. Tomic, N. Hadzic, and S. Malenica. "Global hydroelastic analysis of ultra large container ships by improved beam structural model". In: *International Journal of Naval Architecture and Ocean Engineering* 6.4 (Dec. 2014), pp. 1041–1063. ISSN: 2092-6782. DOI: 10.2478/ijnaoe-2013-0230.

[136] J. K. Hong and T. P. Forte. "Fatigue Evaluation Procedures for Bi-axial Loaded Plate Joints Using the Battelle Structural Stress Method". In: *Procedia Engineering* 133 (2015), pp. 410–419. ISSN: 18777058. DOI: 10.1016/j.proeng.2015.12.611.

[137] J. Mei and P. Dong. "An equivalent stress parameter for multi-axial fatigue evaluation of welded components including non-proportional loading effects". In: *International Journal of Fatigue* 101 (2017), pp. 297–311. ISSN: 01421123. DOI: 10.1016/j.ijfatigue.2017.01.006.

[138] H. F. Bueckner. *Weight functions and fundamental fields for the penny-shaped and the half-plane crack in three-space*. 1987.

[139] P. Dong, J. Hong, D. Osage, and M. Prager. "Master S-N curve method for fatigue evaluation of welded components". In: *Welding Research Council Bulletin* (Aug. 2002), pp. 1–44.

[140] H. Tada, P. C. Paris, and G. R. Irwin. *The Stress Analysis of Cracks Handbook, Third Edition*. ASME Press, July 2000. DOI: 10.1115/1.801535.

[141] E. Amsterdam and F. Grooteman. "The influence of stress state on the exponent in the power law equation of fatigue crack growth". In: *International Journal of Fatigue* 82 (Jan. 2016), pp. 572–578. ISSN: 01421123. DOI: 10.1016/j.ijfatigue.2015.09.013.

[142] E. Amsterdam, J. W. Wiegman, M. Nawijn, and J. T. M. D. Hosson. "The effect of crack length and maximum stress on the fatigue crack growth rates of engineering alloys". In: *International Journal of Fatigue* 161 (Aug. 2022). ISSN: 01421123. DOI: 10.1016/j.ijfatigue.2022.106919.

[143] K. Sadananda and A. K. Vasudevan. "Short crack growth and internal stresses". In: *International Journal of Fatigue* 19 (1 1997), pp. 99–108.

[144] K. Sadananda and A. Vasudevan. "Crack tip driving forces and crack growth representation under fatigue". In: *International Journal of Fatigue* 26.1 (2004), pp. 39–47. ISSN: 0142-1123. DOI: https://doi.org/10.1016/S0142-1123(03)00105-1.

[145] K. Sadananda, M. Nani Babu, and A. Vasudevan. "The unified approach to subcritical crack growth and fracture". In: *Engineering Fracture Mechanics* 212 (2019), pp. 238–257. ISSN: 0013-7944. DOI: https://doi.org/10.1016/j.engfracmech.2019.03.010.

[146] J.-S. Kim, C. Kim, T.-E. Jin, and P. Dong. "Mean load effect on fatigue of welded joints using structural stress and fracture mechanics approach". In: *Nuclear engineering and technology* 38.3 (2006), pp. 277–284.

[147] W. Zhou, P. Dong, I. Lillemäe, and H. Remes. "Analytical treatment of distortion effects on fatigue behaviors of lightweight shipboard structures". In: *International Journal of Fatigue* 130 (2020), p. 105286. ISSN: 0142-1123. DOI: https://doi.org/10.1016/j.ijfatigue.2019.105286.

[148] P. Dong. "Length scale of secondary stresses in fracture and fatigue". In: *International Journal of Pressure Vessels and Piping* 85.3 (2008), pp. 128–143.

[149] E. K. Tschegg. "Mode III and Mode I fatigue crack propagation behaviour under torsional loading". In: *Journal of Materials Science* 18.6 (June 1983), pp. 1604–1614. ISSN: 1573-4803. DOI: 10.1007/bf00542053.

[150] S. Beretta, S. Foletti, M. G. Tarantino, and J. Lai. "Comparison between Mode I and Mode III crack propagation under pure shear and RCF conditions". In: (Feb. 2011).

[151] S. Qi, L. X. Cai, K. K. Shi, and C. Bao. "A Prediction Model for Mode-III Fatigue Crack Growth". In: *Applied Mechanics and Materials* 853 (Sept. 2016), pp. 41–45. ISSN: 1662-7482. DOI: 10.4028/www.scientific.net/amm.853.41.

[152] M. Duda, D. Rozumek, G. Lesiuk, M. Smolnicki, B. Babiarczuk, and J. Warycha. "Fatigue crack growth under mixed-mode I+II and I+III in heat treated 42CrMo4 steel". In: *International Journal of Fracture* 234.1–2 (Sept. 2021), pp. 235–248. ISSN: 1573-2673. DOI: 10.1007/s10704-021-00585-0.

[153] E. Macha and D. Rozumek. "Fatigue crack growth in 18G2A steel under mixed mode I+III loading". In: European Structural Integrity Society. 2015.

[154] D. Rozumek, Z. Marciniak, G. Lesiuk, and J. A. Correia. "Mixed mode I/II/III fatigue crack growth in S355 steel". In: vol. 5. Elsevier B.V., 2017, pp. 896–903. DOI: 10.1016/j.prostr.2017.07.125.

[155] K. Tanaka. "Small fatigue crack propagation in notched components under combined torsional and axial loading". In: *Procedia Engineering* 2.1 (Apr. 2010), pp. 27–46. ISSN: 1877-7058. DOI: 10.1016/j.proeng.2010.03.004.

[156] K. Tanaka. "Crack initiation and propagation in torsional fatigue of circumferentially notched steel bars". In: *International Journal of Fatigue* 58 (Jan. 2014), pp. 114–125. ISSN: 0142-1123. DOI: 10.1016/j.ijfatigue.2013.01.002.

[157] M. Vormwald. "Observations and modelling of non-proportional mixed mode cyclic loading". In: *MATEC Web of Conferences* 300 (2019). Ed. by T. Palin-Luc, F. Morel, and A. Carpinteri, p. 01002. ISSN: 2261-236X. DOI: 10.1051/matecconf/201930001002.

[158] H. Richard, A. Eberlein, and G. Kullmer. "Concepts and experimental results for stable and unstable crack growth under 3D-mixed-mode-loadings". In: *Engineering Fracture Mechanics* 174 (Apr. 2017), pp. 10–20. ISSN: 0013-7944. DOI: 10.1016/j.engfracmech.2016.12.005.

[159] S. Sajith, K. S. Murthy, and P. S. Robi. "Fatigue life prediction under mixed-mode loading using equivalent stress intensity factor models". In: vol. 172. EDP Sciences, June 2018. DOI: 10.1051/matecconf/201817203005.

[160] M. Schöllmann, H. A. Richard, G. Kullmer, and M. Fulland. In: *International Journal of Fracture* 117.2 (2002), pp. 129–141. ISSN: 0376-9429. DOI: 10.1023/a:1020980311611.

[161] L. Liu. "Modeling of mixed-mode fatigue crack propagation". PhD thesis. Vanderbilt University, 2008.

[162] J. Qian and A. Fatemi. "Mixed mode fatigue crack growth: A literature survey". In: *Engineering Fracture Mechanics* 55.6 (Dec. 1996), pp. 969–990. ISSN: 0013-7944. DOI: 10.1016/s0013-7944(96)00071-9.

[163] F. Fremy, S. Pommier, M. Poncelet, B. Raka, E. Galenne, S. Courtin, and J.-C. L. Roux. "Load path effect on fatigue crack propagation in I+II+III mixed mode conditions – Part 1: Experimental investigations". In: *International Journal of Fatigue* 62 (May 2014), pp. 104–112. ISSN: 0142-1123. DOI: 10.1016/j.ijfatigue.2013.06.002.

[164] J. Predan, V. Močilnik, and N. Gubeljak. "Stress intensity factors for circumferential semi-elliptical surface cracks in a hollow cylinder subjected to pure torsion". In: *Engineering Fracture Mechanics* 105 (June 2013), pp. 152–168. ISSN: 0013-7944. DOI: 10.1016/j.engfracmech.2013.03.033.

[165] J. Rethore, A. Gravouil, F. Morestin, and A. Combescure. "Estimation of mixed-mode stress intensity factors using digital image correlation and an interaction integral". In: *International Journal of Fracture* 132.1 (Mar. 2005), pp. 65–79. ISSN: 1573-2673. DOI: 10.1007/s10704-004-8141-4.

[166] J. K. Hong. "Re-Evaluation of Fatigue Evaluation Procedures for Weld Root Failure". In: *SAE Technical Paper Series*. ANNUAL. SAE International, Apr. 2019. DOI: 10.4271/2019-01-0529.

[167] H. Yang, P. Wang, H. Qian, and P. Dong. "Analysis of fatigue test conditions for reproducing weld toe cracking into U-rib wall in orthotropic bridge decks". In: *International Journal of Fatigue* 162 (Sept. 2022), p. 106976. ISSN: 0142-1123. DOI: 10.1016/j.ijfatigue.2022.106976.

[168] P. Dong and J. K. Hong. "A robust structural stress parameter for evaluation of multiaxial fatigue of weldments". In: *ASTM Special Technical Publication* 1480 STP (2007), pp. 206–222. ISSN: 00660558. DOI: 10.1520/STP45516S.

[169] Z. Wei and P. Dong. "Multiaxial fatigue life assessment of welded structures". In: *Engineering Fracture Mechanics* 77.15 (Oct. 2010), pp. 3011–3021. ISSN: 0013-7944. DOI: 10.1016/j.engfracmech.2010.03.045.

[170] Z. Mikulski and T. Lassen. "Fatigue crack initiation and subsequent crack growth in fillet welded steel joints". In: *International Journal of Fatigue* 120 (Mar. 2019), pp. 303–318. DOI: 10.1016/j.ijfatigue.2018.11.014.

[171] U. Zerbst, M. Madia, and B. Schork. "Fracture mechanics based determination of the fatigue strength of weldments". In: *Procedia Structural Integrity* 1 (2016), pp. 10–17. DOI: 10.1016/j.prostr.2016.02.003.

[172] U. Zerbst, M. Madia, and M. Vormwald. "Fatigue strength and fracture mechanics". In: *Procedia Structural Integrity* 5 (2017), pp. 745–752. DOI: 10.1016/j.prostr.2017.07.165.

[173] D. Benasciutti, F. Sherratt, and A. Cristofori. "Basic principles of spectral multi-axial fatigue analysis". In: *Procedia Engineering* 101 (C 2015), pp. 34–42. ISSN: 18777058. DOI: 10.1016/j.proeng.2015.02.006.

[174]   M. Quaresimin and L. Susmel. "Multiaxial Fatigue Behaviour of Composite Laminates". In: *Key Engineering Materials* 221–222 (Dec. 2001), pp. 71–80. ISSN: 1662-7795. DOI: 10.4028/www.scientific.net/kem.221-222.71.

[175]   P. Costa, R. Nwawe, H. Soares, L. Reis, M. Freitas, Y. Chen, and D. Montalvão. "Review of Multiaxial Testing for Very High Cycle Fatigue: From 'Conventional' to Ultrasonic Machines". In: *Machines* 8.2 (May 2020), p. 25. DOI: 10.3390/machines8020025. URL: https://doi.org/10.3390/machines8020025.

[176]   M. Kamaya. "Development of disc bending fatigue test technique for equi-biaxial loading". In: *International Journal of Fatigue* 82 (2016), pp. 561–571. ISSN: 0142-1123. DOI: https://doi.org/10.1016/j.ijfatigue.2015.09.012.

[177]   M. K. Almamoori, Y. Alizadeh, and M. Abolghasemzadeh. "A Review of Multi-Axial Fatigue Tests". In: *IOP Conference Series: Materials Science and Engineering* 1094.1 (Feb. 2021), p. 012058. DOI: 10.1088/1757-899x/1094/1/012058. URL: https://doi.org/10.1088/1757-899x/1094/1/012058.

[178]   M. Morishita, K. Gotoh, Y. Anai, S. Tsumura, and T. Niwa. "Fatigue surface crack growth behavior in flat plate and out-of-plane gusset-welded joints under biaxial cyclic loads with different phases". In: *Journal of Marine Science and Technology* 26.3 (Sept. 2020), pp. 655–672. ISSN: 1437-8213. DOI: 10.1007/s00773-020-00762-1.

[179]   J. Chen and J. Zhang. "Optimal Boundary Shape of the Center-Reduced Cruciform Specimen for the In-Plane Biaxial Test". In: *Advances in Machinery, Materials Science and Engineering Application*. IOS Press, Sept. 2022. DOI: 10.3233/atde220463.

[180]   A. Gryguc, S. Behravesh, H. Jahed, M. Wells, W. Macek, and B. Williams. "The Multiaxial Load Proportionality Effect on the Fracture Surface Topography of Forged Magnesium Alloys". In: *13th International Conference on Multiaxial Fatigue and Fracture (ICMFF13)*. Nov. 2022.

[181]   J.-W. Seo, H.-M. Hur, H.-K. Jun, S.-J. Kwon, and D.-H. Lee. "Fatigue Design Evaluation of Railway Bogie with Full-Scale Fatigue Test". In: *Advances in Materials Science and Engineering* 2017 (2017), pp. 1–11. ISSN: 1687-8442. DOI: 10.1155/2017/5656497.

[182]   Y. Kvistedal and P. Nielsen. "Investigating stress-strain properties of in-vivo human skin using multiaxial loading experiments and finite element modeling". In: *The 26th Annual International Conference of the IEEE Engineering in Medicine and Biology Society*. Vol. 2. 2004, pp. 5096–5099. DOI: 10.1109/IEMBS.2004.1404408.

[183]   C. French, A. Schultz, J. Hajjar, C. Shield, D. Ernie, R. Dexter, C. Du, S. Olson, D. Daugherty, and C. Wan. "Multi-axial subassemblage testing (MAST) system: description and capabilities". In: *13th World Conference on Earthquake Engineering (WCEE)*. Aug. 2004.

[184] M. Becerra-Vargas and E. Morgado Belo. "Application of H ∞ theory to a 6 DOF flight simulator motion base". In: *Journal of the Brazilian Society of Mechanical Sciences and Engineering* 34.2 (June 2012), pp. 193–204. ISSN: 1678-5878. DOI: 10.1590/s1678-58782012000200011.

[185] M. Karimi, C. Kosinski, and L. Brosset. "Comparison of Sloshing Model Test Results at Scales 1:10 and 1:40". In: *Proc. of the 23rd Int. Offshore and Polar Engineering Conf. (ISOPE)*. Vol. 3. July 2013, pp. 224–234.

[186] W. J.L., d. B. J.H., S. H.C., S. R.L.G., and D. Rick. "Multiaxial Stress Response in TLP-type FOWT Substructures: An Investigation into Fatigue Assessment of Critical Weld Seams in the Time Domain". Master's thesis. Delft University of Technology, 2024.

[187] L. Wang, X. Qian, and L. Feng. "Effect of welding residual stresses on the fatigue life assessment of welded connections". In: *International Journal of Fatigue* 189 (Dec. 2024), p. 108570. ISSN: 0142-1123. DOI: 10.1016/j.ijfatigue.2024.108570.

[188] H. Xin, J. A. Correia, M. Veljkovic, F. Berto, and L. Manuel. "Residual stress effects on fatigue life prediction using hardness measurements for butt-welded joints made of high strength steels". In: *International Journal of Fatigue* 147 (June 2021), p. 106175. ISSN: 0142-1123. DOI: 10.1016/j.ijfatigue.2021.106175.

[189] S. Lippardt. "Influence of the geometry on the fatigue strength of welded joints using the effective notch stress approach". In: *Welding in the World* 67.3 (Nov. 2022), pp. 669–681. ISSN: 1878-6669. DOI: 10.1007/s40194-022-01409-y.

[190] S. Sedmak, Z. Burzić, S. Perković, R. Jovičić, M. Aranđelović, L. Radović, and N. Ilić. "Influence of welded joint microstructures on fatigue behaviour of specimens with a notch in the heat affected zone". In: *Engineering Failure Analysis* 106 (Dec. 2019), p. 104162. ISSN: 1350-6307. DOI: 10.1016/j.engfailanal.2019.104162.

[191] J.-S. Zhao, X.-C. Sun, and S.-T. Wei. "Kinematics and statics of the Gough-Stewart platform". In: *Appl. Sci. (Basel)* 13.18 (Sept. 2023), p. 10150.

[192] P. P. Darcis, T. Lassen, and N. Récho. "Fatigue behavior of welded joints Part 2: Physical modeling of the fatigue process". In: *Welding Journal* 85 (2006).

[193] B. Schork, U. Zerbst, Y. Kiyak, M. Kaffenberger, M. Madia, and M. Oechsner. "Effect of the parameters of weld toe geometry on the FAT class as obtained by means of fracture mechanics-based simulations". In: *Welding in the World* 64.6 (May 2020), pp. 925–936. ISSN: 1878-6669. DOI: 10.1007/s40194-020-00874-7.

[194] J. Schubnell, M. Jung, C. H. Le, M. Farajian, M. Braun, S. Ehlers, W. Fricke, M. Garcia, A. Nussbaumer, and J. Baumgartner. "Influence of the optical measurement technique and evaluation approach on the determination of local weld geometry parameters for different weld types". In: *Welding in the World* 64.2 (Dec. 2019), pp. 301–316. ISSN: 1878-6669. DOI: 10.1007/s40194-019-00830-0.

[195]   E. Bain and A. S. for Metals. *Functions of the Alloying Elements in Steel*. American Society for Metals, 1939.

[196]   A. Casagrande, G. Cammarota, and L. Micele. "Relationship between fatigue limit and Vickers hardness in steels". In: *Materials Science and Engineering: A* 528.9 (Apr. 2011), pp. 3468–3473. ISSN: 0921-5093. DOI: 10.1016/j.msea.2011.01.040.

[197]   G. Bufalari, J. H. den Besten, J. K. Hong, and M. L. Kaminski. "Mode-{I, III} multiaxial fatigue of welded joints in steel maritime structures: Total stress based resistance incorporating strength and mechanism contributions". In: *International Journal of Fatigue* (July 2024), p. 108499. ISSN: 0142-1123. DOI: 10.1016/j.ijfatigue.2024.108499.

[198]   P. Luo, W. Yao, and P. Li. "A notch critical plane approach of multiaxial fatigue life prediction for metallic notched specimens". In: *Fatigue & Fracture of Engineering Materials & Structures* 42.4 (Dec. 2018), pp. 854–870. ISSN: 1460-2695. DOI: 10.1111/ffe.12956.

[199]   J. Schijve. *Biaxial Fatigue of Metals: The Present Understanding*. Springer International Publishing, 2016. ISBN: 9783319236063. DOI: 10.1007/978-3-319-23606-3.

[200]   C. M. Sonsino. "Course of SN-curves especially in the high-cycle fatigue regime with regard to component design and safety". In: *International Journal of Fatigue* 29.12 (Dec. 2007), pp. 2246–2258. ISSN: 0142-1123. DOI: 10.1016/j.ijfatigue.2006.11.015.

[201]   C. M. Sonsino. "Effects on Lifetime under Spectrum Loading". In: *Materials Testing* 52.7–8 (July 2010), pp. 440–451. ISSN: 0025-5300. DOI: 10.3139/120.110146.

[202]   K. O. Ronold and I. Lotsberg. "On the estimation of characteristic S–N curves with confidence". In: *Marine Structures* 27.1 (July 2012), pp. 29–44. ISSN: 0951-8339. DOI: 10.1016/j.marstruc.2012.03.002.

[203]   K. Rother and W. Fricke. "Effective notch stress approach for welds having low stress concentration". In: *International Journal of Pressure Vessels and Piping* 147 (Nov. 2016), pp. 12–20. ISSN: 0308-0161. DOI: 10.1016/j.ijpvp.2016.09.008.

[204]   G. Fu, W. Yang, and C.-Q. Li. "Stress intensity factors for mixed mode fracture induced by inclined cracks in pipes under axial tension and bending". In: *Theoretical and Applied Fracture Mechanics* 89 (June 2017), pp. 100–109. ISSN: 0167-8442. DOI: 10.1016/j.tafmec.2017.02.001.

[205]   M. Margetin, R. Durka, and V. Chmelko. "Multiaxial fatigue criterion based on parameters from torsion and axial S-N curve". In: *Frattura ed Integrità Strutturale* 10.37 (June 2016), pp. 146–152. DOI: 10.3221/igf-esis.37.20.

[206] M. Mršnik, J. Slavič, and M. Boltežar. "Frequency-domain methods for a vibration-fatigue-life estimation – Application to real data". In: *International Journal of Fatigue* 47 (Feb. 2013), pp. 8–17. ISSN: 0142-1123. DOI: `10.1016/j.ijfatigue.2012.07.005`.

[207] S. K. Ravi and P. Dong. "A spectral fatigue method incorporating non-proportional multiaxial loading". In: *International Journal of Fatigue* 131 (Feb. 2020), p. 105300. ISSN: 0142-1123. DOI: `10.1016/j.ijfatigue.2019.105300`.

[208] S. K. Ravi, P. Dong, and Z. Wei. "Data-driven modeling of multiaxial fatigue in frequency domain". In: *Marine Structures* 84 (July 2022), p. 103201. ISSN: 0951-8339. DOI: `10.1016/j.marstruc.2022.103201`.

[209] D. Benasciutti, F. Sherratt, and A. Cristofori. "Recent developments in frequency domain multi-axial fatigue analysis". In: *International Journal of Fatigue* 91 (Oct. 2016), pp. 397–413. ISSN: 0142-1123. DOI: `10.1016/j.ijfatigue.2016.04.012`.

ACKNOWLEDGEMENTS

for his contribution to Chapter 4, and for always being very kind and helpful; Niels Troost, for his contribution to Chapter 5, and for being as solid as a rock in his support as a room mate and a good friend. I should also mention Yanxin Qin for his great contribution as a fellow Ph.D. student, studying the same topic. I hope to read your thesis soon. And to Paula van Lieshout, for having initiated the 4D-Fatigue project and all that meant, for having been a great discussion partner, and for being a lively and unconventional spirit. A special thank goes to the memory of Sandro; his spark ignited my passion for sailing, and everything has followed from there.

I would like to thank my former room mates, Reinier Bos and Peter Wellens, for always being there for a chat, coffee, discussion, gossip, beer, advice, dinner, Dutch culture lesson, joke, and masterclasses on Italian cuisine. And mostly, for being there as real friends.

I would like to thank all the colleagues and friends, both past and present, who were part of my experience as a Ph.D. candidate: Hugo, Martin, Marco, Pengpeng, Bart, Saloni, Gracia, Hans, Peter, Arno, Hanna, Evelien, Anna, Monique, Tessa, Nikos, Wei Jun, Cecilia, Vasu, Sanne, Mohammed, Pascal, Menno, Bijan, Reza, Tao, Mathieu, Angeliki, Kevin, Ad, Bong Jun, Xiabo, Pieter, Carey, Pooria, Harleigh, Andrea, Joost, Cornel, Tom, Henk, Antonio, Sebastian, Apostolos, Gabe, Anouk, Dineke, Bendiks Jan and all the others I might have forgotten. You have been part of my daily life for years, thank you for being such a beautiful family.

I would like to thank all my students who patiently followed my lessons, you have been my joy and pain for years. And the students I supervised for their master's thesis – it has been a pleasure to see you shine in your success.

I would like to thank my house mates from Brahmslaan – Vittorio (and Raffa), Francesco (and Anika), Filippo, Brian, Marina and Michela –, from Hippolytusbuurt and Oostplein; Lorenzo, Tony and Marta – who owns a Ph.D. in propositions. There's no need to spend words to express to each one of you how grateful I am for the time we have spent together; it lives rent-free in my heart. By the way, after years of complaining with you about how miserable the life of a Ph.D. student is, this is what you get from me (alongside some Sunday lunch memories). I know you won't read this book, so please use it as a nice stand for your monitors.

I would like to thank my parents Paola and Stefano, my brother Giorgio with Alessandra and "little sausage" Vittoria, my aunt Anna Rita, grandma Renè, uncle Sergio, the memory of Felice, Nerino, Adele and all the other family members for always being there, for accepting my decisions, and for loving me. Your support has been fundamental, more than what you can reasonably imagine.

I would like to thank all my friends, from the old ones belonging to my childhood, to those I met during my university studies in La Spezia, and finally to the most recent ones. You are a mighty, indestructible part of my life, and I love you.

CURRICULUM VITÆ

Gabriele BUFALARI

31-08-1991   Born in Orvieto, Italy.

EDUCATION

2019–2024   Ph.D. research
Department of Maritime and Transport Technology
Delft University of Technology, Delft, the Netherlands

Thesis: On Multiaxial Fatigue of Welded Joints in Steel Maritime Structures: strength and mechanism contributions

Promotor: Prof. dr. ir. M.L. Kaminski
Copromotor: Dr. ir. J.H. den Besten

2017 – 2019   Junior researcher
Delft University of Technology

2014–2017   M.Sc. study *with honors*
Yacht Design
University of Genova, La Spezia, Italy

2010–2014   B.Sc. study
Ingegneria Nautica
University of Genova, La Spezia, Italy

LIST OF PUBLICATIONS

1. G. Bufalari, P. S. Van Lieshout, M. L. Kaminski, and J. H. Den Besten. "Numerical comparative study of multiaxial fatigue methods applied to welded joints in a container vessel". In: *5th Symposium on Structural Durability (SoSDiD)* (May 2017)

2. G. Bufalari, J. H. Den Besten, and M. L. Kaminski. "Mode-III fatigue of welded joints in steel maritime structures: Weld notch shear stress distributions and effective notch stress based resistance". In: *International Journal of Fatigue* (Aug. 2022), p. 107210. ISSN: 0142-1123. DOI: 10.1016/J.IJFATIGUE.2022.107210

3. G. Bufalari, J. H. den Besten, and M. L. Kaminski. "Mode-{I, III} multiaxial fatigue of welded joints in steel maritime structures: Effective notch stress based resistance incorporating strength and mechanism contributions". In: *International Journal of Fatigue* 180 (2024), p. 108067. ISSN: 0142-1123. DOI: https://doi.org/10.1016/j.ijfatigue.2023.108067

4. G. Bufalari, J. H. den Besten, J. K. Hong, and M. L. Kaminski. "Mode-{I, III} multiaxial fatigue of welded joints in steel maritime structures: Total stress based resistance incorporating strength and mechanism contributions". In: *International Journal of Fatigue* (July 2024), p. 108499. ISSN: 0142-1123. DOI: 10.1016/j.ijfatigue.2024.108499

5. G. Bufalari, N. C. H. Troost, J. H. den Besten, and M. L. Kaminski. "Mode-{I, III} multiaxial fatigue testing of high-performance welds in steel maritime structures using a hexapod". In: *International journal of Fatigue* (2025). (submitted to the Journal).